The Dissertation Committee for Robin Paul Forslund Certifies that this is the approved version of the following Dissertation:

Perovskite and Ruddlesden-Popper Oxides for Electrochemical Energy Conversion and Storage

Committee:

David A. Vanden Bout, Supervisor

Keith P. Johnston, Co-Supervisor

Keith J. Stevenson

Charles B. Mullins

Graeme A. Henkelman

Perovskite and Ruddlesden-Popper Oxides for Electrochemical Energy Conversion and Storage

by

Robin Paul Forslund

Dissertation

Presented to the Faculty of the Graduate School of

The University of Texas at Austin

in Partial Fulfillment

of the Requirements

for the Degree of

Doctor of Philosophy

The University of Texas at Austin

December 2018

Dedication

To my parents Eric and Kelly.

Acknowledgements

This dissertation would not have been possible without the brilliant work and dedication by many other scientists across a range of disciplines. First, I would like to thank Prof. Keith Stevenson for the intellectual support and opportunities he has given me over the last four years. I would also like to thank Prof. Keith Johnston for all of the support he has given me and the resources he has provided for myself and my collaborators. I would like to thank Prof. David Vanden Bout for taking over as my advisor in the chemistry department after the departure of Prof. Stevenson from the university, and I would also like to thank Prof. Buddie Mullins and Prof. Graeme Henkelman for serving on my doctoral committee and for taking the time to evaluate this dissertation.

To Tyler Mefford and Will Hardin, I owe a special thanks. Not only did you develop a fantastic platform from which to work on these materials and catalytic reactions, but you served as mentors and taught me not just about our science but how to organize and undertake research in an effective manner. You two weren't just coworkers, you were great friends and this would not have been possible without you. I would also like to thank Caleb Alexander for working alongside me in close quarters and accommodating my erratic work schedule, you taught me a great deal and we'll always be friends.

I would also like to thank my collaborators including, Artem Abakumov, Xi (Jerry) Rong, and Alexie Kolpak. We were able to overcome the great distances between us to create some incredible science and that would not have been possible without your drive and perseverance. Additionally, I would like to thank all of my fellow graduate students I have had the opportunity to work alongside including Andrew Worthen and Amro Elhag,

your friendship and insight helped a great deal in handling the highs and lows of life as a graduate student.

Thank you to all of my friends, both old and new, for the roles you have played in my time at UT Austin and well before, I wouldn't have made it through this process without your support. J. Cutty, our watch is finally over.

Finally, my deepest thanks and love to my family, especially my mother, Kelly, and my father, Eric. I can't even begin to grasp how much you have sacrificed to give me the opportunities that have brought me here. While I have improved a lot over the years, even doctoral candidates need to be told to do their homework every once in a while.

Abstract

Perovskite and Ruddlesden-Popper Oxides for Electrochemical Energy Conversion and Storage

Robin Paul Forslund, Ph.D.

The University of Texas at Austin, 2018

Supervisors: David A. Vanden Bout, Keith P. Johnston

With the growing threat of climate change and impending scarcity of fossil fuels it has become necessary to develop more efficient means of converting and storing energy from intermittent, renewable sources such as wind and solar. In an effort to help solve these broad issues, perovskite oxides with the nominal formula ABO_3 and derivatives of the perovskite crystal structure have been selected to investigate their possible application as materials to convert and store energy, either to catalyze the anodic reaction in the generation of hydrogen or to store charge themselves as pseudocapacitor materials. One commonly studied anodic reaction used in tandem with the evolution of hydrogen gas is the oxygen evolution reaction, and a series of Ruddlesden-Popper $La_{0.5}Sr_{1.5}Ni_{0.7}Fe_{0.3}O_{4+\delta}$ materials, a derivative of the perovskite structure, were used to demonstrate how previously proposed descriptors such as increased M – O bond covalency, Ni – Fe interactions, and utilization of a reaction mechanism that involves lattice oxygen in the evolution of oxygen gas could all be incorporated to yield a highly active catalyst and demonstrate how hybridization of electronic bands near the Fermi level may serve as a guiding design principle for future catalysts. In an effort to further reduce the cell voltage

needed to generated hydrogen, these types of materials were applied to the electrooxidations of urea, methanol and ethanol. $LaNiO_3$ perovskite was shown to display greater activity than materials containing Ni in lower oxidation states, and further raising the oxidation state of Ni in a series of Ruddlesden-Popper $La_{2-x}Sr_xNiO_{4+\delta}$ materials past Ni^{3+} continued to raise their activities toward the oxidations of these small molecules. Finally, $CaMnO_{3-\delta}$ perovksite and $Ca_2MnO_{4-\delta}$ Ruddlesden-Popper oxides were used to demonstrate the roles of surface redox reactions and bulk oxygen diffusion at varius scan rates in psedocapacitive charge storage through anion intercalation.

Table of Contents

List of Tables xiv

List of Figures xv

List of Illustrations xix

Chapter 1: Introduction 1

1.1: Perovskite and Ruddlesden-Popper Oxides 2

1.2: Oxygen Evolution 5

1.3: The Electrooxidation of Small Molecules 6

1.4: Batteries, Pseudocapacitors, and Supercapacitors: Faradaic and Non-Faradaic Charge Storage 8

1.4.1: Faradaic Charge Storage and Batteries. 9

1.4.2: Non-Faradaic Charge Storage, Supercapacitors, and Pseudocapacitors. 10

1.5: Outline 13

1.6: References 15

Chapter 2: Exceptional Electrocatalytic Oxygen Evolution Via Tunable Charge Transfer Interactions in $La_{0.5}Sr_{1.5}Ni_{1-x}Fe_xO_{4+\delta}$ Ruddlesden-Popper Oxides 20

2.1: Introduction 20

2.2: Experimental 23

2.2.1: Catalyst Synthesis 23

2.2.2: Electrochemical Analysis 24

2.2.3: Powder X-ray Diffraction (PXRD) 26

2.2.4: Surface Area Analysis 27

2.2.5: Transmission Electron Microscopy (TEM) 27

2.2.6: Iodometric Titrations 27

2.2.7: X-ray Photoelectron Spectroscopy (XPS) 28
2.2.8: Determination of Ni and Fe Oxidation States.....28
2.3: Results and Discussion 28
2.3.1: Material Characterization 28
2.3.2: Electrochemistry.....30
2.3.3: Density Functional Theory (DFT) Modeling 39
2.3.4: Mechanistic Insights.....44
2.4: Conclusions.....46
2.5: References.....47
Chapter 3: The Electrooxidation of Urea on $LaNiO_3$ Perovskite Oxide.....53
3.1: Introduction.....53
3.2: Experimental.....55
3.2.1: Catalyst Synthesis.....55
3.2.2: Electrochemical Analysis 56
3.3: Results and Discussion 57
3.3.1: Material Characterization 57
3.3.2: Catalyst Activity.....58
3.3.3: Mechanistic Insights.....60
3.3.4: Catalyst Stability.....64
3.4: Conclusions.....72
3.5: References.....73
Chapter 4: Tuning Ruddlesden-Popper Oxide Catalysts for the Electrochemical Oxidations of Urea and Small Alcohols 75
4.1: Introduction.....75

4.2: Experimental....78
4.2.1: Catalyst Synthesis....78
4.2.2: Electrochemical Analysis....79
4.2.3: Quantification of Urea and Alcohol Electrooxidation Activities....80
4.2.4: Powder X-ray Diffraction (PXRD)....80
4.2.5: Surface Area Analysis....81
4.2.6: Transmission Electron Microscopy (TEM)....81
4.2.7: Iodometric Titrations....81
4.2.8: X-ray Photoelectron Spectroscopy (XPS)....82
4.3: Results and Discussion....82
4.3.1: Materials Characterization....82
4.3.2: Catalyst Activity....84
4.3.3: Catalyst Stability....89
4.4: Conclusions....92
4.5: References....93
Chapter 5: Comparison of Perovskite and Perovskite Derivatives for use in Anion-based Pseudocapacitor Applications....98
5.1: Introduction....98
5.2: Experimental....101
5.2.1: Material Synthesis....101
5.2.2: Powder X-ray Diffraction (PXRD)....101
5.2.3: Surface Area Analysis....102
5.2.4: Scanning Electron Microscopy (SEM)....102
5.2.5: Iodometric Titrations....102

5.2.6: Electrochemical Characterization 103

5.3: Results and Discussion 104

5.3.1: Physical Characterization 104

5.3.2: Electrochemical Characterization 106

5.4: Conclusions 113

5.5: References 113

Appendices 117

Appendix A: Exceptional Electrocatalytic Oxygen Evolution Via Tunable Charge Transfer Interactions in $La_{0.5}Sr_{1.5}Ni_{1-x}Fe_xO_{4+\delta}$ Ruddlesden-Popper Oxides 117

A.1: Supplementary Notes 117

A.1.1: Concerning the Persistent Oxygen Hyperstoichiometry and High Oxidation States Measured for the LSNF Series 117

A.1.2: Density Functional Theory (DFT) Modeling Details: determinations of effective Hubbard U_{eff}, atomic, magnetic and electronic structures, and oxygen hyper-stoichiometry effects 118

A.2: Supplementary Figures 121

A.3: Supplementary Tables 143

A.4: References 147

Appendix B: The Electrooxidation of Urea on $LaNiO_3$ Perovskite Oxide 151

B.1: Supplementary Figures 151

B.2: References 157

Appendix C: Tuning Ruddlesden-Popper Oxide Catalysts for the Electrochemical Oxidations of Urea and Small Alcohols 159

C.1: Supplementary Figures 159

C.2: Supplementary Tables 166

C.3: References 167

Appendix D: Comparison of Perovskite and Perovskite Derivatives for use in Anion-based Pseudocapacitor Applications 168

D.1: Supplementary Figures 168

D.2: Supplementary Tables.....170

Bibliography 171

List of Tables

Table 2.1: Oxygen hyperstoichiometry (δ) and B-site oxidation states in $La_{0.5}Sr_{1.5}Ni_{1-x}Fe_xO_{4+\delta}$. 39

Table 5.1: Physical characterization of $CaMnO_{3-\delta}$ and $Ca_2MnO_{4-\delta}$ materials. 106

Table A.1: The results of Rietveld refinement for the LSNF series. 143

Table A.2: Comparison of LSNF30 with other promising OER catalysts and accompanying notes. 144

Table A.3: Summary of the physical, chemical and electrochemical properties of the LSNF series. 145

Table A.4: 298K temperature ^{57}Fe Mossbauer hyperfine parameters for the LSNF series. 146

Table A.5: The 78K temperature ^{57}Fe Mossbauer hyperfine parameters for LSNF30 and LSNF45 of the LSNF series. 146

Table A.6: Computed oxygen vacancy formation for modeled LSNF compositions...147

Table C.1: Summary of physical characterization for the LSN series as well as LSNF. 166

Table C.2: Summary of electrochemical characterization for the LSN series as well as LSNF, $LaNiO_3$, and NiO. 166

Table D.1: Electrochemical oxygen diffusion rates in $Ca_{n+1}Mn_nO_{3n+1-\delta}$ materials. 170

List of Figures

Figure 1.1: The elements capable of adopting perovskite and Ruddlesden-Popper crystal structures and unit cells of perovskite and Ruddlesden-Popper oxide materials. 3

Figure 1.2: Electrochemical elements of different charge storage devices. 10

Figure 1.3: Ragone plot of various electrochemical energy storage devices. 11

Figure 2.1: Crystallographic characterization of the $La_{0.5}Sr_{1.5}Ni_{1-x}Fe_xO_{4+\delta}$ series. 30

Figure 2.2: Oxygen evolution results and catalytic activities for the LSNF series. 33

Figure 2.3: Cyclic voltammetry stability tests of LSNF30 dropcast on Ni foam electrodes. 35

Figure 2.4: Cyclic voltammetry (CV) of LSNF catalysts in O_2-saturated 0.1 M KOH. 37

Figure 2.5: Density functional theory modeling of atomic and electronic structures of bulk LSNF in ferromagnetic configuration. 41

Figure 3.1: XRD spectra of $LaNiO_3$ perovskite before and after repeated cycling. 58

Figure 3.2: CVs of $LaNiO_3$ and NiO in 5 M and 1 M KOH containing 0.33 M urea. 59

Figure 3.3: Peak mass activity dependence of $LaNiO_3$ on KOH and urea concentration. 61

Figure 3.4: Effect of repeated cycling on urea oxidation mass activities. 65

Figure 3.5: Effect of carbon support and CO on peak activities with repeated cycling. 67

Figure 3.6: Constant potential and current stability tests. 71

Figure 4.1: Physical characterization of the LSN series. 83

Figure 4.2: Electrooxidation activities of the LSN series toward urea oxidation. 85

Figure 4.3: Catalytic activities of the LSN series toward methanol and ethanol oxidation. 89
Figure 4.4: Effect of repeated cycling on urea oxidation mass activities. 91
Figure 5.1: Physical characterization of $CaMnO_{3-\delta}$ and $Ca_2MnO_{4-\delta}$ materials. 105
Figure 5.2: Electrochemical characterization of $CaMnO_{3-\delta}$ and $Ca_2MnO_{4-\delta}$ materials as pseudocapacitors. 108
Figure 5.3: Electrochemical cycling stability of r-CMO and r-CMO RP materials as pseudocapacitors. 112
Figure A.1: Electron diffraction patterns of the LSNF series. 121
Figure A.2: Unit cell volume as a function of x in $La_{0.5}Sr_{1.5}Ni_{1-x}Fe_xO_{4+\delta}$ solid solutions. 122
Figure A.3: Rietveld refinement of the $La_{0.5}Sr_{1.5}Ni_{0.7}Fe_{0.3}O_{4+\delta}$. 122
Figure A.4: The crystal structure of the $La_{0.5}Sr_{1.5}Ni_{0.7}Fe_{0.3}O_{4+\delta}$. 123
Figure A.5: HAADF-STEM images of $La_{0.5}Sr_{1.5}Ni_{1-x}Fe_xO_{4+\delta}$. 124
Figure A.6: Nitrogen sorption isotherms for BET surface area analysis of the LSNF series. 125
Figure A.7: Representative polarization curves of the LSNF series for the OER. 126
Figure A.8: Reversible hydrogen electrode (RHE) calibration. 127
Figure A.9: Additional LSNF series OER activity data. 128
Figure A.10: Calibration of RRDE with Ferrocene-methanol. 129
Figure A.11: Oxygen evolution results and catalytic activities for the unsupported LSNF series. 130
Figure A.12: Galvanostatic stability test of LSNF30. 131
Figure A.13: Cyclic voltammetry stability tests of LSNF30 on Ni Foam electrodes. 132
Figure A.14: First and second CVs of LSNF30 in various concentrations of KOH. 133

Figure A.15: Surface redox and anion intercalation CVs for the entire LSNF series. 134
Figure A.16: Fitted surface redox and anion intercalation CVs for the entire LSNF series. 135
Figure A.17: Electrochemical oxygen diffusion rate data for the LSNF series. 136
Figure A.18: Room temperature Mössbauer spectroscopy for the LSNF series. 137
Figure A.19: Mössbauer spectroscopy taken at 78 K for LSNF30 and LSNF45. 138
Figure A.20: XPS deconvolution of the Ni 3p spectra for the LSNF series. 139
Figure A.21: DFT modeling of atomic and electronic structures of bulk LSNF. 140
Figure A.22: Comparison of ferromagnetic, anti-ferromagnetic and non-magnetic structures from DFT modeling. 141
Figure A.23: DFT modeling of the electronic structures of bulk SNF. 142
Figure B.1: SEM micrographs of $LaNiO_3$ particles. 151
Figure B.2: SEM micrographs of NiO particles. 151
Figure B.3: BET adsorption of desorption curves for unsupported $LaNiO_3$ used to calculate surface area. 152
Figure B.4: XRD pattern of NiO catalyst material. 152
Figure B.5: Specific Activities for previously reported materials toward urea electrooxidation. 153
Figure B.6: Dependence of urea oxidation activities on KOH and urea concentrations. 153
Figure B.7: Cyclic voltammogram of 0.33 M 1,3-dimethylurea and a saturated electrolyte of 1,1-dimethylurea. 154
Figure B.8: Rotation rate dependence of urea oxidation activities on $LaNiO_3$. 154
Figure B.9: Scan rate dependence of urea oxidation activities on $LaNiO_3$. 155

Figure B.10: Effect of repeated cycling and CO on the electrooxidation of urea by $LaNiO_3$. 155
Figure B.11: Ex-situ raman spectroscopy of $LaNiO_3$ at various points during urea oxidation testing. 156
Figure B.12: Select Raman modes for relevant species involved in the electrooxidation of urea. 157
Figure C.1: Crystallographic characterization of LSN25. 159
Figure C.2: Nitrogen sorption isotherms (BET). 160
Figure C.3: XPS of the LSN series. 161
Figure C.4: UOR activities for $LaNiO_3$ and NiO. 162
Figure C.5: Dependence of UOR activities on urea concentration for the LSN series. .162
Figure C.6: PXRD patterns for NiO, $LaNiO_3$, and LSNF25. 163
Figure C.7: Rotating ring disk electrode experiments for the UOR. 163
Figure C.8: Urea oxidation activities and Ni redox of LSNF30. 164
Figure C.9: Cycling stability tests for LSN25 towards methanol and ethanol electrooxidation. 165
Figure D.1: Electrochemical pseudocapacitance of $CaMnO_{3.11}$ and $Ca_2MnO_{3.85}$ 168
Figure D.2: Comparison of diffusion limited processes versus charge transfer limitations in $Ca_{n+1}Mn_nO_{3n+1-\delta}$ materials. 169
Figure D.3: Electrochemical measurement of oxygen diffusion rates in $Ca_{n+1}Mn_nO_{3n+1-\delta}$ materials. 170

List of Illustrations

Illustration 1.1: Perovskite synthesis via reverse-phase hydrolysis. 4

Illustration 1.2: Perovskite synthesis via a modified Pechini method. 5

Chapter 1: Introduction

With the growing threat of climate change and impending scarcity of fossil fuels the need has developed to rapidly advance the technologies involved in converting and storing energy from intermittent, renewable sources such as wind and solar. In an effort to solve these broad issues a great deal of research has been devoted to improving the efficiencies of devices that generate, convert, and store energy and while devices that generate and store energy electrochemically have already been demonstrated to have energy densities near those of fossil fuels,[1] the bottleneck in the widespread development and adoption of these technologies has been the poor efficiencies of the anodic reaction, whether it be the oxygen evolution reaction[2] (OER) or the electrooxidations of small molecules,[3] that lead to decreased device performance. Furthermore, most devices of this type currently use precious metal catalysts which further limits their large-scale implementation.[4–6] Much of this dissertation is devoted to the discussion of how a class of metal oxides were studied using techniques from multiple fields such as materials chemistry and solid-state physics during material synthesis to analytical chemistry, electrochemistry, and computational chemistry which were used to study these electrocatalysts that outperform their precious metal predecessors at a fraction of the cost. Elsewhere batteries, most notably lithium ion batteries, have rightfully attracted a great deal of interest in this regard, but the slow charge and discharge rates of these devices have proven to be a major drawback. With an eye toward applications such as improving acceleration of electric vehicles, we have investigated perovskite and Ruddlesden-Popper oxides as materials for high energy density pseudocapacitors to bridge the gap between high power double layer capacitors and high energy density batteries.

1.1: PEROVSKITE AND RUDDLESDEN-POPPER OXIDES

Perovskite oxides with the nominal formula ABO_3 where A is an alkali-earth or rare earth metal and B is a transition metal are ideal materials to use as model systems due to the fact that their crystal structure can accommodate a wide variety of elemental substitutions which makes ~90% of the periodic table available for use (Figure 1.1).[7,8] For this reason perovskites have been studied for decades as catalysts for reactions such as the OER,[9] however, a poor understanding of the reaction mechanisms taking place on these types of materials limited their usefulness. Furthermore, synthesis of many of these materials occurs through reactions to form precursor particles that then require high temperature calcination, which leads to large particle sizes when compared to metal nanoparticle catalysts and low surface areas.[10] In addition to the ideal perovskite structure there are many derivatives of this structure that can be synthesized in similar ways, including the Ruddlesden-Popper crystal structure. The Ruddlesden-Popper (RP) oxide crystal structure is represented as $A_{n+1}B_nO_{3n+1}$ or equivalently $(AO)(ABO_{3\pm\delta})_n$, wherein perovskite layers with a thickness of n (BO_6) octahedra are separated by rocksalt (AO)(OA) double layers. The RP phase can accommodate all of the elemental substitutions available to perovskites as well as additional compositions that are not stable in the perovskite structure, and we turn to this crystal structure to synthesize highly covalent materials not stable in the perovskite structure as is described in later chapters.[11]

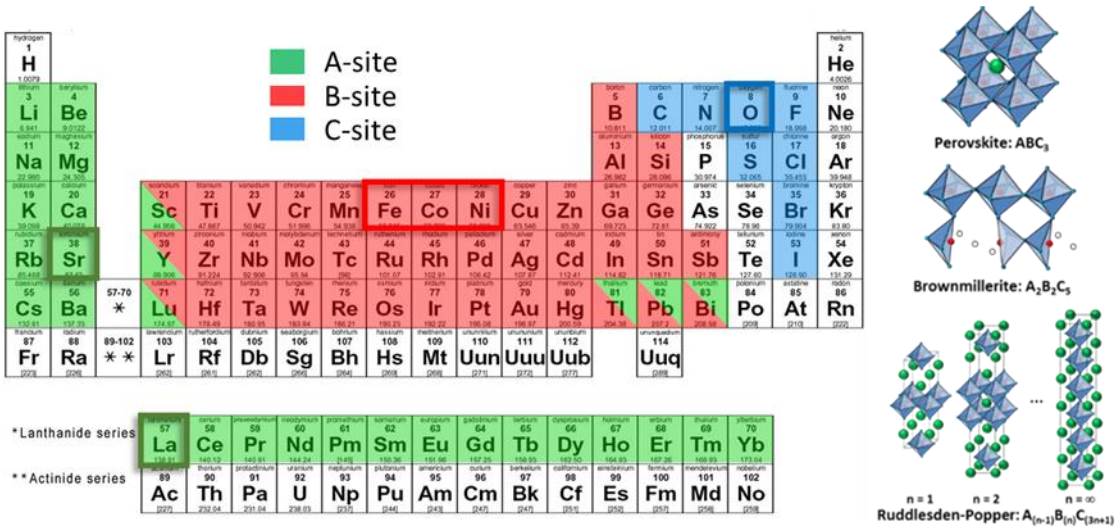

Figure 1.1: The elements capable of adopting perovskite and Ruddlesden-Popper crystal structures and unit cells of perovskite and Ruddlesden-Popper oxide materials.

Previous work by our group established how a reverse-phase-hydrolysis synthesis of precursor particles followed by freeze drying and calcination could be used to increase the surface area of the final perovskite material by limiting the size of the mixed metal hydroxide precursor particles and particle agglomeration prior to calcination. In this synthesis a solution of metal nitrates containing the A and B-site cations in the appropriate stoichiometric ratio are added dropwise to a solution of strong base that contains tetrapropylammonium bromide (TPAB) capping ligands that arrest mixed metal hydroxide particle growth at >50 nm. The colloidal suspension of precursor particles is then freeze-dried on a rotating metal drum at cryogenic temperatures followed by lyophilization, all of which is done to prevent agglomeration of particles that would occur during the evaporation of water. The particles are finally calcined at 700-950°C to form the perovskite structure. This method (Illustration 1.1) produces final materials with surface areas between 3-20 $m^2 g^{-1}$ and can be used to make catalysts with a wide variety

of elemental compositions, however the many steps involved mean the whole synthesis takes an extended period of time and yields are generally low (~50 mg).

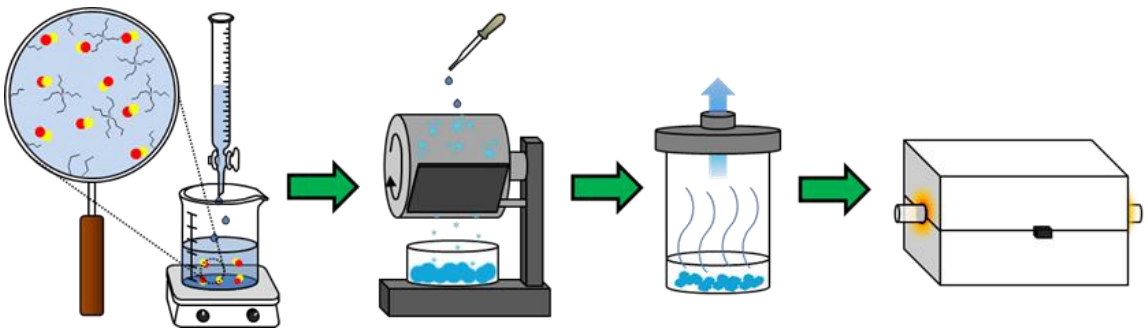

Illustration 1.1: Perovskite synthesis via reverse-phase hydrolysis.

To overcome these issues we turned to a different synthesis method in which precursor particles are made of mixed metal oxides instead of hydroxides. In this method, referred to as a modified Pechini synthesis[12] (Illustration 1.2), A and B-site metal nitrate salts are dissolved in water in the appropriate stoichiometric ratios followed by the addition of citric acid and ethylenediaminetetraacetic acid (EDTA). Tetramethylammonium hydroxide (TMAOH) is then added dropwise until the pH is ~7.5 in order to completely dissolve the EDTA and ensure deprotonation of at least 3 of the 4 carboxylic acid groups. Finally, diethylene glycol (DEG) is added and the solution is heated to 85°C. Upon evaporation of the water a dehydration reaction occurs between the DEG and the carboxylic acid groups of the chelates to form a polyester gel with chelated metal cations homogeneously intermixed. The resulting gel is combusted at 350°C to form mixed metal oxide precursor particles, followed by calcination. This synthesis can accommodate the same range of compositions as the previous method and materials

produced using this method have surface areas commensurate with the reverse-phase-hydrolysis synthesis, but large synthesis are much easier to perform (500 mg - 1 g) and the total time to synthesize a material is less than 24 hours.

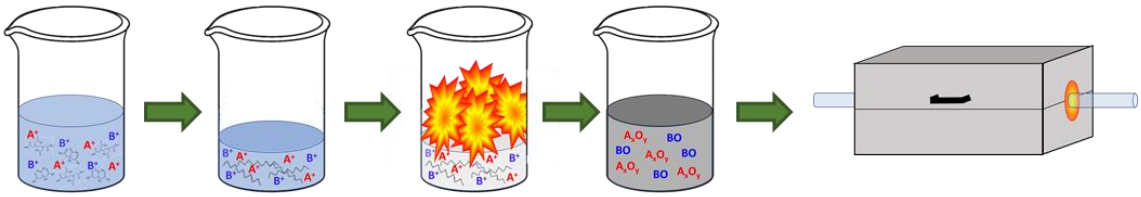

Illustration 1.2: Perovskite synthesis via a modified Pechini method.

1.2: Oxygen Evolution

Of the many issues that plague the success of regenerative alkaline fuel cells, electrolyzers, and metal air batteries, one of the most pressing is the need to improve the performance of electrode materials towards the OER. The sluggish kinetics of the OER mean that thus far large mass loadings and precious metal catalysts are necessary for device operation, limiting the energy density and affordability of such devices. By using alkaline electrolytes materials such as metal oxides become available which dramatically lower cost. In order to develop catalysts capable of replacing precious metals, a fundamental understanding of the OER reaction mechanism and how this depends on the electronic structure of the catalyst is necessary. Originally, the elementary reaction steps suggested by Cushing and Goodenough[13] were thought to mirror those for the ORR and as discussed by Matsumoto[14–17] the governing descriptor as to the rate of electron transfer was thought to be the character of the transition metal 3*d* σ* and the degree to which this predominantly metal-character band overlapped with the O 2*p* σ band. Later, Bockris and

Otagawa explored various possible reaction mechanisms and proposed that the rate of desorption of OH^- was the rate limiting step (RLS) and that the number of *d* electrons in the transition metal and the enthalpy of formation of the metal hydroxide in alkaline conditions were governing descriptors for the activity of perovskites towards the OER.[18,19] The work of Suntivich and Shao-Horn leveraged this work as well as the earlier development of $Ba_{0.5}Sr_{0.5}Co_{0.8}Fe_{0.2}O_{3-\delta}$ (BSCF) as a cathode material in solid oxide fuel cells[20] to develop a descriptor for OER activity that relied on e_g filling and that a filling of 1 was the optimum number of electrons to perform the OER.[10,21] Despite these efforts, no one set of descriptors has been proven to govern the activity of perovskites for the OER. Recent work has focused less on the idea of localized orbital filling and more so on the degree of overlap between the B-site 3*d* bands and the O 2*p* bands. Mefford et al. concluded that increased bond covalency and the introduction of oxygen vacancies in $La_{1-x}Sr_xCoO_{3-\delta}$. catalysts governed their catalytic activity and proposed a new OER mechanism in which lattice oxygen is utilized to evolve oxygen gas,[22] and Grimaud has since confirmed the existence of this mechanism on the same catalyst system using isotopic labeling experiments.[23] It is with these findings in mind that we have endeavored to design highly covalent perovskite and Ruddlesden popper catalysts to further enhance their performance for the OER.

1.3: The Electrooxidation of Small Molecules

While a great deal of progress has been made on improving the kinetics of the OER through the design of better catalysts, they still remain an obstacle in the development of efficient electrolyzers and fuel cells. As an alternative to the OER as the anodic reaction in the generation of hydrogen for energy storage, the electrooxidations of

small molecules have attracted a significant amount of attention. Recently, urea has become a molecule of great interest in this field as it can be oxidized at the anode at a potential of -0.46 V vs. SHE while hydrogen is produced at the cathode at a potential of -0.83 V vs. SHE for a window of 0.37 V, much lower than the 1.23 V theoretically required when the OER is used. Furthermore, urea is relatively non-toxic, non-flammable, and can be transported as a solid that readily dissolves in water, qualities that make it an attractive option as a means for storing chemical energy.[3,24]

Botte and others have used DFT modeling to propose various steps through which the urea oxidation reaction (UOR) may take place,[25] however, the elementary mechanistic steps have not yet been experimentally elucidated. Botte and coworkers have proposed a simple, generalized mechanism for the reaction on nickel-based catalysts in which the reaction follows an indirect, electrochemical-chemical (EC') mechanism that was developed using in-situ Raman spectroscopy.[26,27] In this 6-electron pathway nickel hydroxide is oxidized to the catalytically active oxidation state of Ni^{3+} in nickel oxyhydroxide. Urea then reacts to form the products CO_2, N_2, and H_2O while regenerating the nickel hydroxide catalyst in a chemical step at the anode, and hydrogen is produced at the cathode, as shown below.

Anode:

$$6Ni^{2+}(OH)_{2(s)} + 6OH^- \rightarrow 6Ni^{3+}OOH_{(s)} + 6H_2O + 6e^- \quad (1.1)$$

$$6Ni^{3+}OOH_{(s)} + CO(NH_2)_{2(aq)} + 6OH^- \rightarrow 6Ni^{2+}(OH)_{2(s)} + N_{2(g)} + 5H_2O + CO_{2(g)} \quad (1.2)$$

Cathode:

$$6H_2O + 6e^- \rightarrow 3H_{2(g)} + 6OH^- \quad (1.3)$$

Overall:

$$CO(NH_2)_{2(aq)} + H_2O \rightarrow N_{2(g)} + 3H_{2(g)} + CO_{2(g)} \quad (1.4)$$

Inspection of the above reaction reveals that Ni in the +3 oxidation state is responsible for the oxidation of urea, reacting with urea and getting reduced in the process. Therefore, utilizing a material with an inherent oxidation state of Ni^{3+} should lead to a more efficient electrocatalytic cycle. Furthermore, the electrooxidations of other small molecules including methanol and ethanol have been shown to proceed through the same type of mechanism and should benefit from the same oxidation state augmentation.[28,29]

1.4: Batteries, Pseudocapacitors, and Supercapacitors: Faradaic and Non-Faradaic Charge Storage

In general, electrical energy can be stored in two ways, the first of which is though static charges on positive and negative plate electrodes and the second of which is faradaically through oxidation and reduction reactions within the electrodes of a battery. The main difference between the two is that one ideally excludes the transfer of electrons into and out of the electrode, relying on static, double layer charge accumulation on the positive and negative electrodes, while the other necessitates electron transfer into and out of the electrode material during chemical changes in the electrode material itself. While faradaic charge storage increases the amount of energy stored, the chemical changes that occur can lead to phase changes, degradation, and side reactions that ultimately cause irreversibility. Between these two extremes exist pseudocapacitors,

materials that store charge through both electric double layer capacitance and faradaic charge transfer.

1.4.1: Faradaic Charge Storage and Batteries.

In batteries all electrical energy is stored faradaically meaning every electron transferred corresponds to a charge transfer within the electrode material itself. In Li-ion batteries this occurs when every electron transferred corresponds to a lithiation or delithiation event whether it be in the anode between layers of graphite or in the cathode when cobalt in CoO_2 is reduced from Co^{4+} to Co^{3+} to form $LiCoO_2$ as well as the reverse reaction.[30] The potential at which this reaction occurs is governed by the Nernst equation, given as:[31]

$$E = E^0 + \frac{RT}{nF} ln \frac{[ox]}{[red]} \quad (1.5)$$

where E is the potential of the electrode or cell potential, E^0 is the standard reduction potential of the electrode or cell, R is the ideal gas constant (8.3145 J K^{-1} mol^{-1}), T is the absolute temperature (K), n is the number of electrons transferred per mole of active material, F is Faraday's constant (96,584 C mol^{-1}), and [ox] and [red] refer to the concentrations of the active material in the oxidized and reduced state. Thus the total theoretical energy the battery is able to store goes as:[32]

$$U = Q\Delta E_{cell} \quad (1.6)$$

where U is the energy stored, Q is the charge, and ΔE is the potential difference between the cathode and anode, and the total theoretical charge the battery is able to store is:[32]

$$Q = \frac{nF}{m} \tag{1.7}$$

where *m* is the mass of the limiting electrode active material. When performing cycling voltammetry this behavior manifests itself as a CV containing sharp peaks that correspond to completely faradaic charge transfer (Figure 1.2)

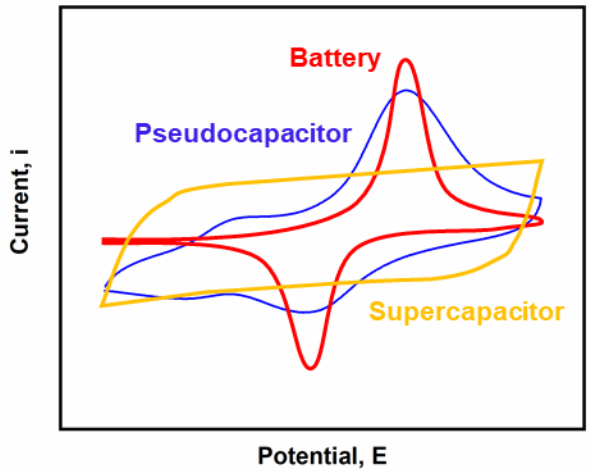

Figure 1.2: Electrochemical elements of different charge storage devices.

1.4.2: Non-Faradaic Charge Storage, Supercapacitors, and Pseudocapacitors.

A simple capacitor is made up of two plates that are electrically conductive and are separated by a material with a high dielectric constant. Charge is stored non-faradaically as electrostatic charge via electric double layer formation and the capacitance goes as:[32]

$$C = \frac{\varepsilon \varepsilon_0 A}{d} \tag{1.8}$$

where C is the capacitance (F), ε is the dielectric constant, ε_0 is the permittivity of free space (8.854 x 10^{-12} F m^{-1}), A is the area of the plates, and d is the separation of the plates (i.e. thickness of the dielectric). The charge stored is a function of an applied potential and the total energy stored goes as shown below:[32]

$$Q = CE \tag{1.9}$$

$$U = \frac{1}{2} CE \tag{1.10}$$

Devices known as Supercapacitors utilize high surface area materials such as carbons with surface areas >1000 m^2 g^{-1} as electrodes and rely on the concept of electric double layer capacitance to achieve over 300 F g^{-1}, however, these power densities come at a const to the total energy density of the device (Figure 1.3).[33] When performing cycling voltammetry this behavior manifests itself as a CV with a rectangular shape (Figure 1.2).

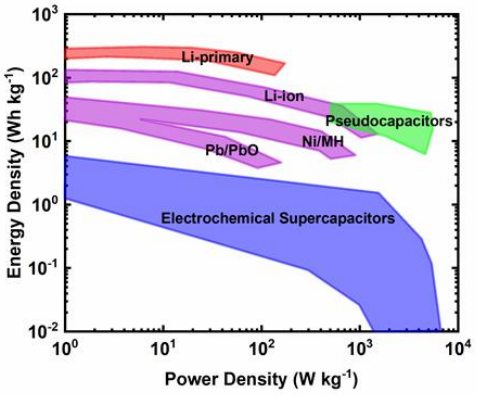

Figure 1.3: Ragone plot of various electrochemical energy storage devices.

Pseudocapacitors bridge the gap between batteries and supercapacitors in that they store charge both faradaically and non-faradaically and thus have power and energy densities between them as well, however they are generally more similar to supercapacitors in that most of the charge stored occurs at the electrode surface, including faradaic charge transfer. There are four generally accepted mechanisms of pseudocapacitance. The first is surface redox reactions that occur in materials such as metal oxides and hydroxides. For example, $Ni(OH)_2$ can be reversibly oxidized as is shown below as well as in Chapters 3 and 4:[34]

$$Ni(OH)_2 + OH^- \rightleftharpoons NiOOH + H_2O + e^- \quad (1.11)$$

The second mechanism of pseudocapacitive charge storage utilizes underpotential deposition and electrosorption such as in the case of proton underpotential deposition on Pt:[35,36]

$$Pt + H^+ + e^- \rightleftharpoons PtH \quad (1.12)$$

The third and fourth mechanisms utilize rapid intercalation and deintercalation of ions. For example, Mo in MoO_3 can be reversibly reduced to intercalate and oxidized to deintercalate Li^+ (Equation 1.9) while it has been recently shown by Mefford et al. that this can be done with anions as well as in the case with $LaMnO_3$ perovskite:[37,38]

$$Mo^{6+}O_3 + Li^+ + e^- \rightleftharpoons LiMo^{5+}O_3 \quad (1.13)$$

$$LaMnO_{3-\delta} + 2OH^- \rightleftharpoons LaMnO_3 + H_2O + e^- \quad (1.14)$$

It is this last method of pseudocapacitive charge storage, through anion intercalation, that we investigate in this dissertation.

1.5: OUTLINE

We begin in Chapter 2 focusing on the synthesis of a series of Ruddlesden-Popper catalysts having highly oxidized and covalent Ni 3*d* - O 2*p* - Fe 3*d* bonds that give rise to exceptional OER activity. Sr substitution into the perovskite $LaNiO_3$ has previously been proposed as an avenue to increase the oxidation state if Ni and Ni-O covalency but has not been fully realized, and in this work we avoid inactive secondary phases resulting from poor solubility of Sr in the perovskite phase through utilization of the RP crystal structure. Additionally, by using $La_{0.5}Sr_{1.5}NiO_{4\pm\delta}$ (LSN) as the host lattice we achieved complete substitution of Fe for Ni across the entire compositional range, and we refer to these materials as members of the LSNF series. The crystalline RP structure and the high degree of phase purity enabled precise study of the impact of Fe substitution on the chemical and electronic properties of the LSNF series, something that has not been possible up to this point with amorphous materials. Fe substitution results in cross-gap hybridization where the Fe 3*d* e_g band is hybridized with both the Ni 3*d* e_g and the top of the O 2*p* density of states across the Fermi level. The increased covalency of the Ni-O bonds as well as facile charge transfer through Fe-O-Ni bridges explains the enhanced catalytic activity upon optimum Fe substitution. Furthermore, the increased covalency demonstrated via calculated partial density of states for LSNF and a simplified SNF that is a requirement for the OER to take place via a lattice oxygen mediated (LOM) mechanism resembles the band structure of other highly active OER catalysts with varying crystal or amorphous structures for which this mechanism has already been

verified. This methodology of selective A and B-site substitution to promote cross-gap hybridization in RP oxides reveals important fundamental aspects related to their structure and the exceptional electrocatalytic activities of these materials as well as other metal oxide catalysts.

Chapter 3 focuses on the synthesis of $LaNiO_3$ nanoparticles via the reverse phase hydrolysis technique described above for the electrochemical oxidation of urea. $LaNiO_3$ with Ni in the 3+ oxidation state displays catalytic activity towards urea oxidation much greater than previously reported materials that generally contain various morphologies of NiO wherein nickel is in the 2+ oxidation. Lowered activity of the catalyst was observed during repeated cycling at high pH due to restructuring of the perovskite surface, as well as possible catalyst poisoning due to reaction products. Despite these issues, galvanostatic experiments generating currents of a relevant magnitude for use in applications such as hydrogen generation and fuel cells showed $LaNiO_3$ perovskite to be stable and generate the same currents as similarly-prepared NiO at a lower overpotential.

In Chapter 4 we discuss the synthesis of a series of nanostructured $La_{2-x}Sr_xNiO_{4+\delta}$ ($1 \leq x \leq 1.5$) materials via the modified Pechini method described above resulting in a collection of n = 1 Ruddlesden-Popper catalysts that were utilized to investigate the effect of increasing Ni oxidation state on the electrochemical oxidations of urea, methanol, and ethanol. Building on the work in Chapter 3, we have demonstrated how systematic incorporation of Sr^{2+} into the Perovskite derivative n = 1 Ruddlesden-Popper crystal structure in place of La^{3+} steadily increases the bulk oxidation state of Ni past +3 leading to greater activities towards small molecule oxidations. LSN25, in which La makes up 25% of the A-site and Sr makes up 75%, displayed the highest activities for all three electrochemical oxidations. Furthermore, we discovered that this material can maintain its activity over long periods of time and at very high current densities but that reduction

of the catalyst surface at sufficiently cathodic potentials leads to deactivation towards these reactions. This is the first time the fundamental guiding principle of increasing Ni oxidation state past Ni^{3+} to increase catalyst activity towards the urea oxidation reaction has been shown and the activities of LSN25 towards the electrooxidations of urea, methanol, and ethanol are among the highest ever reported.

Chapter 5 takes a look at the electrochemical pseudocapacitance of $CaMnO_{3-\delta}$ and $Ca_2MnO_{4-\delta}$ materials that were studied via cyclic voltammetry measurements. Reduced versions of both catalysts were formed by annealing in a reducing atmosphere and displayed greater pseudocapacitive performance than their unreduced counterparts, verifying that greater oxygen vacancy concentrations within the bulk of these materials increases their ability to store charge via oxygen anion intercalation. Furthermore, we demonstrate how a governing descriptor for pseudocapacitive performance changes from a dependence on the number of surface redox sites at high scan rates to a dependence on oxygen vacancy content at slower rates where fast oxygen diffusion through the bulk lattice dominates. Finally, we demonstrate how both materials maintain their impressive performance with repeated cycling and even increase their performance with continued use.

1.6: REFERENCES

1. Cheng, F. & Chen, J. Metal-air batteries: from oxygen reduction electrochemistry to cathode catalysts. *Chem Soc Rev* **41**, 2172–2192 (2012).

2. Zhu, H., Zhang, P. & Dai, S. Recent Advances of Lanthanum-Based Perovskite Oxides for Catalysis. *ACS Catal.* **5**, 6370–6385 (2015).

3. Rollinson, A. N., Jones, J., Dupont, V. & Twigg, M. V. Urea as a hydrogen carrier: a perspective on its potential for safe, sustainable and long-term energy supply. *Energy Environ. Sci.* **4**, 1216–1224 (2011).

4. Evans, U. R. Cathodic Reduction of Oxygen in Fuel Cells and Corrosion Cells. *Nature* **218**, 602–603 (1968).

5. Ge, X. *et al.* Oxygen Reduction in Alkaline Media: From Mechanisms to Recent Advances of Catalysts. *ACS Catal.* **5**, 4643–4667 (2015).

6. Gorlin, Y. & Jaramillo, T. F. A Bifunctional Nonprecious Metal Catalyst for Oxygen Reduction and Water Oxidation. *J. Am. Chem. Soc.* **132**, 13612–13614 (2010).

7. Tejuca, L. G. Properties of perovskite-type oxides I: Bulk and surface studies. *Journal of the Less Common Metals* **146**, 251–259 (1989).

8. Tejuca, L. G., Fierro, J. L. G. & Tascón, J. M. D. Structure and Reactivity of Perovskite-Type Oxides. in *Advances in Catalysis* (eds. Eley, D. D., Pines, H. & Weisz, P. B.) **36**, 237–328 (Academic Press, 1989).

9. Meadowcroft, D. B. Low-cost Oxygen Electrode Material. *Nature* **226**, 847–848 (1970).

10. Suntivich, J., May, K. J., Gasteiger, H. A., Goodenough, J. B. & Shao-Horn, Y. A Perovskite Oxide Optimized for Oxygen Evolution Catalysis from Molecular Orbital Principles. *Science* **334**, 1383–1385 (2011).

11. Sharma, I. B. & Singh, D. Solid state chemistry of Ruddlesden-Popper type complex oxides. *Bull. Mater. Sci.* **21**, 363–374 (1998).

12. Gilev, A. R., Kiselev, E. A. & Cherepanov, V. A. Homogeneity range, oxygen nonstoichiometry, thermal expansion and transport properties of $La_{2-x}Sr_xNi_{1-y}Fe_yO_{4+\delta}$. *RSC Adv.* **6**, 72905–72917 (2016).

13. Goodenough, J. B. & Cushing, B. L. Oxide-based ORR catalysts. in *Handbook of Fuel Cells* (American Cancer Society, 2010). doi:10.1002/9780470974001.f205040

14. Matsumoto, Y. & Sato, E. Electrocatalytic properties of transition metal oxides for oxygen evolution reaction. *Materials Chemistry and Physics* **14**, 397–426 (1986).

15. Matsumoto, Y., Yoneyama, H. & Tamura, H. Influence of the nature of the conduction band of transition metal oxides on catalytic activity for oxygen reduction. *Journal of Electroanalytical Chemistry and Interfacial Electrochemistry* **83**, 237–243 (1977).

16. Matsumoto, Y., Manabe, H. & Sato, E. Oxygen Evolution on $La_{1-x}Sr_xCoO_3$ Electrodes in Alkaline Solutions. *J. Electrochem. Soc.* **127**, 811–814 (1980).

17. Matsumoto, Y., Yamada, S., Nishida, T. & Sato, E. Oxygen Evolution on $La_{1-x}Sr_xFe_{1-y}Co_yO_3$ Series Oxides. *J. Electrochem. Soc.* **127**, 2360–2364 (1980).

18. Bockris, J. O. & Otagawa, T. Mechanism of oxygen evolution on perovskites. *J. Phys. Chem.* **87**, 2960–2971 (1983).

19. Bockris, J. O. & Otagawa, T. The Electrocatalysis of Oxygen Evolution on Perovskites. *J. Electrochem. Soc.* **131**, 290–302 (1984).

20. Shao, Z. & Haile, S. M. A high-performance cathode for the next generation of solid-oxide fuel cells. *Nature* **431**, 170–173 (2004).

21. Suntivich, J. *et al.* Design principles for oxygen-reduction activity on perovskite oxide catalysts for fuel cells and metal–air batteries. *Nature Chemistry* **3**, 546–550 (2011).

22. Mefford, J. T. *et al.* Water electrolysis on $La_{1-x}Sr_xCoO_{3-\delta}$ perovskite electrocatalysts. *Nat. Commun.* **7**, 11053 (2016).

23. Grimaud, A. *et al.* Activating lattice oxygen redox reactions in metal oxides to catalyse oxygen evolution. *Nat. Chem.* **9**, 457–465 (2017).

24. Lan, R., Tao, S. & Irvine, J. T. S. A direct urea fuel cell – power from fertiliser and waste. *Energy Environ. Sci.* **3**, 438–441 (2010).

25. Daramola, D. A., Singh, D. & Botte, G. G. Dissociation Rates of Urea in the Presence of NiOOH Catalyst: A DFT Analysis. *J. Phys. Chem. A* **114**, 11513–11521 (2010).

26. Vedharathinam, V. & Botte, G. G. Direct evidence of the mechanism for the electro-oxidation of urea on $Ni(OH)_2$ catalyst in alkaline medium. *Electrochim. Acta* **108**, 660–665 (2013).

27. Vedharathinam, V. & Botte, G. G. Understanding the electro-catalytic oxidation mechanism of urea on nickel electrodes in alkaline medium. *Electrochim. Acta* **81**, 292–300 (2012).

28. Zhang, Z., Liu, J., Gu, J., Su, L. & Cheng, L. An overview of metal oxide materials as electrocatalysts and supports for polymer electrolyte fuel cells. *Energy Environ. Sci.* **7**, 2535–2558 (2014).

29. Antolini, E. Catalysts for direct ethanol fuel cells. *Journal of Power Sources* **170**, 1–12 (2007).

30. Mizushima, K., Jones, P. C., Wiseman, P. J. & Goodenough, J. B. Li_xCoO_2 ($0<x<-1$): A new cathode material for batteries of high energy density. *Materials Research Bulletin* **15**, 783–789 (1980).

31. Bard, A. J. & Faulkner, L. R. *Electrochemical Methods: Fundamentals and Applications*. (Wiley, 2000).

32. Conway, B. E. *Electrochemical Supercapacitors*. (Springer, 1999).

33. Zhang, L. L., Zhou, R. & Zhao, X. S. Graphene-based materials as supercapacitor electrodes. *J. Mater. Chem.* **20**, 5983–5992 (2010).

34. Wang, H., Casalongue, H. S., Liang, Y. & Dai, H. $Ni(OH)_2$ Nanoplates Grown on Graphene as Advanced Electrochemical Pseudocapacitor Materials. *J. Am. Chem. Soc.* **132**, 7472–7477 (2010).

35. Zolfaghari, A., Chayer, M. & Jerkiewicz, G. Energetics of the Underpotential Deposition of Hydrogen on Platinum Electrodes I. Absence of Coadsorbed Species. *J. Electrochem. Soc.* **144**, 3034–3041 (1997).

36. Marković, N. M., Lucas, C. A., Gasteiger, H. A. & Ross, P. N. Bromide adsorption on Pt(100): rotating ring-Pt(100) disk electrode and surface X-ray scattering measurements. *Surface Science* **365**, 229–240 (1996).

37. Brezesinski, T., Wang, J., Tolbert, S. H. & Dunn, B. Ordered mesoporous α-MoO_3 with iso-oriented nanocrystalline walls for thin-film pseudocapacitors. *Nature Materials* **9**, 146–151 (2010).

38. Mefford, J. T., Hardin, W. G., Dai, S., Johnston, K. P. & Stevenson, K. J. Anion charge storage through oxygen intercalation in $LaMnO_3$ perovskite pseudocapacitor electrodes. *Nat. Mater.* **13**, 726–732 (2014).

Chapter 2: Exceptional Electrocatalytic Oxygen Evolution Via Tunable Charge Transfer Interactions in $La_{0.5}Sr_{1.5}Ni_{1-x}Fe_xO_{4+\delta}$ Ruddlesden-Popper Oxides*

2.1: INTRODUCTION

Increasing global energy demand requires greater efficiency in both water electrolyzers for low cost hydrogen generation as well as rechargeable metal-air batteries to continue the pragmatic development of these key technologies. Given that the efficiencies of these technologies are limited primarily by the sluggish kinetics of the oxygen evolution reaction (OER, $4OH^- \rightarrow O_2 + 2H_2O + 4e^-$), extensive efforts have been made to reduce the overpotential for the OER in alkaline media with advanced catalysts.[1] Whereas precious metals such as Ir and Ru are standard OER catalysts in acidic conditions, alkaline electrolytes enable the use of earth-abundant, non-precious metals. For example, Ni-M oxyhydroxides such as $Ni_{1-x}Fe_xOOH$ are known to be very active for the OER; however, lack of long-range order and uncontrolled electronic structure stemming from different synthetic methods[2] complicates elucidation of the mechanism(s) by which the OER activity is improved.[3–5] In fact, recent reports question whether Fe is part of the catalytic cycle or if it promotes partial charge transfer between Ni and Fe metal centers.[2,4,6] Additionally, recent work on Ni-Fe oxyhydroxides demonstrated that a significant portion of the measured OER current may be due to other processes and highlighted the need for careful electrochemical analysis of what reactions are contributing to the high activities reported.[7] Collectively this means that while $Ni_{1-x}Fe_xOOH$ materials have been reported as

* Adapted with permission from R.P. Forslund, W.G. Hardin, X. Rong, A.M Abakumov, C.T. Alexander, J.T. Mefford, H. Iyer, A.M. Kolpak, K.P. Johnston, K.J. Stevenson. Exceptional Electrocatalytic Oxygen Evolution Via Tunable Charge Transfer Interactions in $La_{0.5}Sr_{1.5}Ni_{1-x}Fe_xO_{4+\delta}$ Ruddlesden-Popper Oxides. *Nature Comm.* **9**, 3150 (2018). Copyright © 2014 Nature Publishing Group. R.P. Forslund and W.G. Hardin contributed equally to the work in collecting and analyzing data and writing the manuscript.

highly active catalysts, the large variations in electronic configuration and the resulting catalytic activity in these studies complicate establishment of precise structure-property correlations for Ni-Fe oxyhydroxides.[2,5,8]

In contrast, perovskite oxides with the nominal formula $ABO_{3\pm\delta}$, in which A is a rare-earth or alkaline earth element and B is a transition metal, have recently been shown to promote OER catalysis through high ionic and electronic conductivities, good structural stability, and synthetic versatility, all of which enable the development of rational catalyst design criteria.[9–11] Importantly, the ability to substitute elements of varying valence, electronegativity, or ionic size into A and B-sites directly influences the resultant properties of these catalysts.[1,12] An example of this was the substitution of Cu into the A-site of the quadruple perovskite $CaCu_3Fe_4O_{12}$ to increase stability of the catalyst.[13] Recently, it was demonstrated that highly covalent Co 3*d* – O 2*p* bonding in $SrCoO_{2.7}$ improved OER activity via a more energetically favorable lattice oxygen mediated (LOM) reaction pathway, consistent with prior reports and theory.[14–16] This LOM mechanism does not require the redox switching of transition metal sites, but rather utilizes lattice oxygen in the OER when the Fermi level (E_F^0) crosses the transition metal 3*d* - O 2*p* hybridized bands. This results in ligand holes that activate lattice oxygen which may combine with chemisorbed OH to produce O_2^-. This mechanism has since been confirmed by others using isotopic labeling experiments to detect exchanged oxygen from the lattice of $SrCoO_3$.[17] In a separate report, $SrNiO_3$ perovskite was predicted to be more covalent, even more prone to oxygen deficiency, and thus be more catalytically active than $SrCoO_3$.[18] Unfortunately, this prediction is hard to validate experimentally as $SrNiO_3$ adopts a non-perovskite structure based on a hexagonal close packing of Sr and O atoms.[19] In addition, it is known that the substitution of Sr into $LaNiO_3$ is limited to ~5-20% after which phase impurities appear that result in poor catalytic activity.[20,21]

To overcome this limitation, we investigate an alternative crystal structure to the perovskite-phase $SrNiO_3$ that promotes high OER activity but does not suffer from limited Sr solubility and can stabilize highly oxidized, covalently bound Ni. The Ruddlesden-Popper (RP) crystal structure is represented as $A_{n+1}B_nO_{3n+1}$ or equivalently $(AO)(ABO_{3\pm\delta})_n$, wherein perovskite layers with a thickness of n (BO_6) octahedra are separated by rocksalt (AO)(OA) double layers. This RP phase can accommodate all the elemental substitutions available to perovskites as well as additional compositions that are not stable in the perovskite structure.[22] While Ruddlesden-Popper materials have been explored as solid oxide fuel cell cathodes owing to their chemical flexibility and labile lattice oxygen, they have not been fully examined for room temperature water oxidation.[23–29]

Herein, we report a series of $La_{0.5}Sr_{1.5}Ni_{1-x}Fe_xO_{4+\delta}$ (LSNF, x = 0 to 1) OER catalysts that have enabled us to achieve exceptionally high catalytic activities at low overpotentials with small OER Tafel slopes. We show that Sr substitution promotes high catalytic activity by further oxidizing Ni via charge compensation, enhancing Ni-O covalency and electronic conductivity. Chemical substitution of Fe for Ni introduces and tunes the overlap between the Ni and Fe 3*d* bands and the O *2p* band. Density functional theory (DFT) modeling confirms that cross-gap hybridization between e_g(Ni), *p*(O) and e_g(Fe) bands across the Fermi level enhances charge transfer interactions across Fe-O-Ni bridges and the bandwidth available for electrode-adsorbate electron transfer. The increased covalency and cross-gap hybridization[30] of transition metal 3*d* states and O2*p* orbitals are an effective new catalyst design criteria for improving OER activity that supports oxygen evolution taking place via the LOM mechanism, a mechanism which has already been demonstrated to apply to other catalyst materials as well. Furthermore, our work illustrates the remarkable catalytic activity of the RP LSNF series that encompasses a range of chemical substitutions

and electronic configurations not accessible in other crystalline metal oxide phases and that enables the elucidation of crucial structural-chemical-electronic relationships and the OER mechanism that has not been possible with Ni-M oxyhydroxides and other reported metal oxide catalysts for OER.

2.2: EXPERIMENTAL

2.2.1: Catalyst Synthesis

$La_{0.5}Sr_{1.5}Ni_{1-x}Fe_xO_{4\pm\delta}$ (LSNF, x = 0 to 1) samples were synthesized using a modified Pechini method[29] followed by crystallization and annealing. A- and B-site nitrate salts, in the proper stoichiometric ratios, were dissolved in water to create a solution with a total metal salt concentration of 0.1 M. Citric acid and EDTA were added to the solution each at a concentration of 0.1 M as well. TMAOH was added dropwise to the solution until the pH had reached 7.5 in order to deprotonate and dissolve the EDTA. DEG was then added to the solution at a concentration of 0.067 M and the solution was heated to 85° C while stirring. The EDTA and citric acid were both added to ensure complete chelation of the metal cations, preventing agglomerations or particle formations that may lead to catalyst inhomogeneity. DEG and heat were added to the solution to drive a dehydration reaction between the polyhydroxyl alcohol and the carboxylic acid groups of the chelates to form a polyester gel. Once all the water had been evaporated the gel was combusted on a hot plate at 350°C to form mixed metal oxide precursor particles. This step was performed on a hot place and not in a sealed tube furnace to avoid possible explosions from rapid evolution of gasses upon combustion. Finally, precursor particles were crystallized at 950°C (heated at 20°C min^{-1}) for 5 hours, then cooled to 400° C and left to anneal for 6 hours in a tube furnace. The entire crystallization and annealing routine was done under

pure O_2 flowing at 200 mL min^{-1}. Catalysts were recovered and immediately stored under Ar gas to prevent catalyst surface amorphization. Total catalyst yields per synthesis ranged from 500 to 750 mg. More details regarding the synthesis can be found in Kakihana et al.[31]

$SrCoO_{2.7}$ and $LaNiO_3$ were synthesized via a coprecipitation method previously reported elsewhere[13,32] in which A and B-site nitrate salts in a 1:1 ratio were dissolved in a 1 wt% solution of TMAOH containing an equimolar amount of TPAB to the total moles of metal cations in order to form mixed metal hydroxide precursor particles. These solutions were flash-frozen on a rotating metal drum at cryogenic temperatures and collected before lyophilization to remove water. The precursor particles were then calcined at 700° C ($LaNiO_3$) or 950° C ($SrCoO_{2.7}$) to form the perovskite phase.

2.2.2: Electrochemical Analysis

Catalyst inks were prepared by adding 2 mL of a NaOH-neutralized 0.05 wt% Nafion solution[33] to 2 mg of catalyst powder and bath sonicated for at least one hour. A volume of ink (10 μL) was drop cast onto a clean 5 mm (0.196 cm^2, Pine Instruments) glassy carbon electrode and dried under ambient conditions overnight. The glassy carbon electrodes were cleaned prior to drop casting by sonication in a 1:1 DI water:ethanol solution. The electrode was then polished using 0.05 μm alumina powder, sonicated in a fresh DI water:ethanol solution, and dried in ambient air. All electrochemical tests were performed on electrodes prepared by this method, obtaining a composite catalyst loading of 51 μg_{total} cm^{-2}_{geo}, yielding 15.3 μg_{oxide} cm^{-2}_{geo} for catalysis and intercalation tests (30 wt% on carbon).

Electrochemical testing was performed on either a CH Instruments CHI832a or a Metrohm Autolab PGSTAT302N potentiostat, both equipped with high speed rotators from Pine Instruments. All testing was done at room temperature in 0.1 M KOH (measured

pH ≈ 12.8). Current interrupt and positive feedback methods were used to determine the electrolyte resistance (46 Ω) and all data was iR compensated after testing unless stated otherwise. Each test was performed in a standard 3 electrode cell using a CH Instruments Hg/HgO (1 M KOH) reference electrode, an Au wire counter electrode, and a film of catalyst ink on glassy carbon as the working electrode. All potentials are reported versus the reversible hydrogen electrode (RHE), which was determined experimentally to be +0.8976 V vs. Hg/HgO (1 M KOH).

All OER testing was performed on newly drop cast electrodes which had not undergone previous testing, drop-cast with 30 wt% catalyst on VC (15.3 μg_{oxide} cm^{-2}_{geo}) or unsupported catalyst. Cyclic voltammetry scans were performed from 1 to 2 V vs RHE at 10 mV s^{-1} with a rotation rate of 1600 rpm in O_2-saturated 0.1 M KOH. The anodic and cathodic scans were averaged and iR corrected, and the current at 1.63 V vs RHE-iR was selected from the polarization curves to compare OER activities. Scatter in the data at high current densities is due to oxygen bubble formation and desorption on the electrode surface. Data reported herein is the average taken from at least three tests on fresh electrodes. OER testing using Ni foam supports were performed under the same electrolyte conditions but drop cast at 1 mg cm^{-2} and held stationary.

All intercalation testing was performed under the same conditions as described above except that electrodes were cycled 20 times at 100 mV s^{-1} to ensure stable peaks were observed. For comparison of charge passed for all oxidative waves, the last cycle at 10 mV s^{-1} was used to compute specific current density. The baseline of each CV was fit and subtracted from the specific current density. The background subtracted CVs (Figure A1.16) were then integrated to find the total charge transferred.

All rotating ring disk electrode (RRDE) tests were performed in argon-saturated, 0.1 M KOH on fresh 30 wt% oxide films. LSNF30 was cycled at 10 mV s^{-1} on the disk

while the Pt ring was held at -0.4 V vs. RHE. One-fourth the normal geometric loading of catalyst was used (3.8 $\mu g_{oxide}\, cm^{-2}_{geo}$) to limit the amount of oxygen generated a minimize bubble formation which reduces collection efficiency. Additional information regarding the RRDE calibration data can be found in Figure A.10.

All oxygen diffusion tests were performed in argon-saturated, 1 M KOH on fresh 85 wt% oxide films. Each LSNF composition was cycled at 20 mV s-1 until the oxidative peak potential did not change upon further cycling. Chronoamperometry was then performed at potentials 10 mV more anodic than Ep to ensure diffusion-limited intercalation. A linear regression was performed to determine the diffusion rate. Particle sizes were estimated using the surface area calculated from BET measurements and densities determined by Rietveld analysis. All values reported are the average of at least three tests.

2.2.3: Powder X-ray Diffraction (PXRD)

Catalyst structure was probed by X-ray diffraction using a Rigaku MiniFlex600 Diffractometer at 298 K in ambient conditions, utilizing Cu Kα radiation (1.54 Å wavelength) operating at 40 kV and 15 mA. For all tests, argon-sealed catalyst powder was exposed to ambient air and scanned over 10 - 100° 2θ in 0.01° increments with a dwell time of 0.35 seconds per step. PXRD patterns for the Rietveld refinement were taken with a Huber G670 Guinier diffractometer (Cu $K_{\alpha 1}$ radiation; curved Ge(111) monochromator; image plate). The refinement was done with the JANA2006 package.[34] As the electron diffraction patterns of all compositions revealed no deviation from the RP n = 1 *I*4/*mmm* structure, the La_2NiO_4 structure[35] was used as a starting model. The La/Sr occupancy factors of the A positions were refined; the Fe/Ni occupancy factors for the B positions were assigned according to the results of the EDX analysis. The crystallographic data,

positional and atomic displacement parameters, interatomic distances and reliability factors are listed in Table A.1.

2.2.4: Surface Area Analysis

Nitrogen sorption analysis was performed on a Quantachrome Instruments NOVA 2000 high-speed surface area BET analyzer at a temperature of 77 K. Prior to measurements, the samples were ball milled for three minutes followed by degassing in vacuum for a minimum of 12 hours at room temperature. The specific surface area was calculated using the BET method from the nitrogen adsorption data in the relative pressure range (P/P_0) of 0.05 to 0.30, with a minimum R^2 of 0.995 and C value of 20.

2.2.5: Transmission Electron Microscopy (TEM)

The TEM samples were prepared by crushing the crystals in a mortar in ethanol and depositing drops of suspension onto a porous carbon grid. Electron diffraction patterns, high angle annular dark field scanning TEM (HAADF-STEM) images and energy dispersive X-ray (EDX) spectra were obtained with an aberration-corrected Titan G^3 electron microscope equipped with a Super-X EDX system, operated at 200 kV using a convergence semi-angle of 21.6 mrad.

2.2.6: Iodometric Titrations

Iodometric titrations were performed according to the referenced procedure.[13] 3 mL of deoxygenated 2 M KI solution was added to a flask containing 15 – 20 mg of perovskite under an argon atmosphere and allowed to disperse for three minutes. After a few minutes 25 ml of 1 M HCl was added and the perovskite was allowed to dissolve. This solution was then titrated to a faint golden color with a solution of ~26 mM solution of $Na_2S_2O_3$ that had

been pre-standardized with 0.1 N KIO_3. Corn starch indicator was then added and the solution was titrated until clear, marking the end point.

2.2.7: X-ray Photoelectron Spectroscopy (XPS)

Chemical states were characterized by a Kratos AXIS Ultra DLD XPS in 0.1 eV steps using a dwell time of 4 s per step and a monochromatic Al X-ray source (Al α, 1.4866 eV). Charge compensation was used for all samples. Binding energies were for all spectra were calibrated against the adventitious carbon peak at 285 eV. CasaXPS was used for all data analysis and deconvolution. Details regarding the deconvolution of the Ni 3p spectrum are found in the text accompanying Figure A.20.

2.2.8: Determination of Ni and Fe Oxidation States

Together, the iodometric titrations and the Mössbauer spectroscopy enable the calculation of Ni's average oxidation state and the relative percentage of $Fe^{3+/4+}$. Figure A1.18 contains the deconvolution method and Mössbauer spectra.

2.3: RESULTS AND DISCUSSION

2.3.1: Material Characterization

$La_{0.5}Sr_{1.5}Ni_{1-x}Fe_xO_{4\pm\delta}$ (LSNF, x = 0 to 1) samples were synthesized using a modified Pechini method[31] followed by crystallization and annealing. Electron diffraction and powder X-ray diffraction (PXRD) patterns correspond to a body-centered tetragonal unit cell with the *I*4/*mmm* space group, characteristic of the *n* = 1 Ruddlesden-Popper (RP) crystal structure (Figure 2.1 and Figure A.1). No superlattice reflections were detected that could be attributed to the La/Sr or Fe/Ni ordering, ordering of hyperstoichiometric oxygen atoms, or lattice distortions. The *a* and *c* unit cell parameters (Figure 2.1) and unit cell

volume (Figure A.2) increase almost linearly with Fe substitution reflecting that the $La_{0.5}Sr_{1.5}Ni_{1-x}Fe_xO_{4+\delta}$ solid solution is homogeneous over the entire substitutional range. The *I*4/*mmm* structure has been confirmed with Rietveld refinement from PXRD data (Table A.1, Figures A.3, A.4). Unit cell volume increases with Fe substitution are in agreement with the increasing fraction of Fe cations that have larger ionic radii than Ni cations ($r(Fe^{3+}$, HS) = 0.645 Å, $r(Fe^{4+}$, HS) = 0.585 Å, $r(Ni^{3+}$, LS) = 0.56 Å, $r(Ni^{4+}$, LS) = 0.48 Å).[36] The ratio of the apical to equatorial Ni/Fe – O distances increases from 1.038 in LSN to 1.073 in LSF, reflecting slight apical elongation of the $(Ni/Fe)O_6$ octahedra. The *I*4/*mmm* crystal structure is also directly viewed with annular bright field scanning transmission electron microscopy (ABF-STEM, Figure 2.1), which visualizes heavier cations and lighter oxygen anions simultaneously. The ABF-STEM image shows perfect stacking of the perovskite (BO_2) (B = Ni, Fe) layers and the rock salt (AO)(OA) (A = La, Sr) layers without stacking faults and the crystal structure propagates to the surface without amorphization.

The consistent morphology of catalysts is crucial to the analytical comparison of electrochemical OER activity. High-angle annular dark-field scanning transmission electron microscopy (HAADF-STEM) and Brunauer-Emmet-Teller (BET) surface area analysis were performed and the results, presented in Figure A.5, indicate similar morphology across the LSNF series regardless of Fe substitution. All compositions consist of 50 – 300 nm crystallites loosely sintered into agglomerates that are up to several microns in size. This morphological similarity is reinforced by BET surface area results which range from 3.3 to 8.0 $m^2\ g^{-1}$ (Figure A.6).

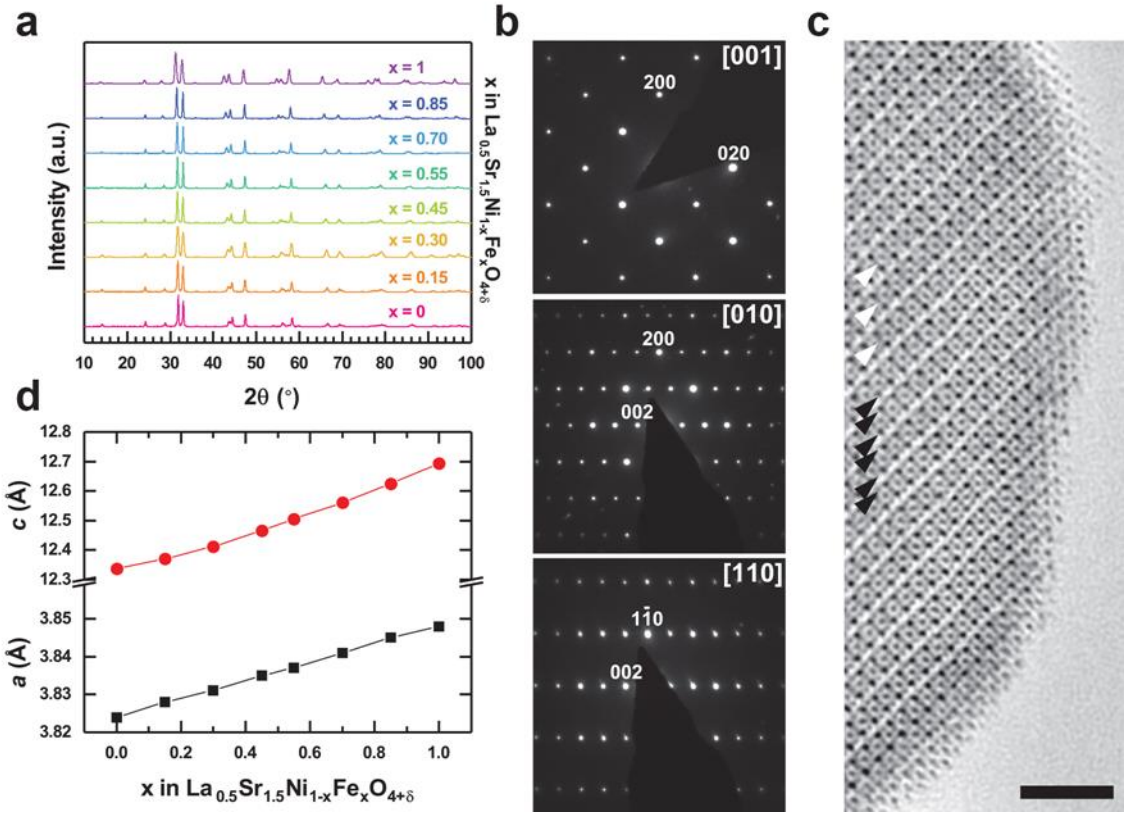

Figure 2.1: Crystallographic characterization of the $La_{0.5}Sr_{1.5}Ni_{1-x}Fe_xO_{4+\delta}$ series.

(a) PXRD patterns of $La_{0.5}Sr_{1.5}Ni_{1-x}Fe_xO_{4+\delta}$ demonstrate all compositions have the tetragonal $n = 1$ Ruddlesden-Popper *I4/mmm* structure. (b) Electron diffraction patterns of LSNF30 confirm the absence of cation and/or anion ordering. (c) [100] ABF-STEM image of LSNF30 directly visualizes the stacking of the (BO2) octahedra (white arrowheads, B = Ni, Fe) and (AO)(OA) layers (black arrowheads, A = La, Sr) in the Ruddlesden-Popper structure. The scale bar is 2 nm. (d) Compositional dependence of a and c unit cell parameters showing $0 < x < 1$ homogeneity range.

2.3.2: Electrochemistry

The $La_{0.5}Sr_{1.5}Ni_{1-x}Fe_xO_{4+\delta}$ (LNSF) series was supported at 30 wt% on Vulcan carbon (VC) and tested for the OER with the results presented in Figure 2.2. Supporting the catalyst on VC increases the conductivity of the composite by facilitating increased electrical contact between the glassy carbon RDE and the catalyst particles as well as

between catalyst particles themselves. While carbon has its limitations as a support for device-level applications, the issue of carbon corrosion is a matter of kinetics and for fundamental studies such as this one it is quite common to support metal oxide catalysts on carbon when doing OER studies at room temperature. A major reason for this is to eliminate possible contributions from other supports, such as Ni foam, that while more appropriate for device-level mass loadings and performance can contribute a great deal to the OER current generated or have their own redox features that can convolute the examination of the material of interest and the fundamental principles explored in this work. The carbon ratio used in this paper was chosen as a result of our past work in which we carefully studied the effect of the catalyst to carbon ratio to determine that a 30:70 weight-ratio resulted in optimal catalyst utilization.[37]

Representative polarization curves for all supported compositions are shown in Figure 2.2a and Figure A.7. For all amounts of Fe substitution, except for 100% (LSF), the onset potential for the OER decreases and the corresponding catalytic activity increases significantly compared to LSN. Merely 15% replacement of Ni with Fe increases the specific activity (mA cm^{-2}_{oxide}) by over an order of magnitude at 1.63 V vs the reversible hydrogen electrode corrected for electrolyte resistance (RHE-iR) as seen in Figure 2.2. Further substitution of Fe for Ni yields a volcano-like catalytic trend with 30% Fe substitution in LSNF30 being the most active composition. LSNF30 displays exceptionally high catalytic activities of 32.7 mA cm^{-2}_{oxide} and 1930 mA mg^{-1}_{oxide} at 1.63 V, over 20 and 40 times higher than the respective values for LSN, with a Tafel slope of 44 mV dec^{-1} and achieves the common benchmark of 10 mA cm^{-2}_{geo} at only a 360 mV overpotential which is remarkable considering the relatively small mass loading used (Figure 2.2). Details regarding conversion of potentials from Hg/HgO to RHE can be found in Appendix A and Figure A.8. Figures 2.2 and A.9 demonstrate the significantly higher mass activity of

LSNF30 compared to other leading metal oxide OER catalysts with LSNF30 being over 5 times more active than the recently reported $SrCoO_{2.7}$ (1930 vs 332 mA mg^{-1}_{oxide}) and over an order of magnitude more active than IrO_2 (173 mA mg^{-1}_{oxide}), a leading precious-metal oxide benchmark catalyst.[14] The LSNF30 composition generates 3 times as much current per surface area as $SrCoO_{2.7}$ (32.7 vs 9.2 mA cm^{-2}_{oxide}) and over an order of magnitude more than IrO_2 (1.2 mA cm^{-2}_{oxide}) at 1.63 V (Table A.2). The catalytic activity of VC is negligible, contributing only 7 mA mg^{-1} (Figures A.7 and A.9) at 1.63 V. Cyclic voltammetry experiments using a rotating ring disk electrode (RRDE) were performed to ensure the measured currents for LSNF30VC were due to oxygen evolution and not carbon oxidation or other reactions. As can be seen in Figure 2.2, at 1.63 V, the same potential at which we base our activity measurements, the measured collection efficiency of 34% closely matches the theoretical collection efficiency. While carbon corrosion may become a factor at much higher potentials where the VC support would oxidize, at the potentials we use to examine the catalyst in this fundamental context the only current measured is due to oxygen evolution, lending further validity to the trends we observe. Additional RRDE experimental details can be found in Appendix A and Figure A.10. In the absence of the VC support, much lower activities were observed (Figure A.11) due to the lack of a carbon matrix to increase conductivity, however, the same volcano trend in activities was observed across the LSNF series and LSNF30 exhibited catalytic activity comparable to IrO_2. Table A.2 summarizes the catalytic activities of other promising catalysts to enable comparison with LSNF30 using multiple metrics. Examined in the context of both precious and non-precious metal OER catalysts, LSNF30 is one of the most active catalysts ever reported for the OER.

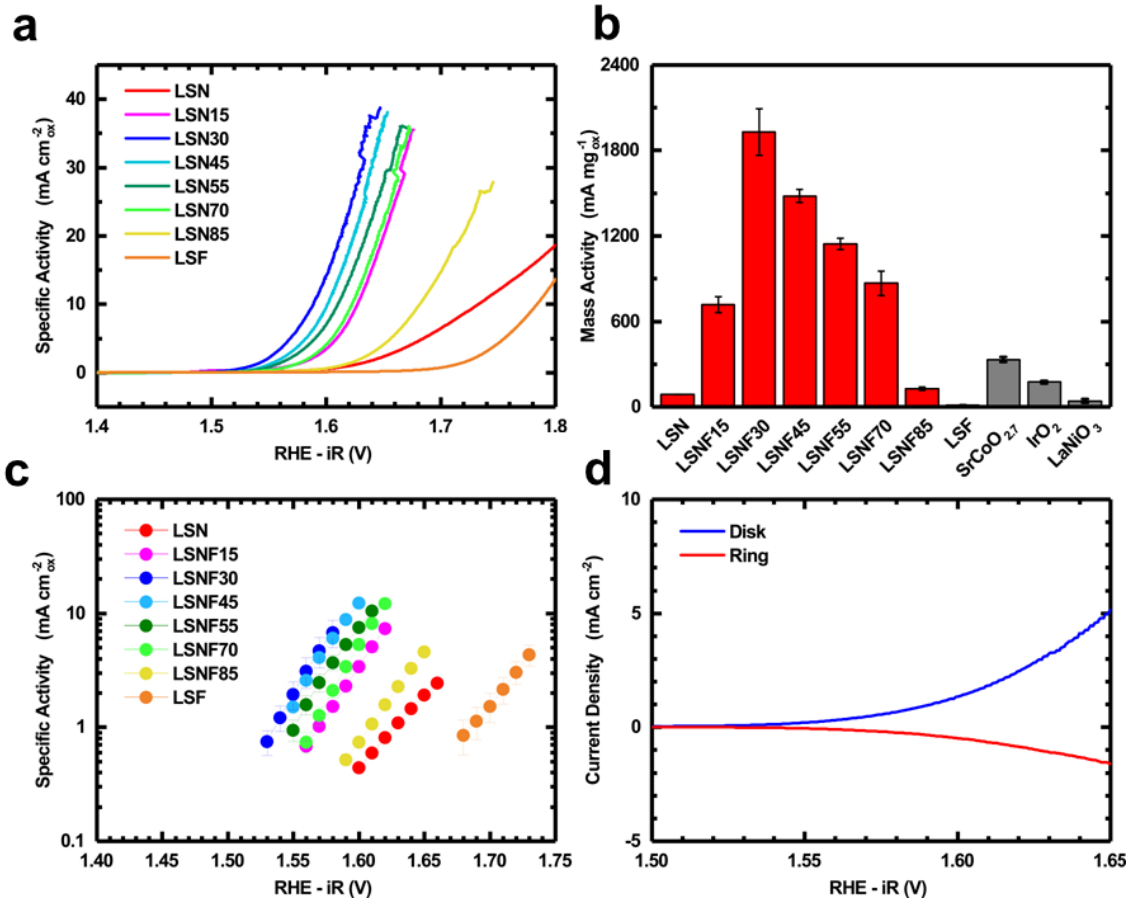

Figure 2.2: Oxygen evolution results and catalytic activities for the LSNF series.

(a) Averaged (anodic and cathodic) OER polarization curves presented in geometric current density (5 mm GCE, A = 0.196 cm^2). (b) Oxide mass activities of the LSNF series at 1.63 V vs RHE-iR compared to leading OER catalysts $SrCoO_{2.7}$, $LaNiO_3$ and IrO_2 on VC, all tested in the same experimental setup and conditions. Error bars are the standard deviations of measurements performed in triplicate. (c) Tafel plots of the specific activity of each LSNF catalyst. Error bars are the standard deviations of measurements performed in triplicate (d) RRDE test to confirm that current is due to oxygen evolution. The disk has a thin layer of 30 wt% LSNF30/VC and the ring is Pt. O_2 generated at the disk is then reduced back to OH^- at the ring which is poised at -0.4 V versus Hg/HgO (1 M). The collection efficiency of the RRDE at 1.63 V was found to be 34%. RRDE measurements were performed in Ar-saturated 0.1 M KOH.

The stability of LSNF30 was investigated using multiple types of electrochemical tests. One such experiment was a galvanostatic current hold during which the supported

catalyst sustained 10 A g^{-1}_{ox} for over 24 hours without failure (Figure A.12). To further investigate the stability of the catalyst both supported and unsupported LSNF30 materials were drop cast at 1 mg cm^{-2} onto Ni foam electrodes and cycled 100 times in 0.1 M KOH. The currents measured at 1.63 V on the Ni foam that is capable of performing the OER on its own, both drop cast with VC and without, were subtracted out. As can be seen in Figure 2.3 and Figure A.13 the OER current generated by the LSNF30VC composite stabilizes very quickly and displays a much higher mass activity than the unsupported catalyst due to the added conductivity of the composite that comes from the VC support. These activities are much lower than measured on RDE due to the inefficient catalyst utilization that comes from using higher mass loadings as well as mass transport limitations and the buildup of oxygen on the electrode without rotation. These stability experiments demonstrate that while a small amount of amorphization may occur at the surface during the first CV (Figure A.14) as a result of wetting or an initial restructuring such has been seen for other perovskite catalysts[38] and as was seen for the bare Ni foam electrodes, the exceptionally high activities we observe are due to the covalency imparted by Sr substitution into the crystalline RP phase and the stability of the structure with repeated cycling. Were a transformation to amorphous oxyhydroxide phases taking place and governing the catalytic activity of the LSNF materials then we would expect much lower currents due to the decreased surface areas of active sites formed at high temperature as well as the majority of oxide mass that is made up of catalytically inactive La and Sr sites. The stability of LSNF materials was further studied using DFT and is discussed below.

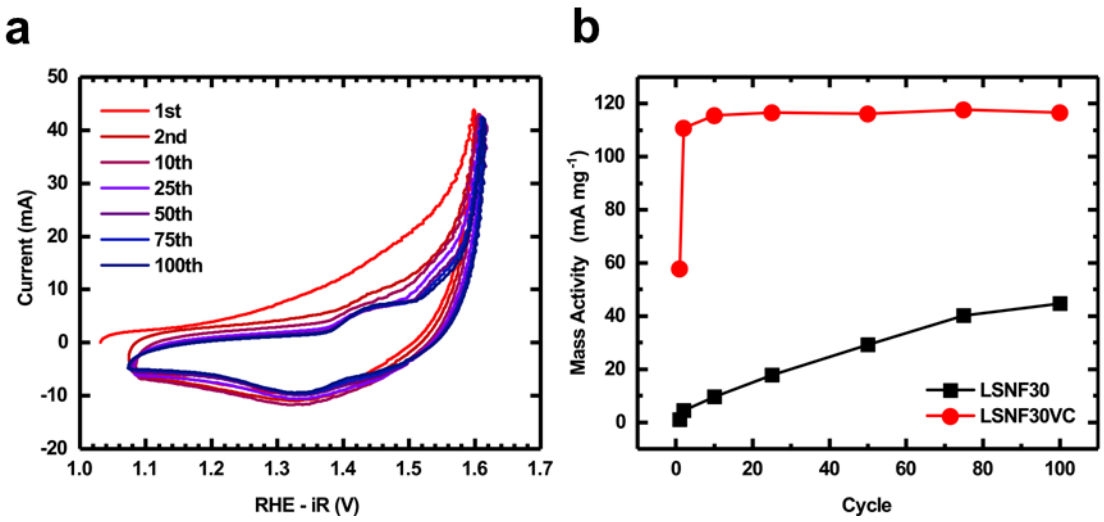

Figure 2.3: Cyclic voltammetry stability tests of LSNF30 dropcast on Ni foam electrodes. (a) 100 cycles of LSNF30 supported at 30 wt% on VC performed in O_2-saturated 0.1 M KOH at 10 mV s^{-1}. (b) Mass activities measured at 1.63 V for both LSNF30VC and unsupported LSNF30 at various points during the 100 cycle stability tests. Stability tests of LSNF30 were dropcast on Ni foam electrodes at 1 mg cm^{-2}. Mass activities were calculated by subtracting the current at 1.63 V for a Ni foam electrode with or without carbon but without catalyst from the current measured from the catalyst on Ni foam with or without the VC support and then dividing by the mass of catalyst used.

Upon exposure to alkaline electrolyte the surface of the catalyst is hydroxylated and reduced. The $Ni^{2+/3+}$ redox couple in LSNF is observed to shift to more positive potentials with Fe substitution, indicating a direct modulation of Ni's reactivity with Fe substitution. This redox couple exists in the incipient OER region, as indicated in the reversible cyclic voltammetry (CV) peaks in Figure 2.4. The potential range over which the redox peaks are observed is consistent with prior studies of Ni-based electrocatalysts[3,39,40] with Fe substitution shifting the peak potential (EP) of $Ni^{2+/3+}$ oxidation as documented with Ni-Fe oxyhydroxides.[3,4,39] Integration of the oxidation

waves reveals that the specific oxidative charge ($\mu C\ cm^{-2}_{oxide}$) transferred during oxidation/intercalation consistently decreases upon continued replacement of Ni with Fe, with the exception of the initial introduction of Fe in LSNF15 (Figure 2.4). Similar behavior was previously reported for 10% Fe substitution into NiOOH electrodes[3] and was speculated to be due to increased oxygen and electrolyte diffusivity. This interpretation is supported here by the increased electrochemical oxygen diffusion rate measured in LSNF15 as compared to LSN (1.04E-12 $cm^2\ s^{-1}$ vs 8.03E-13 $cm^2\ s^{-1}$) and confirms that along with the surface redox of $Ni^{2+/3+}$, oxygen intercalation concomitant with Ni redox is likely given the labile nature of oxygen in $La_2NiO_{4+\delta}$. The observation that the pH dependence of the $Ni^{2+/3+}$ oxidation E_p in Figure A1.14 behaves like a Nernstian pseudocapacitor using OH^- as the intercalating ion further indicates that the intercalation of oxygen is taking place.[14,37,41,42]

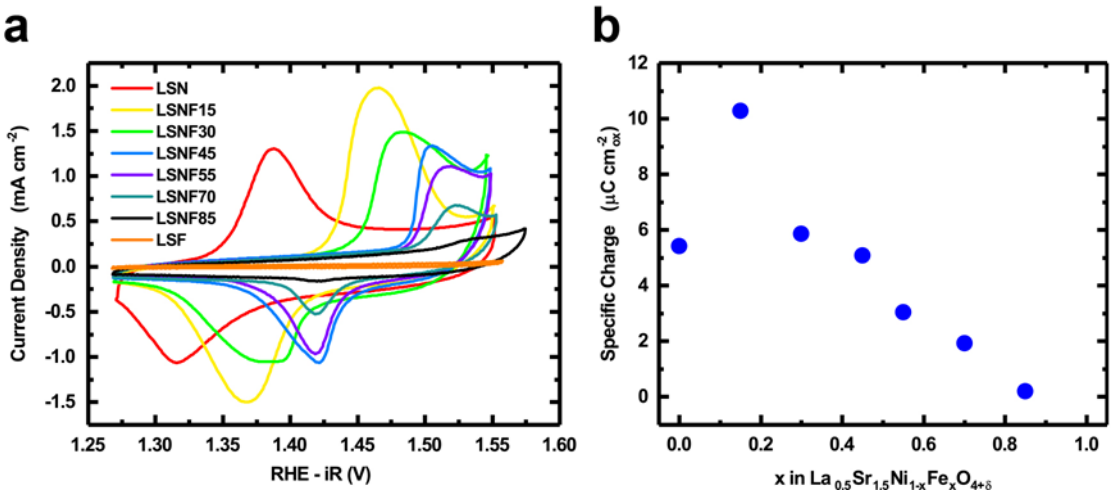

Figure 2.4: Cyclic voltammetry (CV) of LSNF catalysts in O_2-saturated 0.1 M KOH.

(a) CVs of LSNF at 100 mV s^{-1} revealing a systematic anodic shift in $Ni^{2+/3+}$ oxidation/intercalation potentials with increasing Fe substitution. CVs at 100 mV s^{-1}, taken after 3 to 4 cycles, are depicted to aid the reader in distinguishing peak potential shifts and relative areas, but at 100 mV s^{-1} contributions to E_P from capacitance and mass transport resistance cannot be ignored. To address this, peak potentials reported in Figure A.8 were taken from stable CVs at 10 mV s^{-1}. (b) Specific oxidative charge (μC cm^{-2}_{oxide}) resulting from the integration of oxidation waves. Integrations were performed using specific current density (μA cm^{-2}_{oxide}) to normalize differences in catalyst surface area (Figure A.8). The OER baselines for stable CVs at 10 mV s-1 were fit and subtracted. Figure A.14 contains the CVs used for integration.

It is known that over 50% Sr substitution for La induces metal-like conductivity[25,43] in the charge transfer insulator $La_2NiO_{4+\delta}$ due to hole doping in the O 2*p* band.[44] Furthermore, the remarkable improvement of the catalytic activity of LSN upon Fe substitution for Ni may be explained by the impact of the Fe 3*d* states on the electronic structure of LSNF. Earlier studies of the electronic structure of $La_{1.1}Sr_{0.9}Ni_{0.8}Fe_{0.2}O_{4+\delta}$ with resonant photoemission spectroscopy suggest that the Fe 3*d* states make a substantial contribution to the valence band near the Fermi level (E_F) by strongly hybridizing with the O 2*p* and Ni 3*d* states which facilitates cation oxidation and

redox processes.[28] The mixed Fe 3*d* and Ni 3*d* bands pinned at E_F in close proximity to the O 2*p* band should give rise to a mixture of $Ni^{3+/4+}$ and $Fe^{3+/4+}$ where the relative proportion of oxidation states changes with the amount of Fe substitution.[27,29,45] This was confirmed by *ex-situ* room temperature Mössbauer spectroscopy (Figures A.18, A.19, Table 2.1) in conjunction with iodometric titrations. Knowing the average B-site oxidation state as well as the oxidation state of Fe allows for the calculation of the Ni oxidation state and Table 2.1 contains the results of this analysis. The average oxidation state of Ni increases with increasing Fe content from +3.54 in LSN to +3.95 in LSN85, as does the oxygen hyperstoichiometry (δ) and the average B-site oxidation state. The increase in the oxidation state of Ni is further demonstrated by the observation that the Ni 3*p* spectrum obtained by X-ray photoelectron spectroscopy (XPS) shifts to higher binding energies with increasing Fe content (Figure A.20), and again by the positive shift in potential of the $Ni^{2+/3+}$ redox features upon Fe substitution (Figure 2.4). Fitting parameters for Mössbauer spectroscopy can be found in Tables A.4 and A.5. Additional discussion of oxygen stoichiometry and LSNF oxidation states can be found in Appendix A.

LSNF Series Oxidation State Characterization									
Catalyst	Fe sub.	δ, hyperst.	δ st. dev	B^{+} avg	B^{+} st. dev	Fe^{4+} (Moss.)	Fe^{3+} (Moss.)	Ni^{x+} avg	Ni^{x+} st. dev
LSN	0%	0.018	0.013	3.54	0.03	-	-	3.54	0.03
LSNF15	15%	0.046	0.007	3.59	0.01	73%	27%	3.57	0.02
LSNF30	30%	0.042	0.010	3.58	0.02	62%	38%	3.57	0.03
LSNF45	45%	0.065	0.027	3.63	0.05	57%	43%	3.68	0.10
LSNF55	55%	0.088	0.011	3.68	0.02	58%	42%	3.80	0.05
LSNF70	70%	0.076	0.022	3.65	0.04	58%	42%	3.82	0.14
LSNF85	85%	0.081	0.036	3.66	0.07	61%	39%	3.95	0.48
LSF	100%	0.143	0.037	3.79	0.07	62%	38%	-	-

Table 2.1: Oxygen hyperstoichiometry (δ) and B-site oxidation states in $La_{0.5}Sr_{1.5}Ni_{1-x}Fe_xO_{4+\delta}$. Average B-site oxidation states were determined by iodometry, the results of Mössbauer spectroscopy and the calculated average Ni oxidation state. Figures A.18 and A.19 contain the deconvoluted Mössbauer spectra.

2.3.3: Density Functional Theory (DFT) Modeling

To further understand the electronic structure evolution across the LSNF series and its implications for the OER activity, as well as confirm the results of the Mössbauer spectroscopy and iodometric titrations, we model the bulk phase of LSNF and a simplified $Sr_2Ni_{1-x}Fe_xO_4$ (SNF) series by density functional theory (DFT). While the SNF system was not investigated experimentally, it was modelled to confirm that the same trends in electronic structure evolution that occur in LSNF also take place in a sample with a different A-site composition. Additionally, modelling the SNF series also eliminates a possible source of variation between the atomic arrangements of A-site

elements in the modeled LSNF system versus the arrangements in the synthesized samples and verifies our results on a simplified catalyst system.

A series of LSNF compositions are modeled by 2x2x1 primitive unit cells, allowing for unit compositions of $La_{0.5}Sr_{1.5}NiO_4$ (LSN), $La_{0.5}Sr_{1.5}Ni_{0.75}Fe_{0.25}O_4$ (LSNF25), LSNF50, LSNF75 and LSF. The SNF series was modeled using the same Ni and Fe ratios, and details regarding cell formation and magnetic investigation are given in Appendix A. Figure 2.5 shows the (001) atomic layers of the most stable LSNF structures based on our screening. First, we look at LSN (Figure 2.4) and we find a uniform, proportional distribution of La/Sr.[46] Using this La/Sr distribution we determine the minimum energy Ni/Fe ordering which results in two key features governing the Fe arrangement in LSNF (Figure 2.5). First, each of the two $B(B')O_2$ layers has an equal number of Fe cations in order to prevent an unbalanced charge distribution between them. Second, the Fe cations in each $B(B')O_2$ plane are distributed such that the number of Fe-O-Ni bridges is maximized.[2] This arrangement mitigates the effects of the induced O 2*p* electron hole at Ni-O-Ni bridges due to more effective electron donation by Fe at Fe-O-Ni bridges, which increases stability.[18] Compared with Fe-O-Fe bridges, the Fe-O-Ni bridges induce shorter Fe-O bond lengths and indicate higher Fe oxidation states, a trend that also occurs in the simplified SNF system. This observation agrees with the experimentally observed predominance of Fe^{4+} over Fe^{3+} at low Fe substitution as well as the increase in unit cell parameters as Fe content increases (Figure 2.1, Table A.1).

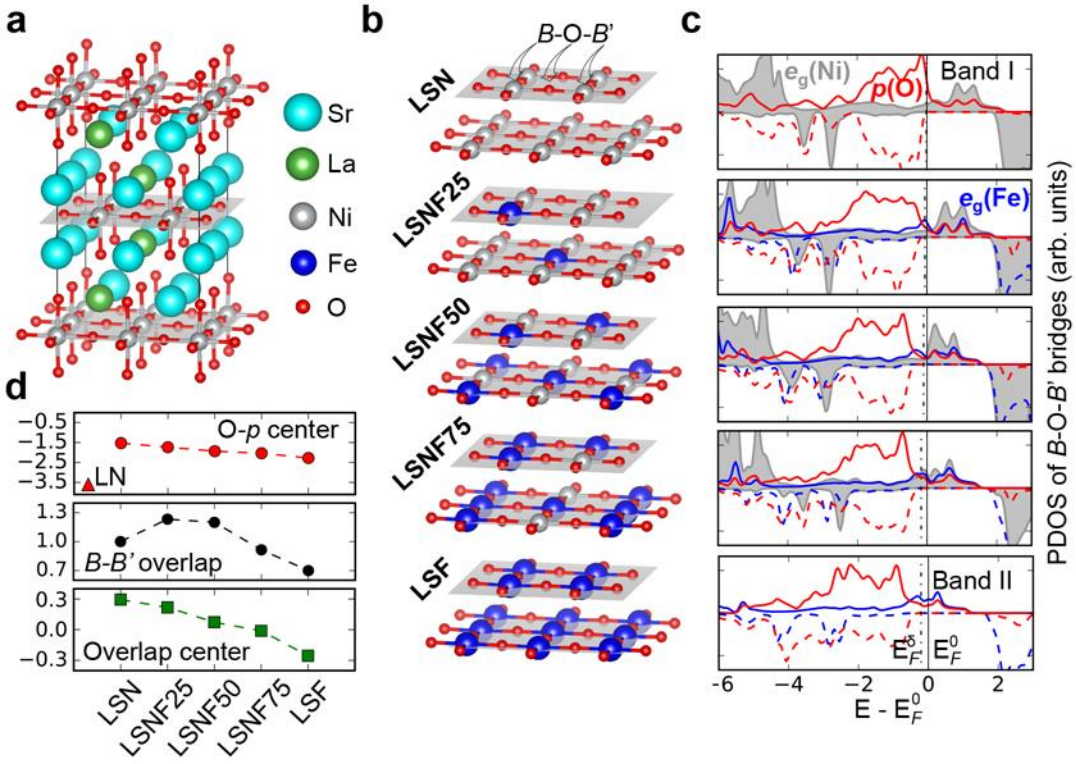

Figure 2.5: Density functional theory modeling of atomic and electronic structures of bulk LSNF in ferromagnetic configuration.

(a) Density functional theory modeling of atomic and electronic structures of bulk LSNF in ferromagnetic configuration. (a) The ground-state 2x2x1 cell of $La_{0.5}Sr_{1.5}NiO_4$, with uniformly distributed La in each [001] *A*O layer. (b) Representations of the two *B*(*B*')O_2 layers for each ground state $La_{0.5}Sr_{1.5}Ni_{1-x}Fe_xO_4$, with x at 0, 0.25, 0.5, 0.75 and 1; for each x, the ground state Fe arrangement is characterized by equal numbers of Fe in the two *B*(*B*')O_2 layers, with the Fe in each layer arranged to maximize the number of Fe-O-Ni bridges. (c) The corresponding spin polarized PDOS of e_g (Ni: grey shaded area, and Fe: blue line) and 2*p* (O: red line) with respect to Fermi level (E_F^0) for the *B*-O-*B*' bridges; the PDOS are the average of existing *B*-O-*B*' bridges; the adapted Fermi level (E_F^δ) to oxygen hyperstoichiometry is estimated via the rigid band model, with $E_F^\delta = E_F^0 - 2e^-\delta/\mathrm{DOS}(E_F^0)$ (Equation 2.1), where $\mathrm{DOS}(E_F^0)$ is the total density of states at E_F^0 per formula unit of LSNF. (d) Top: Computed values of the O-*p* band center (top panel), with La_2NiO_4 calculated as reference. Middle: The magnitude of band overlap, determined by the integration of maximum PDOS between e_g(*B*) and e_g(*B*') from -2 to 2 eV, normalized to e_g(Ni) in LSN. Bottom: The corresponding overlap center (centroid) of maximum PDOS between e_g(*B*) and e_g(*B*'). Additional details can be found in Supplementary Note A.1.

The computed projected density of states (PDOS) of the Fe-O-Ni bridges in both LSNF and SNF confirm that the Ni cations are in the low-spin state with fully occupied $t_{2g}^{\downarrow}$ states (Figures A.21-A.23) while the Fe cations are in the high-spin state with mostly unoccupied $t_{2g}^{\downarrow}$ states for all LSNF and SNF.[47] These spin states lead to e_g bands positioned around the Fermi level (E_F^0), thus becoming the most relevant for Fe-O-Ni interactions of interest and the focus of our study. Inspection of the Fe-O-Ni bridges reveals significant overlap of O 2p, Ni $e_g^{\uparrow}$ and Fe $e_g^{\uparrow}$ bands for all compositions in the LSNF series (Figure 2.5), in agreement with our predictions. The same overlap is observed in the SNF series with only a small downward shift in E_F due to increased oxidation of the B-site elements to differentiate the two (Figure A.23). This overlap leads to two important observations. First, the unoccupied O $2p^{\uparrow}$ states indicate oxygen electron holes with finite PDOS across E_F^0, thus bridging charge transfer between neighboring cations.[36,47] Second, the similar energies of the Ni and Fe $e_g^{\uparrow}$ states (denoted Band I and Band II in the following) open up the possibility of electron exchange through oxygen. These two factors govern the evolution of the PDOS from LSN to LSF and from SN to SF. On one hand, the substitution of Ni by less electronegative Fe stabilizes O 2p electrons and increases the Ni-O distances, shifting the O 2p band center downwards relative to E_F (Figure 2.5, Figure A.23) and decreasing the bandwidth[47] which reduces electron hole concentration and charge transfer ability.[44] This condition is consistent with the experimentally observed increase in oxygen hyperstoichiometry going from LSN to LSF (Table 2.1, Table A.3). On the other hand, the partially filled Band II (Fe) significantly hybridizes with both O 2p and Band I (Ni), driving the latter towards E_F^0. Both Bands I and II make significant contributions to the occupied (valence) and unoccupied (conduction) states, respectively, and this dramatically increases the bandwidth of the triple band overlap going from LSN to LSNF50 and from SN to SNF50, with its center approaching E_F^0. As the e_g states are relevant for surface

chemisorption, the increasing bandwidth around E_F^0 would decrease the energetic cost to accept/donate electrons[28] at the adsorbate-catalyst interface, and therefore should increase the rate of reaction according the Gerischer-Marcus model of charge transfer.[48] The increased Fe concentrations in LSNF75 and SNF75, however, drive Band I (Ni) into the similar distribution of Band II (Fe) and this reduces the bandwidth (Figure 2.5). This suggests that the optimal OER activity will occur for a composition between LSNF25 and LSNF50, consistent with experimental observations. Although these calculations are performed for the bulk structure of LSNF, the surface electronic structure is expected to be strongly correlated to that of bulk, similar to ABO_3 perovskites as was demonstrated in previous work,[32] thus preserving the key feature of Ni-O-Fe hybridization and its evolution across LSNF and SNF compositions.

The computed band structure of LSNF is similar to that reported for other highly active OER catalysts, especially those compositions with mixed transition metal sites such as Ni-Fe layered double hydroxide (LDH) catalysts.[2] Conesa calculated the DOS of one such polymorph, $FeNi_7O_8(OH)_8$ in the $2H_C$ structure with Fe in $O_4(OH)_2$ coordination, and their result is strikingly similar to that of LSNF in that Ni and Fe 3*d* bands are strongly hybridized just above E_F. They concluded that Fe^{4+} is stabilized by induced charge transfer between Ni sites, which is also seen in Ni-Fe oxyhydroxides,[6] and this explanation agrees with our observation of Fe in the 4+ oxidation state in LSNF (Table 2.1). The shifting of the $Ni^{2+/3+}$ redox couple upon Fe substitution that we observe (Figure 2.4) has previously been reported in NiOOH upon incorporation of Fe and is further evidence of this partial charge transfer between Fe and/or Ni.[4,5,33] A change in covalency by the introduction of FeO_6 units into LSN must have an inductive effect on Ni through next nearest neighbor interactions via Fe-O-Ni bridges,[49] which is consistent with the observation that our activity

is maximized for the composition having the highest probability of Fe-O-Ni bridging interactions, LSNF30.

The band structure of LSNF is also similar to the computed band structures of $LaCo_{1-x}Fe_xO_3$,[50] $Sr_{2-x}La_xMO_{4\pm\delta}$[34] and $Ba_{0.5}Sr_{0.5}Co_{0.75}Fe_{0.25}O_{3\pm\delta}$ (BSCF).[39] Merkle calculated the band diagram for BSCF and found a similar electronic configuration as in LSNF, and Schmidt and coworkers saw that the catalytic activity of $Ba_{0.5}Sr_{0.5}Co_{0.8}Fe_{0.2}O_{3\pm\delta}$ was much higher than that of $Ba_{0.5}Sr_{0.5}CoO_{3\pm\delta}$.[38] Thus it is possible that the high activity of BSCF, $SrNb_{0.1}Co_{0.7}Fe_{0.2}O_{3-\delta}$[38,51] as well as others with similar mixed transition metal sites may be rationalized not just by the covalent bonding, but also by triply-overlapping Co/Ni and Fe 3*d* states with O 2*p* near E_F similar to the LSNF series, which has largely been overlooked up to now. Furthermore, the similarities between the band structures of LSNF materials and these other active catalysts of varying structures, some of them amorphous, reinforces how the principle of cross-gap hybridization may apply to many different metal oxide catalysts and applies to the LSNF series even in the event of surface restructuring.

2.3.4: Mechanistic Insights

As we have discussed in previous work, the OER can proceed by the adsorbate exchange mechanism (AEM) or the lattice oxygen mediated (LOM) mechanism.[14,18] In the AEM, chemisorbed intermediates undergo a series of electrochemical oxidations as the transition metal active site undergoes oxidation and reduction, and these redox reactions are the most energetically intensive and thus rate limiting steps.[14] The lattice oxygen mediated (LOM) OER mechanism, on the other hand, does not require significant redox switching of transition metal sites but instead requires the participation of lattice oxygen in the OER. Ligand holes that arise when transition metal 3*d* bands are highly covalent with

O 2p bands and exist around E_F^0 activate lattice oxygen that combines with chemisorbed OH to produce O_2^-. In previous studies we found that the DFT-computed O_{vac} formation energy in bulk ABO_3 perovskites (donated as ΔE_{V_O}) served as an effective indicator of OER mechanism.[18] Highly covalent perovskites favor O_{vac} formation that results from an overall high-energy lying O 2p band relative to E_F^0 and the appearance of electron holes that facilitate reversible lattice oxygen participation under OER conditions. Employing ΔE_{V_O}, we showed that the OER mechanism switches from the AEM to the LOM with decreasing ΔE_{V_O} for the $La_xSr_{1-x}CoO_{3-\delta}$ series when x > 0.4.[14] The decrease in oxygen vacancy formation energy in these materials occurred in concert with an increase in oxygen diffusion rates and catalytic activity.[14] This proposed mechanistic switch was experimentally confirmed by a recent report from the Shao Horn group who used isotopic labeling of lattice oxygen to observe a transition from the AEM on $LaCoO_3$ to the LOM on $La_{0.5}Sr_{0.5}CoO_{3-\delta}$ and $SrCoO_{3-\delta}$.[17]

The same type of band overlap and resulting covalency that is a requirement of the LOM mechanism and that occurs in the previously reported materials discussed above also occurs in LSNF. The hybridization of e_g(Ni) and e_g(Fe) bands with the p(O) band across E_F^0 results in increased oxygen electron holes, and DFT computations reveal that ΔE_{V_O} in LSN, LSNF25 and LSNF50 at Ni-O-Fe bridges is more negative than in $LaNiO_3$ and $La_{0.5}Sr_{0.5}CoO_{3-\delta}$[18] while ΔE_{V_O} in LSNF75 and LSF is larger (Table A.6). Thus ΔE_{V_O}, a proven indicator of the LOM mechanism, works in conjunction with the experimentally measured increased oxygen diffusion rates from LSN to LSNF45 (Figure A.17, Table A.3), to suggest that the exchange of surface lattice O plays a key role in OER and that the highly active LSNF materials utilize a LOM-type mechanism. The catalytic effect from the LOM mechanism is further enhanced by the substitution of Fe that causes broadening of e_g bandwidth through Ni-O-Fe cross-gap hybridization. Altogether this demonstrates how the

LOM applies to a new series of materials and solidifies the importance of both increased covalency that results in oxygen electron holes, as well as the cross-gap hybridization that causes broadening of the overall bandwidth near E_F in the design and optimization of oxide catalysts.

2.4: CONCLUSIONS

We have precisely synthesized a series of RP catalysts having highly oxidized and covalent Ni 3*d* - O 2*p* - Fe 3*d* bonds that give rise to exceptional OER activity. Sr substitution into the perovskite $LaNiO_3$ has previously been proposed as an avenue to increase the oxidation state if Ni and Ni-O covalency but has not been fully realized. In this work we were able to avoid inactive secondary phases resulting from poor solubility of Sr in the perovskite phase through utilization of the RP crystal structure. Additionally, by using $La_{0.5}Sr_{1.5}NiO_{4\pm\delta}$ as the host lattice we achieved complete substitution of Fe for Ni across the entire compositional range. The crystalline RP structure and the high degree of phase purity enabled precise study of the impact of Fe substitution on the chemical and electronic properties of the LSNF series, something that has not been possible up to this point with other, amorphous materials. Iodometric titrations coupled with Mössbauer spectroscopy indicate that the average Ni oxidation state in the LSNF series increases from +3.46 to +3.95 with increasing Fe substitution while the $Ni^{2+/3+}$ redox peaks also shift to more positive potentials, consistent with Ni developing a more oxidized character. The influence of Fe substitution extends beyond increasing the oxidative strength of Ni, however, as the electrocatalytic activity increases by over an order of magnitude from LSN to LSNF30 despite possessing statistically equivalent Ni oxidation states. DFT calculations reveal that Fe substitution results in cross-gap hybridization where the Fe 3*d* e_g band is

hybridized with both the Ni 3*d* e_g and the top of the O 2*p* density of states across the Fermi level. The increased covalency of the Ni-O bonds as well as facile charge transfer through Fe-O-Ni bridges due to incorporation of Fe explains the enhanced catalytic activity going from LSN to LSNF30. Furthermore, the increased covalency demonstrated via calculated partial density of states for LSNF and a simplified SNF that is a requirement for the OER to take place via a lattice oxygen mediated (LOM) mechanism resembles the band structure of other highly active OER catalysts with varying crystal or amorphous structures for which this mechanism has already been verified. Decreased oxygen vacancy formation energies and increased rates of oxygen diffusion, descriptors already accepted in the literature as indications of the LOM, are seen on LSNF and further support the hypothesis that the OER proceeds via a LOM mechanism on LSNF. This methodology of selective A and B-site substitution to promote cross-gap hybridization in RP oxides reveals important fundamental aspects related to their structure and the exceptional electrocatalytic activities of these materials as well as other metal oxide catalysts.

2.5: REFERENCES

1. Zhu, H., Zhang, P. & Dai, S. Recent Advances of Lanthanum-Based Perovskite Oxides for Catalysis. *ACS Catal.* **5**, 6370–6385 (2015).
2. Conesa, J. C. Electronic Structure of the (Undoped and Fe-Doped) NiOOH O<sub>2 Evolution Electrocatalyst. *J. Phys. Chem. C* **120**, 18999–19010 (2016).
3. Corrigan, D. A. The Catalysis of the Oxygen Evolution Reaction by Iron Impurities in Thin Film Nickel Oxide Electrodes. *J. Electrochem. Soc.* **134**, 377–384 (1987).

4. Trotochaud, L., Young, S. L., Ranney, J. K. & Boettcher, S. W. Nickel–Iron Oxyhydroxide Oxygen-Evolution Electrocatalysts: The Role of Intentional and Incidental Iron Incorporation. *J. Am. Chem. Soc.* **136**, 6744–6753 (2014).

5. Dionigi, F. & Strasser, P. NiFe-Based (Oxy)hydroxide Catalysts for Oxygen Evolution Reaction in Non-Acidic Electrolytes. *Adv. Energy Mater.* **6**, (2016).

6. Chen, J. Y. C. *et al.* Operando Analysis of NiFe and Fe Oxyhydroxide Electrocatalysts for Water Oxidation: Detection of Fe^{4+} by Mössbauer Spectroscopy. *J. Am. Chem. Soc.* **137**, 15090–15093 (2015).

7. Görlin, M. *et al.* Tracking Catalyst Redox States and Reaction Dynamics in Ni–Fe Oxyhydroxide Oxygen Evolution Reaction Electrocatalysts: The Role of Catalyst Support and Electrolyte pH. *J. Am. Chem. Soc.* **139**, 2070–2082 (2017).

8. Hunter, B. M., Gray, H. B. & Müller, A. M. Earth-Abundant Heterogeneous Water Oxidation Catalysts. *Chem. Rev.* **116**, 14120–14136 (2016).

9. Bockris, J. O. & Otagawa, T. Mechanism of oxygen evolution on perovskites. *J. Phys. Chem.* **87**, 2960–2971 (1983).

10. Suntivich, J., May, K. J., Gasteiger, H. A., Goodenough, J. B. & Shao-Horn, Y. A Perovskite Oxide Optimized for Oxygen Evolution Catalysis from Molecular Orbital Principles. *Science* **334**, 1383–1385 (2011).

11. Hardin, W. G. *et al.* Tuning the Electrocatalytic Activity of Perovskites through Active Site Variation and Support Interactions. *Chem. Mater.* **26**, 3368–3376 (2014).

12. Structure, Properties and Preparation of Perovskite-Type Compounds. in (ed. Galasso, F. S.) iv (Pergamon, 1969).

13. Yagi, S. *et al.* Covalency-reinforced oxygen evolution reaction catalyst. *Nat. Commun.* **6**, 9249 (2015).

14. Mefford, J. T. *et al.* Water electrolysis on $La_{1-x}Sr_xCoO_{3-\delta}$ perovskite electrocatalysts. *Nat. Commun.* **7**, 11053 (2016).

15. Zhou, W., Zhao, M., Liang, F., Smith, S. C. & Zhu, Z. High activity and durability of novel perovskite electrocatalysts for water oxidation. *Mater. Horiz.* **2**, 495–501 (2015).

16. Man, I. C. *et al.* Universality in Oxygen Evolution Electrocatalysis on Oxide Surfaces. *ChemCatChem* **3**, 1159–1165 (2011).

17. Grimaud, A. *et al.* Activating lattice oxygen redox reactions in metal oxides to catalyse oxygen evolution. *Nat. Chem.* **9**, 457–465 (2017).

18. Rong, X., Parolin, J. & Kolpak, A. M. A Fundamental Relationship between Reaction Mechanism and Stability in Metal Oxide Catalysts for Oxygen Evolution. *ACS Catal.* **6**, 1153–1158 (2016).

19. Takeda, Y. *et al.* Synthesis of SrNiO3 and related compound, $Sr_2Ni_2O_5$. *J. Inorg. Nucl. Chem.* **34**, 1599–1601 (1972).

20. Oliveira, F. S., Pimentel, P. M., Oliveira, R. M. P. B., Melo, D. M. A. & Melo, M. A. F. Effect of lanthanum replacement by strontium in lanthanum nickelate crystals synthetized using gelatin as organic precursor. *Mater. Lett.* **64**, 2700–2703 (2010).

21. Seki, H., Saito, T. & Shimakawa, Y. High Pressure Synthesis of SrFe1−xNixO3. *J. Jpn. Soc. Powder Powder Metall.* **63**, 609–612 (2016).

22. Sharma, I. B. & Singh, D. Solid state chemistry of Ruddlesden-Popper type complex oxides. *Bull. Mater. Sci.* **21**, 363–374 (1998).

23. Amow, G., Davidson, I. J. & Skinner, S. J. A comparative study of the Ruddlesden-Popper series, $La_{n+1}Ni_nO3_{n+1}$ (n=1, 2 and 3), for solid-oxide fuel-cell cathode applications. *Solid State Ion.* **177**, 1205–1210 (2006).

24. Zhang, Z. & Greenblatt, M. Synthesis, Structure, and Properties of $Ln_4Ni_3O_{10-\delta}$ (Ln = La, Pr, and Nd). *J. Solid State Chem.* **117**, 236–246 (1995).

25. Takeda, Y. *et al.* Crystal chemistry and physical properties of $La_{2-x}Sr_xNiO_4$ ($0 \leq x \leq 1.6$). *Mater. Res. Bull.* **25**, 293–306 (1990).

26. Benloucif, R., Nguyen, N., Greneche, J. M. & Raveau, B. $La_{2-2x}Sr_{2x}Ni_{1-x}Fe_xO_{4-(x2)+\delta}$: Magnetic and electron transport properties. *J. Phys. Chem. Solids* **50**, 435–440 (1989).

27. Rao, C. N. R., Ganguly, P., Singh, K. K. & Ram, R. A. M. A comparative study of the magnetic and electrical properties of perovskite oxides and the corresponding two-dimensional oxides of K_2NiF_4 structure. *J. Solid State Chem.* **72**, 14–23 (1988).

28. F. Howlett, J. *et al.* Electronic structure, reactivity and solid-state chemistry of $La2-xSr_xNi_{1-y}Fe_yO_{4+\delta}$. *Faraday Discuss.* **105**, 337–354 (1996).

29. Gilev, A. R., Kiselev, E. A. & Cherepanov, V. A. Homogeneity range, oxygen nonstoichiometry, thermal expansion and transport properties of $La_{2-x}Sr_xNi_{1-y}FeyO_{4+\delta}$. *RSC Adv.* **6**, 72905–72917 (2016).

30. Cohen, R. E. Origin of ferroelectricity in perovskite oxides. *Nature* **358**, 136–138 (1992).

31. Kakihana, M. & Yoshimura, M. Synthesis and Characteristics of Complex Multicomponent Oxides Prepared by Polymer Complex Method. *Bull. Chem. Soc. Jpn.* **72**, 1427–1443 (1999).

32. Akhade, S. A. & Kitchin, J. R. Effects of strain, *d* -band filling, and oxidation state on the surface electronic structure and reactivity of 3 *d* perovskite surfaces. *J. Chem. Phys.* **137**, 084703 (2012).

33. Corrigan, D. A., Conell, R. S., Fierro, C. A. & Scherson, D. A. In-situ Moessbauer study of redox processes in a composite hydroxide of iron and nickel. *J. Phys. Chem.* **91**, 5009–5011 (1987).

34. Lee, Y.-L. *et al.* Kinetics of Oxygen Surface Exchange on Epitaxial Ruddlesden–Popper Phases and Correlations to First-Principles Descriptors. *J. Phys. Chem. Lett.* **7**, 244–249 (2016).

35. Merkle, R., Mastrikov, Y. A., Kotomin, E. A., Kuklja, M. M. & Maier, J. First Principles Calculations of Oxygen Vacancy Formation and Migration in $Ba_{1-x}Sr_xCo_{1-y}Fe_yO_{3-\delta}$ Perovskites. *J. Electrochem. Soc.* **159**, B219–B226 (2011).

36. Erat, S. *et al.* Entanglement of charge transfer, hole doping, exchange interaction, and octahedron tilting angle and their influence on the conductivity of $La_{1-x}Sr_xFe_{0.75}Ni_{0.25}O_{3-\delta}$: A combination of x-ray spectroscopy and diffraction. *J. Appl. Phys.* **108**, 124906 (2010).

37. Mefford, J. T., Hardin, W. G., Dai, S., Johnston, K. P. & Stevenson, K. J. Anion charge storage through oxygen intercalation in $LaMnO_3$ perovskite pseudocapacitor electrodes. *Nat. Mater.* **13**, 726–732 (2014).

38. Fabbri, E. *et al.* Dynamic surface self-reconstruction is the key of highly active perovskite nano-electrocatalysts for water splitting. *Nat. Mater.* **16**, 925–931 (2017).

39. Louie, M. W. & Bell, A. T. An Investigation of Thin-Film Ni–Fe Oxide Catalysts for the Electrochemical Evolution of Oxygen. *J. Am. Chem. Soc.* **135**, 12329–12337 (2013).

40. Forslund, R. P. *et al.* Nanostructured $LaNiO_3$ Perovskite Electrocatalyst for Enhanced Urea Oxidation. *ACS Catal.* **6**, 5044–5051 (2016).

41. Bhavaraju, S., DiCarlo, J. F., Scarfe, D. P., Jacobson, A. J. & Buttrey, D. J. Electrochemical oxygen intercalation in $La_2NiO_{4+\delta}$ crystals. *Solid State Ion.* **86**, 825–831 (1996).

42. Conway, B. E. *Electrochemical Supercapacitors*. (Springer, 1999).

43. Sreedhar, K. & Honig, J. M. Low-Temperature Electron Transport Properties of $La_{2-x}Sr_xNiO_4$ with $0.5 \leq x \leq 1.3$. *J. Solid State Chem.* **111**, 147–150 (1994).

44. Torrance, J. B., Lacorre, P., Nazzal, A. I., Ansaldo, E. J. & Niedermayer, C. Systematic study of insulator-metal transitions in perovskites $RNiO_3$ (R=Pr,Nd,Sm,Eu) due to closing of charge-transfer gap. *Phys. Rev. B* **45**, 8209–8212 (1992).

45. Falcón, H., Carbonio, R. E. & Fierro, J. L. G. Correlation of Oxidation States in $LaFe_xNi_{1-x}O_{3+\delta}$ Oxides with Catalytic Activity for H_2O_2 Decomposition. *J. Catal.* **203**, 264–272 (2001).

46. Ritzmann, A. M., Muñoz-García, A. B., Pavone, M., Keith, J. A. & Carter, E. A. Ab Initio DFT+U Analysis of Oxygen Vacancy Formation and Migration in $La_{1-x}Sr_xFeO_{3-\delta}$ (x = 0, 0.25, 0.50). *Chem. Mater.* **25**, 3011–3019 (2013).

47. Mogni, L. *et al.* Synthesis, crystal chemistry and physical properties of the Ruddlesden–Popper phases $Sr_3Fe_{2-x}Ni_xO_{7-\delta}$ ($0 \leqslant x \leqslant 1.0$). *J. Solid State Chem.* **178**, 1559–1568 (2005).

48. Bard, A. J. & Faulkner, L. R. *Electrochemical Methods: Fundamentals and Applications*. (Wiley, 2000).

49. Goodenough, J. B. *Magnetism And The Chemical Bond*. (John Wiley And Sons, 1963).

50. Duan, Y. *et al.* Tailoring the Co 3d-O 2p Covalency in $LaCoO_3$ by Fe Substitution To Promote Oxygen Evolution Reaction. *Chem. Mater.* **29**, 10534–10541 (2017).

51. Zhu, Y. *et al.* SrNb0.1Co0.7Fe0.2O3−δ Perovskite as a Next-Generation Electrocatalyst for Oxygen Evolution in Alkaline Solution. *Angew. Chem. Int. Ed. Engl.* **127**, 3969–3973 (2015).

Chapter 3: The Electrooxidation of Urea on $LaNiO_3$ Perovskite Oxide[≠]

3.1: INTRODUCTION

Urea is an abundant waste product and large amounts of urea in industrial and human wastewater naturally break down into ammonia and nitrate, which can find their way into the atmosphere and the groundwater and cause health problems.[1] In addition to providing a pathway to eliminate urea as a possible health and environmental hazard, the electrooxidation of urea has been considered as a possible anodic reaction for the generation of hydrogen.[2] Theoretically, urea is oxidized at the anode at a potential of -0.46 V vs. SHE while hydrogen is evolved at the cathode at a potential of -0.83 V vs. SHE, giving a total theoretical cell potential of 0.37 V vs. SHE. This is much lower than water at 1.23 V, allowing for cheaper hydrogen production via urea oxidation than through water electrolysis.[2,3] Urea is non-flammable, relatively non-toxic, and can be stored as a solid; all promising qualities for use as a hydrogen carrier as hydrogen grows in its use as a fuel in sustainable energy sources such as fuel cells, and it has even been shown that urea can be used directly in a fuel cell.[1,4] As such, the electrooxidation of urea provides a means of remediating a potentially harmful environmental waste while also generating a valuable fuel.

Nickel catalysts have been used as alternatives to precious metals as catalysts for the electrooxidation of urea.[2,5,6] Partially substituting nickel compounds with other metals has been demonstrated to reduce the onset potential for urea oxidation while improving catalyst activity and longevity.[3,7,8] Inspired by the catalytic activity of $NiMoO_4$ towards other anodic reactions such as oxygen evolution, chlorine evolution, and methanol

[≠] Adapted with permission from R.P. Forslund, J.T. Mefford, W.G. Hardin, C.T. Alexander, K.P. Johnston, K.J. Stevenson. Nanostructured $LaNiO_3$ Perovskite Electrocatalyst for Enhanced Urea Oxidation. *ACS Catal.* **6** (8), 5044-5051 (2016). Copyright © 2016, American Chemical Society.

oxidation, a recent study showed it to be an active catalyst for urea oxidation.[9] Although the elementary mechanistic steps through which the electrooxidation of urea takes place are unknown, the prevalent hypothesis states that it proceeds through a 6-electron process.[10] Botte and coworkers have proposed a basic, generalized mechanism for the reaction on nickel-based catalysts. They have proposed that the reaction follows an indirect, electrochemical-chemical (EC') mechanism that was developed using in-situ Raman spectroscopy where nickel hydroxide is oxidized to the catalytically active oxidation state of Ni^{3+} in nickel oxyhydroxide.[11] Urea then reacts to form the products CO_2, N_2, and H_2O, and regenerate the nickel hydroxide catalyst while hydrogen is produced at the cathode, as shown below.

Anode:

$$6Ni^{2+}(OH)_{2(s)} + 6OH^- \rightarrow 6Ni^{3+}OOH_{(s)} + 6H_2O + e^- \quad (3.1)$$

$$6Ni^{3+}OOH_{(s)} + CO(NH_2)_{2(aq)} + 6OH^- \rightarrow 6Ni^{2+}(OH)_{2(s)} + N_{2(g)} + 5H_2O + CO_{2(g)} + 6e^- \quad (3.2)$$

Cathode:

$$6H_2O + 6e^- \rightarrow 3H_{2(g)} + 6OH^- \quad (3.3)$$

Overall:

$$CO(NH_2)_{2(aq)} + H_2O \rightarrow N_{2(g)} + 3H_{2(g)} + CO_{2(g)} \quad (3.4)$$

By inspection of these reaction steps it is evident that nickel in the 3+ oxidation state reacts with the urea molecule and becomes reduced in the process. Therefore, the synthesis of a material in which Ni^{3+} is the inherent oxidation state may lead to a more efficient electrocatalytic cycle. Perovskite oxides, with the nominal formula ABO_3, where

A is an alkaline earth or rare earth cation and B is a transition metal, are optimally suited to perform urea electrooxidation when A is La^{3+}, resulting in formation of B^{3+} due to charge neutrality. We have previously investigated perovskite oxide nanoparticles for the oxygen reduction and evolution reactions, as well as for oxygen intercalation-based pseudocapacitors in the context of the role of lattice oxygen and the covalency between the oxygen 2p and transition metal 3d bands.[12–15] Herein we present a detailed study on the use of $LaNiO_3$ as a catalyst for the electrooxidation of urea in alkaline conditions. An exceptional mass activity of ca. 371 mA mg_{ox}^{-1} and specific activity of 2.25 A mg^{-1} cm_{ox}^{-2} for the electrooxidation of urea in 1 M KOH is observed that on a per nickel atom basis is a fraction of the cost of other nickel-rich materials. It is revealed through mechanistic studies that surface restructuring and selective CO_2 poisoning of the $LaNiO_3$ likely occurs upon extended cycling. At low overpotentials that generate relevant current densities for uses such as in direct urea fuel cells, the $LaNiO_3$ catalyst appears to be stable.

3.2: EXPERIMENTAL

3.2.1: Catalyst Synthesis

$LaNiO_3$ perovskite and NiO nanoparticles were prepared using the reverse phase hydrolysis method as described in our previous work in order to increase surface area and thus catalytic activity.[12] For the $LaNiO_3$ nanoparticles lanthanum and nickel nitrates were mixed in a 1:1 ratio by concentration and added drop-wise to a concentrated solution of tetramethylammonium hydroxide (TMAOH) containing tetrapropylammonium bromide (TPAB), followed by washing with de-ionized water that resulted in a green colloidal suspension of precursor mixed-hydroxide nanoparticles. The gel was dispersed in water using probe-sonication and then collected via thin film freezing on a metal drum filled with

dry ice and isopropyl alcohol. The frozen material on the surface of the drum was scraped off into a recrystallization dish filled with liquid nitrogen using a mounted metal plate in contact with the drum. After lyophilization, particles consisting of lanthanum and nickel hydroxides were calcined at 700°C for 4 hours to form the perovskite phase. The same procedure was used to synthesize NiO except only nickel nitrate was used to form precursor nickel hydroxide particles.

3.2.2: Electrochemical Analysis

To evaluate the catalytic activity of $LaNiO_3$ and investigate the role of OH^- ions in the electrooxidation of urea, cyclic voltammetry was performed in N_2-saturated solutions of KOH ranging in concentration from 0.1 M to 5 M, containing 0.33 M urea. A urea concentration of 0.33 M was used because it is the approximate concentration of urea in human urine and also because it is by far the most common concentration used to benchmark activities in the literature.[1] Using a urea concentration of 0.33 M enables direct comparison of our results to previously reported materials. Additionally, some studies were performed where the concentration of urea was varied between 0.01 M and 0.66 M in 5 M KOH to investigate the effect of urea concentration on catalyst activities. To compare the catalytic activity of $LaNiO_3$ to an analogous material to those reported in the literature with nickel in the 2+ oxidation state, cyclic voltammetry of a NiO catalyst prepared in a similar manner to $LaNiO_3$ was performed in 1 M and 5 M KOH electrolytes containing 0.33 M urea.

In all cases unless otherwise noted, $LaNiO_3$ and NiO catalysts were supported on Vulcan carbon XC-72 (VC) in order to ensure good conductivity of the composite catalyst electrodes. 10 μL of catalyst ink containing 1 mg of 30 wt% $LaNiO_3$ on VC per 1 ml of 0.05 wt% Na^+-substituted Nafion in ethanol was dropcast onto a 5 mm diameter glassy

carbon electrode (GCE). When testing unsupported $LaNiO_3$ catalyst, 10 μL of an ink containing 1 mg of perovskite per mL of 0.05 wt% Na^+-substituted Nafion in ethanol was used.

In all cyclic voltammetry experiments, except those that used 50 cycles to test catalyst stability, the electrode was cycled twice at 100 mV s^{-1} from 0.2 to 0.6 V vs. Hg/HgO before testing at a scan rate of 10 mV s^{-1} to ensure a reproducible onset potential for the oxidation of urea. The electrode was held stationary for all cyclic voltammetry experiments except when investigating the effect of rotation rate on the urea oxidation reaction kinetics.

For all chronoamperometry and galvanostatic experiments the $LaNiO_3$ and NiO catalysts were supported at 30 wt% on Vulcan carbon and dropcast onto glassy carbon electrodes as described above. The electrodes were rotated at 1600 rpm during all chronoamperometry and galvanostatic experiments to prevent accumulation of evolved gas at the electrode surface as well as avoid mass transfer limitations that may convolute the results.

3.3: Results and Discussion

3.3.1: Material Characterization

Calcination caused sintering of precursor particles for both $LaNiO_3$ and NiO but still resulted in a nanostructured material as shown in Figure B.1 and B.2, respectively. BET analysis gave a specific surface area of 5.5 m^2 g^{-1} for $LaNiO_3$ (Figure B.3). X-ray diffraction (XRD) analysis confirmed a high phase purity of the perovskite structure as seen in Figure 3.1. Scherrer analysis of the peak at $2\theta = 47.5°$ yielded an average crystallite

domain size of 13.5 Å for $LaNiO_3$. The XRD spectrum for the NiO catalyst shown in Figure B.4 indicates a phase-pure NiO material.

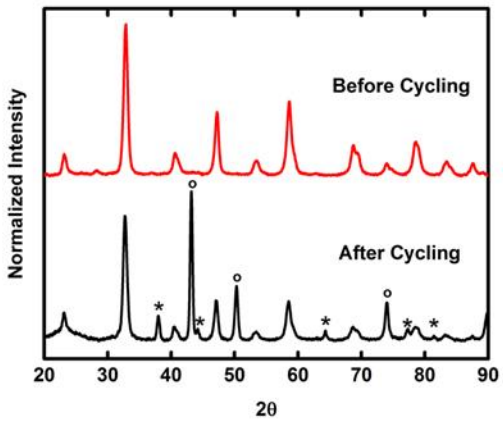

Figure 3.1: XRD spectra of $LaNiO_3$ perovskite before and after repeated cycling.

CVs were performed in 5 M KOH were performed. Peaks due to copper impurities are denoted with a (o). Catalyst phase impurities from cycling indexed to NiO are denoted with an (*). $LaNiO_3$ spectrum indexed to LaNiO3 PDF # 01-088-0633.

3.3.2: Catalyst Activity

Cyclic voltammetry of $LaNiO_3$ supported on Vulcan carbon (VC) was performed in solutions of KOH ranging from 0.1 M to 5 M with a urea concentration of 0.33 M at a sweep rate of 10 mV s^{-1} while the electrodes were held stationary. CVs of supported NiO were also performed in 1 M and 5 M KOH with 0.33 M urea. Representative CVs for the oxidation of urea in both 1 M KOH and 5 M KOH for both $LaNiO_3$ and NiO are shown in Figure 3.2. The peak mass activity for $LaNiO_3$ in 1 M KOH was found to be 371 mA mg_{ox}^{-1} and 747 mA mg_{ox}^{-1} in 5 M KOH while the peak mass activities for NiO were found to be 79 mA mg_{ox}^{-1} and 258 mA mg_{ox}^{-1} in 1 M and 5 M KOH, respectively. These results support the hypothesis that the 3+ oxidation state of nickel in $LaNiO_3$ leads to a more active catalyst

than nickel in the 2+ oxidation state in NiO. We report the activities in 1 M and 5 M KOH here in order to be able to make direct comparisons to other previously reported urea oxidation catalysts. Using a BET surface area of 5.5 m^2 g^{-1} for $LaNiO_3$, the specific activity was 2,246 mA mg^{-1} cm_{ox}^{-2} in 1 M KOH and 4,528 mA mg^{-1} cm_{ox}^{-2}, much higher than the reported 830 mA mg^{-1} cm_{ox}^{-2} in 1 M KOH for NiMoO4 as reported by Sun.[9] Comparisons to other materials reported in the literature for use in the electrooxidation of urea oxidation under similar testing conditions are shown in Figure B.5 of the supporting information. It is important to note that the specific activities reported here for $LaNiO_3$ may be underreported due to the fact that the current was normalized by BET surface area as opposed to the electrochemically active surface area. The electrochemically active surface area is often times smaller than the area measured via nitrogen sorption, thus using it to normalize activities would result in greater values.

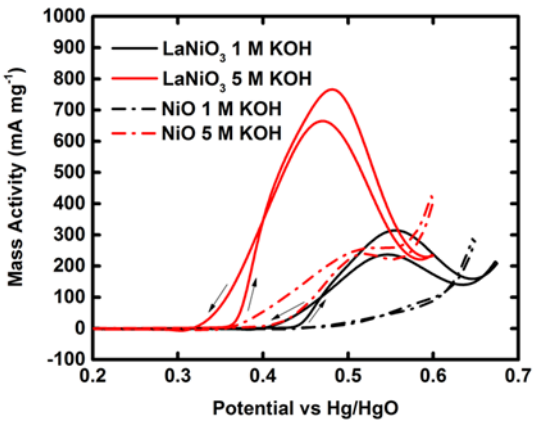

Figure 3.2: CVs of $LaNiO_3$ and NiO in 5 M and 1 M KOH containing 0.33 M urea.

CVs were performed in 5 M KOH were performed. Both catalysts were supported at 30 wt% on VC. CVs were performed at 10 mV s^{-1} and currents were normalized by the mass of catalyst on the electrode to obtain mass activities.

3.3.3: Mechanistic Insights

The effects of KOH and urea concentrations on the activity of $LaNiO_3$ for urea oxidation were examined using cyclic voltammetry. This was done instead of using other techniques such as chronoamperometry because no steady state current is achieved due to the continued deactivation of the catalyst, as discussed below. To investigate the effects of KOH concentration on catalyst activity CVs were collected in electrolyte containing 0.33 M KOH and a range of KOH concentrations varying from 0.1 M to 5 M. As shown in Figure 3.3, increasing the concentration of hydroxide ions in solution resulted in larger peak currents. Also, the onset potential, which we define as the potential at which the current is 1% of the peak current corrected for capacitive current, shifted to less anodic potentials with increasing concentrations of KOH, shown in Figure B.6. To deconvolute the influence of pH on the reference electrode potential when comparing onset potentials with varying KOH concentrations, potentials are reported vs. RHE in Figure B.6 as opposed to Hg/HgO.

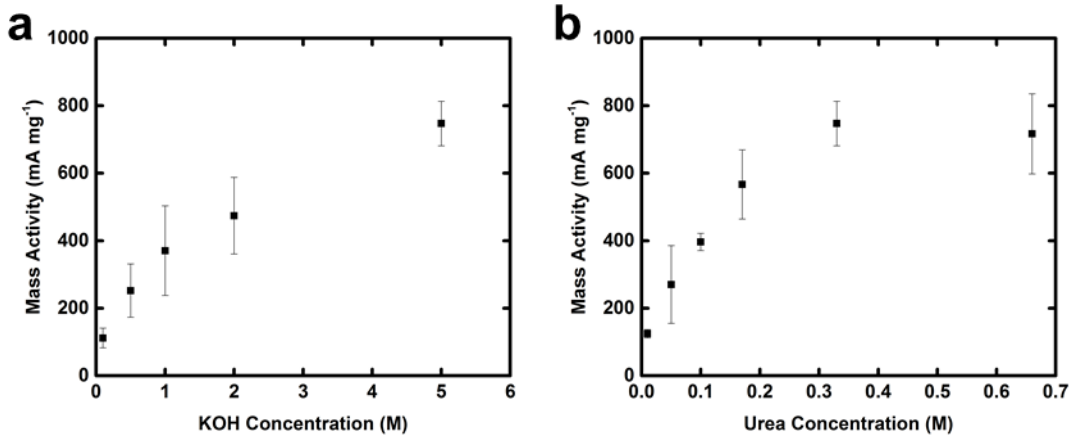

Figure 3.3: Peak mass activity dependence of $LaNiO_3$ on KOH and urea concentration. KOH concentrations were varied in the presence of 0.33 M urea. Urea concentration was varied in solutions of 5 M KOH. All currents were normalized by the mass of perovskite, in mg, drop cast on the electrode to obtain mass activities. Error bars represent standard deviations of measurements taken in triplicate.

The effect of urea concentration on catalytic activity was investigated by varying the concentration of urea between 0.01 M and 0.66 M in an electrolyte containing 5 M KOH. As can be seen in Figure 3.3, increasing concentrations of urea give rise to larger activities until concentrations above 0.17 M. At a concentration between 0.17 M and 0.33 M KOH the surface of the electrode appears to become saturated with urea and the activity does not improve with increased concentration from 0.33 M to 0.66 M. Also, the onset potential does not shift towards negative potentials with increasing urea concentration as it did with increasing concentrations of KOH (Figure B.6).

These results indicate that urea oxidation on $LaNiO_3$ may proceed via a reaction pathway similar to the mechanism described above for $Ni(OH)_2$ catalysts in which hydroxide present in solution deprotonates a surface hydroxide group to form the active Ni^{3+} species that then oxidizes urea and is chemically reduced back to the inactive Ni^{2+}

species in the process. With more hydroxide present, Ni^{3+} is regenerated more quickly, leading to higher activities and a shift in onset potential. This is supported by previous work, in which it is observed through XPS analysis that the surface of $LaNiO_3$ is significantly hydroxylated.[13]

To probe urea adsorption steps, several substituted urea analogues were investigated with the perovskite catalyst. Cyclic voltammetry studies on the supported catalyst in solutions of 5 M KOH and 0.33 M 1,3-dimethylurea or 1,1-dimethylurea are shown in Figure B.7. Surprisingly, these methyl substituted urea variants do not show significant electrooxidation activity. Especially interesting is that even when one of the amine groups is unobstructed as is the case with 1,1-dimethylurea, no activity is seen, pointing to a bridging interaction of both amine groups with the catalyst surface. Another possibility is that the catalyst interacts with the carbonyl group and the added methyl groups of the urea variants provide too much steric hindrance for the reaction to take place. However, theoretical modeling of these adsorption geometries is needed in order to confirm which of these two scenarios is preferred.

Rotation rate analysis was performed by varying the rotation rate of the electrode from 100 to 1600 rpm in two electrolytes, one containing 5 M KOH and 0.33 M urea and another containing 1 M KOH and 0.1 M urea. The experiment was performed in two different electrolytes due to the observation above that the catalyst surface is likely saturated by urea at 0.33 M, possibly affecting the dependence of peak activity on electrode rotation rate. We found, as shown in Figure B.8, that the peak current density had no dependence on rotation rate in either electrolyte. This would indicate that the oxidation process is limited by reaction kinetics and not mass transport limitations. The shape of the CVs, specifically the existence of a peak for urea oxidation on both the anodic and cathode scans, also remained unchanged between stationary testing and when electrodes were

rotated. This indicates that the peak is not a consequence of traditional mass transfer limitations from electrolyte flux but rather is more strongly influenced by reaction kinetics.

The occurrence of peaks during the urea oxidation reaction has been attributed to blockage of active sites by reaction products or intermediates on the forward scan that are then oxidized on the reverse scan, regenerating the catalyst surface.[10] While this may explain the formation of a peak on the forward scan, it does not satisfactorily describe the mechanism leading to a peak on the reverse cathodic scan. We instead propose that at potentials past those at which the urea oxidation peak occurs on the forward scan, the electrode potential is sufficiently anodic that Ni^{3+} in the perovskite cannot be significantly reduced to Ni^{2+} as described in Reaction 3.1. Instead, Ni^{3+} reacts with hydroxide and lattice oxygen anions to evolve oxygen gas as we have shown in previous work on the oxygen evolution reaction (OER).[13–15] When the potential decreases on the reverse scan, out of the OER region, the nickel active sites are again able to modulate their oxidation state and participate in urea oxidation, causing an increase in activity until the potential is further lowered to the point that Ni^{3+} is reduced to Ni^{2+}, the anodic current goes to zero, and a reduction peak is seen.

Scan rate analysis was performed by varying the scan rate from 10 to 144 mV s-1. Figure B.9 shows a linear dependence of increasing peak current density with the square root of the scan rate. This points to the existence of a diffusion limited process at the surface of the catalyst, within the diffusion layer or within the material itself, that is unaffected by rotation of the electrode. Without mechanistic information as to how the reaction proceeds, these results are difficult to explain except to say that it is possible that complex charge transfer or mass transfer within the electrode material itself may play a role. Our previous work on the OER has shown that oxygen vacancies play an important role in the reaction in oxygen deficient perovskites and $LaNiO_3$ has been shown to contain oxygen

vacancies.[12,13] These vacancies may contribute to the enhanced activity of $LaNiO_3$ for urea oxidation as well as the interesting combination of mass transfer and kinetic limitations on the reaction.

3.3.4: Catalyst Stability

Cyclic voltammograms of the first, second, and 50th cycles for the electrooxidation of urea in 5 M KOH and 0.33 M urea are shown in Figure 3.4. The onset of urea oxidation during the first cycle occurs at 0.40 V vs. Hg/HgO. The onset potential shifts to 0.37 V for the second cycle and all subsequent cycles. Peaks are observed in both the anodic and cathodic scans and the potential at which the peak current density of the anodic scan occurs decreases from 0.50 V on the first cycle to 0.47 V on the second cycle. While the shift in onset potential for urea oxidation only occurs after the first cycle, the peak current density decreases with each cycle. CVs were taken from 0.2 to 0.6 V in 5 M KOH due to the fact that past 0.6 V on the anodic scan the current begins to increase again with the onset of the oxygen evolution reaction, observed in the CVs for urea oxidation taken in lower concentrations of KOH shown in Figure B.6, as well as the fact that the Vulcan carbon support is not stable at higher potentials, an issue discussed in our group's previous work on the OER.[13,15] A pair of peaks is seen in the absence of urea corresponding to the $Ni^{2+/3+}$ oxygen intercalation based redox reactions and the potentials at which these features occur shift, just as the onset potential for the urea oxidation reaction did, after the first cycle to less positive potentials, as seen in Figure 3.4.

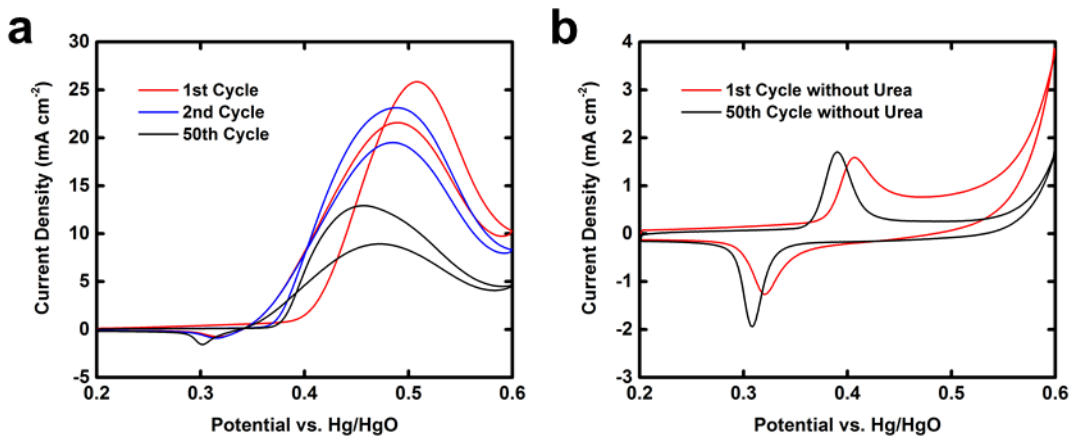

Figure 3.4: Effect of repeated cycling on urea oxidation mass activities.

(a) Selected CVs of $LaNiO_3$ obtained in 5 M KOH and 0.33 M urea at a scan rate of 100 mV s^{-1} for 50 cycles. (b) Selected CVs of $LaNiO_3$ in the absence of urea over 50 cycles showing a set of redox peaks corresponding to nickel oxidation and reduction due to oxygen (hydroxide) intercalation and surface redox reactions at a scan rate of 100 mV s^{-1}. All currents were normalized by the surface area, in cm^2, of the amount of perovskite, in mg, dropcast on the electrode to obtain mass activities.

Multiple explanations for the decrease in peak current density were investigated. In a study that used Density Functional Theory (DFT) to investigate possible reaction mechanisms for the oxidation of urea, Botte and coworkers proposed carbon dioxide dissociation from the catalyst surface as the rate-limiting step in the electrochemical oxidation of urea and that buildup of CO_2 may lead to lower reaction rates.[16] It has also been proposed that carbon monoxide may be an intermediate of the reaction and remain adsorbed to both nickel oxide and platinum catalysts during the reaction.[10,17] Another possibility is that the decrease in activity is due to restructuring or degradation of the catalyst with repeated cycling evidenced by the shift in oxygen (hydroxide) intercalation peaks and urea oxidation onset potential after the first cycle.

To investigate whether degradation of the catalyst or Vulcan carbon support was the cause, $LaNiO_3$ without the carbon support was tested to determine if a similar decrease

in current density was observed without the carbon support. The elimination of carbon also reduces the possibility of interference with analysis of catalyst material post-cycling using XRD and Raman spectroscopy.

The unsupported catalyst is only connected to the electrode through point contacts compared to supporting the perovskite on Vulcan carbon, a process that creates a conductive network for the catalyst and greater contact with the electrode surface. For this reason, peak current densities were much lower without the carbon support. Still, as shown in Figure 3.5, the activity dropped during cycling by 38%, compared to the 52% drop in activity for the supported catalyst, suggesting that while carbon support degradation may play a role, changes in the perovskite itself or the buildup of intermediates or products on the catalyst might also be responsible for the decrease in catalytic activity. To verify a change in the perovskite structure had taken place, XRD analysis was performed on $LaNiO_3$ that had been cycled 50 times in 5 M KOH, and new diffraction peaks were detected which are shown in Figure 3.1. Copper peaks appear due to the use of copper tape to remove catalyst material from the electrode after cycling. In addition to peaks from copper, new peaks were detected that index to NiO, indicating that a new crystal structure is formed at the surface of the catalyst. As XRD is a bulk technique, these results indicate significant restructuring of the perovskite catalyst takes place with repeated cycling. This is consistent with the observation that the onset potential for urea oxidation shifts to lower potentials from the first cycle to the second.

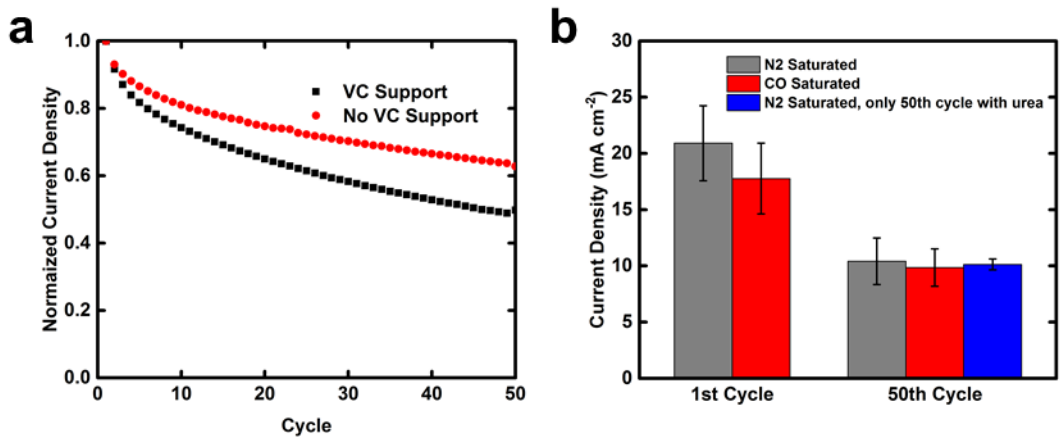

Figure 3.5: Effect of carbon support and CO on peak activities with repeated cycling.

(a) Normalized decreasing peak current densities with repeated cycling, with and without the VC support. (b) Current densities of $LaNiO_3$/VC on the first and 50th cycles in N_2 (grey) and CO (red) saturated 5 M KOH electrolyte containing 0.33 M urea, and the 50th cycle in the presence of 0.33 M urea after 49 cycles in 5 M KOH without urea (blue). Error bars represent standard deviations of measurements taken in triplicate.

To examine whether catalyst poisoning was contributing to the decrease in activity we first performed cyclic voltammetry in 5 M KOH with 0.33 M urea for 50 cycles as shown above in Figure 3.4 and by the set of black data points in Figure 3.5. This was followed by cycling of an electrode dropcast with supported catalyst in the absence of urea for 49 cycles before the 50th cycle was performed in the presence of urea. Figure 3.5 shows the results of these experiments with the grey bars showing the decrease in current density for urea oxidation from the first to the 50th cycles while the blue bar shows the current density for urea oxidation during the 50th cycle when the previous 49 cycles had been performed in the absence of urea. The peak current densities were approximately the same for the two experiments during the 50th cycle regardless of whether urea was present to be oxidized during the first 49 cycles. If reaction intermediates or products were contributing significantly to the electrode deactivation then the peak current density for the electrodes

that only performed urea oxidation on the 50th cycle would be the same as the first or second cycles for the electrode cycled 50 times in the presence of urea, which we did not observe. This indicates that poisoning due to reaction intermediates or products is not the major cause of the decrease in activity during urea oxidation in N_2-saturated electrolyte.

To examine whether CO was causing deactivation of the electrode, possibly from oxidation of the carbon support or GCE, 5 M KOH electrolyte containing 0.33 M urea was saturated with CO instead of N_2 and the electrode with unsupported $LaNiO_3$ was cycled repeatedly. After 50 cycles in the presence of CO and urea the peak current density had dropped 48% and was not statistically different than the 52% drop observed with N_2-saturated electrolyte, showing that CO poisoning is not a significant factor in the catalyst deactivation process (Figure 3.5, Figure B.10). Performing 49 cycles in a N_2-saturated electrolyte before performing the 50th cycle in CO-saturated electrolyte also did not result in a significant decrease in activity (Figure B.10).

As can be seen from the post-cycling XRD spectrum shown in Figure 3.1, no peaks due to $NiCO_3$ are detected. This is not surprising, however, because XRD is a bulk-technique and the formation of $NiCO_3$ would only take place at the surface of the catalyst. In an effort to detect a species resulting from the introduction of CO_2 as a reaction product to the electrolyte, Raman spectroscopy was performed on unsupported $LaNiO_3$ both before and after cycling, in addition to powder samples of pure urea, $LaNiO_3$, and $NiCO_3$, as well as the neat glassy carbon electrode both before and after cycling in N_2-saturated 5 M KOH. These spectra are shown in Figure B.11 and most notable is a peak at 1088 cm^{-1} present in the spectrum of pure $NiCO_3$ that is attributed to a symmetric carbonate stretching mode and is also seen in spectra for $LaNiO_3$ on GCEs after cycling in N_2-saturated electrolyte, confirming the presence of nickel carbonate at the electrode surface after cycling.

Assignments of peaks for all of the spectra are included in Figure B.12 of the supporting information.

Our hypothesis as to electrode deactivation is that CO_2 in solution at high pH forms carbonate and reacts with surface Ni^{2+} to form nickel carbonate. We believe the amount of CO_2 generated from urea oxidation only plays a minor role in catalyst deactivation and that restructuring of the catalyst surface is the major factor leading to decreased catalyst activity. This is supported by the observations that the same amount of catalyst deactivation occurs regardless of whether urea oxidation is taking place (Figure 3.5). If significant deactivation due to CO_2 production occurred during the oxidation of urea, we would expect to see a decrease in the $Ni^{2+/3+}$ reduction peak that is seen during the reverse scan. The formation of nickel carbonate is limited to the surface of the catalyst therefore it is not detected by bulk techniques such as XRD but is detectable via Raman spectroscopy.

We propose that during the first cycle of cyclic voltammetry, urea is oxidized on the perovskite catalyst and at the same time the surface of the perovskite catalyst is restructured, possibly on the reverse scan when Ni^{3+} is reduced to Ni^{2+}. This is supported by the observation that during subsequent cycles urea is oxidized at a less anodic potential on this restructured surface. The newly restructured surface is less active than the original perovskite phase, however, and the peak current density observed on the second CV is considerably lower than the first, shown in Figure 3.4. Continued cycling results in further decreases in peak current densities. We believe this is primarily due to continued restructuring of the perovskite catalyst. Additionally, we hypothesize that the generation of CO_2 during urea oxidation results in the formation of nickel carbonate on the catalyst surface.

The currents generated during cyclic voltammetry as well as reduction of nickel on the reverse scan may destabilize the $LaNiO_3$ and cause deactivation that would not be seen

at lower overpotentials and currents that are more relevant for applications of $LaNiO_3$ for urea oxidation. To investigate the feasibility of $LaNiO_3$ for use in applications such as a direct urea fuel cell (DUFC) and hydrogen generation we conducted chronoamperometry and galvanostatic experiments to examine catalyst stability under more steady-state conditions. Chronoamperometry experiments were performed in electrolyte containing 5 M KOH and 0.33 M urea in order to investigate the stability of the catalyst at a constant potential. The potentials chosen were based on the first CV for urea oxidation in 5 M KOH and 0.33 M urea on $LaNiO_3$ shown in Figure 3.4. They were 0.40 V, 0.45 V, and 0.50 V vs. Hg/HgO. The first potential, 0.40 V, is located right at the onset of urea oxidation for the first cycle, 0.45 V is approximately the half wave potential of the forward scan for urea oxidation, and 0.50 V is just before the peak activity is observed. The results are shown in Figure 3.6. A completely stable steady state current was not observed over a 20 minute test for either catalyst at 0.45 V or 0.50 V although the NiO catalyst material may be approaching a steady state current at both of these potentials while generating much less current than the perovskite catalyst. These results show that with such high currents being generated at larger overpotentials, on the order of hundreds of amps per gram of catalyst, the perovskite catalyst is unstable and undergoes deactivation as described above.

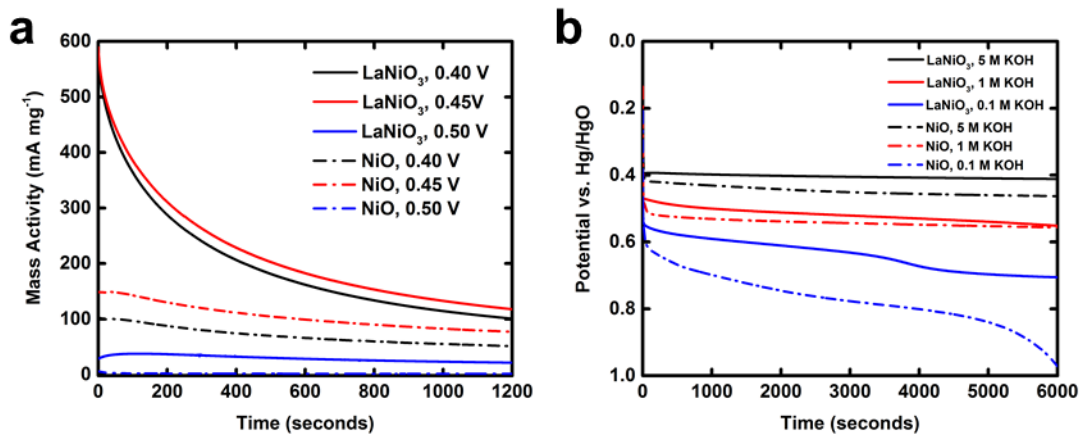

Figure 3.6: Constant potential and current stability tests.

(a) Chronoamperometry experiments performed in 5 M KOH containing 0.33 M urea on supported $LaNiO_3$ and supported NiO at 0.4 V, 0.45 V, and 0.5 V. (b) Galvanostatic experiments generating 10 A g^{-1} performed on $LaNiO_3$ in electrolytes containing 0.33 M urea and various concentrations of KOH. For both (a) and (b) the electrodes were rotated at 1600 rpm.

Galvanostatic constant current experiments were performed for both $LaNiO_3$ and NiO in 5 M, 1 M, and 0.1 M KOH containing 0.33 M urea at a constant current of 30 μA, or 10 A g^{-1} of catalyst. This current was chosen based our group's previous work on the OER and ORR and existing literature that tests stability of catalysts for hydrogen generation through water electrolysis, and is much less than the currents generated for the activities reported above.[15,18] As can be seen in Figure 3.6, $LaNiO_3$ in 5 M KOH appears to be stable throughout the entire test with a terminal voltage of +0.409 V vs. Hg/HgO after 6000 seconds, 54 mV less anodic than for the NiO catalyst. In 1M KOH $LaNiO_3$ required a potential of 0.555 V to produce 10 A g^{-1} after 6000 seconds while the NiO, required 0.556 to produce 10 A g^{-1}. In 0.1 M KOH the $LaNiO_3$ catalyst appears to undergo an initial deactivation or restructuring before stabilizing at 0.714 V while the NiO catalyst is unstable, approaching 1 V at 6000 seconds and increasing rapidly. These results indicate that lower overpotentials are required to produce 10 A g^{-1} for urea oxidation on $LaNiO_3$

versus NiO and that $LaNiO_3$ appears to be a stable catalyst at current densities that are relevant for use in applications such as hydrogen generation and direct urea fuel cells.

3.4: CONCLUSIONS

$LaNiO_3$ nanoparticles were synthesized via reverse phase hydrolysis to form mixed metal hydroxide precursor particles followed by thin-film freezing, lyophilization, and calcination. A phase-pure perovskite was obtained that shows a higher catalytic activity towards urea oxidation than previously reported materials and at a fraction of the cost of other nickel-rich catalysts. While previously reported materials for the electrooxidation of urea, such as various morphologies of NiO, contain Ni^{2+} it appears from the proposed reaction mechanism that a catalyst containing Ni^{3+} would be much more active. Lowered activity of the catalyst was observed during repeated cycling at high pH due to restructuring of the perovskite surface, as well as possible catalyst poisoning due to reaction products. This phenomena applies not only to the electrooxidation of urea on $LaNiO_3$ but also to all oxidative reactions on nickel-containing perovskites. Despite these issues, galvanostatic experiments generating currents of a relevant magnitude for use in applications such as hydrogen generation and fuel cells showed $LaNiO_3$ perovskite to be stable and generate the same currents as similarly-prepared NiO at a lower overpotential. $LaNiO_3$ remains a promising catalyst for the electrooxidation of urea and by supporting perovskite nanoparticles on Vulcan carbon they may be used as a low-cost catalyst for the generation of hydrogen as a fuel and the remediation of an abundant waste.

3.5: REFERENCES

1. Rollinson, A. N., Jones, J., Dupont, V. & Twigg, M. V. Urea as a hydrogen carrier: a perspective on its potential for safe, sustainable and long-term energy supply. *Energy Environ. Sci.* **4**, 1216–1224 (2011).

2. Boggs, B. K., King, R. L. & Botte, G. G. Urea electrolysis: direct hydrogen production from urine. *Chem. Commun.* 4859–4861 (2009). doi:10.1039/B905974A

3. King, R. L. & Botte, G. G. Investigation of multi-metal catalysts for stable hydrogen production via urea electrolysis. *J. Power Sources* **196**, 9579–9584 (2011).

4. Lan, R., Tao, S. & Irvine, J. T. S. A direct urea fuel cell – power from fertiliser and waste. *Energy Environ. Sci.* **3**, 438–441 (2010).

5. Wang, D., Yan, W., Vijapur, S. H. & Botte, G. G. Enhanced electrocatalytic oxidation of urea based on nickel hydroxide nanoribbons. *J. Power Sources* **217**, 498–502 (2012).

6. Wang, D., Yan, W. & Botte, G. G. Exfoliated nickel hydroxide nanosheets for urea electrolysis. *Electrochemistry Communications* **13**, 1135–1138 (2011).

7. Yan, W., Wang, D. & Botte, G. G. Nickel and cobalt bimetallic hydroxide catalysts for urea electro-oxidation. *Electrochim. Acta* **61**, 25–30 (2012).

8. Yan, W., Wang, D., Diaz, L. A. & Botte, G. G. Nickel nanowires as effective catalysts for urea electro-oxidation. *Electrochim. Acta* **134**, 266–271 (2014).

9. Liang, Y., Liu, Q., Asiri, A. M. & Sun, X. Enhanced electrooxidation of urea using $NiMoO_4 \cdot xH2O$ nanosheet arrays on Ni foam as anode. *Electrochim. Acta* **153**, 456–460 (2015).

10. Vedharathinam, V. & Botte, G. G. Understanding the electro-catalytic oxidation mechanism of urea on nickel electrodes in alkaline medium. *Electrochim. Acta* **81**, 292–300 (2012).

11. Vedharathinam, V. & Botte, G. G. Direct evidence of the mechanism for the electro-oxidation of urea on $Ni(OH)_2$ catalyst in alkaline medium. *Electrochim. Acta* **108**, 660–665 (2013).

12. Hardin, W. G. *et al.* Highly Active, Nonprecious Metal Perovskite Electrocatalysts for Bifunctional Metal–Air Battery Electrodes. *J. Phys. Chem. Lett.* **4**, 1254–1259 (2013).

13. Hardin, W. G. *et al.* Tuning the Electrocatalytic Activity of Perovskites through Active Site Variation and Support Interactions. *Chem. Mater.* **26**, 3368–3376 (2014).

14. Mefford, J. T., Hardin, W. G., Dai, S., Johnston, K. P. & Stevenson, K. J. Anion charge storage through oxygen intercalation in $LaMnO_3$ perovskite pseudocapacitor electrodes. *Nat. Mater.* **13**, 726–732 (2014).

15. Mefford, J. T. *et al.* Water electrolysis on $La_{1-x}Sr_xCoO_{3-\delta}$ perovskite electrocatalysts. *Nat. Commun.* **7**, 11053 (2016).

16. Daramola, D. A., Singh, D. & Botte, G. G. Dissociation Rates of Urea in the Presence of NiOOH Catalyst: A DFT Analysis. *J. Phys. Chem. A* **114**, 11513–11521 (2010).

17. Bezerra, Â. C. S., de Sá, E. L. & Nart, F. C. In Situ Vibrational Study of the Initial Steps during Urea Electrochemical Oxidation. *J. Phys. Chem. B* **101**, 6443–6449 (1997).

18. Gorlin, Y. & Jaramillo, T. F. A Bifunctional Nonprecious Metal Catalyst for Oxygen Reduction and Water Oxidation. *J. Am. Chem. Soc.* **132**, 13612–13614 (2010).

Chapter 4: Tuning Ruddlesden-Popper Oxide Catalysts for the Electrochemical Oxidations of Urea and Small Alcohols

4.1: INTRODUCTION

As discussed in previous chapters, in order to continue the pragmatic development of clean energy sources new avenues to increase the efficiencies of electrochemical energy storage devices are needed. Given that the efficiencies of these devices are limited in large part by the sluggish kinetics of the oxygen evolution reaction (OER, $4OH^- \rightarrow O_2 + 2H_2O + 4e^-$), increased efforts have been made to reduce the overpotential for the OER in alkaline conditions with innovative catalysts.[1] Recently, many have turned to the electrooxidations of small molecules as an alternative to the OER as the anodic reaction in the production of hydrogen[2] or to produce electricity directly from direct methanol, ethanol, and urea fuel cells due to the lower overpotential required to drive these reactions.[3–5] For example, while the theoretical cell potential for hydrogen generation via the OER is 1.23 V, when urea is oxidized at the anode at a theoretical potential of -0.46 V vs. SHE at pH 14 while hydrogen is evolved at the cathode at a theoretical potential of -0.83 V this window shrinks to 0.37 V, allowing for much cheaper hydrogen production and energy storage.[6] Furthermore, urea is relatively non-toxic, non-flammable, and can be transported as a solid that readily dissolves in water, qualities that make it an attractive option as a means for storing chemical energy.[2,7] By utilizing urea and other nitrogenous products present in the waste streams of such processes as ammonia and fertilizer production we can generate a chemical fuel while simultaneously remediating possible sources of environmental pollution.[2]

While the electrooxidations of methanol and ethanol have been well-studied, recent advances have been made towards catalyzing the urea oxidation reaction (UOR) using nickel-based catalysts as alternatives to precious metals and partially substituting nickel

compounds with other metals has been demonstrated to reduce the onset potential for urea oxidation and improve catalyst activity and longevity.[6,8,9] Not long ago $NiMoO_4$ was demonstrated to be an active catalyst for the UOR and served as a model for how oxygen vacancies within the catalyst lattice can lead to an improvement in catalytic activity toward urea oxidation.[10,11] Elsewhere, efforts have been made to take advantage of more sophisticated supports and possible catalyst-support interactions to boost electrocatalytic activity, such as combining Ni-based nanoparticles with carbon nanotube[12,13] or tungsten carbide supports.[14,15] Still, others have sought to increase activities by employing extensively nanostructured materials to increase the surface area available for reaction.[16,17] While many approaches have been taken to improve catalyst performance, no fundamental descriptor has been developed to aid in the systematic design of materials to increase activities towards the UOR.

Botte and others have used DFT modeling to propose various steps through which the UOR may take place,[18] however, the elementary mechanistic steps have not yet been experimentally elucidated. Botte and coworkers have proposed a simple, generalized mechanism for the reaction on nickel-based catalysts in which the reaction follows an indirect, electrochemical-chemical (EC') mechanism that was developed using in-situ Raman spectroscopy.[19,20] In this 6-electron pathway nickel hydroxide is oxidized to the catalytically active oxidation state of Ni^{3+} in nickel oxyhydroxide. Urea then reacts to form the products CO_2, N_2, and H_2O while regenerating the nickel hydroxide catalyst in a chemical step at the anode, and hydrogen is produced at the cathode, as shown below.

Anode:

$$6Ni^{2+}(OH)_{2(s)} + 6OH^- \rightarrow 6Ni^{3+}OOH_{(s)} + 6H_2O + 6e^- \quad (4.1)$$

$$6Ni^{3+}OOH_{(s)} + CO(NH_2)_{2(aq)} + 6OH^- \rightarrow 6Ni^{2+}(OH)_{2(s)} + N_{2(g)} + 5H_2O + CO_{2(g)} \quad (4.2)$$

Cathode:

$$6H_2O + 6e^- \rightarrow 3H_{2(g)} + 6OH^- \quad (4.3)$$

Overall:

$$CO(NH_2)_{2(aq)} + H_2O \rightarrow N_{2(g)} + 3H_{2(g)} + CO_{2(g)} \quad (4.4)$$

By inspection of the above reaction it is evident that Ni in the +3 oxidation state is responsible for urea oxidation, reacting with urea and getting reduced in the process. Therefore, utilizing a material with an inherent oxidation state of Ni^{3+} should lead to a more efficient electrocatalytic cycle. Furthermore, the electrooxidations of other small molecules including methanol and ethanol have been shown to proceed through the same type of mechanism and should benefit from the same oxidation state augmentation.[3,4]

Perovskite oxides have the nominal formula ABO_3 in which the A-site is most often an alkaline earth or rare earth metal and the B-site is a transition metal. Discussed in Chapter 3, after examining the above EC' mechanism we demonstrated how the use of the perovskite $LaNiO_3$ in which La^{3+} forces Ni into the +3 oxidation state via charge compensation led to the highest activities for the UOR at that time.[21] Additionally, previous work by our group also utilized perovskite materials as highly active catalysts for the OER[22–24] and for Co-based perovskites[25] and Ni-based Ruddlesden-Popper[26] phases we demonstrated how increased M – O bond covalency upon substitution of La^{3+} for Sr^{2+} led to an increase in OER activity. Based on these studies we predicted that increasing the transition metal oxidation state past Ni^{3+} may lead to elevated activities for the UOR. However, upon any significant amount of Sr^{2+} substitution, the $LaNiO_3$ perovskite structure becomes unstable leading to phase segregation and decreased catalytic activity.[27]

To avoid phase segregation and incorporate Sr^{2+} into a phase-pure catalyst material we turn to the Ruddlesden-Popper (RP) crystal structure. A derivative of the perovskite structure, the RP structure has the nominal formula $A_{n+1}B_nO_{3n+1}$ or equivalently $(AO)(ABO_3)_n$ where n layers of perovskite are separated by single (AO)(OA) rocksalt slabs and as $n \rightarrow \infty$ the RP structure becomes the perovskite structure. The RP structure is able to accommodate the various elemental compositions of the perovskite structure as well as many the perovskite structure cannot.[28] Herein we report the synthesis of a series of $La_{2-x}Sr_xNiO_{4+\delta}$ catalysts with the n = 1 Ruddlesden-Popper crystal structure that we use to demonstrate a new governing descriptor of how systematically increasing Ni oxidation state leads to greater activities toward the UOR. Furthermore, we are able to apply this descriptor to the oxidations of methanol and ethanol, two other reactions of interest for energy storage. While efforts to modulate the properties of metal oxide catalysts, including perovskites, to improve catalytic activity have been investigated before for the electrooxidations of methanol and ethanol,[29,30] this is the first time the RP structure has been used to systematically elevate the oxidation state of Ni above +3 to improve catalyst activity for these reactions. Furthermore, the most active catalyst of the series for all three reactions, $La_{0.5}Sr_{1.5}NiO_{4+\delta}$, is the most active catalyst ever reported, to our knowledge, for the UOR and is very active for methanol and ethanol electrooxidations as well.[3]

4.2: EXPERIMENTAL

4.2.1: Catalyst Synthesis

$La_{2-x}Sr_xNiO_{4+\delta}$ (LSN, x = 1 – 1.5) precursor particles were synthesized using a modified Pechini method as discussed in previous chapters. A and B-site nitrate salts were mixed in stoichiometric ratios and dissolved in water to make a solution with a total metal

salt concentration of 0.1 M. Citric acid and EDTA were added to the solution each at a ratio of 1:1 with the total metal nitrate salts. TMAOH was added to the solution until the pH reached 7.5 to ensure the EDTA was adequately deprotonated to dissolve and act as a chelating agent. DEG was then added to the solution at a concentration of 0.067 M and the solution was heated to 85° C while stirring. Upon heating, a dehydration reaction between the polyhydroxyl alcohol and the carboxylic acid groups of the chelates formed a polyester gel. After all the water had been evaporated the gel was fired at 350° C to form mixed metal oxide precursor particles. This step was performed on a hot plate and not in a sealed furnace to avoid possible explosions from rapid evolution of gasses upon combustion. Finally, precursor particles were crystallized at 950° C for 5 hours under pure O_2 flowing at 150 mL min^{-1}, in a tube furnace. Catalysts were recovered and immediately stored under Ar gas to prevent catalyst surface amorphization in the form of $SrCO_3$.

4.2.2: Electrochemical Analysis

The catalyst and Vulcan carbon were each ball-milled for three minutes before being mixed together in a ball mill for three minutes in a 30:70 perovskite:carbon weight ratio. Catalyst inks were prepared by adding 2 mL of a NaOH neutralized 0.05 wt% Nafion solution in ethanol to 2 mg of catalyst powder (1 mg mL^{-1}) and bath sonicated for at least one hour. A volume of ink (10 μL) was drop cast onto a clean 5 mm (0.196 cm^2, Pine Instruments) glassy carbon electrode and dried under ambient conditions overnight. The glassy carbon electrodes were cleaned prior to drop casting by sonication in a 1:1 by volume DI water:ethanol solution. The electrode was then polished using 0.05 μm alumina powder, rinsed with DI water, sonicated in a fresh DI water:ethanol solution, and rinsed with DI water again before being dried in ambient air. All electrochemical tests were performed on electrodes prepared by this method, obtaining a composite catalyst loading

of 51 μg_{total} cm^{-2}_{geo}, yielding 15.3 μg_{ox} cm^{-2}_{geo} for catalysis and intercalation tests (30 wt% on carbon).

Electrochemical testing was performed on a Metrohm Autolab PGSTAT302N potentiostat equipped with high speed rotators from Pine Instruments at room temperature in 1 M KOH (measured pH ≈ 13.7). Positive feedback methods were used to determine electrolyte resistance (6 Ω) and all data was iR compensated after testing unless stated otherwise. Each test was performed in a standard 3-electrode cell using a CH Instruments Hg/HgO (1 M KOH) reference electrode, a fritted Au wire counter electrode, and a film of catalyst ink on glassy carbon as the working electrode. All potentials are reported versus the Hg/HgO (1 M KOH) reference electrode.

4.2.3: Quantification of Urea and Alcohol Electrooxidation Activities

All activity testing was performed on fresh electrodes prepared via drop-casting inks with 30 wt% catalyst on VC (15.3 μg_{ox} cm^{-2}_{geo}). Cyclic voltammetry scans were performed at 10 mV s^{-1} in Ar-saturated 1 M KOH. The current at 0.6 V vs Hg/HgO - iR was selected from the anodic scan for comparison between materials and electrolytes. Data reported herein is the average taken from at least three tests on fresh electrodes.

4.2.4: Powder X-ray Diffraction (PXRD)

The crystal structures of the LSN materials were probed by powder X-ray diffraction using a Rigaku MiniFlex600 Diffractometer at 298 K in ambient conditions, utilizing Cu Kα radiation (1.54 Å wavelength) operating at 40 kV and 15 mA. For all tests, Ar-sealed catalyst powder was exposed to ambient air and scanned over 20 - 80° 2θ. The PXRD patterns used for Rietveld refinement were taken with a Huber G670 Guinier

diffractometer (Cu $K_{\alpha 1}$ radiation; curved Ge(111) monochromator; image plate) and the refinement was performed with the JANA2006 package.[31]

4.2.5: Surface Area Analysis

Nitrogen sorption analysis for the LSN series was performed on a Quantachrome Instruments NOVA 2000 high-speed surface area BET analyzer at a temperature of 77 K. Prior to measurements, all samples were ball milled followed by degassing in vacuum for a minimum of 12 hours at 120° F. The specific surface area was calculated using the BET method from the nitrogen adsorption data in the relative pressure range (P/P_0) of 0.05 to 0.30, with a minimum R^2 of 0.995 and minimum C value of 20.

4.2.6: Transmission Electron Microscopy (TEM)

The TEM samples were prepared by crushing the crystals in a mortar in ethanol and depositing drops of suspension onto a porous carbon grid. Electron diffraction patterns, high angle annular dark field scanning TEM (HAADF-STEM) images and energy dispersive X-ray (EDX) spectra were obtained with an aberration-corrected Titan G^3 electron microscope equipped with a Super-X EDX system, operated at 200 kV using a convergence semi-angle of 21.6 mrad.

4.2.7: Iodometric Titrations

Iodometric titrations were performed according to the referenced procedure[32–34] in which 3 mL of deoxygenated 2 M KI solution was first added to a flask containing 15 – 20 mg of perovskite under an argon atmosphere and allowed to disperse for three minutes. After a few minutes 6 ml of 1 M HCl was added and the perovskite was allowed to dissolve. This solution was then titrated to a faint golden color with a solution of ~25 mM solution

of $Na_2S_2O_3$ that had been pre-standardized with standard 0.1 N KIO_3. Starch indicator was then added and the solution was titrated until clear, marking the end point.

4.2.8: X-ray Photoelectron Spectroscopy (XPS)

Chemical states were characterized by a Kratos AXIS Ultra DLD XPS in 0.1 eV steps using a dwell time of 1500 ms per step with four sweeps and a monochromatic Al X-ray source (Al α, 1.4866 eV). A charge neutralizer was used for all samples. Binding energies for all spectra were calibrated relative to the adventitious carbon peak set to 284.8 eV. CasaXPS was used for all data analysis and deconvolution.

4.3: RESULTS AND DISCUSSION

4.3.1: Materials Characterization

Calcination of mixed metal oxide precursor particles resulted in nanostructured, phase-pure Ruddlesden-Popper materials for all compositions as can be seen in Figure 4.1. For simplicity the names of the materials are abbreviated to LSN*X* where the letters refer to the various elements in the material and *X* refers to the percentage of La in the A-site. Electron diffraction, Rietveld refinement (Figure C.1), and powder X-ray diffraction (PXRD, Figure 4.1) patterns confirm a body-centered tetragonal unit cell and the *I*4/*mmm* space group that is consistent with the crystal structure of a $n = 1$ member of Ruddlesden-Popper (RP) homologous series. Precursor particles measuring between 50 nm and 200 nm sintered at high temperatures to form larger particles, and BET measurements indicate a close range of surface areas from 2.5 $m^2\ g^{-1}$ for $La_{0.5}Sr_{1.5}NiO_{4+\delta}$ (LSN25) up to 2.8 $m^2\ g^{-1}$ for $La_{0.75}Sr_{1.25}NiO_{4+\delta}$ (LSN37) and $LaSrNiO_{4+\delta}$ (LSN50, Figure C.2), thus all three samples have similar particle morphology and surface area, an important characteristic if the

electrochemical properties for varying compositions are to be studied and compared on a consistent basis. Iodometric titrations were used to measure the Ni oxidation state for all three samples. As can be seen in Table C.1, the bulk nickel oxidation state increases with the amount of Sr substitution, as does the oxygen hyperstoichiometry, which is consistent with previous results for $La_{2-x}Sr_xNiO_{4+\delta}$.[31,35,36] XPS measurements of all three samples indicate a surface oxidation state of ~$Ni^{2.1+}$, consistent with a high degree of surface hydroxylation (Figure C.3).[23]

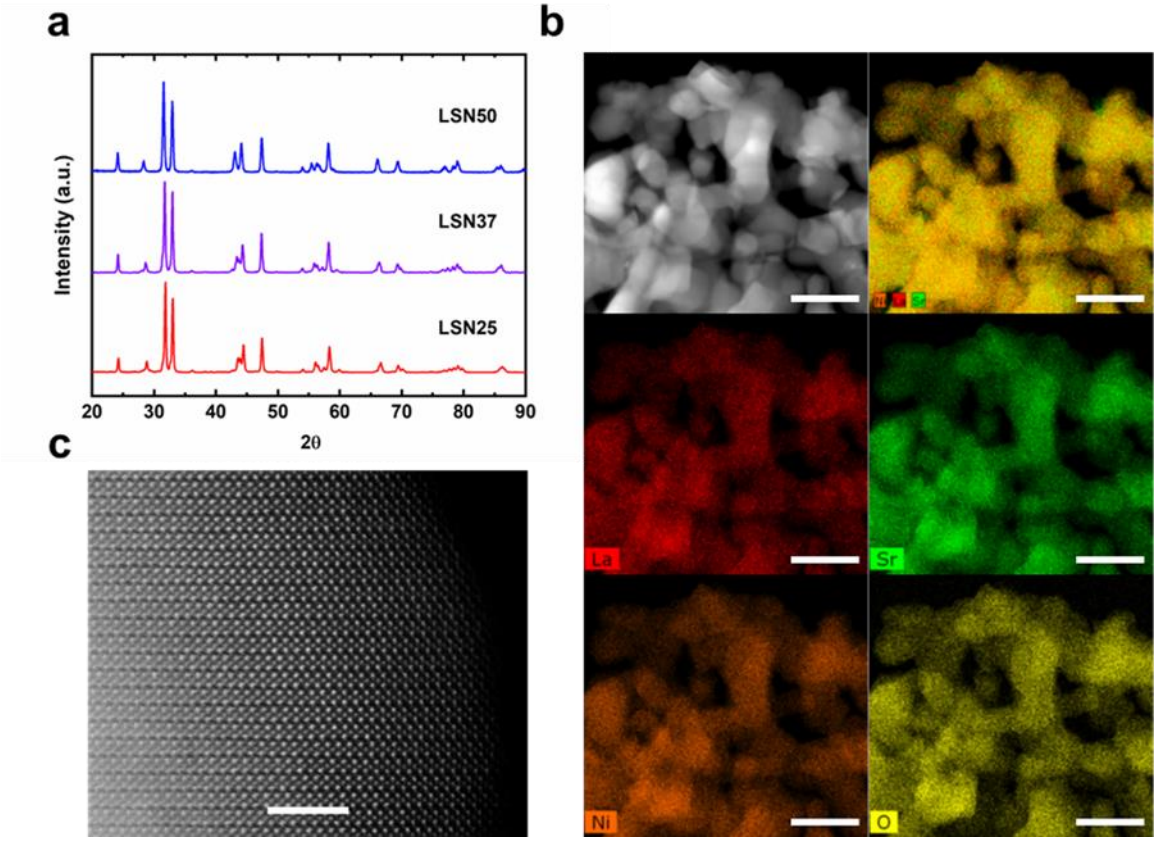

Figure 4.1: Physical characterization of the LSN series.

(a) PXRD patterns for LSN25, LSN37, and LSN50 indicating a phase-pure n = 1 Ruddlesden-Popper structure for all three samples. (b) High angle annular dark field scanning transmission electron microscopy (HAADF-STEM) image and compositional EDX mapping of LSN25 showing sintered particles and homogenous distribution of the constituent elements. Scale bars are 200 nm (c) [100] HAADF-STEM image showing perfect stacking of perovskite (BO_2) and rock salt (AO)(OA) layers that propagate to the particle surface. Scale bar is 3 nm.

4.3.2: Catalyst Activity

To evaluate the catalytic activity of the LSN series, cyclic voltammetry (CV) experiments were performed in N_2-saturated 1 M KOH containing 0.33 M or 1 M urea, methanol, or ethanol. Glassy carbon electrodes (GCEs) were held stationary and CVs were measured at a scan rate of 10 mV s^{-1}. The majority of experiments were performed with 1 M concentrations of urea, methanol, or ethanol, however other concentrations of urea including 0.33 M were also used when quantifying urea oxidation activities to allow for comparison to other materials reported in the literature. The catalysts were supported at 30 wt% on Vulcan carbon XC-72 (VC) because while it has been previously reported that the conductivity switches from semiconducting to metal-like conductivity when x > 1 for the $La_{2-x}Sr_xNiO_{4+\delta}$ series,[37] in the absence of a support the drop cast particles only contact each other and the GCE surface through point contacts. By supporting the LSN series on VC we minimize electrical contact resistances between adjacent catalyst particles and ensure good conductivity between the GCE electrode and the catalyst. Furthermore, VC is used because it lacks surface functionalities that may interact with and significantly alter the electronic structure of the catalyst, which allows us to be confident that the differences in electrochemical performance across the materials examined are due to the elemental compositions of the catalysts themselves.

Representative CVs for the UOR on all three catalysts in the LSN series are shown in Figure 4.2. As the Sr content and subsequent oxidation state of the Ni active site within the catalyst increases the current generated from urea oxidation increases as well. The most active catalyst was LSN25, containing 25% La in the A-site, which generated 1,252 mA mg_{ox}^{-1} in 1 M urea at a potential of 0.6 V vs. Hg/HgO and 16.695 A $mg^{-1}cm_{ox}^{-2}$ when normalized by BET surface area while it also generated 588 mA mg_{ox}^{-1} and 7.846 A $mg^{-1}cm_{ox}^{-2}$ in 0.33 M urea making it one of the most active catalysts for the UOR ever reported.

Figures 4.2 and C.4 show a comparison to the $LaNiO_3$ perovskite material discussed in Chapter 3 as well as NiO, both supported at 30 wt% on VC and tested in the same experimental setup as the LSN series. Representative CVs for LSN25 at additional urea concentrations can be found in Figure C.5 and PXRD patterns confirming the phase purity of the $LaNiO_3$ and NiO materials can be found in Figure C.6.

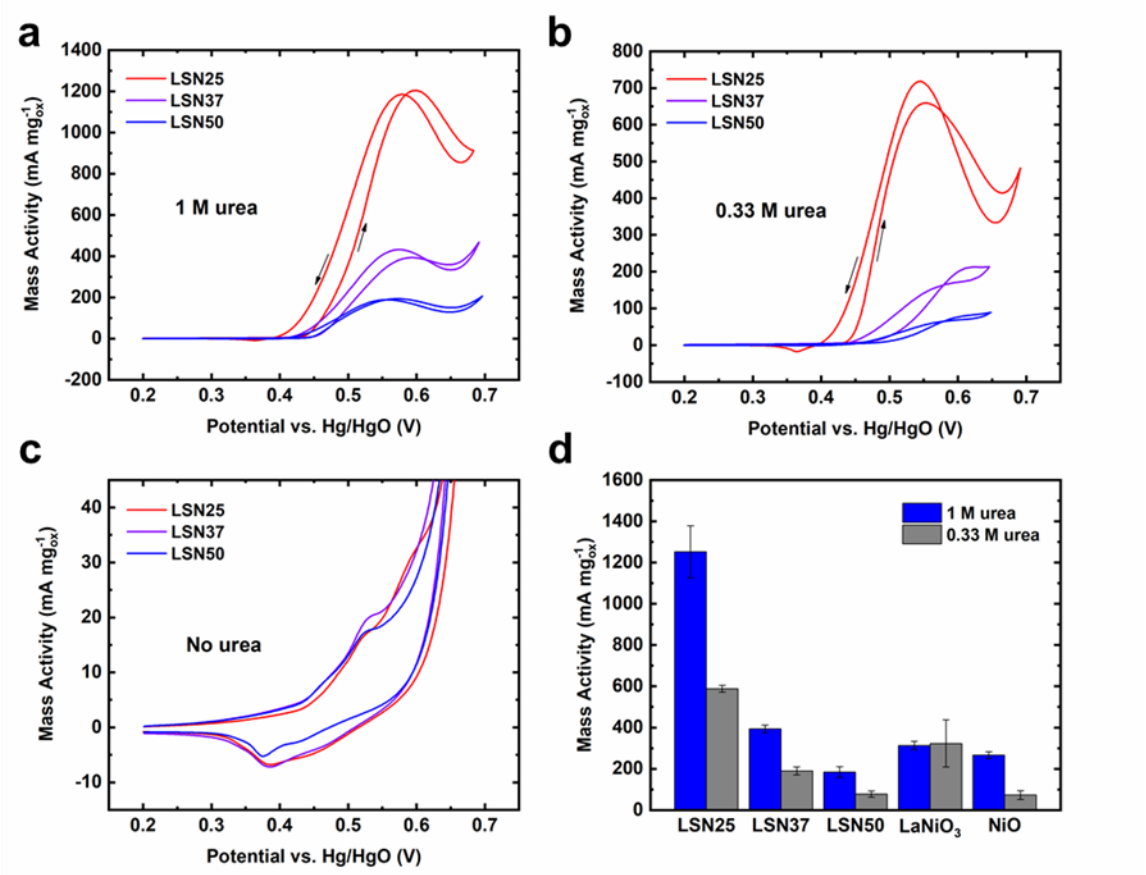

Figure 4.2: Electrooxidation activities of the LSN series toward urea oxidation.

CVs performed in N_2-saturated 1 M KOH with (a) 1 M urea or (b) 0.33 M urea at a scan rate of 10 mV s^{-1}. (c) CVs performed in N_2-saturated 1 M KOH at a scan rate of 10 mV s^{-1} in the absence of a small molecule to oxidize. (d) Mass activities for the LSN series as well as $LaNiO_3$ perovskite and NiO both supported at 30 wt% on VC in 1 M KOH containing either 0.33 or 1 M urea. Activities reported were measured at 0.6 V on the anodic scan. All measurements were performed on fresh electrodes and in triplicate.

CVs of all three catalysts were performed under the same conditions but in the absence of urea and it can be seen in Figure 4.2 that the redox peaks that occur in the incipient OER region on the anodic scan due to the oxidation of Ni^{2+} to Ni^{3+} appear at the same potential of 0.44 V as the onset of the UOR, evidence that the reaction follows a similar process to the widely accepted EC' mechanism discussed above. Furthermore, the amount of charge passed during these surface redox processes is approximately the same across the three LSN catalyst materials, demonstrating that the increase in activity towards the UOR is due to a change in the electronic structure of the catalyst and not a morphological one such as an increase in surface area. This agrees with the measured BET surface areas discussed above. It is interesting to note that while the oxidation state of Ni in the bulk of the material increases with increasing Sr content, evidenced by the iodometric titrations described above, the surface of the catalyst maintains an oxidation state of approximately +2.1 across the LSN series as shown by the XPS spectra in Figure C.3. This lack of shifting in binding energies agrees with the observation that the $Ni^{2+/3+}$ redox peaks and onset potentials for the UOR described above do not shift with the changing Sr content.

To confirm that the measured current was due to urea oxidation and not the OER rotating ring disk electrode (RRDE) experiments were performed under the same conditions as described above except with half the geometric catalyst loading (25.1 μg_{total} $cm^{-2}{}_{geo}$) and with the electrode rotating at 1600 rpm in order to reduce bubble formation at the disk that can result in poor sensitivity of the ring electrode toward oxygen production. During these experiments the potential at the disk electrode, containing the

catalyst, is swept while the Pt ring potential is held at -0.4 V vs. Hg/HgO, a potential negative-enough to reduce any oxygen that may contact it after it is evolved at the disk. As can be seen in Figure C.7 the ring current only begins to increase as a result of the onset of the OER past 0.67 V, confirming that the current we measure at 0.6 V vs Hg/HgO is due entirely to urea oxidation. This agrees with the CVs in Figure 4.2 that show an increase in current at 0.67 V as the OER begins.

Efforts have been made elsewhere to improve the activity of nickel-based catalysts for the UOR by incorporation of other transition metals. In previous work, described in Chapter 2, we utilized an Fe-substituted series of LSN25 catalysts for the OER in which the A-site composition was held constant while Fe was substituted into the B-site. It was discovered that Fe substitution did in fact result in both shifting surface oxidation states and subsequently the observed $Ni^{2+/3+}$ redox peaks,[26] thus it appears the mechanism by which the electronic structure of the catalyst is affected by elemental substitution differs based on whether the A or B-site is modified. To illustrate this, we synthesized a sample that contained 75% Sr in the A-site, the same as LSN25, but with 30% Fe (LSNF25) substituted into the B-site. Fe substitution was shown above to lead to an anodic shift in the $Ni^{2+/3+}$ redox peaks but it also leads to an increase in the current generated from this redox process.[26] Figure C.8 shows both $Ni^{2+/3+}$ redox peaks in 1 M KOH and activity CVs for both samples in 1 M KOH and either 1 M or 0.33 M urea. Fe substitution does in fact shift both the $Ni^{2+/3+}$ redox peaks and the onset of urea oxidation anodically, and these shifts in redox peaks and UOR onset agree with XPS results in Figure C.3 in which the Ni peaks shift to higher binding energies upon 30% substitution

for Fe. Our previous studies showed that 30% Fe substitution was an optimal amount to increase OER activity[26] and while it did increase the peak current density for the $Ni^{2+/3+}$ redox reactions in the absence of urea it substantially decreased peak activities toward the UOR generating just 650 mA mg_{ox}^{-1} in 1 M urea and 131 mA mg_{ox}^{-1} in 0.33 M urea.

In addition to the UOR, methanol and ethanol oxidation reactions were performed using the LSN series. Similar to the trend in activities observed for the UOR, the currents at 0.6 V for the oxidations of both alcohols at a concentration of 1 M in 1 M KOH increased with increasing Sr content (Figure 4.3) with activities for LSN25 in 1 M MeOH being 1,554 mA mg_{ox}^{-1} and 1,547 mA mg_{ox}^{-1} for the electrochemical oxidation of ethanol. Furthermore, the onset potential for both reactions of 0.44 V was the same as the onset potential for the UOR as well as the $Ni^{2+/3+}$ redox reactions in the absence of a small molecule, indicating that the methanol and ethanol oxidation reactions utilize a similar EC' mechanism as the UOR, in agreement with the literature.[35]

Based on the observations above that the Ni redox peaks and onset potentials for the oxidations of all three small molecules remain constant regardless of Sr content, it is probably the case that in such highly covalent materials where the 3*d* bands of the highly oxidized Ni overlap with the O 2*p* band the Fermi level becomes pinned at the top of the O 2*p* band[25,36] resulting in ligand holes that then become filled by oxidizing the small molecule of interest. As more Sr^{2+} is substituted in, the hybridization of the Ni 3*d* and O 2*p* bands increases, rendering the Ni-O bond more covalent and increasing the number of ligand holes and the rate at which the chemical step of the EC' mechanism takes place. Upon the addition of a less electronegative transition metal such as Fe the Ni and Fe 3*d*

bands hybridize and increase the density of states at the Fermi level.[26] While this has been shown to help improve catalyst activity for reactions such as the OER,[37,38] the ability to transfer charge more readily across Ni - O - Fe bridges reduces the formation of these reactive ligand holes and the electrocatalytic activity of the material towards the UOR as well as the oxidations of methanol and ethanol. A summary of the activities for all the materials tested for all three reactions can be found in Table C.2.

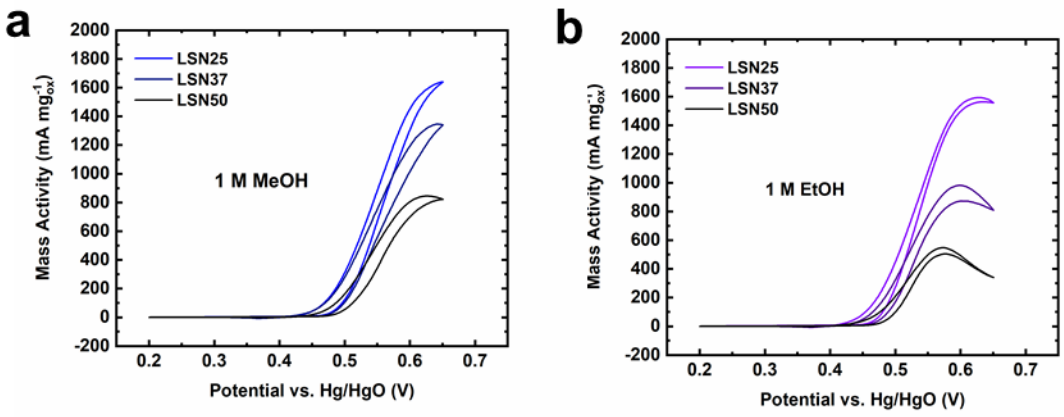

Figure 4.3: Catalytic activities of the LSN series toward methanol and ethanol oxidation. Representative CVs performed in (a) 1 M methanol and (b) 1 M ethanol at a scan rate of 10 mV s^{-1}. All measurements were performed in Ar-saturated 1 M KOH on fresh electrodes and in triplicate

4.3.3: Catalyst Stability

To investigate the stability of the catalysts both repeated cyclic voltammetry and constant-current tests were performed. These tests were performed under the same conditions described above except that the electrodes were rotated to prevent the accumulation of bubbles on the surface of the electrode that may lead to a decrease in measured currents. Cyclic voltammetry stability tests were performed by cycling the

catalyst 20 consecutive times over one of two potential windows, either from 0.41 V to 0.7 V or 0.2 V to 0.7 V. The lower end of the potential window of 0.41 V was chosen by looking at the CVs in Figure 4.2 where it can be seen that the onset potential for the reduction of Ni^{3+} to Ni^{2+} on the cathodic scan occurs below 0.41 V vs Hg/HgO. By cycling in this window the surface of the catalyst should not be reduced due to the applied potential, but only due to reaction with urea or an alcohol, versus the potential window of 0.2 V to 0.7 V that does include the Ni^{3+} reduction peak. As can be seen in Figure 4.4, when cycled over the shortened window in which Ni is not reduced the activity at 0.6 V for LSN25 is stable or actually increases slightly over 20 cycles for the UOR as well as for both methanol and ethanol oxidation (Figure C.9). When the potential window is widened to include the $Ni^{3+/2+}$ reduction peak the activities decrease with each subsequent cycle, eventually displaying less than 50% of the original activity, thus when the catalyst surface is reduced by an applied potential it must restructure and deactivate. This agrees with our previous work described in Chapter 3 that showed how repeated cycling over the full potential window resulted in $LaNiO_3$ catalyst deactivation due to carbonate formation.[21] By keeping the potential above 0.41 V, LSN25 may remain stable and act as a highly active catalyst for the UOR as well as the electrooxidations of methanol and ethanol.

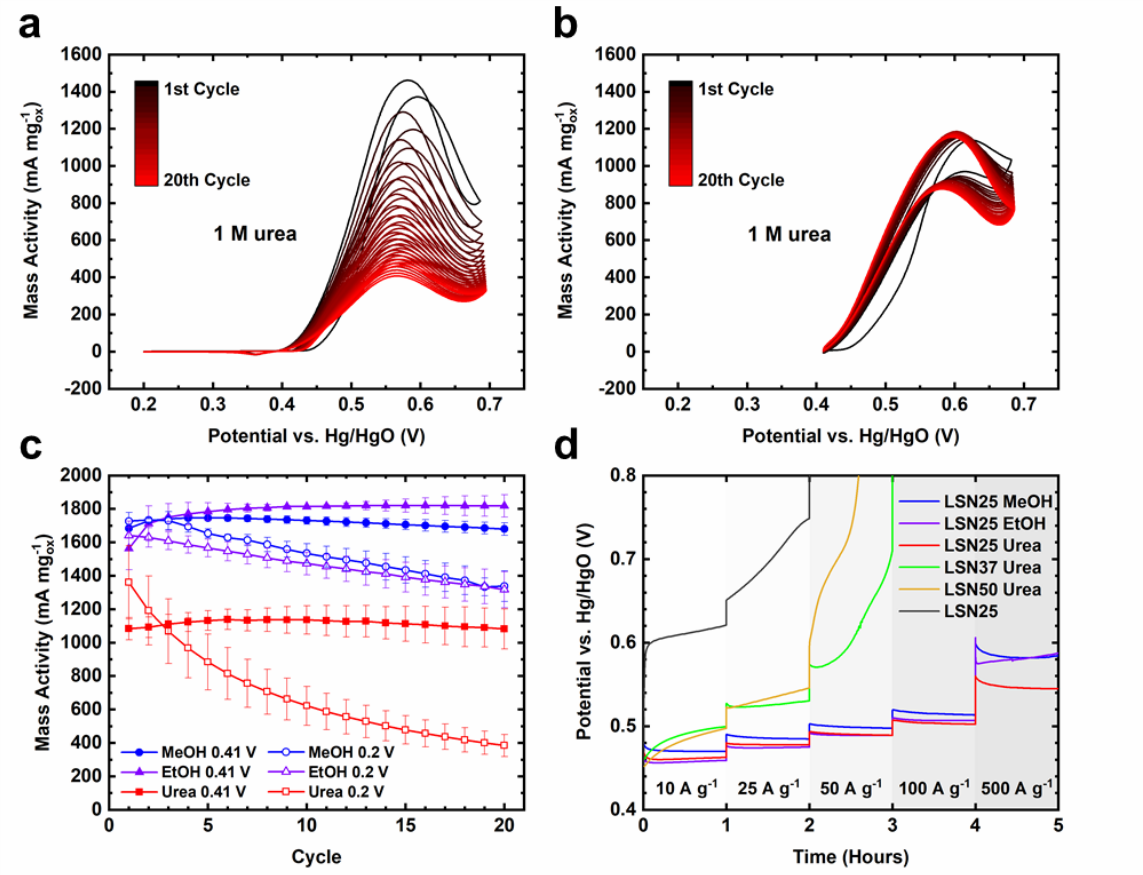

Figure 4.4: Effect of repeated cycling on urea oxidation mass activities.

(a) 20 cycles on LSN25 in Ar-saturated 1 M KOH with 1 M urea at a scan rate of 10 mV s^{-1} over a potential window of 0.41 V to 0.7 V. (b) 20 cycles on LSN25 in Ar-saturated 1 M KOH with 1 M urea at a scan rate of 10 mV s^{-1} over a potential window of 0.2 V to 0.7 V. (c) The mass activities measured at 0.6 V of the anodic scan for LSN25 over 20 cycles for the electrooxidations of 1 M urea, methanol, and ethanol. (d) Galvanostatic stability test for the entire LSN series in Ar-saturated 1 M KOH with 1 M urea as well as for LSN25 in 1 M KOH containing either 1 M methanol or ethanol. In these experiments the current is held for hour long intervals and stepped upwards from 10 A g^{-1} up to 500 A g^{-1} after each hour.

To further confirm the catalyst maintains its high performance over an extended period constant current tests were performed where currents were held for consecutive hour-long periods with the current increasing each hour. The currents used were stepped at intervals from 10 A g^{-1} up to 500 A g^{-1} to demonstrate the stability of the catalysts under a

variety of potential device operating conditions. As can be seen in Figure 4.4, all three compositions in the LSN series were tested for the UOR using 1 M urea in 1 M KOH and LSN25 was examined in 1 M KOH in the absence of urea as well. Even in the absence of urea LSN25 was able to generate 10 A g^{-1} at potentials in the incipient OER region due to surface $Ni^{2+/3+}$ redox and oxygen intercalation into the LSN25 crystal structure, as has been discussed elsewhere.[26] When 1 M urea was present in the electrolyte LSN50 and LSN37 were able to generate 10 A g^{-1} and 25 A g^{-1} for an hour each while maintaining potentials below the onset of the OER, however, when the current was increased to 50 A g^{-1} in the third hour of testing both proved unable to generate enough current due to the UOR alone and the potential increased rapidly into the OER region. Only LSN25 was active enough to be able to maintain a stable potential while generating up to 500 A g^{-1} through urea oxidation alone. LSN25 was then subjected to the same stability test but in the presence of 1 M methanol and ethanol. As can be seen in Figure 4.4, LSN25 was able to maintain a stable potential while generating as much as 500 A g^{-1} through the electrooxidations of methanol and ethanol as well, highlighting the remarkable activity and stability of LSN25 for all three reactions. Similar to the cycling stability experiments performed above, so long as the catalyst surface is not reduced due to an applied potential that may cause restructuring and deactivation, LSN25 performs as a remarkably active, stable catalyst for the electrooxidation of small molecules in alkaline conditions.

4.4: CONCLUSIONS

A series of nanostructured $La_{2-x}Sr_xNiO_{4+\delta}$ ($1 \leq x \leq 1.5$) materials were synthesized via a modified Pechini synthesis followed by calcination at high temperatures. The resulting in a collection of phase-pure $n = 1$ Ruddlesden-Popper catalysts that were utilized

to investigate the effect of increasing Ni oxidation state on the electrochemical oxidations of urea, methanol, and ethanol. Building on the work described in Chapter 3 and inspired by looking at the EC' mechanism described above in equations 4.1 - 4.4 for the UOR in which Ni^{3+} can be seen as the active form of Ni, we have demonstrated how systematic incorporation of Sr^{2+} into the RP crystal structure in place of La^{3+} steadily increases the bulk oxidation state of Ni past +3 leading to greater activities towards small molecule oxidations. LSN25, in which La makes up 25% of the A-site and Sr makes up 75%, displayed the highest activities for all three electrochemical oxidations, most notably generating 1,252 mA mg_{ox}^{-1} in 1 M urea. Furthermore, we discovered that this material can maintain its activity over long periods of time and at very high current densities but that reduction of the catalyst surface at sufficiently cathodic potentials leads to deactivation towards these reactions. This is the first time the fundamental guiding principle of increasing Ni oxidation state past Ni^{3+} to increase catalyst activity towards the urea oxidation reaction has been shown and the activities of LSN25 towards the electrooxidations of urea, methanol, and ethanol are among the highest ever reported.

4.5: REFERENCES

1. Zhu, H., Zhang, P. & Dai, S. Recent Advances of Lanthanum-Based Perovskite Oxides for Catalysis. *ACS Catal.* **5**, 6370–6385 (2015).

2. Rollinson, A. N., Jones, J., Dupont, V. & Twigg, M. V. Urea as a hydrogen carrier: a perspective on its potential for safe, sustainable and long-term energy supply. *Energy Environ. Sci.* **4**, 1216–1224 (2011).

3. Zhang, Z., Liu, J., Gu, J., Su, L. & Cheng, L. An overview of metal oxide materials as electrocatalysts and supports for polymer electrolyte fuel cells. *Energy Environ. Sci.* **7**, 2535–2558 (2014).

4. Antolini, E. Catalysts for direct ethanol fuel cells. *Journal of Power Sources* **170**, 1–12 (2007).

5. Wang, G. *et al.* Energy-efficient electrolytic hydrogen production assisted by coupling urea oxidation with a pH-gradient concentration cell. *Chem. Commun.* **54**, 2603–2606 (2018).

6. Boggs, B. K., King, R. L. & Botte, G. G. Urea electrolysis: direct hydrogen production from urine. *Chem. Commun.* 4859–4861 (2009). doi:10.1039/B905974A

7. Lan, R., Tao, S. & Irvine, J. T. S. A direct urea fuel cell – power from fertiliser and waste. *Energy Environ. Sci.* **3**, 438–441 (2010).

8. Wang, D., Yan, W., Vijapur, S. H. & Botte, G. G. Enhanced electrocatalytic oxidation of urea based on nickel hydroxide nanoribbons. *J. Power Sources* **217**, 498–502 (2012).

9. Yan, W., Wang, D. & Botte, G. G. Nickel and cobalt bimetallic hydroxide catalysts for urea electro-oxidation. *Electrochim. Acta* **61**, 25–30 (2012).

10. Liang, Y., Liu, Q., Asiri, A. M. & Sun, X. Enhanced electrooxidation of urea using $NiMoO_4 \cdot xH2O$ nanosheet arrays on Ni foam as anode. *Electrochim. Acta* **153**, 456–460 (2015).

11. Tong, Y. *et al.* Oxygen Vacancies Confined in Nickel Molybdenum Oxide Porous Nanosheets for Promoted Electrocatalytic Urea Oxidation. *ACS Catal.* **8**, 1–7 (2018).

12. Kakati, N., Maiti, J., Lee, K. S., Viswanathan, B. & Yoon, Y. S. Hollow Sodium Nickel Fluoride Nanocubes Deposited MWCNT as An Efficient Electrocatalyst for Urea Oxidation. *Electrochimica Acta* **240**, 175–185 (2017).

13. Tran, T. Q. N., Yoon, S. W., Park, B. J. & Yoon, H. H. CeO2-modified $LaNi_{0.6}Fe_{0.4}O_3$ perovskite and MWCNT nanocomposite for electrocatalytic oxidation and detection of urea. *Journal of Electroanalytical Chemistry* **818**, 76–83 (2018).

14. Wang, L. *et al.* Ni–WC/C nanocluster catalysts for urea electrooxidation. *Journal of Power Sources* **264**, 282–289 (2014).

15. Wang, L. *et al.* Enhanced activity of urea electrooxidation on nickel catalysts supported on tungsten carbides/carbon nanotubes. *Journal of Power Sources* **280**, 550–554 (2015).

16. Song, X. *et al.* Nickel phosphate-based materials with excellent durability for urea electro-oxidation. *Electrochimica Acta* **251**, 284–292 (2017).

17. Das, G., Tesfaye, R. M., Won, Y. & Yoon, H. H. NiO-Fe_2O_3 based graphene aerogel as urea electrooxidation catalyst. *Electrochimica Acta* **237**, 171–176 (2017).

18. Daramola, D. A., Singh, D. & Botte, G. G. Dissociation Rates of Urea in the Presence of NiOOH Catalyst: A DFT Analysis. *J. Phys. Chem. A* **114**, 11513–11521 (2010).

19. Vedharathinam, V. & Botte, G. G. Direct evidence of the mechanism for the electro-oxidation of urea on $Ni(OH)_2$ catalyst in alkaline medium. *Electrochim. Acta* **108**, 660–665 (2013).

20. Vedharathinam, V. & Botte, G. G. Understanding the electro-catalytic oxidation mechanism of urea on nickel electrodes in alkaline medium. *Electrochim. Acta* **81**, 292–300 (2012).

21. Forslund, R. P. *et al.* Nanostructured $LaNiO_3$ Perovskite Electrocatalyst for Enhanced Urea Oxidation. *ACS Catal.* **6**, 5044–5051 (2016).

22. Hardin, W. G. *et al.* Tuning the Electrocatalytic Activity of Perovskites through Active Site Variation and Support Interactions. *Chem. Mater.* **26**, 3368–3376 (2014).

23. Hardin, W. G. *et al.* Highly Active, Nonprecious Metal Perovskite Electrocatalysts for Bifunctional Metal–Air Battery Electrodes. *J. Phys. Chem. Lett.* **4**, 1254–1259 (2013).

24. Alexander, C. T., Abakumov, A. M., Forslund, R. P., Johnston, K. P. & Stevenson, K. J. Role of the Carbon Support on the Oxygen Reduction and Evolution Activities in $LaNiO_3$ Composite Electrodes in Alkaline Solution. *ACS Appl. Energy Mater.* **1**, 1549–1558 (2018).

25. Mefford, J. T. *et al.* Water electrolysis on $La_{1-x}Sr_xCoO_{3-\delta}$ perovskite electrocatalysts. *Nat. Commun.* **7**, 11053 (2016).

26. Forslund, R. P. *et al.* Exceptional electrocatalytic oxygen evolution via tunable charge transfer interactions in $La_{0.5}Sr_{1.5}Ni_{1-x}Fe_xO_{4\pm\delta}$ Ruddlesden-Popper oxides. *Nature Communications* **9**, 3150 (2018).

27. Takeda, Y. *et al.* Synthesis of $SrNiO_3$ and related compound, $Sr_2Ni_2O_5$. *J. Inorg. Nucl. Chem.* **34**, 1599–1601 (1972).

28. Sharma, I. B. & Singh, D. Solid state chemistry of Ruddlesden-Popper type complex oxides. *Bull. Mater. Sci.* **21**, 363–374 (1998).

29. Levasseur, B. & Kaliaguine, S. Methanol oxidation on $LaBO_3$ (B=Co, Mn, Fe) perovskite-type catalysts prepared by reactive grinding. *Applied Catalysis A: General* **343**, 29–38 (2008).

30. Singh, R. N. *et al.* Perovskite-type $La_{2-x}Sr_xNiO_4$ ($0 \leq x \leq 1$) as active anode materials for methanol oxidation in alkaline solutions. *Electrochimica Acta* **53**, 2322–2330 (2008).

31. Medarde, M. & Rodríguez-Carvajal, J. Oxygen vacancy ordering in $La_{2-x}Sr_xNiO_{4-\delta}$ ($0 \leq \leq 0.5$): the crystal structure and defects investigated by neutron diffraction. *Z. Phys. B* **102**, 307–315 (1997).

32. Millburn, J. E., Green, M. A., Neumann, D. A. & Rosseinsky, M. J. Evolution of the Structure of the K_2NiF_4 Phases $La_{2-x}Sr_xNiO_{4+\delta}$ with Oxidation State: Octahedral

Distortion and Phase Separation (0.2≤x≤1.0). *Journal of Solid State Chemistry* **145**, 401–420 (1999).

33. Aguadero, A. *et al.* Effect of Sr content on the crystal structure and electrical properties of the system $La_{2-x}Sr_xNiO_{4+\delta}$ ($0 \leq x \leq 1$). *Dalton Trans.* 4377–4383 (2006).

34. Takeda, Y. *et al.* Crystal chemistry and physical properties of $La_{2-x}Sr_xNiO_4$ ($0 \leq x \leq 1.6$). *Mater. Res. Bull.* **25**, 293–306 (1990).

35. Lan, A. & Mukasyan, A. S. Perovskite-Based Catalysts for Direct Methanol Fuel Cells. *J. Phys. Chem. C* **111**, 9573–9582 (2007).

36. Zhou, J.-S., Marshall, L. G. & Goodenough, J. B. Mass enhancement versus Stoner enhancement in strongly correlated metallic perovskites: $LaNiO_3$ and $LaCuO_3$. *Phys. Rev. B* **89**, 245138 (2014).

37. Conesa, J. C. Electronic Structure of the (Undoped and Fe-Doped) NiOOH O<sub>2 Evolution Electrocatalyst. *J. Phys. Chem. C* **120**, 18999–19010 (2016).

38. Corrigan, D. A. The Catalysis of the Oxygen Evolution Reaction by Iron Impurities in Thin Film Nickel Oxide Electrodes. *J. Electrochem. Soc.* **134**, 377–384 (1987).

Chapter 5: Comparison of Perovskite and Perovskite Derivatives for use in Anion-based Pseudocapacitor Applications

5.1: INTRODUCTION

Mentioned in previous chapters, as the popularity and necessity of sustainable renewable energy sources such as wind and solar continues to grow so too does the demand for new, efficient means of storing the energy from these intermittent sources. While lithium ion batteries and fuel cells have proven to be effective means of storing electricity, they require extended charging and discharging time periods and fail to handle the rapid charging and discharging rate requirements mandated by the nature of these energy sources. On the other end of the spectrum, traditional electrostatic capacitors can deliver high power but at a significant cost to their energy densities. Electric double layer capacitors (EDLCs) that utilize high surface area carbons, known as supercapacitors, as well as metal-based materials that operate in a similar fashion, known as pseudocapacitors, have shown great promise as an intermediary to bridge this gap in both energy and power densities.[1]

While electric double layer capacitors (EDLCs) rely solely on double layer capacitance to store charge on the surface of the electrode material, pseudocapacitors are able to take advantage of faradaic charge transfer in the forms of underpotential deposition, surface redox processes, and ion intercalation from the electrolyte into the bulk of a material.[2] In addition to the classic rectangular capacitance envelope seen for EDLCs during cyclic voltammetry (CV) experiments, pseudocapacitors also display peaks that are indicative of redox events within the electrode material, which means that the voltage-current response is not the same over the entire window. The energy density of a capacitor is given by:

$$E = \frac{1}{2} C V_{cell}^2 \quad (5.1)$$

where E is the energy density (Wh g^{-1}), C is the specific capacitance (F g^{-1}) of the electroactive material, and V_{cell} is the voltage applied to the entire cell.[2] Binary oxides such as V_2O_5,[3] α-MoO_3,[4] T-Nb_2O_5,[5] and TiO_2 nanotubes[6] paired with high surface area carbons in organic electrolytes[7,8] have been developed to try and take advantage of the larger stability window of these organic electrolytes, however, these devices have fallen out of favor due to the limitations imposed from high cost of materials and safety concerns.[9] Additionally, they display lower power and energy densities than can be achieved with aqueous systems which afford lower materials costs, greater electrolyte ion concentrations that lead to increased power densities, and improved safety and expanded temperature ranges in which they can operate. By replacing organic electrolytes with water we can utilize the entire pH range and a wide variety of solution ions such as H_2SO_4 at low pH, $NaSO_4$ around neutral pH, and NaOH and KOH in alkaline conditions.[10] This opens up the variety of materials that can be used as with oxides such as MnO_2, NiO, Co_3O_4 and V_2O_5 having been recently studied along with numerous others.[2,8–10] Given that the energy density goes as the square of the voltage window as shown above in Equation 5.1, one strategy to improve cell performance has been to utilize different materials at the two electrodes, such as TiO_2/MnO_2, supported on high surface are carbons to expand the voltage window.[11]

Previous work by our group demonstrated how the perovskite $LaMnO_{3-\delta}$ utilized a newly described hydroxide intercalation mechanism to achieve impressive pseudocapacitive performance and how reduction of the bulk structure introduced oxygen vacancies that greatly improved the amount of charge that could be stored.[12] Additionally, we have demonstrated how increased M – O bond covalency in the perovskite La_{1-}

$_{x}Sr_{x}CoO_{3-\delta}$ and in Ruddlesden-Popper (RP) oxides with the formula $La_{2-x}Sr_{x}Ni_{1-y}Fe_{y}O_{4+\delta}$, a derivative of the perovskite structure, allowed for increased rates of oxygen diffusion through oxygen vacancies within the perovskite lattice or through the rock salt layer of the RP structure aided in the exceptional performance of towards the oxygen evolution reaction (OER).[13] Elsewhere, others have demonstrated how perovskite materials can be used as anion-based pseudocapacitors with $Ba_{1-x}Sr_{x}Co_{1-y}Fe_{y}O_{3-\delta}$, $LaNiO_3$, $SrCo_{0.9}Nb_{0.1}O_{3-\delta}$, $CaMnO_3$ proving to be some of the most effective compositions.[14–17]

Herein, we report the synthesis and electrochemical evaluation of $CaMnO_{3-\delta}$ perovskite and $Ca_2MnO_{4-\delta}$ Ruddlesden-Popper materials as pseudocapacitor materials to leverage previously discovered trends in catalytic and capacitive activity to further the understanding of how complex metal oxides can be tuned to increase their ability to store charge via anion intercalation. The specific choice of Ca as the A-site element and Mn in the B-site was made based upon the ability to synthesize both perovskite and Ruddlesden-Popper versions of the same composition under the same conditions and the well-documented ability to introduce large numbers of oxygen vacancies.[18,19] Upon reduction of the as-synthesized materials in a reducing atmosphere both materials displayed greater pseudocapacitive performance compared to their unreduced counterparts, demonstrating how greater oxygen vacancy concentrations within the bulk increases their ability to store charge via oxygen anion intercalation. Furthermore, we demonstrate how a governing descriptor for pseudocapacitive performance changes from a dependence on the number of surface redox active sites at high scan rates and fast charge/discharge rates versus at slower rates where fast oxygen diffusion through the bulk lattice dominates. Finally, we demonstrate how both materials maintain their impressive performance with repeated cycling and even increase their capacity with continued use.

5.2: EXPERIMENTAL

5.2.1: Material Synthesis

Both materials were synthesized using the same modified Pechini method utilized in our previous work and described in previous chapters.[13] Precursor particles were synthesized by dissolving A and B-site nitrate salts in the appropriate stoichiometric ratios in water to make a solution with a total metal salt concentration of 0.1 M. Citric acid and EDTA were added to the solution each at a ratio of 1:1 with the total metal nitrate salts. TMAOH was added to the solution until the pH reached 7.5 to ensure deprotonation of three of the four EDTA carboxylic acid groups and that it had completely dissolved. DEG was then added to the solution at a concentration of 0.067 M and the solution was heated to 85° C while stirring. When heated, a dehydration reaction between the polyhydroxyl alcohol and the carboxylic acid groups of the chelates formed a polyester gel. After complete evaporation of the water the gel was combusted at 350° C to form mixed metal oxide precursor particles. This step was performed on a hot plate and not in a sealed furnace to avoid possible explosions from rapid evolution of gasses upon combustion. Finally, precursor particles were crystallized at 950° C for 5 hours under pure O_2 flowing at 100 mL min^{-1} in a tube furnace. Half of the resulting catalyst material was then annealed at 325° C under an atmosphere of 7% H_2 in Ar flowing at 100 mL min^{-1} to reduce the active material and introduce oxygen vacancies. All catalysts were recovered and immediately stored under Ar gas to prevent possible catalyst surface amorphization.

5.2.2: Powder X-ray Diffraction (PXRD)

Catalyst structure was probed by X-ray diffraction using a Rigaku MiniFlex600 Diffractometer at 298 K in ambient conditions, utilizing Cu Kα radiation (1.54 Å wavelength) operating at 40 kV and 15 mA. For all tests, argon-sealed catalyst powder was

exposed to ambient air and scanned over 10 - 100° 2θ in 0.01° increments with a dwell time of 0.2 seconds per step.

5.2.3: Surface Area Analysis

Nitrogen sorption analysis was performed on a Quantachrome Instruments NOVA 2000 high-speed surface area BET analyzer at a temperature of 77 K. Prior to measurements, the samples were ball milled for three minutes followed by degassing in vacuum for 12 hours at 120° C. The specific surface area was calculated using the BET method from the nitrogen adsorption data in the relative pressure range (P/P_0) of 0.05 to 0.30, with a minimum R^2 of 0.995 and C value of 20.

5.2.4: Scanning Electron Microscopy (SEM)

Samples were prepared by dispersing unsupported material in ethanol (0.1 mg mL^{-1}) and depositing drops of suspension onto silicon wafers which were dried at 85° C for 30 minutes. Images were taken on a Hitachi S5500 SEM using an accelerating voltage of 40 kV and probe current of 15 mA.

5.2.5: Iodometric Titrations

Iodometric titrations were performed by adding 3 mL of deoxygenated 2 M KI solution to a flask containing 15 – 20 mg of perovskite under an argon atmosphere and allowed to disperse for three minutes.[13] After a few minutes 25 ml of 1 M HCl was added and the perovskite was allowed to dissolve. This solution was then titrated to a faint golden color with a solution of ~26 mM solution of $Na_2S_2O_3$ that had been pre-standardized with 0.1 N KIO_3. Potato starch indicator was then added and the solution was titrated until clear, marking the end point.

5.2.6: Electrochemical Characterization

Chemical The catalyst and Vulcan carbon were each ball-milled for three minutes before being mixed together and ball milled again for three minutes in an 85:15 perovskite:carbon weight ratio. Catalyst inks were prepared by adding 3 mL of a NaOH neutralized 0.05 wt% Nafion solution in ethanol to 3 mg of catalyst powder (1 mg mL^{-1}) and bath sonicated for at 45 minutes. 10 μL of ink was drop cast onto a clean 5 mm (0.196 cm^2, Pine Instruments) glassy carbon electrode and dried under ambient conditions overnight. Glassy carbon electrodes were cleaned prior to drop casting by sonication in a 1:1 by volume DI water:ethanol solution. Electrodes were then polished using 0.05 μm alumina powder, rinsed with DI water, sonicated in a fresh DI water:ethanol solution, and rinsed with DI water again before being dried in ambient air. All electrochemical tests were performed on electrodes prepared this way, obtaining a composite catalyst loading of 51 μg_{total} cm^{-2}, yielding 43.3 μg_{oxide} cm^{-2}. Electrochemical testing was performed on a Metrohm Autolab PGSTAT302N potentiostat equipped with high speed rotators from Pine Instruments. All testing was performed at room temperature in Ar-saturated 1 M KOH (measured pH ≈ 13.7). Positive feedback methods were used to determine electrolyte resistance (6 Ω) and all data was iR compensated after testing unless stated otherwise. Each test was performed in a standard 3-electrode cell using a CH Instruments Hg/HgO (1 M KOH) reference electrode, a fritted Au wire counter electrode, and a film of catalyst ink on glassy carbon as the working electrode. All potentials are reported versus the Hg/HgO (1 M KOH) reference electrode. Materials were cycled three times at 100 mV s^{-1} prior to testing to ensure stable spectra were being collected. Specific capacitances (F g^{-1}) were calculated from CVs according to equation 2:

$$C_s = \frac{1}{2mv|V_c - V_a|} \oint_{V_a}^{V_c} i\,(V)dV \qquad (5.2)$$

Where *m* is the mass loading of electroactive material on the electrode (g), ν is the scan rate of the CV (V s^{-1}) while V_c and V_a are the cathodic and anodic limits of the CV window.[2] The integral represents the entire area within the CV loop over the cathodic and anodic sweeps which is divided by 2 to yield the average capacitance for a single sweep. Electrodes for every sample were tested at each scan rate (100, 50, 25, 10, 5 mV s^{-1}) with each electrode's capacitance measured in triplicate on separate electrodes to get an average and standard deviation.

5.3: RESULTS AND DISCUSSION

5.3.1: Physical Characterization

$CaMnO_{3-\delta}$ and $Ca_2MnO_{4-\delta}$ materials were synthesized using a modified Pechini method as described above followed by calcination at 950° C to yield a phase pure orthorhombic perovskite and n = 1 Ruddlesden-Popper structures as confirmed by powder X-ray diffraction (Figure 5.1).[18] Precursor particles measuring between 50 nm and 150 nm sintered during calcination at high temperature to form larger particles ranging from 200 nm up to microns in diameter as shown by SEM, and BET surface areas for the perovskite and Ruddlesden-Popper samples were measured to be 4.5 m^2 g^{-1} and 6.2 m^2 g^{-1}, respectively (Figure 5.1). Between the similarities in particle morphology observed using SEM and the similar BET surface areas we can confirm that both samples have approximately the same morphology, a characteristic that is important in order to reliably compare the electrochemical properties of multiple samples.

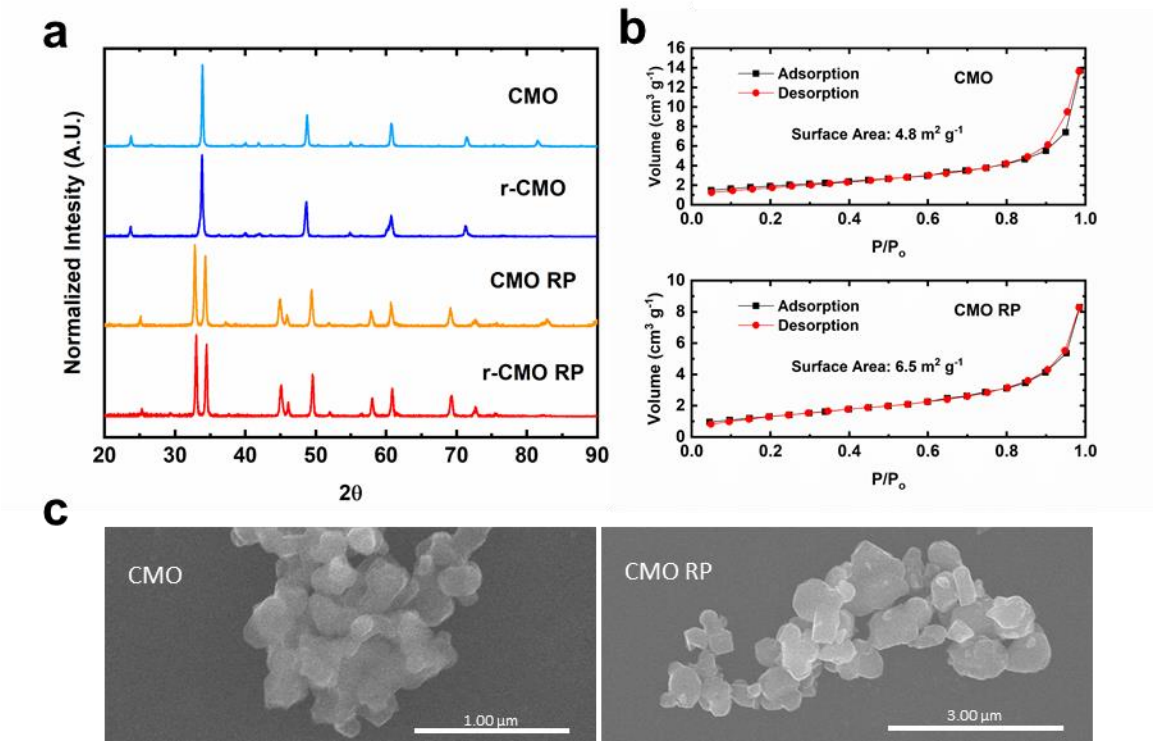

Figure 5.1: Physical characterization of $CaMnO_{3-\delta}$ and $Ca_2MnO_{4-\delta}$ materials.

(a) PXRD patterns of as-synthesized and reduced perovskite and RP materials. (b) BET sorption curves for surface area analysis. (c) SEM images of CMO and CMO RP indicating similar particle morphologies.

Half of the material from each sample was reduced in an atmosphere of 7% H_2 in Ar at 325° C as has been previously reported[18] and iodometric titrations were performed on all four materials to determine the bulk oxygen content and average B-site oxidation state in both the as-synthesized and reduced samples for each crystal structure. For simplicity we will refer to the as-synthesized, more-oxidized $CaMnO_{3-\delta}$ as CMO and the reduced version as r-CMO while the more-oxidized Ruddlesden-Popper will be referred to as CMO RP while the reduced version will be referred to as r-CMO RP. Results of the iodometric titrations are given in Table 5.1. Reduction resulted in increased oxygen

vacancy contents and, correspondingly, decreased Mn oxidation states for both the perovskite and RP crystal structures.

Sample	Composition	B^{AVG+} (Iodometry)	Oxygen Vacancy Content (δ)
CMO	$CaMnO_{3.11}$	4.22 ± 0.006	- 0.11 ± 0.003
r-CMO	$CaMnO_{2.53}$	3.06 ± 0.011	0.47 ± 0.005
CMO RP	$Ca_2MnO_{3.92}$	3.85 ± 0.012	0.08 ± 0.008
r-CMO RP	$Ca_2MnO_{3.61}$	3.23 ± 0.011	0.39 ± 0.005

Table 5.1: Physical characterization of $CaMnO_{3-\delta}$ and $Ca_2MnO_{4-\delta}$ materials.

5.3.2: Electrochemical Characterization

The pseudocapacitance of all four samples was characterized using cycling voltammetry in Ar-saturated 1 M KOH and all samples were supported at 85 wt% on Vulcan carbon XC-72 (VC). A carbon support is used because when unsupported material is used the drop-cast particles only contact each other and the GCE surface through point contacts. By supporting the pseudocapacitive materials on VC the electrical contact resistances between adjacent catalyst particles are minimized and better conductivity between the GCE electrode and the catalyst is achieved. Furthermore, we use VC for these studies because it is a relatively low surface area carbon, minimizing the contribution to the overall capacitance from charging of an electric double layer, and also because it lacks surface functionalities that may interact with and significantly alter the electronic structure of the material, allowing us to be confident that the differences in pseudocapacitive performance across the materials examined are due to differences in the metal oxides

themselves. Low mass loadings of 51 μg_{total} cm^2 were used to ensure efficient material utilization which allows for more detailed study of charge storage mechanisms.

Figure 5.2 shows CVs performed at varying scan rates for r-CMO and r-CMO RP and Figure D.1 shows CVs at multiple scan rates for the unreduced samples. A pair of peaks are seen on the anodic scan for all four samples with a sharp peak appearing near -0.10 V vs. Hg/HgO (1 M KOH) at 100 mV s^{-1} along with a lesser peak at 0.2 V, characteristic of $Mn^{3+/4+}$ and $Mn^{2+/3+}$ redox reactions, respectively.[12] Two peaks are observed on the cathodic scan at low scan rates for each sample as well which correspond to the reverse redox reactions mentioned above, however at 100 mV s^{-1} these peaks merge into a single, broad peak for all samples other than r-CMO RP. While the average Mn oxidation states for all four samples are above 3+ (Table 1), it is well documented that $CaMnO_3$ has very low electrical conductivity and it is possible that without itinerant electron behavior, localized regions of more-reduced Mn may exist.[20] As can be seen in Figure 2c, the capacitances of both the perovskite and the Ruddlesden popper increase with the introduction of (more) oxygen vacancies. Interestingly, at high scan rates the capacitance of r-CMO is significantly greater than that of r-CMO RP while at low scan rates the capacitances are approximately the same. For the unreduced samples, the capacitances of the two different crystal structures is approximately the same at high scan rates but at low scan rates the trend seen for the reduced samples is reversed in that CMO RP displays a much higher pseudocapacitance than CMO. When the peak current densities are plotted versus the scan rate and the square root of the scan rate we find that the peak currents go as $v^{1/2}$ for both intercalation and deintercalation of oxygen on both r-CMO and r-CMO RP, indicating a diffusion limited process is taking place (Figure D.2).[21] While intercalation of oxygen for CMO and CMO RP also appears to be a diffusion limited

process, the deintercalation peaks go as *v*, indicating that this process encounters charge-transfer limitations in the unreduced materials.

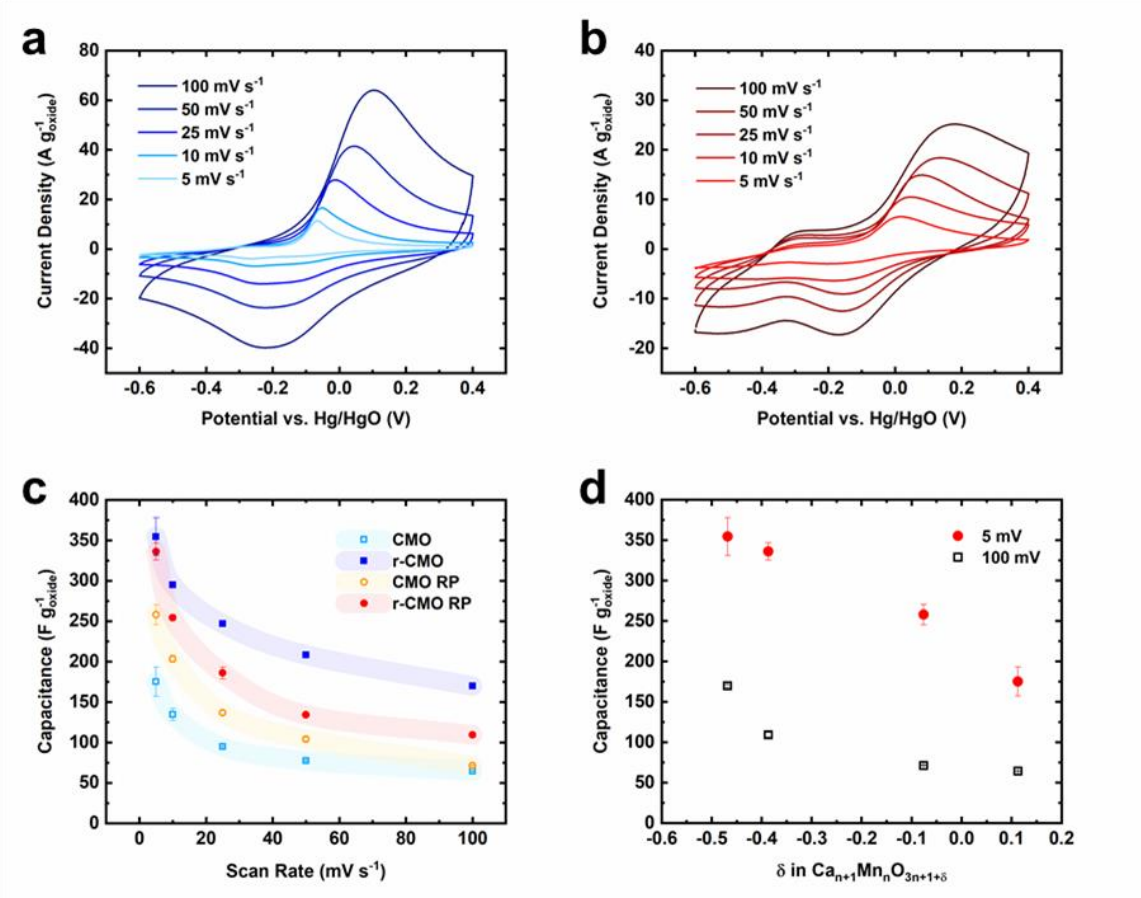

Figure 5.2: Electrochemical characterization of $CaMnO_{3-\delta}$ and $Ca_2MnO_{4-\delta}$ materials as pseudocapacitors.

Representative CVs of (a) r-CMO and (b) r-CMO RP performed at multiple scan rates over a 1 V window. (c) Gravimetric capacitances of all four materials at multiple scan rates. (d) Pseudocapacitance of all four samples at 5 mV $^{-1}$ and 100 mV s^{-1} as a function of oxygen vacancy concentration (δ). All CVs were performed in Ar-saturated 1 M KOH and performed in triplicate.

When the capacitances of all four materials at high and low scan rates are plotted as a function of oxygen vacancy content the picture of what governs their performance

becomes clearer. As can be seen in Figure 5.2, when CVs are performed at 5 mV s^{-1} the resulting capacitance values increase almost linearly with oxygen vacancy concentration. CVs that are performed at 100 mV s^{-1} result in pseudocapacitive performance that also shows a dependence on oxygen vacancy concentration, however, at lower values of δ this somewhat muted. To further probe the mechanism of charge storage the oxygen diffusion rates of both intercalation and deintercalation of oxygen were measured for four materials (Figure D.3). These measurements are made by first performing a CV at 10 mV s^{-1} to identify the peak position for the oxidation of Mn^{3+} to Mn^{4+} on the forward scan or for the reduction of Mn^{3+} to Mn^{2+} on the reverse scan, followed by chronoamperometry at a potential 50 mV more anodic (or cathodic) of these peaks to ensure a diffusion-limited process is taking place. The current is plotted versus $t^{-1/2}$ and the linear portion of each curve is fitted. The time at $i = 0$ is extrapolated and used to calculate the diffusion rate using a bounded diffusion model as described elsewhere.[22–24] Along with an increase in oxygen vacancy content, reduction of both the perovskite and RP structures leads to an increase in oxygen diffusion rates with r-CMO and r-CMO RP displaying diffusion rates on the order of those seen for Li^+ in Li-ion battery materials (Table D.1).[25,26]

The results presented above clearly indicate that oxygen vacancies play a crucial role in in the ability of a material to store charge through anion intercalation as the capacitances for both the perovskite and RP materials increased dramatically after reduction. However, if oxygen vacancy content was the only factor in governing pseudocapacitive performance then we would not see such a dramatic separation in performance between r-CMO and r-CMO RP at high scan rates, so we must look at other properties of the two materials to determine why this occurs, thus we turn our attention to the elemental compositions of the two materials.

After the introduction of oxygen vacancies has been accounted for, the mass percent of Mn in r-CMO is 41% while the mass percentage of Mn in r-CMO RP is only 28%, meaning that per unit mass of each material the perovskite contains 42% more Mn than the Ruddlesden-Popper. Looking at the gravimetric capacitances in Figure 5.2, the pseudocapacitance of r-CMO at 100 mV s^{-1} is 170 F g^{-1}, 55% greater than for r-CMO RP. We propose that at high scan rates, when limited periods of time are spent at potentials capable of causing charge transfer, oxygen intercalation is confined to a region near the surface of the particle and that in this scenario not only does oxygen vacancy content play an important role but so too does the number of Mn active sites. As longer scan rates are used, oxygen diffusion into the bulk of the particle increases, aided by the fast oxygen diffusion rates described above, and because the two materials have similar oxygen vacancy contents and diffusion rates their resulting capacitances are very close. As for the unreduced materials, CMO actually contains excess lattice oxygen while CMO RP contains a small number of oxygen vacancies, and this difference nullifies the effect of having significantly more Mn sites near the surface when high scan rates are used. At slower scan rates the effect of oxygen vacancy concentration dominates and CMO RP displays significantly higher pseudocapacitance at 5 mV s^{-1} than CMO. Furthermore, these trends in pseudocapacitance point to the stability of both crystal structures in basic conditions. If either structure were decomposing into its substituent oxides, CaO and MnO_2, then at low scan rates the perovskite materials would display significantly higher capacitances than their RP counterparts due to their greater Mn content.

The performance of both r-CMO and r-CMO RP with extended use was investigated by repeatedly cycling the electrodes over a potential window of 1 V and the results can be seen in Figure 5.3. For both r-CMO and r-CMO RP the charge stored via pseudocapacitance increases over the first 10 cycles before plateauing, and for r-CMO RP

the performance begins to decrease slightly after 25 cycles. When the amounts of positive and negative current passed are compared for each CV it becomes apparent that for both crystal structures a greater amount of positive current is passed than negative current, meaning more oxygen is being intercalated on the forward scan than is being deintercalated on the reverse scan, causing an overall reduction in the number of oxygen vacancies with repeated cycling. The experiments were then repeated over a potential window shifted cathodically by 100 mV to determine if spending more time at reducing potentials and less time at oxidizing potentials would bring this ratio closer to 1 and how this would affect pseudocapacitive performance. While the performance of r-CMO stayed approximately the same, the performance of r-CMO RP increases and the issue of a decrease in performance with repeated cycling is resolved. Additionally, the ratios of positive to negative current with each cycle are lower for both r-CMO and r-CMO RP when compared to the more positive potential window, and r-CMO RP actually displays a ratio of positive to negative charge less than unity at a low number of cycles before increasing to resemble the ratios observed for r-CMO over both potential windows.

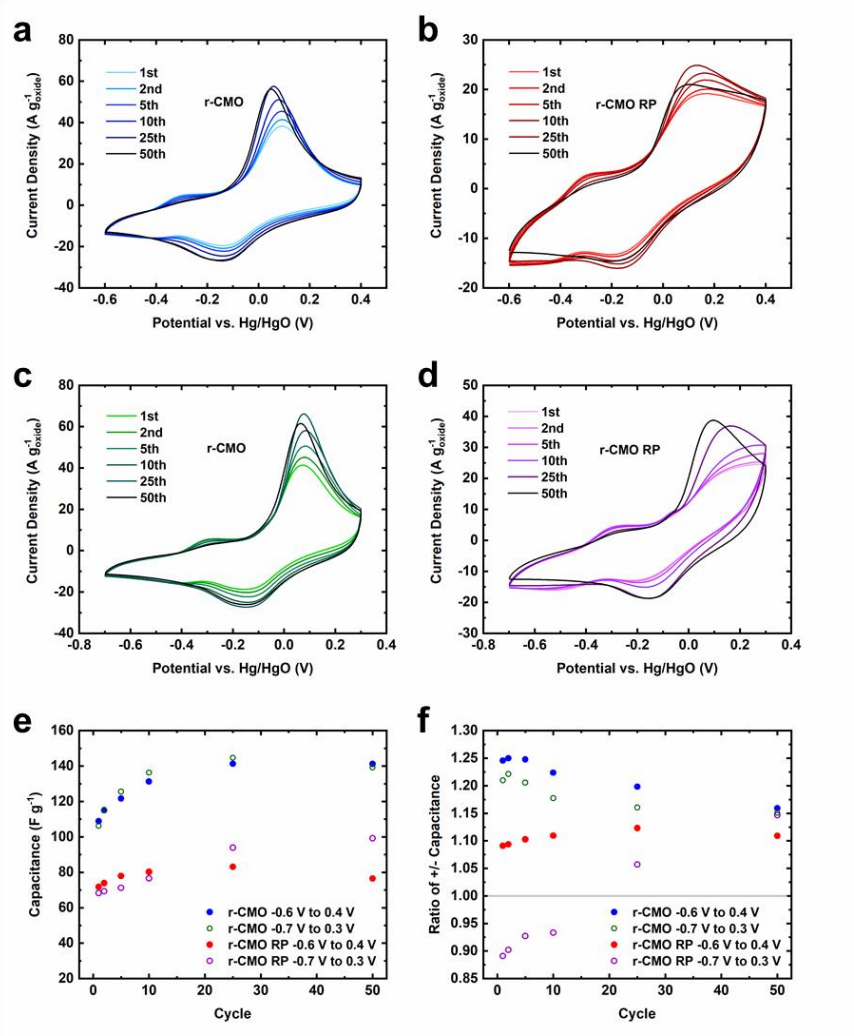

Figure 5.3: Electrochemical cycling stability of r-CMO and r-CMO RP materials as pseudocapacitors.

(a) 50 CVs performed at 100 mV s^{-1} over a potential window of -0.6 V to 0.4 V vs. Hg/HgO (1 M KOH) for r-CMO. (b) 50 CVs performed at 100 mV s^{-1} over a potential window of -0.7 V to 0.3 V for r-CMO. (c) 50 CVs performed at 100 mV s^{-1} over a potential window of -0.6 V to 0.4 V for r-CMO RP. (d) 50 CVs performed at 100 mV s^{-1} over a potential window of -0.7 V to 0.3 V for r-CMO RP. (e) Capacitances of r-CMO and r-CMO RP at various cycle numbers for the CVs shown in (a-d). (f) Ratios of positive to negative charge stored at various cycle numbers for the CVs shown in (a-d). All testing was performed in Ar-saturated 1 M KOH.

5.4: CONCLUSIONS

The electrochemical pseudocapacitance of $CaMnO_{3-\delta}$ and $Ca_2MnO_{4-\delta}$ materials have been studied via cyclic voltammetry measurements. Reduced versions of both catalysts that were formed by annealing in a reducing atmosphere displayed greater pseudocapacitive performance than their unreduced counterparts, verifying that greater oxygen vacancy concentrations within the bulk of these materials increases their ability to store charge via oxygen anion intercalation. Furthermore, we demonstrate how a governing descriptor for pseudocapacitive performance changes from a dependence on the number of surface redox sites at high scan rates versus at slower rates where fast oxygen diffusion through the bulk lattice dominates. Finally, we demonstrate how both materials maintain their impressive performance with repeated cycling and even increase their performance with continued use.

5.5: REFERENCES

1. Miller, J. R. & Simon, P. Electrochemical Capacitors for Energy Management. *Science* **321**, 651–652 (2008).

2. Conway, B. E. *Electrochemical Supercapacitors*. (Springer, 1999).

3. Chernova, N. A., Roppolo, M., Dillon, A. C. & Whittingham, M. S. Layered vanadium and molybdenum oxides: batteries and electrochromics. *J. Mater. Chem.* **19**, 2526–2552 (2009).

4. Brezesinski, T., Wang, J., Tolbert, S. H. & Dunn, B. Ordered mesoporous α-MoO_3 with iso-oriented nanocrystalline walls for thin-film pseudocapacitors. *Nature Materials* **9**, 146–151 (2010).

5. Brezesinski, K. *et al.* Pseudocapacitive Contributions to Charge Storage in Highly Ordered Mesoporous Group V Transition Metal Oxides with Iso-Oriented Layered Nanocrystalline Domains. *J. Am. Chem. Soc.* **132**, 6982–6990 (2010).

6. Xiong, H. *et al.* Self-Improving Anode for Lithium-Ion Batteries Based on Amorphous to Cubic Phase Transition in TiO_2 Nanotubes. *J. Phys. Chem. C* **116**, 3181–3187 (2012).

7. Frackowiak, E. & Béguin, F. Carbon materials for the electrochemical storage of energy in capacitors. *Carbon* **39**, 937–950 (2001).

8. Simon, P. & Gogotsi, Y. Materials for electrochemical capacitors. *Nature Materials* **7**, 845–854 (2008).

9. Wang, G., Zhang, L. & Zhang, J. A review of electrode materials for electrochemical supercapacitors. *Chem. Soc. Rev.* **41**, 797–828 (2012).

10. Wang, F. *et al.* Electrode materials for aqueous asymmetric supercapacitors. *RSC Adv.* **3**, 13059–13084 (2013).

11. Gu, J. *et al.* Asymmetric capacitors based on TiO_2 and mesoporous MnO_2 electrodes using neutral aqueous electrolyte. *J Nanopart Res* **19**, 322 (2017).

12. Mefford, J. T., Hardin, W. G., Dai, S., Johnston, K. P. & Stevenson, K. J. Anion charge storage through oxygen intercalation in $LaMnO_3$ perovskite pseudocapacitor electrodes. *Nat. Mater.* **13**, 726–732 (2014).

13. Forslund, R. P. *et al.* Exceptional electrocatalytic oxygen evolution via tunable charge transfer interactions in $La_{0.5}Sr_{1.5}Ni_{1-x}Fe_xO_{4\pm\delta}$ Ruddlesden-Popper oxides. *Nature Communications* **9**, 3150 (2018).

14. Liu, Y., Dinh, J., Tade, M. O. & Shao, Z. Design of Perovskite Oxides as Anion-Intercalation-Type Electrodes for Supercapacitors: Cation Leaching Effect. *ACS Appl. Mater. Interfaces* **8**, 23774–23783 (2016).

15. Che, W. *et al.* Perovskite $LaNiO_{3-\delta}$ oxide as an anion-intercalated pseudocapacitor electrode. *Journal of Alloys and Compounds* **731**, 381–388 (2018).

16. Lang, X., Mo, H., Hu, X. & Tian, H. Supercapacitor performance of perovskite $La_{1-x}Sr_xMnO_3$. *Dalton Trans.* **46**, 13720–13730 (2017).

17. Ali, G. A. M., Wahba, O. A. G., Hassan, A. M., Fouad, O. A. & Feng Chong, K. Calcium-based nanosized mixed metal oxides for supercapacitor application. *Ceramics International* **41**, 8230–8234 (2015).

18. Poeppelmeier, K. R., Leonowicz, M. E. & Longo, J. M. $CaMnO_{2.5}$ and $Ca_2MnO_{3.5}$: New oxygen-defect perovskite-type oxides. *Journal of Solid State Chemistry* **44**, 89–98 (1982).

19. Poeppelmeier, K. R., Leonowicz, M. E., Scanlon, J. C., Longo, J. M. & Yelon, W. B. Structure determination of $CaMnO_3$ and $CaMnO_{2.5}$ by X-ray and neutron methods. *Journal of Solid State Chemistry* **45**, 71–79 (1982).

20. Kim, J., Chen, X., Pan, Y.-T., Shih, P.-C. & Yang, H. W-Doped $CaMnO_{2.5}$ and $CaMnO_3$ Electrocatalysts for Enhanced Performance in Oxygen Evolution and Reduction Reactions. *J. Electrochem. Soc.* **164**, F1074–F1080 (2017).

21. Bard, A. J. & Faulkner, L. R. *Electrochemical Methods: Fundamentals and Applications*. (Wiley, 2000).

22. Van Buren, F. R., Broers, G. H. J., Bouman, A. J. & Boesveld, C. An electrochemical method for the determination of oxygen ion diffusion coefficients in $La_{1-x}Sr_xCoO_{3-y}$ compounds. *Journal of Electroanalytical Chemistry and Interfacial Electrochemistry* **87**, 389–394 (1978).

23. Van Buren, F. R., Broers, G. H. J., Bouman, A. J. & Boesveld, C. The electrochemical determination of oxygen ion diffusion coefficients in $La_{0.50}Sr_{0.50}CoO_{3-y}$:

Experimental results and related properties. *Journal of Electroanalytical Chemistry and Interfacial Electrochemistry* **88**, 353–361 (1978).

24. Kobussen, A. G. C., van Buren, F. R. & Broers, G. H. J. The influence of the particle size distribution on the measurement of oxygen ion diffusion coefficients in $La_{0.50}Sr_{0.50}CoO_{3-y}$. *Journal of Electroanalytical Chemistry and Interfacial Electrochemistry* **91**, 211–217 (1978).

25. Mizushima, K., Jones, P. C., Wiseman, P. J. & Goodenough, J. B. Li_xCoO_2 (0<x<-1): A new cathode material for batteries of high energy density. *Materials Research Bulletin* **15**, 783–789 (1980).

26. Yu, P., Popov, B. N., Ritter, J. A. & White, R. E. Determination of the Lithium Ion Diffusion Coefficient in Graphite. *J. Electrochem. Soc.* **146**, 8–14 (1999).

Appendices

APPENDIX A: EXCEPTIONAL ELECTROCATALYTIC OXYGEN EVOLUTION VIA TUNABLE CHARGE TRANSFER INTERACTIONS IN $La_{0.5}Sr_{1.5}Ni_{1-x}Fe_xO_{4+\Delta}$ RUDDLESDEN-POPPER OXIDES

A.1: Supplementary Notes

A.1.1: Concerning the Persistent Oxygen Hyperstoichiometry and High Oxidation States Measured for the LSNF Series

There are conflicting reports in the literature surrounding the average Ni oxidation state and oxygen hyperstoichiometry of $La_{2-x}Sr_xNiO_{4+\delta}$ and until the current study data were not available for $La_{0.5}Sr_{1.5}Ni_{1-x}Fe_xO_{4+\delta}$. The results in Table A1.3 indicate that Ni and Fe in Sr-nickelate are highly oxidized and that oxygen hyperstoichiometry increases as more Fe is substituted for Ni. However, others have observed increasing oxygen hyperstoichiometry at room temperature with increasing Fe content in La-rich $(La,Sr)_2Ni_xFe_{1-x}O_{4+\delta}$.[1,2] Medarde and Rodriguez-Carvajal found that ordered oxygen vacancies formed in $La_{2-x}Sr_xNiO_{4-\delta}$ when $x > 0.13$, while Aguadera and coworkers observed initial oxygen hyperstoichiometry when $x = 0.25$ in $La_{2-x}Sr_xNiO_{4+\delta}$, but find all samples to be oxygen deficient at $x \geq 0.5$, in contrast with our results.[3–5] Other reports of $La_{2-x}Sr_xNiO_{4+\delta}$ demonstrate that Sr substitution increases the average oxidation state of Ni due to charge compensation, up to and including $La_{0.5}Sr_{1.5}NiO_{3.98}$ in which Ni has an average oxidation state of +3.46.[6–8] Synthetic methodology and calcination temperature were both demonstrated to significantly affect the oxygen stoichiometry and crystal structure of $La_2NiO_{4+\delta}$,[9] and a similar conclusion was reached by Inprasit in rationalizing their oxygen hyperstoichiometry in $La_{1.2}Sr_{0.8}NiO_{4.2}$.[7] For $La_{2-x}Sr_xNiO_{4+\delta}$ synthesized using solid-state methods and crystallized at higher temperatures, lower Ni oxidation states and

oxygen substoichiometry were observed.[10] Thus, we rationalize that the good molecular intermixing promoted by the polymerizable complex synthesis, the pure oxygen calcination environment, and our relatively low crystallization temperature of 950° C and subsequent 6 hour oxygen anneal at 400° C contribute to the high oxygen content and higher oxidation states listed in Table A1.3, as has been seen for related materials elsewhere.[10,11] Finally, there is precedence for Fe substitution increasing the average oxidation state of a more electronegative B-site in a related n=1 RP system, $NdSrCo_{1-x}Fe_xO_{4+\delta}$.[12] Song et al found that increasing Fe substitution led to an increase in oxygen content and B-site oxidation state, measured by iodometry, which is logically consistent with our results.

A.1.2: Density Functional Theory (DFT) Modeling Details: determinations of effective Hubbard U_{eff}, atomic, magnetic and electronic structures, and oxygen hyper-stoichiometry effects.

Due to DFT self-interaction errors for strongly correlated materials,[13] the DFT+U method is employed to understand the electronic structures of LSNF. The values of U_{eff} of ~6.0eV (Ni) and ~5.0eV(Fe) are chosen based on previous work: In the case of Ni-containing perovskites, Gou et al. found that using U_{eff} (Ni) of ~6.0 eV gives a $LaNiO_3$ electronic structure closest to that obtained from hybrid functional methods and experimental spectroscopic data.[14] Lee et al. showed that this choice of U_{eff} also gives the correct $LaNiO_3$ formation enthalpy.[15] For Fe-contained perovskites, Shein et al. used a U_{eff} (Fe) of ~5.0eV to reproduce the experimental band gap for $LaFeO_3$, as well as the experimental magnetic structures and moments for both $LaFeO_3$ and $SrFeO_3$.[16] This choice of U_{eff} is also suggested by Ritzmann et al, particularly for those perovskites that exhibit some Fe(IV) character.[17,18] It is noteworthy that moderate adjustment of U_{eff} in a typical reported range may not significantly alter the density of states around Fermi level, as

compared between several studies using U_{eff} (Ni) from 5.7 to 6.4eV[14,15] and U_{eff} (Fe) from 4.3 to 5.4eV.[15–17]

We model the LSNF compounds using 2x2x1 primitive unit cells, which enables the unit composition $La_{0.5}Sr_{1.5}NiO_{4+\delta}$ (LSN), $La_{0.5}Sr_{1.5}Ni_{0.75}Fe_{0.25}O_{4+\delta}$ (LSNF25), $La_{0.5}Sr_{1.5}Ni_{0.50}Fe_{0.50}O_{4+\delta}$ (LSNF50), $La_{0.5}Sr_{1.5}Ni_{0.25}Fe_{0.75}O_{4+\delta}$ (LSNF75), and $La_{0.5}Sr_{1.5}FeO_{4+\delta}$ (LSF). Starting from a 2x2x1 cell of *I*4/*mmm* La_2NiO_4 (LN, Figure A1.16a), we first search for the ground state ordering of Sr substitutions for stoichiometric LSN through structural screening and relaxations. For the LSN, we find that La/Sr prefers a uniform (random) distribution with one La in each of the 4 *A*O layers, due to the ionic nature of La/Sr anions. We then perform a second round of screening to determine the minimum energy distributions of Fe substitutions for each stoichiometric LSNF composition.

Magnetic orderings, including ferromagnetic (FM), antiferromagnetic (AFM, A, C and G types) and non-magnetic structures are all investigated across the whole LSNF series to ensure that the magnetic ordering that gives rise to the lowest free energy structure is used in the calculation of PDOS diagrams. In the FM state, the overall spin directions of each individual *B* cation are aligned with each other. In the A-type AFM structure, the spins are parallel within each BO_2 layer, but antiparallel between neighboring BO_2 layers, as illustrated in Figure A1.22. In the G-type AFM state, the spins of neighboring *B* atoms are aligned antiparallel both in the plane of each BO_2 layer and between the BO_2 planes, forming a checkerboard pattern. In this crystal structure, C-type and G-type AFM are identical. Figure A1.22b shows the computed energies of the optimized LSNF cells with different magnetic states. As the figure shows, the FM and A-type AFM structures are very close in energy, while the G-type AFM and non-magnetic orderings are less stable across the whole LSNF series. This condition suggests that the large spatial separation leads to

negligible dipole interactions between neighboring BO_2 layers. Thus, the in-plane charge density distribution is similar for the A-type AFM and FM cases, as shown by comparing the PDOS in Figure A1.22c to that in Figure 2.5. Further investigation of the non-magnetic structure also reveals a similar trend in the *d*(B)-to-*p*(O) covalency from LSN to LSF, suggesting that characteristics of the PDOS for the FM state (shown in Figure 5 in the main text), are representative even above the Neel temperature.

We note that oxygen hyperstoichiometry effects either give rise to the emergence of bound states in conduction bands, a Fermi level shift, or a combination of the two.[19] In the former case, the overall electronic structure is subject to negligible change due to the dilute and localized nature of interstitial oxygen and bound states. In the latter case, the magnitude of the Fermi level shift can be roughly estimated via the rigid band model to accommodate unoccupied band formation, which can be determined by $E_F^{\delta} = E_F^0 - 2e^{-}\delta/\mathrm{DOS}(E_F^0)$, where $\mathrm{DOS}(E_F^0)$ is the total density of states at E_F^0 per formula unit of LSNF. As Figure 5c shows, the slightly adapted Fermi level, E_F^{δ}, does not qualitatively alter our discussions and conclusions. This situation is due to the rich band distribution of O-*p* holes and B-*d* states around the Fermi level.

A.2: Supplementary Figures

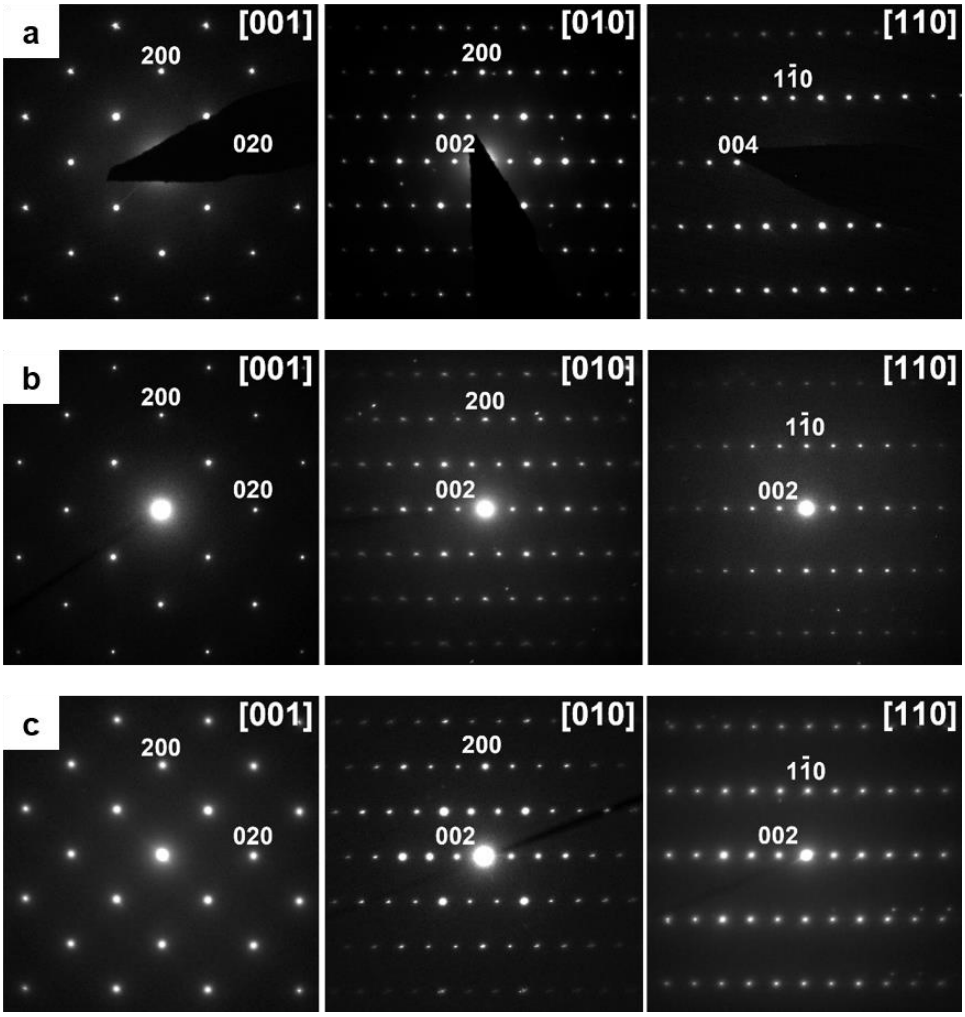

Figure A.1: Electron diffraction patterns of the LSNF series.

(a) LSN. (b) LSNF45. (c) LSF. The ED patterns for LSNF30 are given in Figure 2.1 of the manuscript. The ED patterns are indexed in a body-centered tetragonal unit cell with the unit cell parameters listed in Table A1.1.

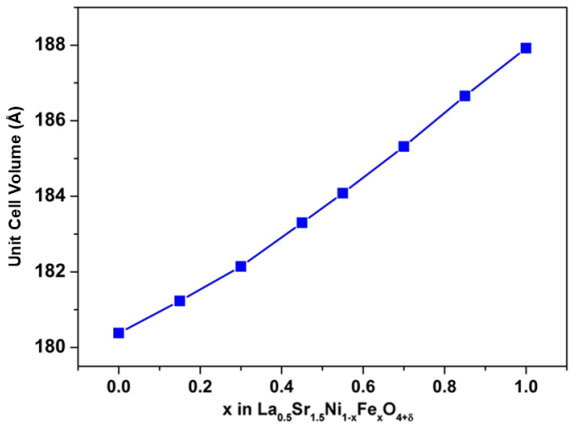

Figure A.2: Unit cell volume as a function of x in $La_{0.5}Sr_{1.5}Ni_{1-x}Fe_xO_{4+\delta}$ solid solutions.

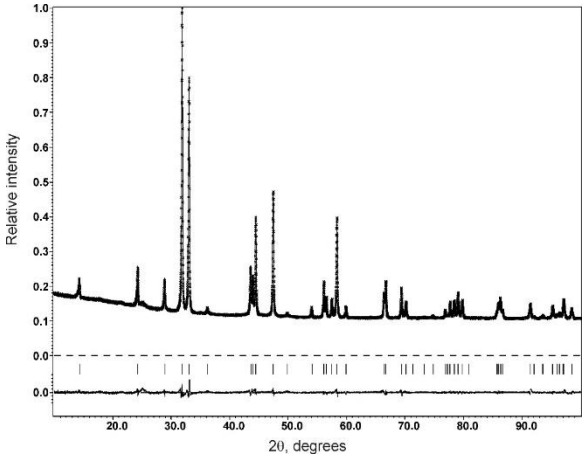

Figure A.3: Rietveld refinement of the $La_{0.5}Sr_{1.5}Ni_{0.7}Fe_{0.3}O_{4+\delta}$.

Typical experimental, calculated and difference curves after the Rietveld refinement of the $La_{0.5}Sr_{1.5}Ni_{1-x}Fe_xO_{4+\delta}$ structures (exemplified for LSNF30). The bars mark the reflection positions of the *I*4/*mmm* structure.

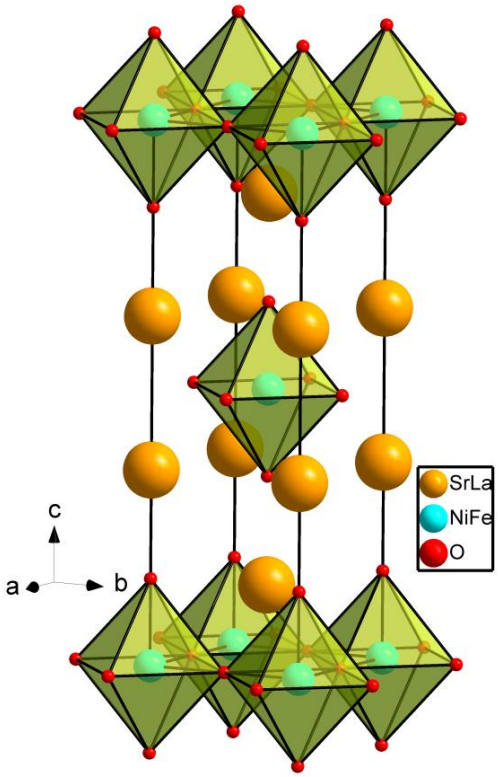

Figure A.4: The crystal structure of the $La_{0.5}Sr_{1.5}Ni_{0.7}Fe_{0.3}O_{4+\delta}$.

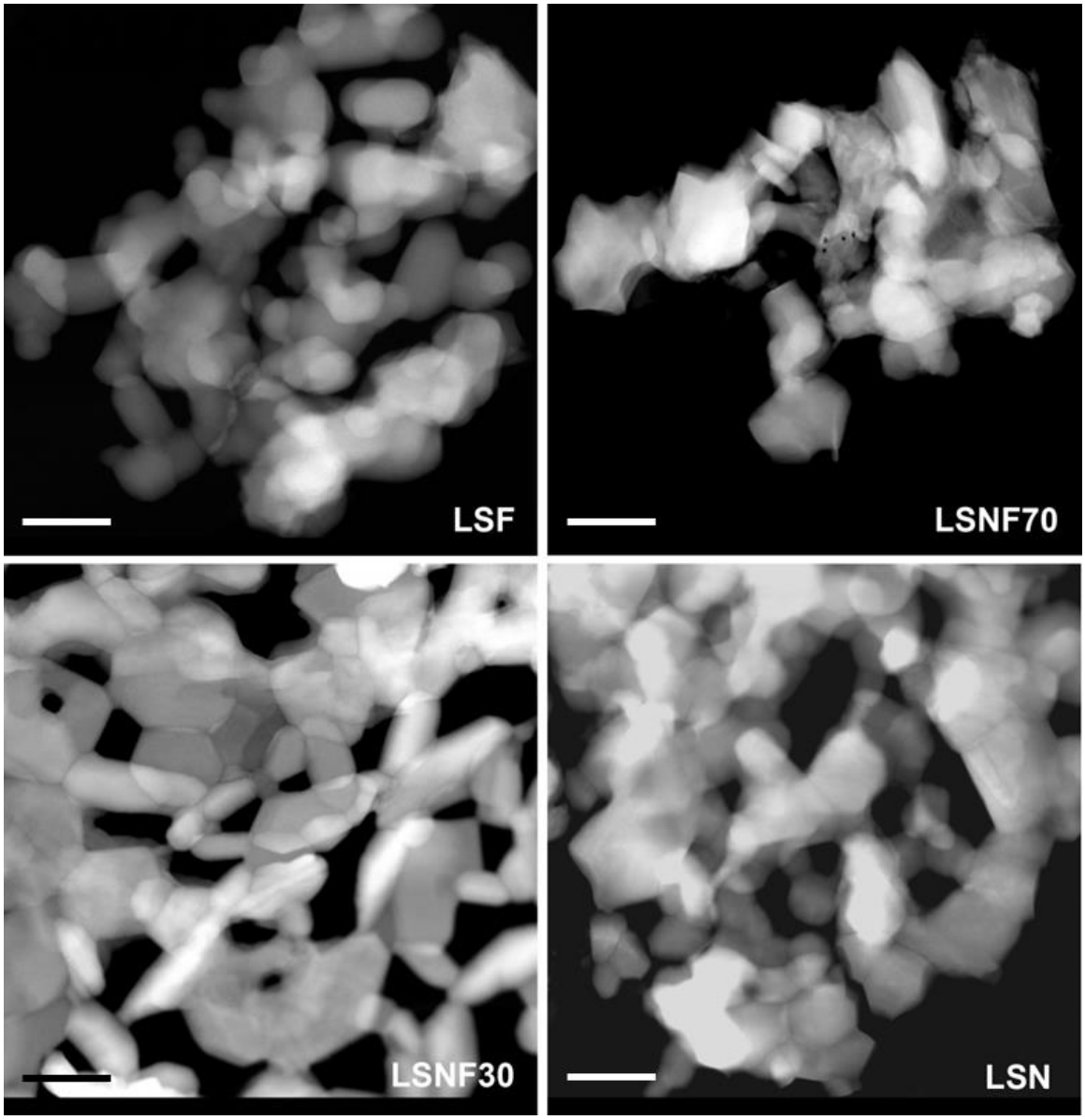

Figure A.5: HAADF-STEM images of $La_{0.5}Sr_{1.5}Ni_{1-x}Fe_xO_{4+\delta}$.

Scale bars are 200 nm. The images demonstrate that the catalysts are comprised of similarly sized primary particles that form loosely sintered aggregates with well-developed porosity.

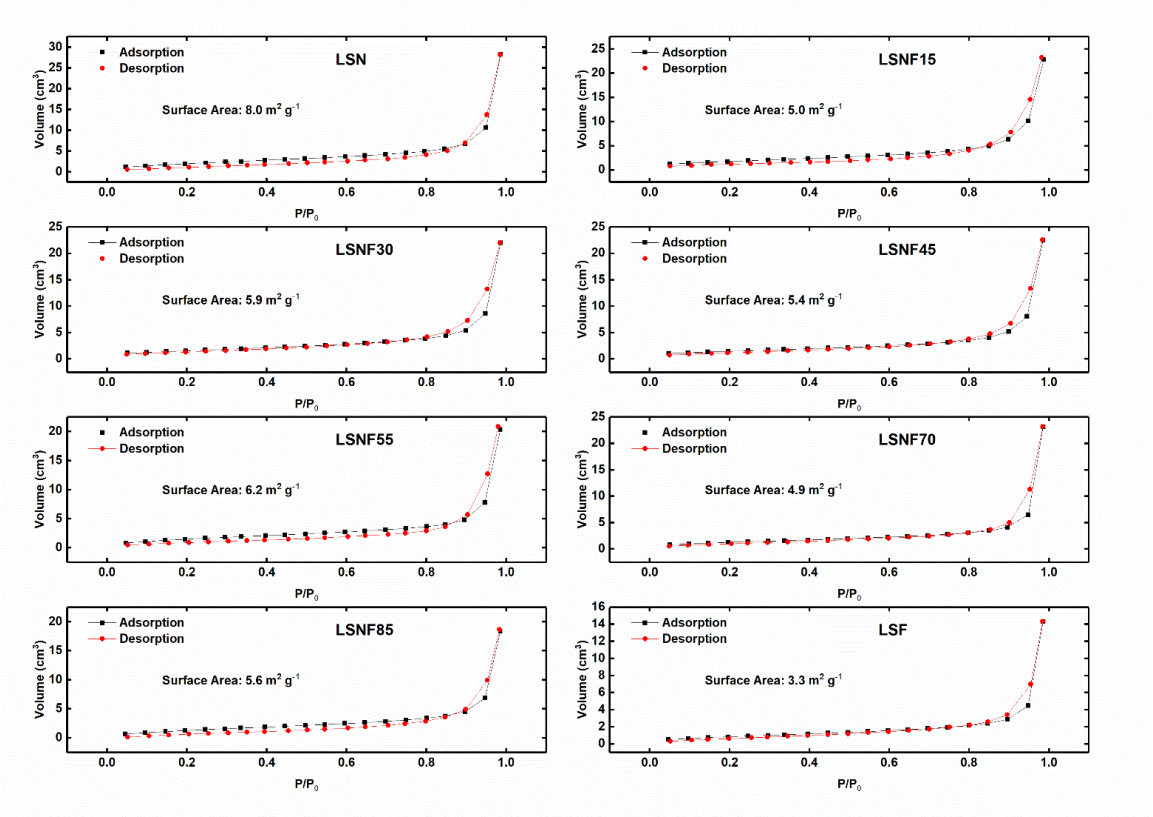

Figure A.6: Nitrogen sorption isotherms for BET surface area analysis of the LSNF series. Samples range in surface area from 3.3 to 8 $m^2 g^{-1}$. All samples underwent the same thermal treatments for mixed metal oxide precursor particle synthesis as well as crystallization and annealing.

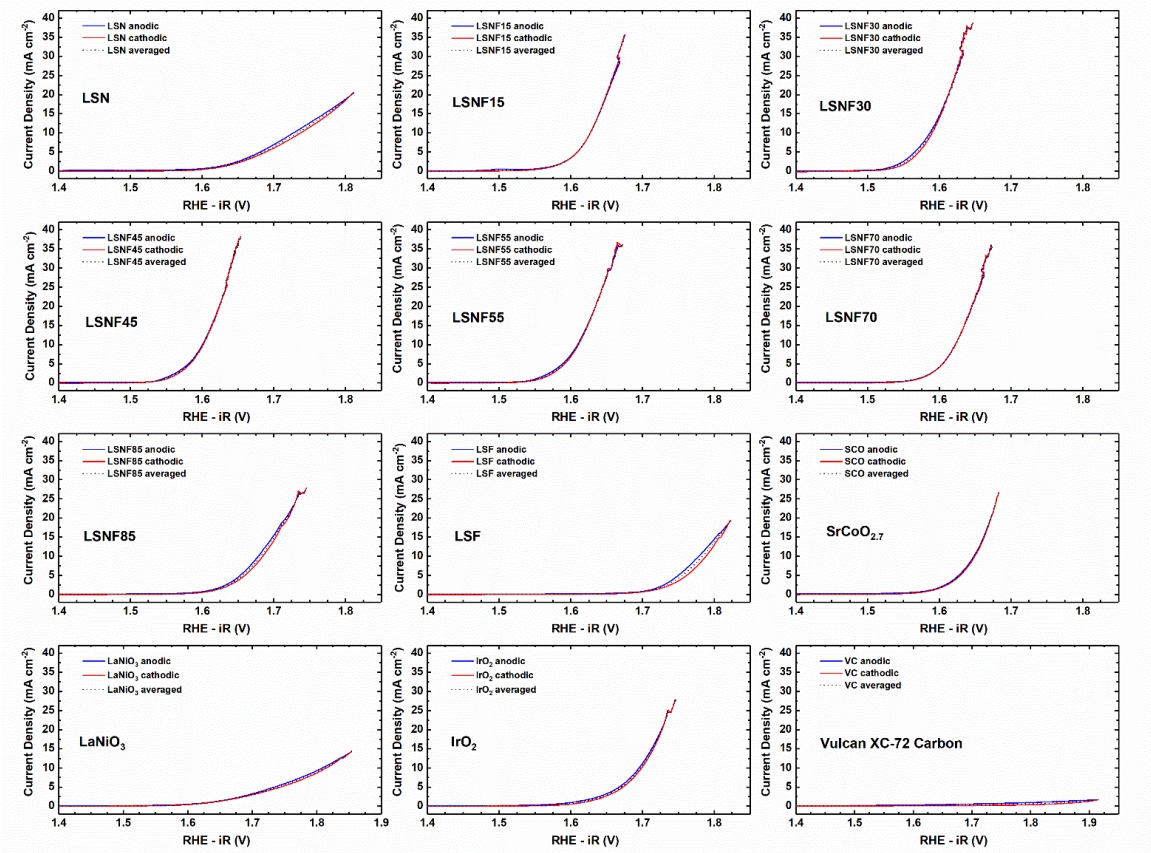

Figure A.7: Representative polarization curves of the LSNF series for the OER.

CVs taken in O_2-saturated 0.1 M KOH at 1600 rpm and 10 mV s^{-1}. Catalysts were first swept positive (anodic), then negative (cathodic), and the curves averaged before iR correction. Electrolyte resistance was measured to be 46 Ω. Total electrode loading is 51 μg_{total} cm^{-2}_{geo} with 30 wt% LSNF or SCO on XC72 Vulcan Carbon (VC), yielding 15.3 μg_{oxide} cm^{-2}_{geo}. IrO_2 was tested at 20 wt% on VC (10.2 μg_{oxide} cm^{-2}_{geo}) and neat VC was tested at 35.7 μg_{carbon} cm^{-2}_{geo} (7 μg carbon, corresponding to the contribution to measured OER current for 30 wt% LSNF on VC). $LaNiO_3$ and $SrCoO_{2.7}$ are the same materials as previously reported,[22, 33] except supported on VC to only probe the effects of catalyst composition.

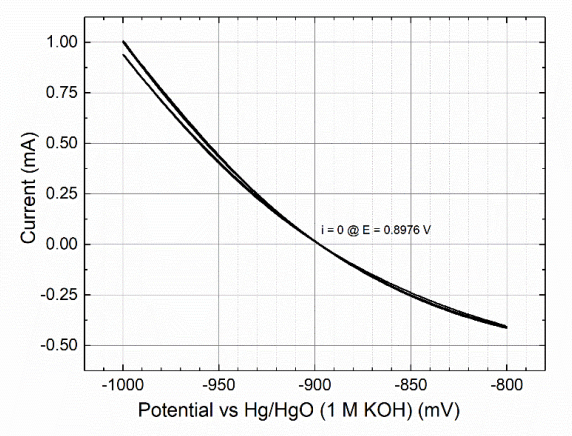

Figure A.8: Reversible hydrogen electrode (RHE) calibration.

A Pt working electrode was cycled at 1 mV s^{-1} in H_2-saturated 0.1 M KOH using a Pt or Au counter electrode to standardize the Hg/HgO (1 M KOH) reference electrode against thermodynamic H_2 evolution and oxidation. The Hg/HgO conversion to RHE was determined by the average potential at which 0 current was measured, -0.8976 V vs Hg/HgO.

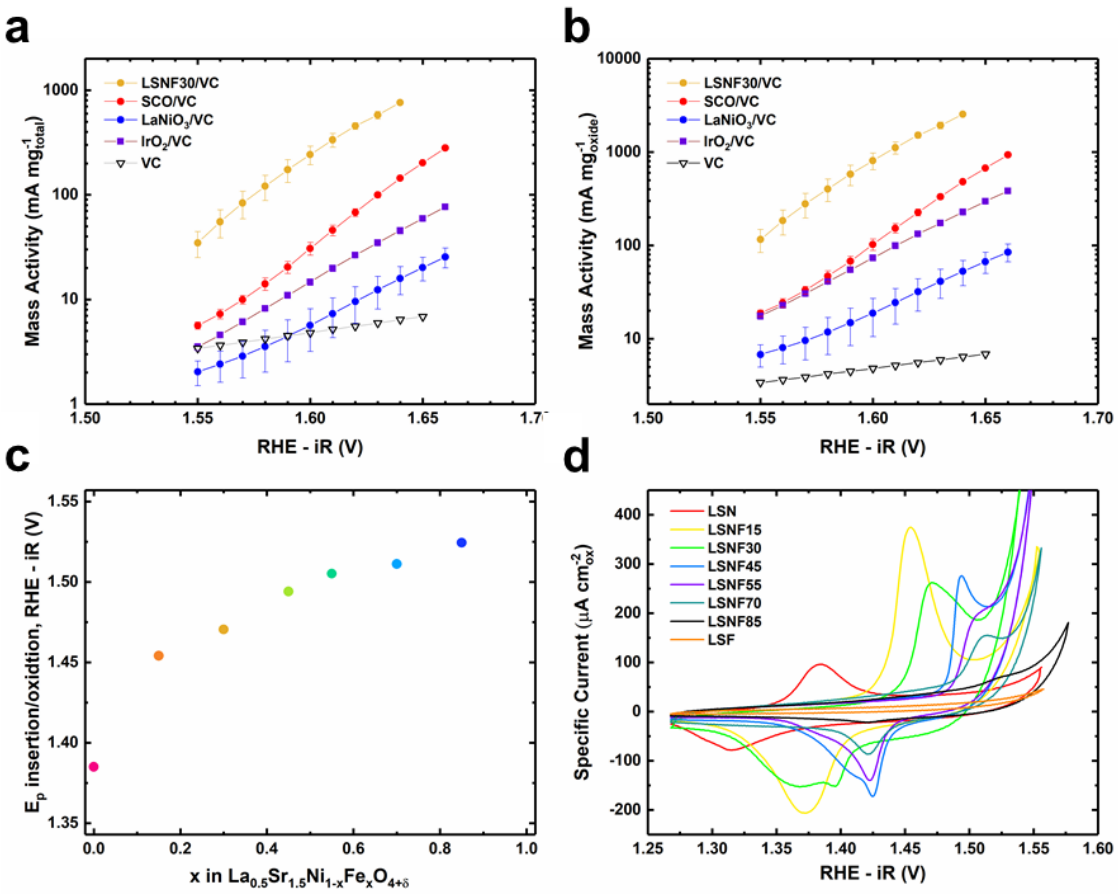

Figure A.9: Additional LSNF series OER activity data.

OER Tafel plot normalized on a on (a) total mass and (b) on a catalyst mass basis. All data in a-b taken in oxygen saturated 0.1 M KOH at 10 mV s^{-1} and 1600 rpm. LSNF30, SCO and $LaNiO_3$ are 30 wt% on VC, IrO_2 is 20 wt%, corresponding to 51 μg_{total} $cm^{-2}{}_{geo}$. VC is XC-72 Vulcan Carbon. Pure VC is tested at 35.7 μg cm^{-2}, corresponding to the 70 wt% carbon used to support LSNF30, SCO and $LaNiO_3$, and the mass activity should be read as mA $mg^{-1}{}_{carbon}$. (c) Shifting of the $Ni^{2+/3+}$ redox peak potentials as a function of Fe substitution. All peak potentials were taken from stable CVs at 10 mV s^{-1}. For LSNF55 and LSNF85, there was no local maximum at 10 mV/s and the peak potential was selected after the OER background was subtracted out, shown in Figure A1.16. (d) Stable intercalation CVs plotted in specific current density. All CVs are at 10 mV s^{-1} in O_2-saturated 0.1 M KOH.

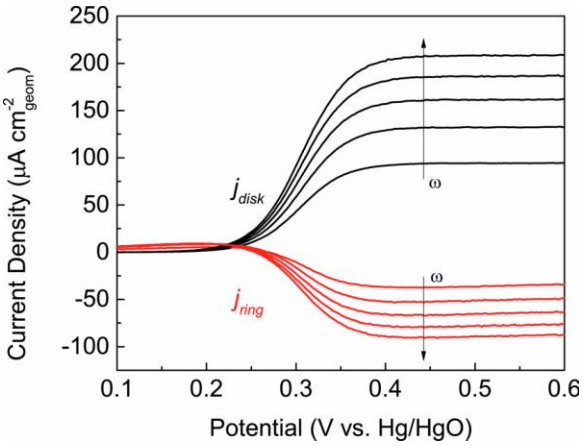

Figure A.10: Calibration of RRDE with Ferrocene-methanol.

Linear sweep voltammetry was performed using a rotating ring-disk electrode (RRDE) with a glassy carbon disk and a Pt ring in 0.3 mM ferrocene-methanol and 0.1M KCl. The disk potential was scanned from 0.1 to 0.6 V vs. Hg/HgO (1M KOH) while the ring was held at 0.1 V vs. Hg/HgO (1M KOH). Rotation rates of ω = 400, 800, 1200, 1600, and 2000 rpm were used. The collection efficiency was measured as N = 0.37.

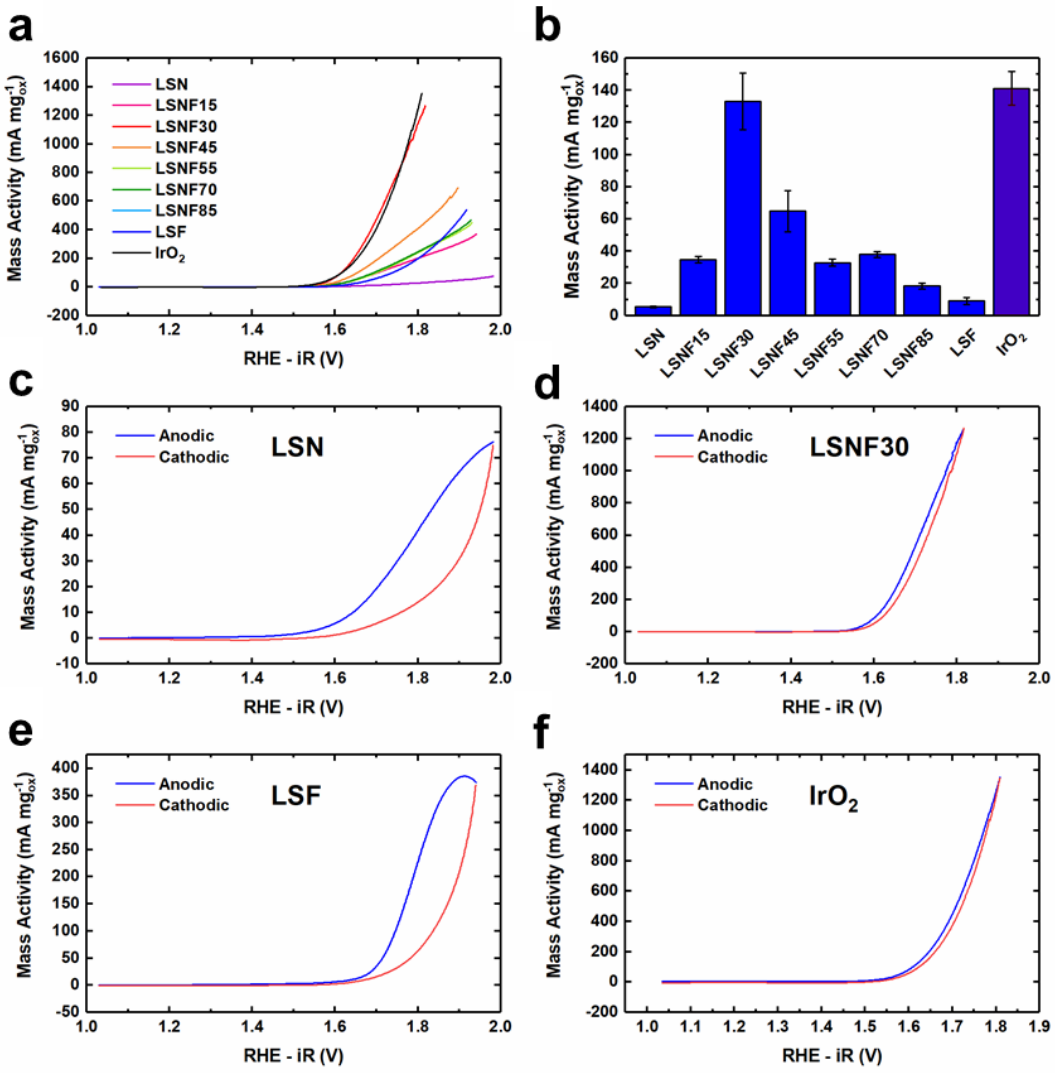

Figure A.11: Oxygen evolution results and catalytic activities for the unsupported LSNF series. (a) Activities measured from averaged anodic and cathodic scans at 1.63 V vs. RHE after iR correction in O_2 saturated 0.1 M KOH at 10 mV s^{-1} and 1600 rpm with a mass loading of 15.3 ug_{ox} cm^{-2}. (b) Bar graph of activities measured at 1.63 V. All measurements were performed in triplicate and averaged and error bars are the calculated standard deviations of these averages. (c-f) Representative CVs for LSN, LSNF30, LSF, and IrO_2 before averaging are shown.

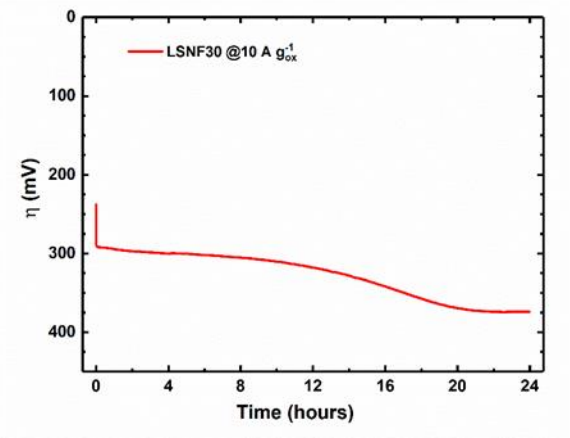

Figure A.12: Galvanostatic stability test of LSNF30.

Galvanostatic stability test of LSNF30 at 10 A/g_{oxide} in O_2 saturated 0.1 M KOH at 1600 rpm. LSNF30 was supported at 30 wt% on XC72 VC and dropcast onto a 5 mm GCE for a total mass loading of 51 $\mu g\ cm^{-2}_{geo}$.

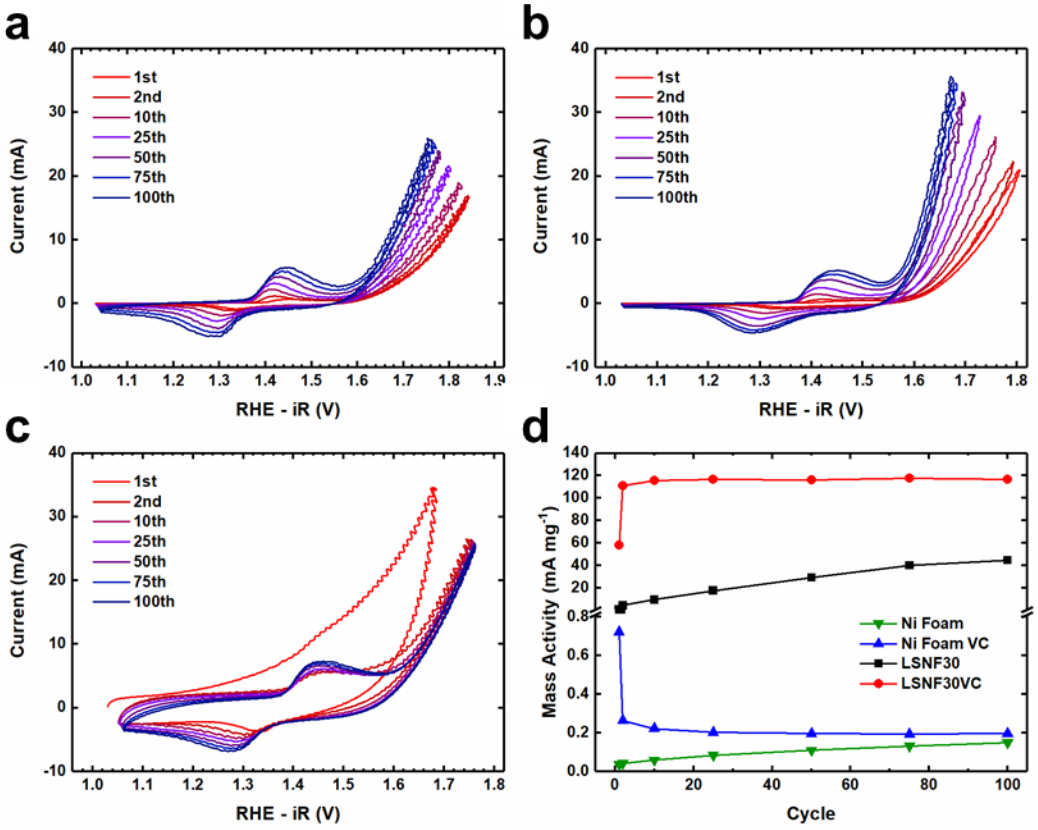

Figure A.13: Cyclic voltammetry stability tests of LSNF30 on Ni Foam electrodes.

(a) 100 cycles of a bare Ni foam electrode. (b) 100 cycles of a Ni foam electrode drop cast with 0.3 mg LSNF30. (c) 100 cycles of a Ni foam electrode drop cast with 0.7 mg of VC. (d) Mass activities for all four types of prepared Ni foam electrodes. Mass activities for the electrodes without LSNF30 were calculated by dividing the current by the mass of the Ni foam electrode. Mass activities for the LSNF were calculated by subtracting the current at 1.63 V for a Ni foam electrode with or without carbon but without catalyst from the current measured from the catalyst on Ni Foam with or without the VC support and then dividing by the mass of catalyst used.

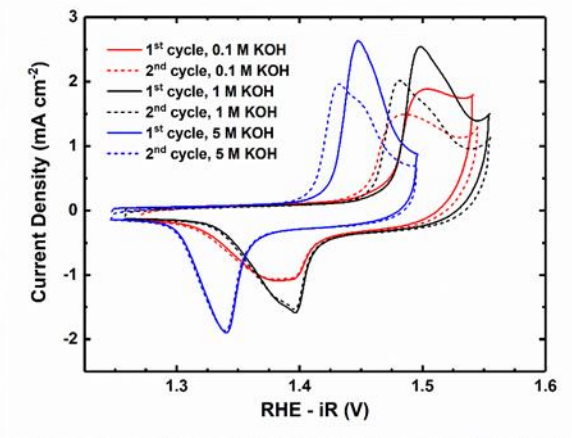

Figure A.14: First and second CVs of LSNF30 in various concentrations of KOH.

Dependence of oxidation wave peak potential (E_p) on pH is consistent with OH^- intercalation. Shifts in peak potential between the first and second cycle indicate an initial amount of catalyst surface restructuring.

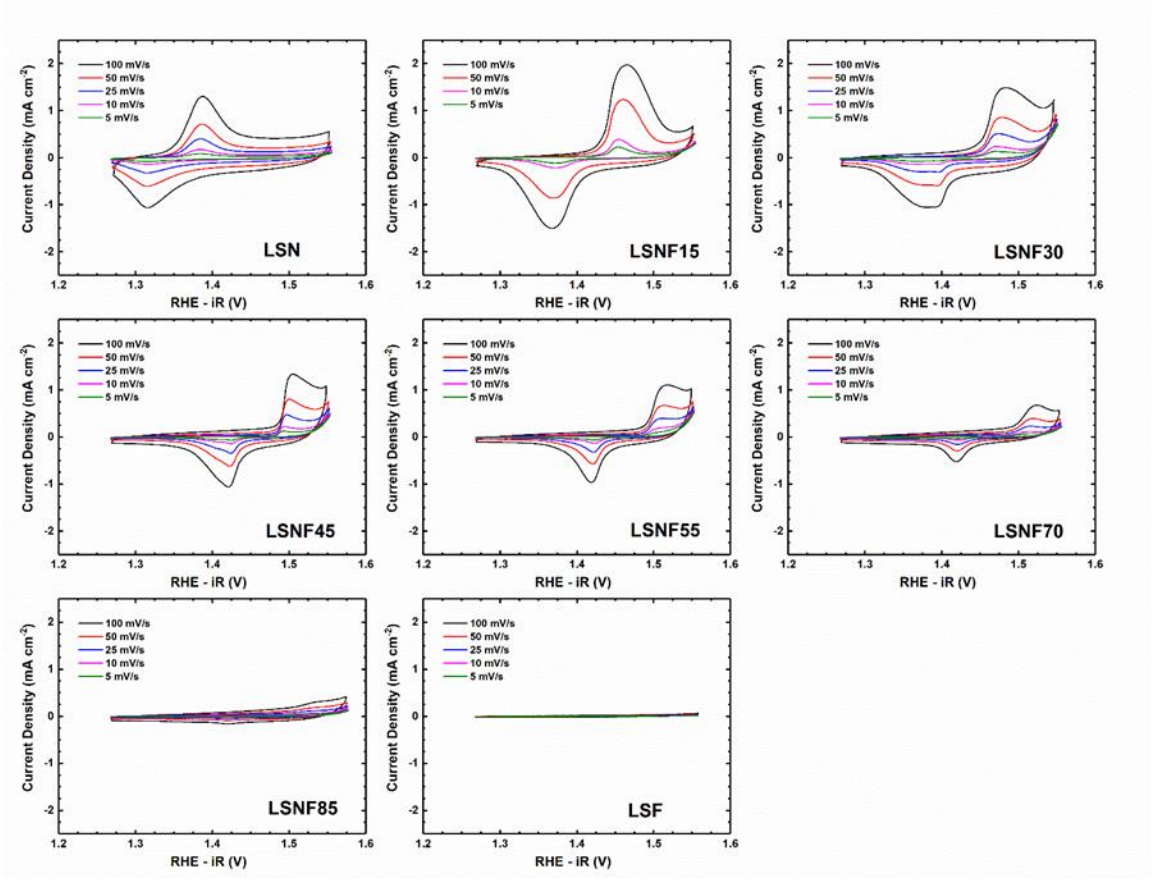

Figure A.15: Surface redox and anion intercalation CVs for the entire LSNF series.

CVs of 30 wt% oxide on VC taken in O_2 saturated 0.1 M KOH after 3 - 4 cycles of preconditioning so that oxidation peak potentials do not change upon subsequent cycling. CVs were taken on pristine electrodes immediately following preconditioning and recorded for varying scan rates, descending from 100 mV s^{-1} to 5 mV s^{-1}, one electrode per material.

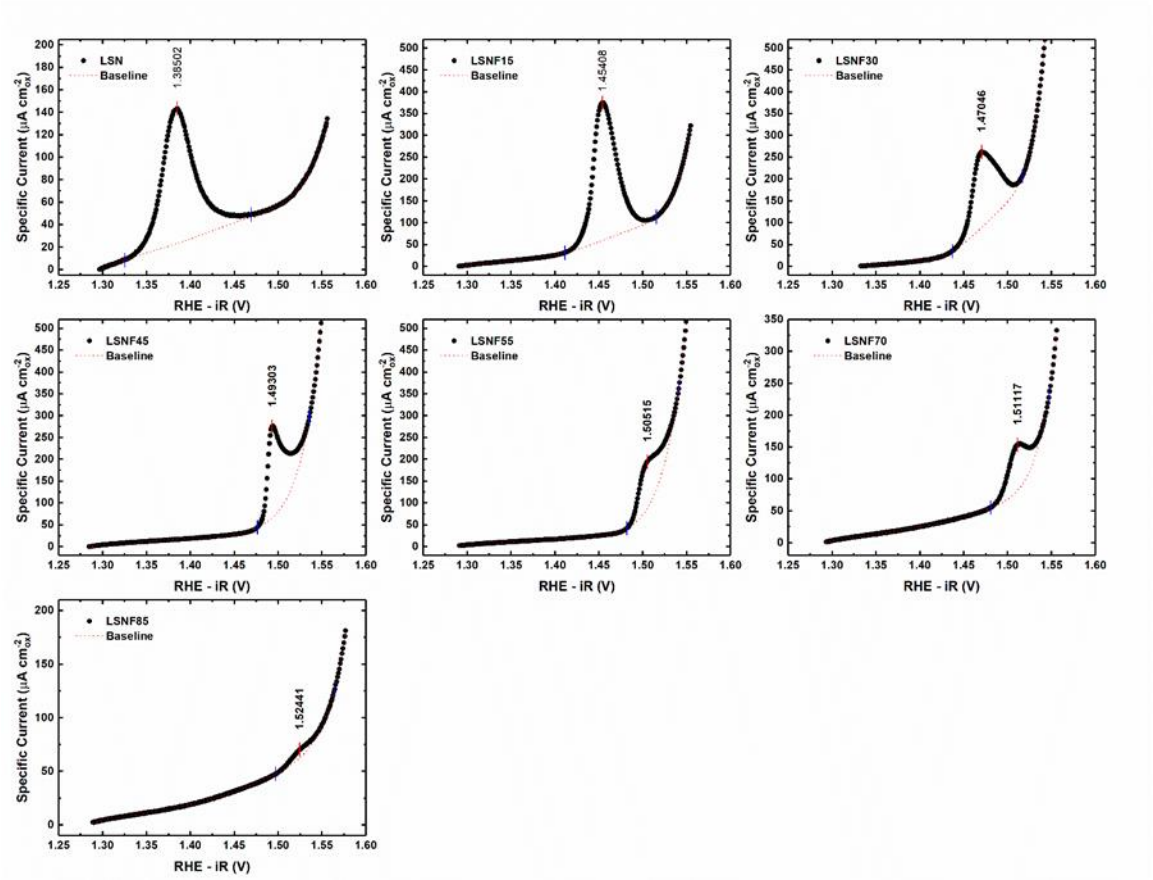

Figure A.16: Fitted surface redox and anion intercalation CVs for the entire LSNF series.

The fitted baseline was subtracted prior to integration of peak areas. Currents were converted into specific activity to account for surface area differences between samples with varying Fe contents. All CVs are in O_2 saturated 0.1 M KOH and were taken at 10 mV s^{-1}. These are the same CVs from Figure A.15, meaning they were collected from a pristine electrode that was conditioned and cycled at 100, 50, and 25 mV s^{-1}. Consult the methods section for more information. Numbers are the computed peak maxima after baseline OER subtraction, used for determination of E_P in Figure A.9 for LSNF55 and LSNF85, in which no local maxima is observed prior to baseline subtraction.

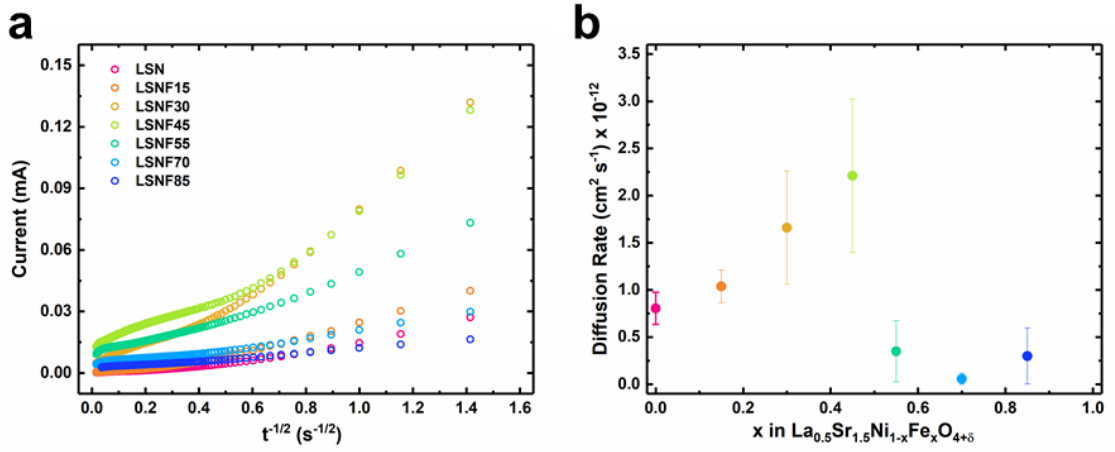

Figure A.17: Electrochemical oxygen diffusion rate data for the LSNF series.

Chronoamperometry experiments were performed in O_2 saturated 0.1 M KOH. (a) Calculated oxygen diffusion rates for LSNF catalysts. (b) Chronoamperometry data used for the calculation of diffusion rates in (a). A linear regression was used on the linear, fast timescale portion of the current decay, and using the mathematical model referenced in the Section 2.2.2 of the main text the diffusion rates were determined. Particle size was estimated from BET data and confirmed by the STEM images in Figure A1.5. The shape factor (λ) was assumed to be 2 for all calculations. All materials are 85 wt% oxide on VC which were dropcast onto 5 mm glassy carbon electrodes (GCE) for a total loading of 51 μg cm^{-2}_{geo}.

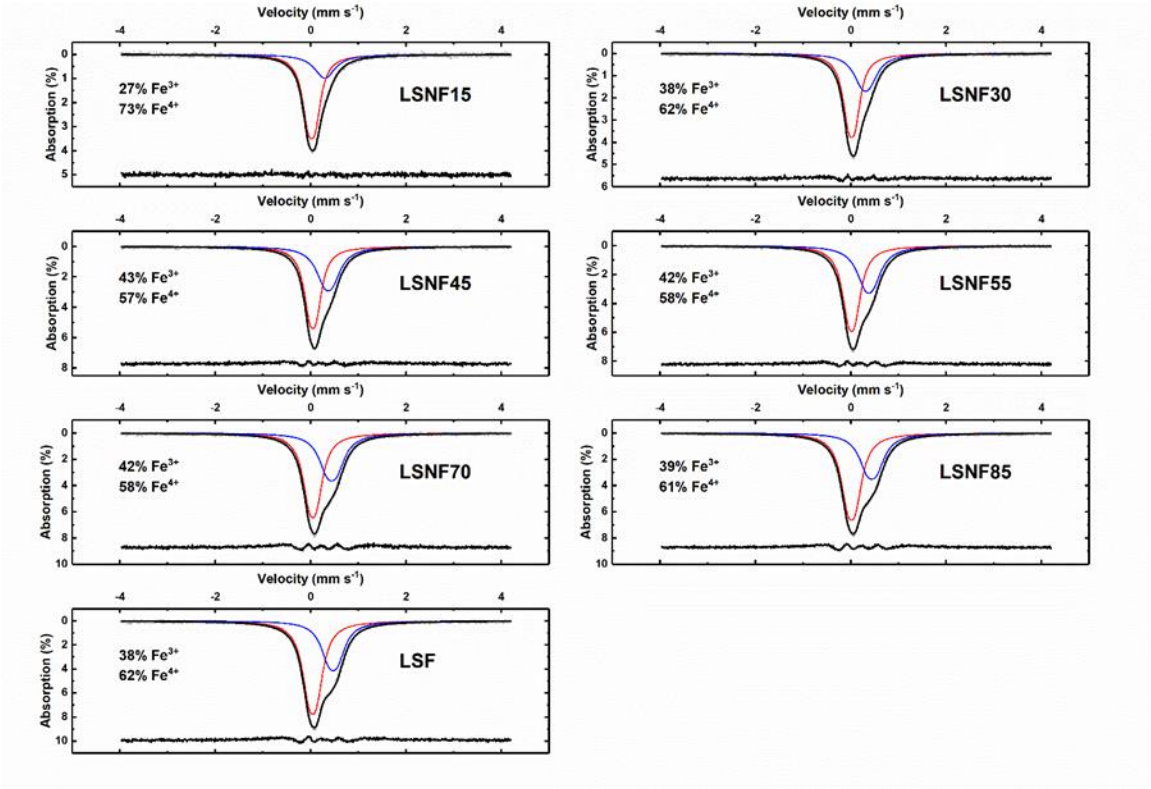

Figure A.18: Room temperature Mössbauer spectroscopy for the LSNF series.

Fitted curves for Fe^{4+} depicted in red while fitted curves for Fe^{3+} are shown in blue. The spectra, measured at room temperature, were deconvoluted into two overlapped paramagnetic doublets. According to their chemical isomer shifts (ISs), the doublets with smaller ISs of ~0.02 - 0.04 mm/s correspond to Fe^{4+} cations, while ones with larger ISs of ~0.32 - 0.45 mm/s correspond to Fe^{3+} cations.[20] It was previously shown that values of quadrupole splitting (QSs) in the $Sr_{2-x}La_xFeO_{4\pm\delta}$ based solid solutions are highly dependent on La and O contents.[21] The observed values of hyperfine parameters, viz. ISs and QSs, for the Sr- nickelate system investigated are consistent with the parameters reported for the related $Sr_{2-x}La_xFeO_{4\pm\delta}$ compounds with high oxygen content.[22,23] It is to note that some of the samples were additionally measured at low temperature of 78K. The 78K Mossbauer spectra obtained were more difficult to analyze to resolve the Fe^{3+} and Fe^{4+} subspectra because of their higher broadening and overlapping, but no significant difference in the $Fe^{3+/4+}$ ratios at 78K and 298K were observed. For the sake of clarity, only the room temperature data are reported.

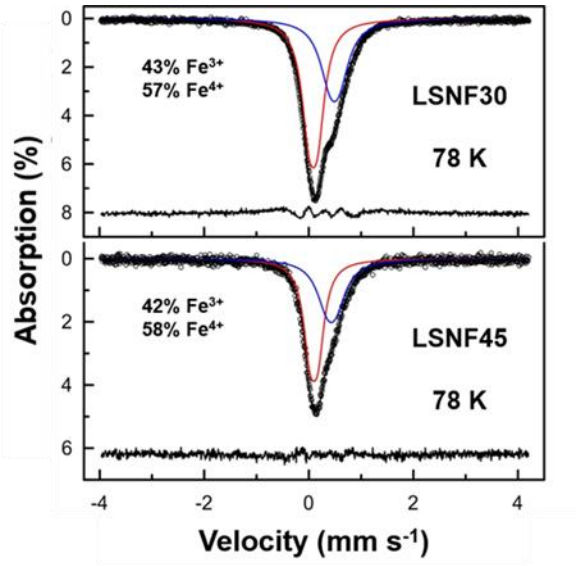

Figure A.19: Mössbauer spectroscopy taken at 78 K for LSNF30 and LSNF45.

LSNF30 and LSNF45 were the two most active compositions of the LSNF series towards the OER. Fitted curves for Fe^{4+} depicted in red while fitted curves for Fe^{3+} are shown in blue. The spectra were deconvoluted into two overlapped paramagnetic doublets in the same manner described in Figure A1.16. The Mossbauer spectra obtained at 78K were more difficult to analyze to resolve the Fe^{3+} and Fe^{4+} subspectra because of their higher broadening and overlapping, but LSNF30 and LSNF45 were able to be analyzed and displayed very similar $Fe^{3+/4+}$ ratios at 78K and 298K and follow the trend observed for measurements taken across the entire series at room temperature.

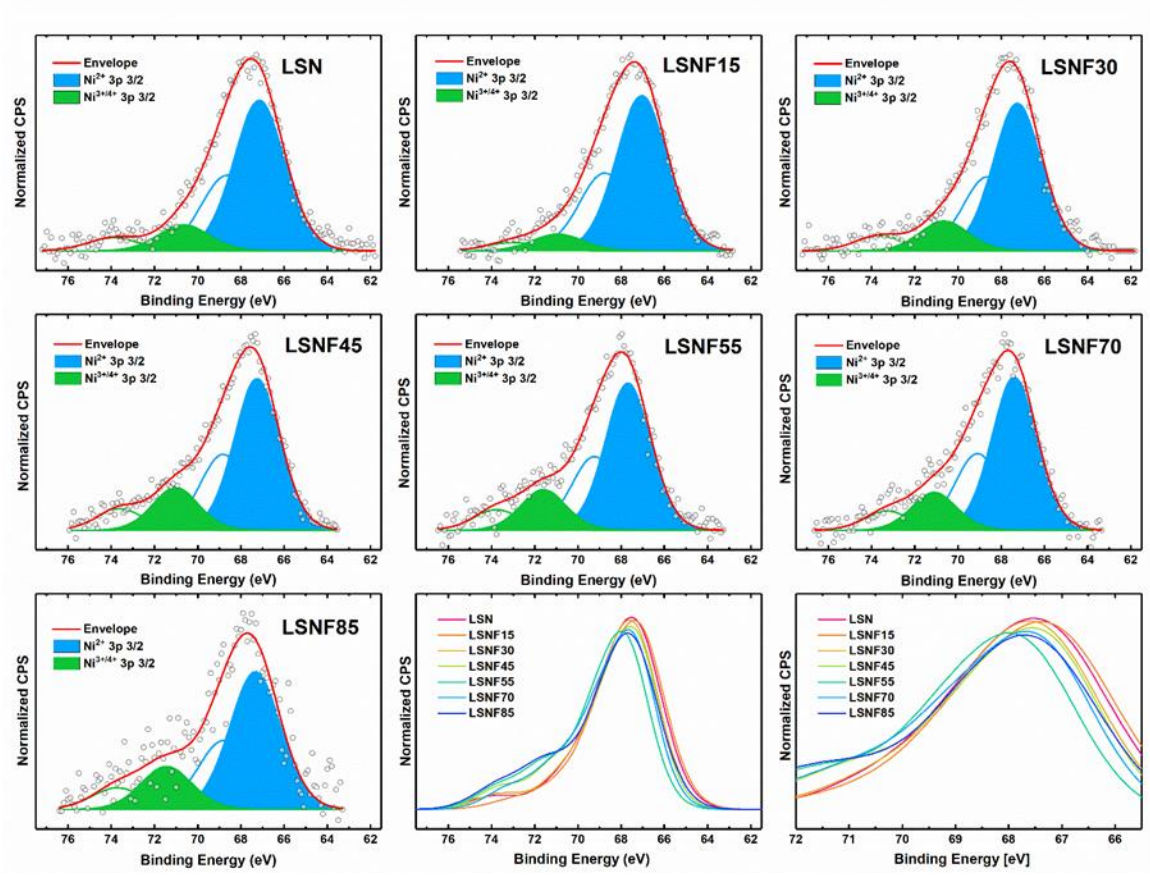

Figure A.20: XPS deconvolution of the Ni 3p spectra for the LSNF series.

Deconvolution was performed by adaptation of the methods developed by Burriel et. al for $La_{2-x}Sr_xNiO_4$.[24] The Ni 3*p* spectrum was decomposed into 4 distinct components; Ni^{2+} and $Ni^{3+/4+}$ in both the $3p_{3/2}$ and $3p_{1/2}$ portions of the Ni doublet. Deconvolution was achieved by fitting error minimization on the 30% Gaussian/Lorentzian components using the Marquardt and Simplex methods within CasaXPS. To ensure self-consistency all components used the same FWHM and components assigned to Ni $3p_{1/2}$ were constricted to have exactly half the area of their counterparts in the Ni $3p_{3/2}$. Binding energy constraints were the same used by Burriel et. al, and the maximum allowed FWHM was increased to account for the multiple chemical states encompassed by the $Ni^{3+/4+}$ components.

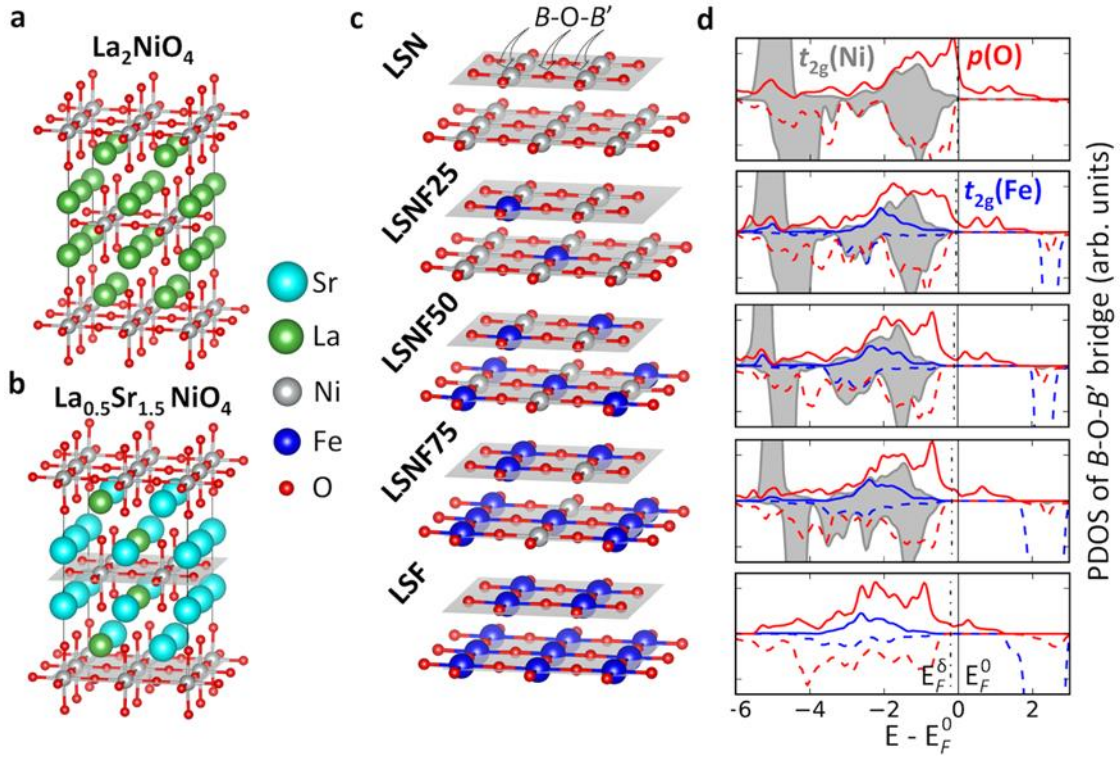

Figure A.21: DFT modeling of atomic and electronic structures of bulk LSNF.

(a) The optimized atomic structure of 2x2x1 La_2NiO_4, as the initial structure for Sr substitution and relaxation. (b) and (c) follow the same as those in Figure 2.5. (d) The projected density of states (PDOS) of t_{2g} (Ni and Fe) and 2*p* (O) with respect to Fermi level for the *B*-O-*B'* bridges; t_{2g} is shown not to come across Fermi level.

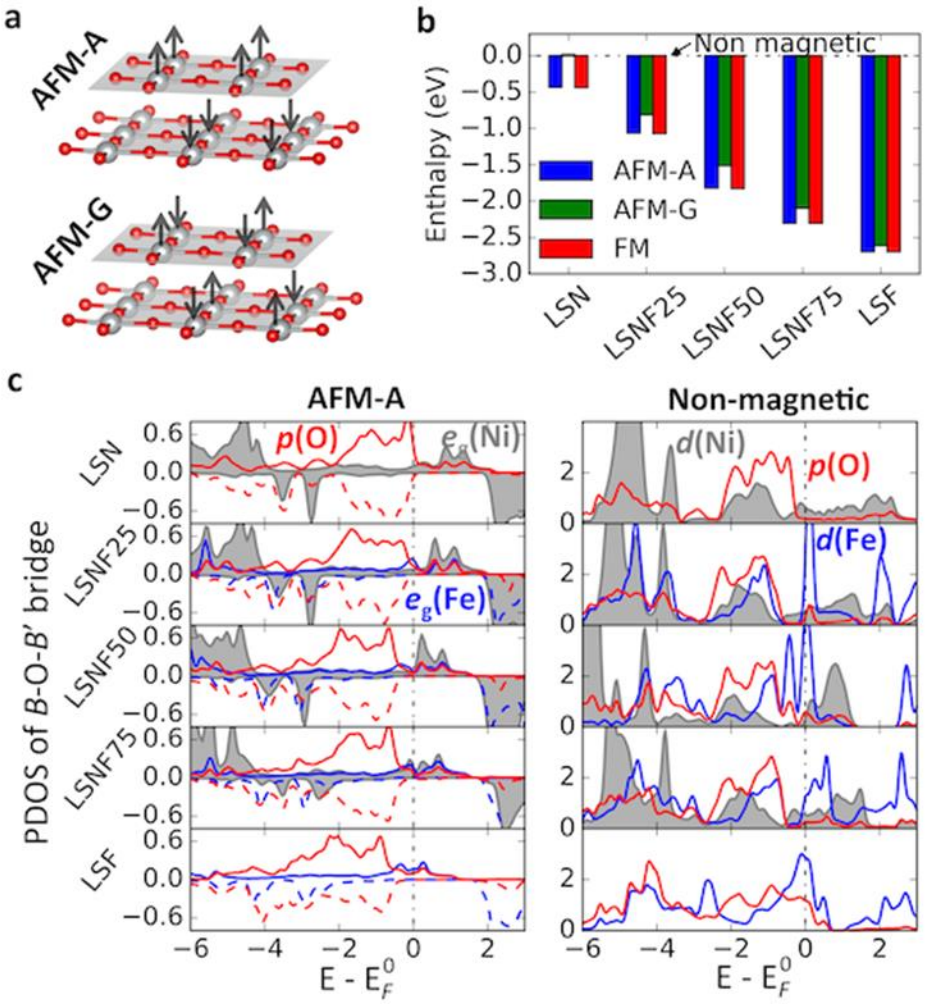

Figure A.22: Comparison of ferromagnetic, anti-ferromagnetic and non-magnetic structures from DFT modeling.

(a) The structures of A-type antiferromagnetic (AFM-A) and G-type antiferromagnetic (AFM-G) orderings. In AFM-A, spin directions only differ between neighborhood BO_2 layers, while in AFM-G, spin directions differ between neighborhood *B* atoms; AFM-C is identical to AFM-G in this atomic structure. (b) Comparison of energetics per unit $La_{0.5}Sr_{1.5}Ni_{1-x}Fe_xO_4$, relative to the corresponding non-magnetic energy in each composition. The energetic comparison clearly indicates FM and AFM-A as more stable configurations. (c) The projected density of states (PDOS) of the *B*-O-*B*' bridges for both AFM-A and non-magnetic structures. PDOS of AFM-A is shown to be similar to that of FM in Figure 2.5, while that of non-magnetic structure gives consistent trend of bands movement as described for Figure 2.5.

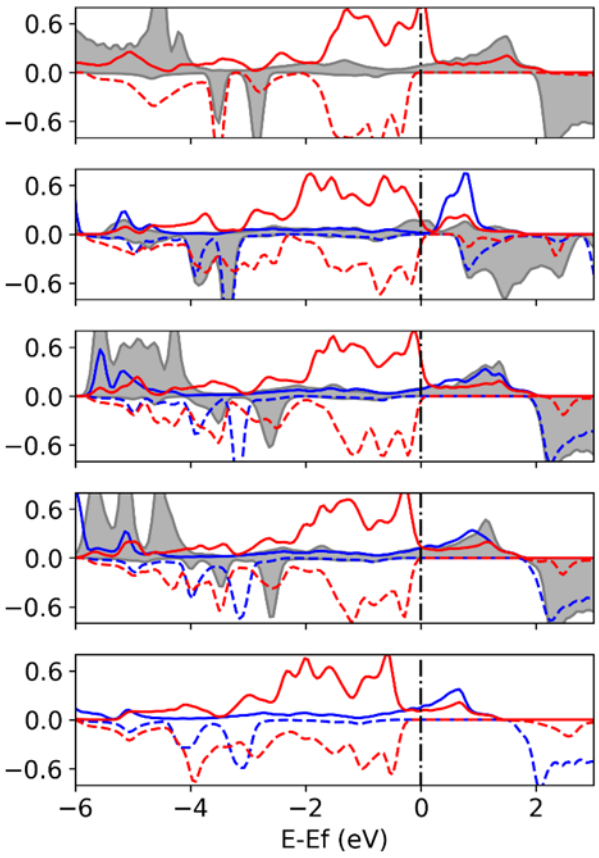

Figure A.23: DFT modeling of the electronic structures of bulk SNF.

The projected density of states (PDOS) of e_g (Ni and Fe) and 2*p* (O) with respect to Fermi level for the *B*-O-*B'* bridges closely resemble that for the LSNF series presented in Figure 2.5 of the main text with only a slight downward shift of the Fermi level with increased B-site oxidation states due to full Sr substitution.

A.3: Supplementary Tables

Sample	*a* [Å]	*c* [Å]	V [Å^3]	Refined composition	*z*/*c* (La,Sr)	*z*/*c* (O2)	*d*(M-O)$_{eq}$ [Å]	*d*(M-O)$_{ap}$ [Å]	R_F, R_p, R_{wP}
LSN	3.82437(2)	12.3331(1)	180.382(2)	$La_{0.518(6)}Sr_{1.482(6)}NiO_4$	0.35979(3)	0.1608(2)	1.91219(2)	1.984(2)	0.013, 0.010, 0.014
LSNF15	3.82806(2)	12.3673(1)	181.231(2)	$La_{0.496(6)}Sr_{1.504(6)}Ni_{0.85}Fe_{0.15}O_4$	0.35951(3)	0.1609(2)	1.91403(2)	1.990(2)	0.015, 0.011, 0.016
LSNF30	3.83130(2)	12.4085(1)	182.143(3)	$La_{0.518(6)}Sr_{1.482(6)}Ni_{0.70}Fe_{0.30}O_4$	0.35924(3)	0.1619(2)	1.91565(2)	2.009(2)	0.020, 0.012, 0.018
LSNF45	3.83506(2)	12.4629(1)	183.300(1)	$La_{0.534(6)}Sr_{1.466(6)}Ni_{0.55}Fe_{0.45}O_4$	0.35863(3)	0.1619(2)	1.91753(2)	2.017(3)	0.018, 0.012, 0.017
LSNF55	3.83724(2)	12.5018(2)	184.082(3)	$La_{0.500(6)}Sr_{1.500(6)}Ni_{0.45}Fe_{0.55}O_4$	0.35821(4)	0.1605(2)	1.91862(2)	2.007(3)	0.022, 0.013, 0.017
LSNF70	3.84143(2)	12.5581(2)	185.315(3)	$La_{0.524(8)}Sr_{1.476(8)}Ni_{0.30}Fe_{0.70}O_4$	0.35773(4)	0.1613(2)	1.92071(2)	2.026(3)	0.021, 0.012, 0.017
LSNF85	3.84533(2)	12.6232(2)	186.654(3)	$La_{0.524(6)}Sr_{1.476(6)}Ni_{0.15}Fe_{0.85}O_4$	0.35748(4)	0.1615(2)	1.92267(2)	2.039(3)	0.019, 0.013, 0.017
LSF	3.84789(3)	12.6919(2)	187.920(3)	$La_{0.536(6)}Sr_{1.464(6)}FeO_4$	0.35704(4)	0.1626(2)	1.92394(2)	2.064(3)	0.017, 0.013, 0.018

Table A.1: The results of Rietveld refinement for the LSNF series.

The refinement was performed in the *I*4/*mmm* space group with the atomic positions La,Sr 4*e* (0, 0, *z*), Ni,Fe 2*a* (0,0,0), O1 4*c* (0, ½, 0) and O2 4*e* (0, 0, *z*).

Catalyst	Support[A]	Surface Area [m^2/g]	Catalyst Loading [mg_{ox}/cm^2_{geo}]	η @ 10 mA/cm^2_{geo} [mV]	Specific Activity @ η = 400 mV [mA/cm^2_{ox}]	Mass Activity @ η = 400 mV [mA/mg_{ox}]	OER Tafel slope [mV/dec]	Testing Conditions	Ref.
$La_{0.5}Sr_{1.5}Ni_{0.7}Fe_{0.3}O_{4.04}$	VC	5.9	0.015	360	32.7	1930	44	0.1 M KOH, O_2 sat, 10 mV/s at 1600 rpm; iR corrected	This work
$SrCoO_{2.7}$	VC	3.6	0.015	419	9.4	332	67	0.1 M KOH, O_2 sat, 10 mV/s at 1600 rpm; iR corrected	This work
$LaNiO_3$	VC	11	0.015	582	0.4	41	99	0.1 M KOH, O_2 sat, 10 mV/s at 1600 rpm; iR corrected	This work
IrO_2	VC	14.5	0.010	468	1.2	175	88	0.1 M KOH, O_2 sat, 10 mV/s at 1600 rpm; iR corrected	This work
$SrSc_{0.025}Nb_{0.025}Co_{0.95}O_{3-\delta}$	C65	0.1	0.360	411	58	58	55-60	0.1 M KOH, O_2 sat, 10 mV/s at 1600 rpm; iR corrected	25
$BaNiO_3$ / $Ba_2Ni_2O_5$	VC	0.3	0.295	421	4.2 (9.1)[B]	13 (27)	--	0.1 M KOH, O_2 sat, 10 mV/s at 1600 rpm; iR corrected	26
$Pr_{0.5}Ba_{0.5}CoO_{3-\delta}$	AB	0.35	0.250	>381[C]	9.1[D]	31[E]	60	0.1 M KOH, O_2 sat, 10 mV/s at 1600 rpm; iR corrected	27
$CaCu_3Fe_4O_{12}$	AB	0.45	0.250	378	15.5	70	59 (44)[B]	0.1 M KOH, O_2 sat, 10 mV/s at 1600 rpm; iR corrected	28
$Ca_{1.75}Pr_{0.25}MnO_{4\pm\delta}$	AB	1.8	0.400	>471[C]	14.5E-3	0.26	86	0.1 M KOH, O_2 sat, 10 mV/s at 1600 rpm; iR corrected	29
$La_{1.2}Ca_{0.8}NiO_4$	C65	10.8	0.397	373	18.8	52.2	42	0.1 M KOH, O_2 sat, 10 mV/s at 1600[F] rpm; iR corrected	30
$La_{0.7}(Ba_{0.5}Sr_{0.5})_{0.3}Co_{0.8}Fe_{0.2}O_{3\pm\delta}$	KB	21.3	0.639	375	0.12	25	97	0.1 M KOH, O_2 sat, 10 mV/s at 1600 rpm; iR corrected	31
Ni-Fe LDH (Ni:Fe 45:55)	--	27	0.051[G]	311	~1.1[H]	~295[I]	37	0.1 M KOH, O_2 sat, 2 mV/s at 1600 rpm; iR corrected	32

Table A.2: Comparison of LSNF30 with other promising OER catalysts and accompanying notes.

[A] Supports: **VC** - Cabot XC-72 Vulcan Carbon; **C65** - TIMCAL Super C65; **AB** - Acetylene Black; **KB** - Ketjenblack EC-600JD

[B] Results in ( ) are after cycling

[C] Current density did not reach 10 mA/cm^2_{geo}, overpotential listed is maximum tested

[D] Potential only reported to 1.61 V, LSNF30's corresponding value is 19 mA/cm^2_{ox}

[E] Potential only reported to 1.61 V, LSNF30's corresponding value is 1100 mA/mg_{ox}

[F] Electrodes rotation rate not reported

[G] Mass was determined only by metal weight, neglecting O(H) contributions. Calculated mass and specific activities will be larger than truly measured.

[H] Current density only reported to ~1.55 V, LSNF30's corresponding value is 2.0 mA/cm^2_{ox}

[I] Current density only reported to ~1.55 V, LSNF30's corresponding value is 115 mA/mg_{ox}

Sample	Surface Area [m^2/g]	Ni^{AVG+}	Oxygen Excess [δ]	E_P $Ni^{2+/3+}$ oxidation [V]	Electrochemical Oxygen Diffusion Rate [cm^2/s]	Specific Activity @ 1.63 V [mA/cm^2_{ox}]	Mass Activity @ 1.63 V [mA/mg_{ox}]
LSN	8.0	3.54 ± 0.03	0.018 ± 0.013	1.385	8.0E-13 ± 1.7E-13	1.1 ± 0.0	87.7 ± 1.2
LSNF15	6.8	3.57 ± 0.02	0.046 ± 0.007	1.454	1.0E-12 ± 1.7E-13	10.6 ± 0.8	717.8 ± 54.6
LSNF30	5.9	3.57 ± 0.03	0.042 ± 0.010	1.470	1.7E-12 ± 6.0E-13	32.7 ± 2.8	1930.8 ± 164.0
LSNF45	5.4	3.68 ± 0.10	0.065 ± 0.027	1.494	2.2E-12 ± 8.2E-13	27.4 ± 0.8	1480.7 ± 45.7
LSNF55	6.2	3.80 ± 0.05	0.088 ± 0.011	1.505	3.5E-13 ± 3.2E-13	18.4 ± 0.6	1143.7 ± 40.2
LSNF70	4.9	3.82 ± 0.14	0.076 ± 0.022	1.511	5.6E-14 ± 6.0E-14	17.7 ± 1.7	868.4 ± 85.1
LSNF85	5.6	3.95 ± 0.48	0.081 ± 0.036	1.524	3.0E-13 ± 3.0E-13	2.3 ± 0.2	128.8 ± 12.3
LSF	3.3	--	0.143 ± 0.037	--	--	0.3 ± 0.1	10.4 ± 3.9

Table A.3: Summary of the physical, chemical and electrochemical properties of the LSNF series.

Surface area was determined by multipoint BET measurements. Average Ni oxidation state was determined by a combination of iodometric titrations and deconvolution of room temperature Mössbauer spectroscopy. Oxygen excess was determined by iodometric titrations. Peak potential for $Ni^{2+/3+}$ oxidation was determined from CVs taken at 10 mV s^{-1} and after iR correction applied. Oxygen diffusion rates were determined electrochemically as outlined in section 2.2.2 of the main text.

Sample	Comp.	IS, mm/s ± 0.02	ΔE_Q, mm/s ± 0.02	I, % ± 2	Γ, mm/s ± 0.02	Comments
LSNF15	D11	0.03	0.15	73	0.30	Fe4+
	D12	0.31	0.14	27	0.47	Fe3+
LSNF30	D21	0.03	0.14	62	0.30	Fe4+
	D22	0.32	0.16	38	0.45	Fe3+
LSNF45	D31	0.03	0.14	57	0.30	Fe4+
	D32	0.35	0.17	43	0.45	Fe3+
LSNF55	D41	0.03	0.14	58	0.34	Fe4+
	D42	0.39	0.17	42	0.47	Fe3+
LSNF70	D51	0.03	0.15	58	0.35	Fe4+
	D52	0.43	0.20	42	0.44	Fe3+
LSNF85	D61	0.03	0.16	61	0.36	Fe4+
	D62	0.45	0.19	39	0.44	Fe3+
LSF	D71	0.03	0.16	62	0.36	Fe4+
	D72	0.45	0.18	38	0.41	Fe3+

Table A.4: 298K temperature ^{57}Fe Mossbauer hyperfine parameters for the LSNF series.

IS, isomer shift relative to α-Fe at ambient temperature; ΔE_Q, apparent quadrupole shift; Γ, line width; I, relative spectral area.

Sample	Comp.	IS, mm/s ± 0.02	ΔE_Q, mm/s ± 0.02	I, % ± 2	Γ, mm/s ± 0.02	Comments
LSNF30	D13	0.11	0.15	57	0.31	Fe4+
	D14	0.44	0.17	43	0.49	Fe3+
LSNF45	D13	0.10	0.16	58	0.34	Fe4+
	D14	0.50	0.18	42	0.48	Fe3+

Table A.5: The 78K temperature ^{57}Fe Mossbauer hyperfine parameters for LSNF30 and LSNF45 of the LSNF series.

IS, isomer shift relative to α-Fe at ambient temperature; ΔE_Q, apparent quadrupole shift; Γ, line width; I, relative spectral area.

Sample	ΔE_{V_O} (eV)
LSN	-0.46
LSNF25	-0.28
LSNF50	-0.04
LSNF75	0.28
LSF	0.75

Table A.6: Computed oxygen vacancy formation for modeled LSNF compositions.

Vacancy formation energies for modeled LSNF compositions were calculated at Fe-O-Ni bridges, relative to that for pseudo-cubic $LaNiO_3$. $LaNiO_3$ is computed to have more negative O_{vac} formation energy than $La_{0.5}Sr_{0.5}CoO_{3-\delta}$.

A.4: References

1. Benloucif, R., Nguyen, N., Greneche, J. M. & Raveau, B. $La_{2-2x}Sr_{2x}Ni_{1-x}Fe_xO_{4-(x2)+\delta}$: Magnetic and electron transport properties. *J. Phys. Chem. Solids* 50, 435–440 (1989).

2. Gilev, A. R., Kiselev, E. A. & Cherepanov, V. A. Homogeneity range, oxygen nonstoichiometry, thermal expansion and transport properties of $La_{2-x}Sr_xNi_{1-y}FeyO_{4+\delta}$. *RSC Adv.* 6, 72905–72917 (2016).

3. Medarde, M. & Rodríguez-Carvajal, J. Oxygen vacancy ordering in $La_{2-x}Sr_xNiO_{4-\delta}$ ($0 \leq \leq 0.5$): the crystal structure and defects investigated by neutron diffraction. *Z. Phys. B* 102, 307–315 (1997).

4. Millburn, J. E., Green, M. A., Neumann, D. A. & Rosseinsky, M. J. Evolution of the Structure of the K_2NiF_4 Phases $La_{2-x}Sr_xNiO_{4+\delta}$ with Oxidation State: Octahedral Distortion and Phase Separation ($0.2 \leq x \leq 1.0$). *Journal of Solid State Chemistry* 145, 401–420 (1999).

5. Aguadero, A. *et al.* Effect of Sr content on the crystal structure and electrical properties of the system $La_{2-x}Sr_xNiO_{4+\delta}$ ($0 \leq x \leq 1$). *Dalton Trans.* 4377–4383 (2006).

6. Takeda, Y. *et al.* Crystal chemistry and physical properties of $La_{2-x}Sr_xNiO_4$ ($0 \leq x \leq 1.6$). *Mater. Res. Bull.* 25, 293–306 (1990).

7. Inprasit, T., Wongkasemjit, S., Skinner, S. J., Burriel, M. & Limthongkul, P. Effect of Sr substituted $La_{2-x}Sr_xNiO_{4+\delta}$ (x = 0, 0.2, 0.4, 0.6, and 0.8) on oxygen stoichiometry and oxygen transport properties. *RSC Adv.* 5, 2486–2492 (2014).

8. Manthiram, A., Tang, J. P. & Manivannan, V. Factors Influencing the Stabilization of Ni+ in Perovskite-Related Oxides. *Journal of Solid State Chemistry* 148, 499–507 (1999).

9. Fontaine, M.-L., Laberty-Robert, C., Ansart, F. & Tailhades, P. Elaboration and characterization of $La_2NiO_{4+\delta}$ powders and thin films via a modified sol–gel process. *Journal of Solid State Chemistry* 177, 1471–1479 (2004).

10. Sharma, I. B. & Singh, D. Solid state chemistry of Ruddlesden-Popper type complex oxides. *Bull. Mater. Sci.* 21, 363–374 (1998).

11. Mogni, L. *et al.* Synthesis, crystal chemistry and physical properties of the Ruddlesden–Popper phases $Sr_3Fe_{2-x}Ni_xO_{7-\delta}$ ($0 \leqslant x \leqslant 1.0$). *J. Solid State Chem.* 178, 1559–1568 (2005).

12. Song, K.-W. & Lee, K.-T. Characterization of $NdSrCo_{1-x}Fe_xO_{4+\delta}$ ($0 \leq x \leq 1.0$) intergrowth oxide cathode materials for intermediate temperature solid oxide fuel cells. *Ceramics International* 37, 573–577 (2011).

13. Anisimov, V. I., Aryasetiawan, F. & Lichtenstein, A. I. First-principles calculations of the electronic structure and spectra of strongly correlated systems: the LDA + U method. *J. Phys.: Condens. Matter* 9, 767 (1997).

14. Gou, G., Grinberg, I., Rappe, A. M. & Rondinelli, J. M. Lattice normal modes and electronic properties of the correlated metal $LaNiO_3$. *Phys. Rev. B* 84, 144101 (2011).

15. Lee, Y.-L., Kleis, J., Rossmeisl, J. & Morgan, D. Ab initio energetics of $LaBO_3$ (001) (B = Mn, Fe, Co, and Ni) for solid oxide fuel cell cathodes. *Phys. Rev. B* 80, 224101 (2009).

16. Shein, I. R., Shein, K. I., Kozhevnikov, V. L. & Ivanovskii, A. L. Band structure and the magnetic and elastic properties of $SrFeO_3$ and $LaFeO_3$ perovskites. *Phys. Solid State* 47, 2082–2088 (2005).

17. Ritzmann, A. M., Muñoz-García, A. B., Pavone, M., Keith, J. A. & Carter, E. A. Ab Initio DFT+U Analysis of Oxygen Vacancy Formation and Migration in $La_{1-x}Sr_xFeO_{3-\delta}$ (x = 0, 0.25, 0.50). *Chem. Mater.* 25, 3011–3019 (2013).

18. Muñoz-García, A. B. *et al.* Unveiling Structure–Property Relationships in $Sr_2Fe_{1.5}Mo_{0.5}O_{6-\delta}$, an Electrode Material for Symmetric Solid Oxide Fuel Cells. *J. Am. Chem. Soc.* 134, 6826–6833 (2012).

19. Malashevich, A. & Ismail-Beigi, S. First-principles study of oxygen-deficient $LaNiO_3$ structures. *Phys. Rev. B* 92, 144102 (2015).

20. Menil, F. Systematic trends of the ^{57}Fe Mössbauer isomer shifts in (FeO_n) and (FeFn) polyhedra. Evidence of a new correlation between the isomer shift and the inductive effect of the competing bond T-X (→ Fe) (where X is O or F and T any element with a formal positive charge). *Journal of Physics and Chemistry of Solids* 46, 763–789 (1985).

21. Takeda, Y., Imayoshi, K., Imanishi, N., Yamamoto, O. & Takano, M. Preparation and characterization of $Sr_{2-x}La_xFeO_4 (0 \leqslant x \leqslant 1)$. *J. Mater. Chem.* 4, 19–22 (1994).

22. Dann, S. E., Weller, M. T., Currie, D. B., Thomas, M. F. & Al-Rawwas, A. D. Structure and magnetic properties of Sr_2FeO_4 and $Sr_3Fe_2O_7$ studied by powder neutron diffraction and Mössbauer spectroscopy. *J. Mater. Chem.* 3, 1231–1237 (1993).

23. Hinatsu, Y., Tezuka, K., Inamura, M. & Masaki, N. M. Magnetic Susceptibilities and Mössbauer Spectra of $Sr_{2-x}La_xFeO_{4-\delta}$ ($0 \leq x \leq 0.5$). *Journal of Solid State Chemistry* 146, 253–257 (1999).

24. Burriel, M. *et al.* Absence of Ni on the outer surface of Sr doped La_2NiO_4 single crystals. *Energy Environ. Sci.* 7, 311–316 (2013).

25. Zhu, Y. *et al.* $SrNb_{0.1}Co_{0.7}Fe_{0.2}O_{3-\delta}$ Perovskite as a Next-Generation Electrocatalyst for Oxygen Evolution in Alkaline Solution. *Angew. Chem.* 127, 3969–3973 (2015).

26. Lee, J. G. *et al.* A New Family of Perovskite Catalysts for Oxygen-Evolution Reaction in Alkaline Media: $BaNiO_3$ and $BaNi_{0.83}O_{2.5}$. *J. Am. Chem. Soc.* 138, 3541–3547 (2016).

27. Grimaud, A. *et al.* Double perovskites as a family of highly active catalysts for oxygen evolution in alkaline solution. *Nat. Commun.* 4, ncomms3439 (2013).

28. Yamada, I., Murakami, M., Hayashi, N. & Mori, S. Inverse Charge Transfer in the Quadruple Perovskite $CaCu_3Fe_4O_{12}$. *Inorg. Chem.* 55, 1715–1719 (2016).

29. Ebrahimizadeh Abrishami, M. *et al.* Oxygen Evolution at Manganite Perovskite Ruddlesden-Popper Type Particles: Trends of Activity on Structure, Valence and Covalence. *Materials* 9, 921 (2016).

30. Jung, K.-N. *et al.* Doped Lanthanum Nickelates with a Layered Perovskite Structure as Bifunctional Cathode Catalysts for Rechargeable Metal–Air Batteries. *ACS Appl. Mater. Interfaces* 5, 9902–9907 (2013).

31. Jung, J.-I. *et al.* Optimizing nanoparticle perovskite for bifunctional oxygen electrocatalysis. *Energy Environ. Sci.* 9, 176–183 (2016).

32. Louie, M. W. & Bell, A. T. An Investigation of Thin-Film Ni–Fe Oxide Catalysts for the Electrochemical Evolution of Oxygen. *J. Am. Chem. Soc.* 135, 12329–12337 (2013).

APPENDIX B: THE ELECTROOXIDATION OF UREA ON $LaNiO_3$ PEROVSKITE OXIDE

B.1: Supplementary Figures

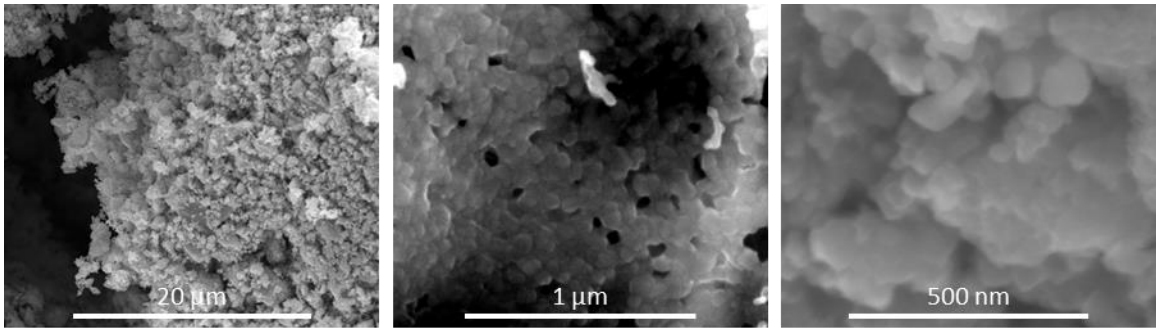

Figure B.1: SEM micrographs of $LaNiO_3$ particles.

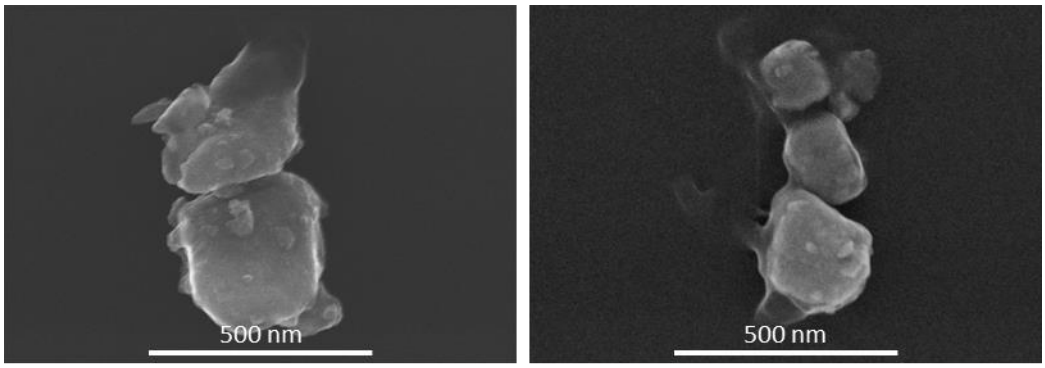

Figure B.2: SEM micrographs of NiO particles.

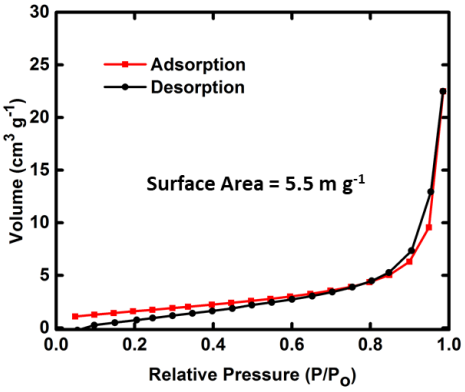

Figure B.3: BET adsorption of desorption curves for unsupported $LaNiO_3$ used to calculate surface area.

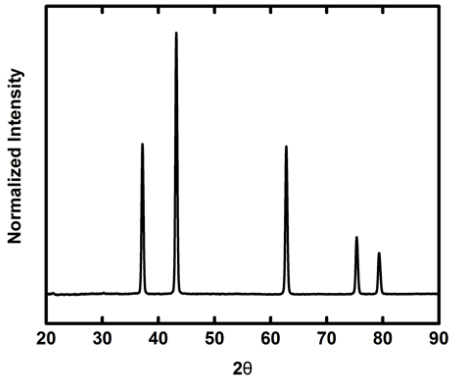

Figure B.4: XRD pattern of NiO catalyst material.

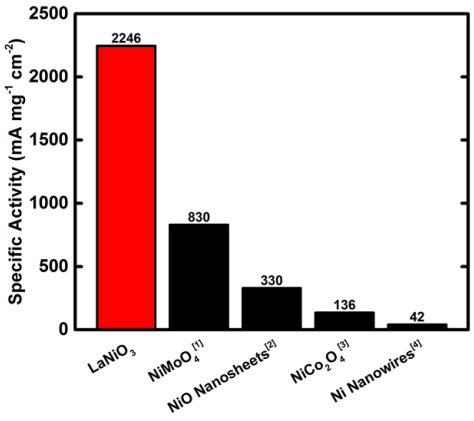

Figure B.5: Specific Activities for previously reported materials toward urea electrooxidation.

All materials tested in 1 M KOH, 0.33 M urea at a scan rate of 10 mV s^{-1} with stationary electrodes.[25–28] Specific activities were obtained by normalized all currents by the mass of perovskite.

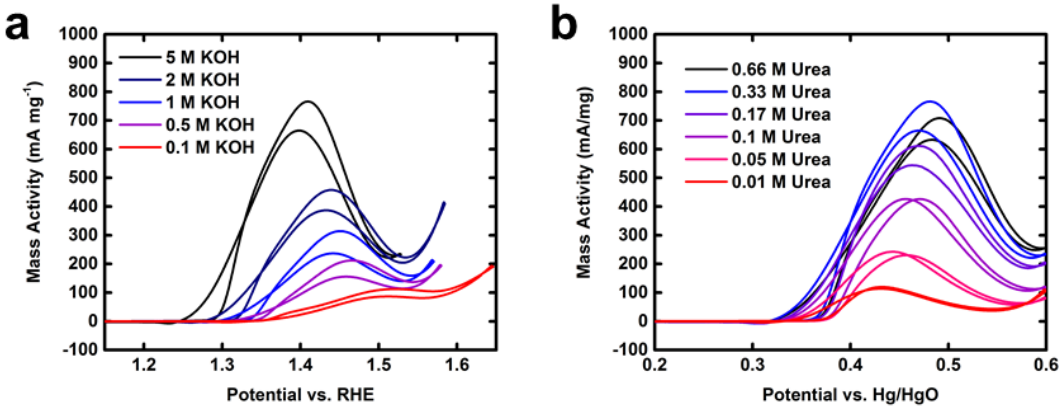

Figure B.6: Dependence of urea oxidation activities on KOH and urea concentrations.

(a) CVs of supported $LaNiO_3$ for urea oxidation as the concentration of KOH was varied in the presence of 0.33 M urea. (b) CVs of supported $LaNiO_3$ for urea oxidation as the concentration of urea was varied in 5 M KOH electrolyte. In (a) potentials have been adjusted to RHE to remove the influence of Nernstian potential shifts of the reference electrode in electrolytes with varying pH. The RHE potential was defined as E_{RHE} = [E vs. $E_{Hg/HgO\ (1M\ KOH)}$] + $E^0_{Hg/HgO}$ + 0.059 x pH; $E_{Hg/HgO}$ was measured as +0.102V vs. SHE. All currents in both (a) and (b) were normalized by the mass of perovskite, in mg, drop cast on the electrode to obtain mass activities.

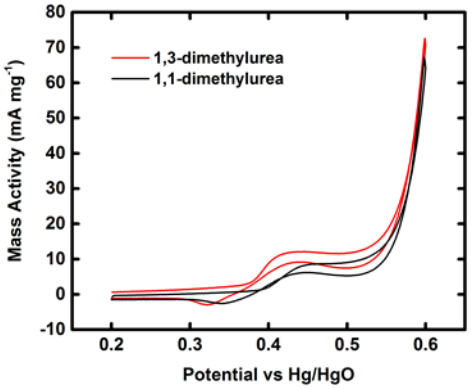

Figure B.7: Cyclic voltammogram of 0.33 M 1,3-dimethylurea and a saturated electrolyte of 1,1-dimethylurea.

CVs of dimethylurea in 5 M KOH at a sweep rate of 10 mV s^{-1} showing negligible electrooxidation of either urea variant (for comparison the oxidation of urea at a concentration of 0.33M in 5M KOH generates a peak current density of 747 mA mg^{-1}, ~75x larger current that the urea variants). All currents were normalized by the mass of perovskite drop cast on the electrode to obtain mass activities.

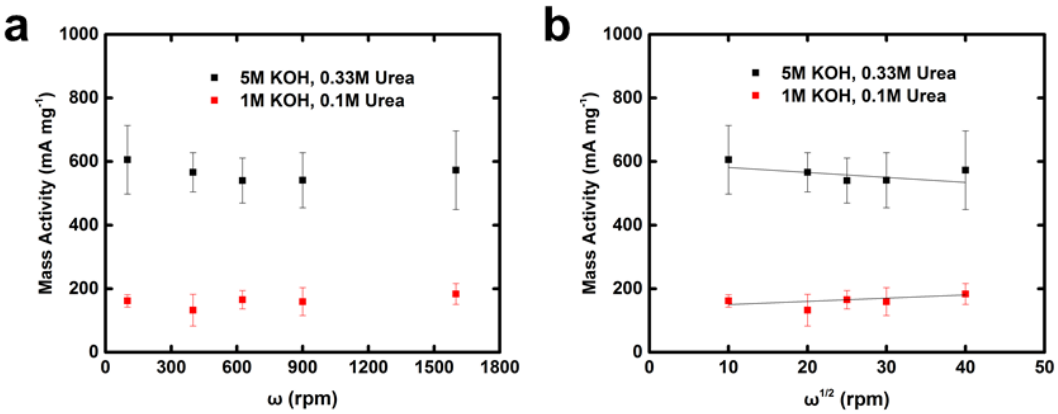

Figure B.8: Rotation rate dependence of urea oxidation activities on $LaNiO_3$.

$LaNiO_3$ mass activity measured in 5 M KOH, 0.33 M urea versus the rotation rate (a) and square root of the rotation rate (b). Correlation coefficients for linear fits to the data in (b) are $R^2 = 0.264$ and $R^2 = 0.314$ for the 5 M KOH, 0.33 M urea and 1 M KOH, 0.1 M urea, respectively. Error bars represent standard deviations of triplicate measurements. All currents were normalized by the mass of perovskite drop cast on the electrode to obtain mass activities.

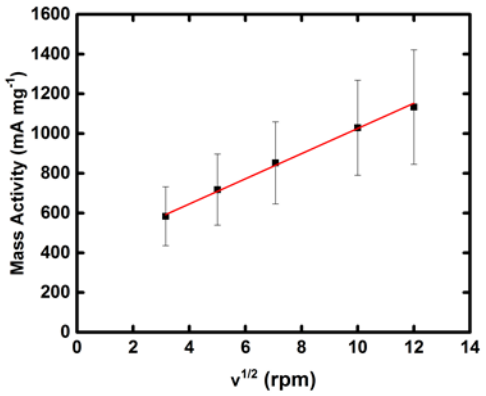

Figure B.9: Scan rate dependence of urea oxidation activities on $LaNiO_3$.

Plot of catalyst mass activity versus the square root of the sweep rate showing a linear dependence of peak current with the square root of sweep rate. Performed in 5 M KOH and 0.33 M urea. The correlation coefficient for the linear trend line is $R^2 = 0.971$. Error bars represent standard deviations of triplicate measurements. All currents were normalized by the mass of perovskite drop cast on the electrode to obtain mass activities.

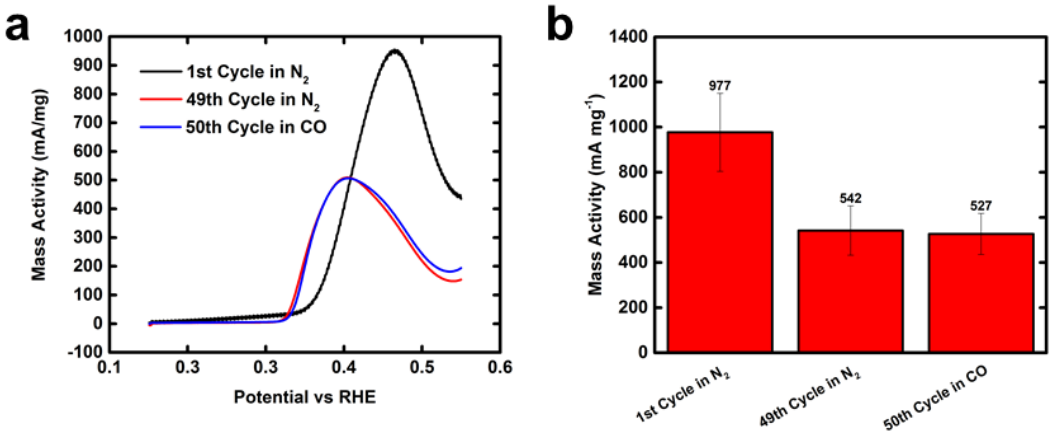

Figure B.10: Effect of repeated cycling and CO on the electrooxidation of urea by $LaNiO_3$.

(a) Representative CVs performed in 5 M KOH, 0.33 M urea electrolyte of electrodes drop cast with $LaNiO_3$ supported on Vulcan carbon for the first, 49th, and 50th cycles of a 50 cycle test in which the first 49 cycles were performed in N_2-saturated electrolyte and the 50th cycle was performed in CO saturated electrolyte. (b) Peak mass activities of the CVs represented in (a). All currents were normalized by the mass of perovskite drop cast on the electrode to obtain mass activities. Error bars represent standard deviations of triplicate measurements.

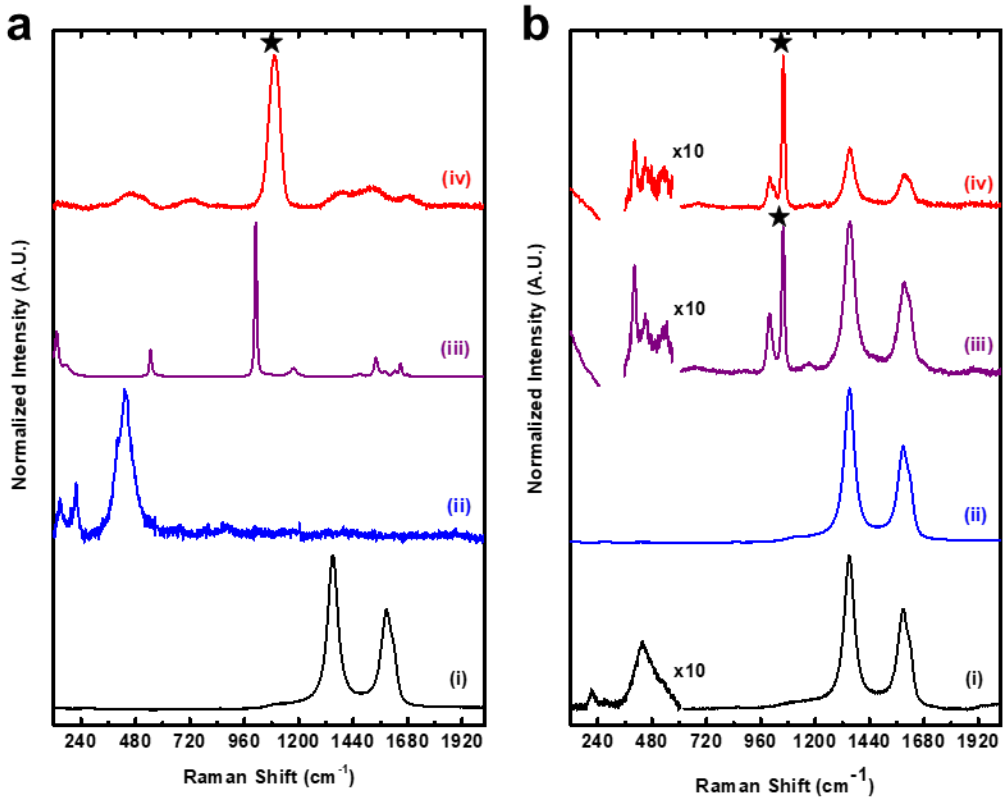

Figure B.11: Ex-situ raman spectroscopy of $LaNiO_3$ at various points during urea oxidation testing.

(a) Raman spectra of neat samples (i) Glassy Carbon Electrode, (ii) $LaNiO_3$, (iii) Urea, (iv) $NiCO_3$. (b) Raman spectra of cycled samples (i) $LaNiO_3$ dropcast on GCE but not exposed to electrolyte or cycled, (ii) GCE cycled 50x in N_2 saturated 5M KOH, (iii) $LaNiO_3$/GCE cycled 50x in N_2 saturated 5M KOH, (iv) $LaNiO_3$/GCE cycled 50x in CO_2 saturated 5M KOH. The peak corresponding to the symmetric CO_3^{2-} stretching is labeled in both (a) and (b) with a (⋆).

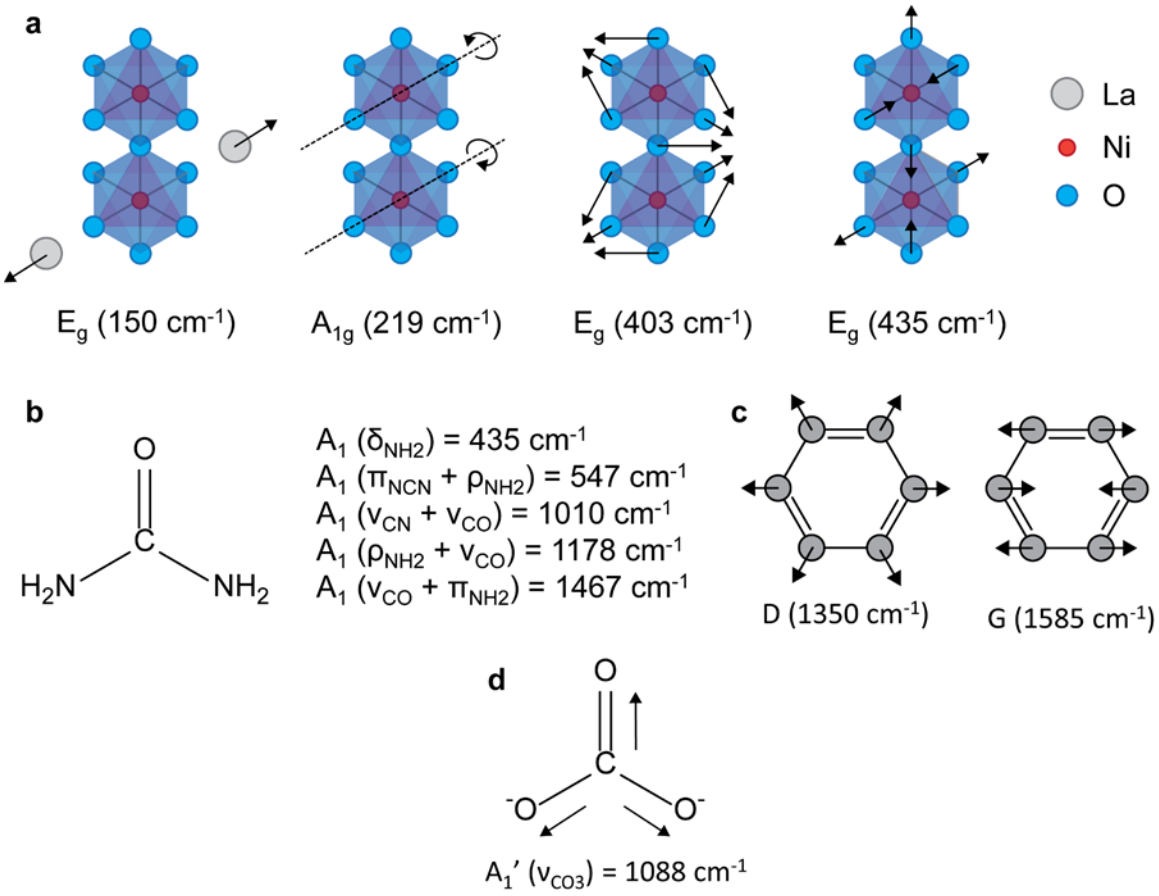

Figure B.12: Select Raman modes for relevant species involved in the electrooxidation of urea. Select Raman modes for (a) $LaNiO_3$, (b) Urea, (c) Carbon, and (d) CO_3^{2-}. δ = in-plane bending, ν = symmetric stretching, π = scissoring, ρ = rocking.[14,29–31]

B.2: References

1. Liang, Y., Liu, Q., Asiri, A. M. & Sun, X. Enhanced electrooxidation of urea using $NiMoO_4$·xH2O nanosheet arrays on Ni foam as anode. *Electrochimica Acta* **153**, 456–460 (2015).

2. Wu, M.-S., Lin, G.-W. & Yang, R.-S. Hydrothermal growth of vertically-aligned ordered mesoporous nickel oxide nanosheets on three-dimensional nickel framework for

electrocatalytic oxidation of urea in alkaline medium. *Journal of Power Sources* **272**, 711–718 (2014).

3. Ding, R., Qi, L., Jia, M. & Wang, H. Facile synthesis of mesoporous spinel $NiCo_2O_4$ nanostructures as highly efficient electrocatalysts for urea electro-oxidation. *Nanoscale* **6**, 1369–1376 (2014).

4. Yan, W., Wang, D., Diaz, L. A. & Botte, G. G. Nickel nanowires as effective catalysts for urea electro-oxidation. *Electrochimica Acta* **134**, 266–271 (2014).

5. Ferrari, A. C. & Basko, D. M. Raman spectroscopy as a versatile tool for studying the properties of graphene. *Nat Nano* **8**, 235–246 (2013).

6. Frost, R. L., Dickfos, M. J. & Jagannadha Reddy, B. Raman spectroscopy of hydroxy nickel carbonate minerals nullaginite and zaratite. *J. Raman Spectrosc.* **39**, 1250–1256 (2008).

7. Gou, G., Grinberg, I., Rappe, A. M. & Rondinelli, J. M. Lattice normal modes and electronic properties of the correlated metal $LaNiO_3$. *Phys. Rev. B* **84**, 144101 (2011).

8. Hermet, P. & Ghosez, P. First-principles study of the dynamical and nonlinear optical properties of urea single crystals. *Phys. Chem. Chem. Phys.* **12**, 835–843 (2010).

APPENDIX C: TUNING RUDDLESDEN-POPPER OXIDE CATALYSTS FOR THE ELECTROCHEMICAL OXIDATIONS OF UREA AND SMALL ALCOHOLS

C.1: Supplementary Figures

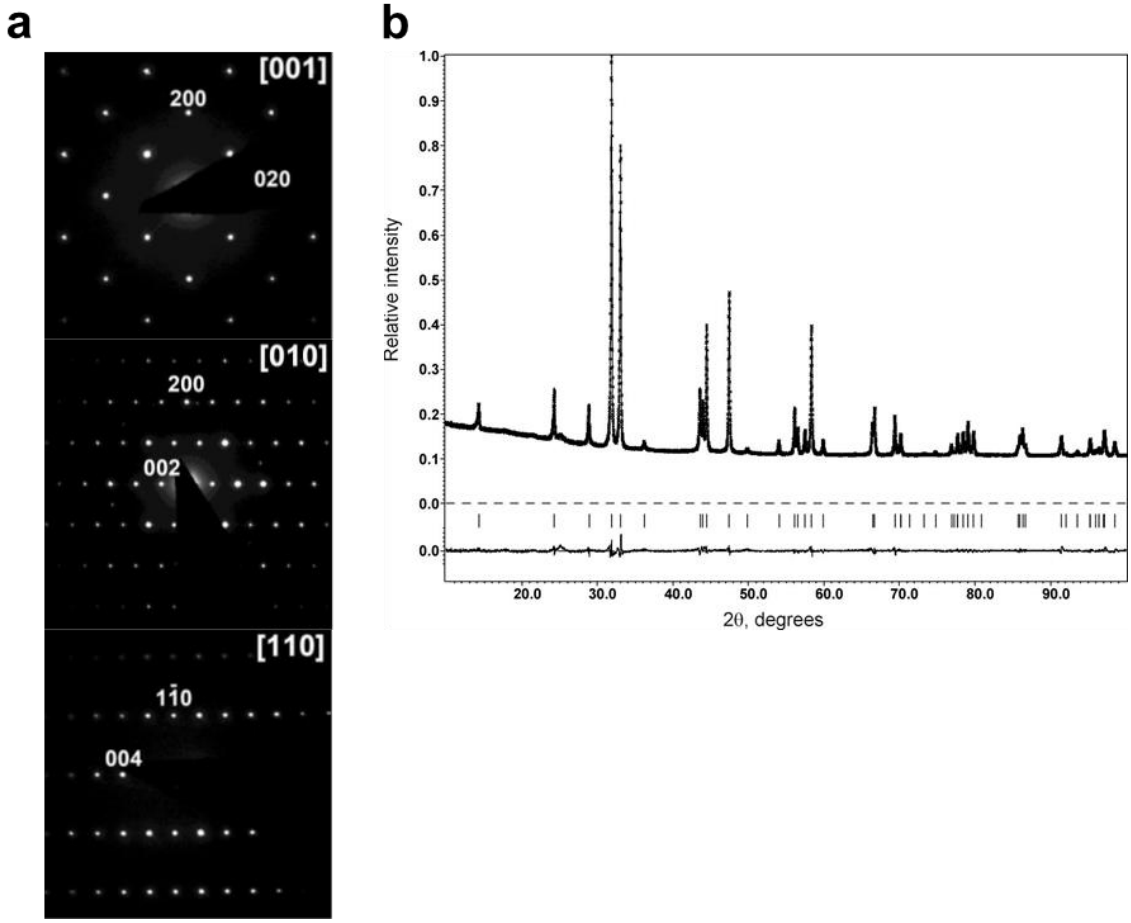

Figure C.1: Crystallographic characterization of LSN25.

(a) Electron diffraction patterns of the LSN phase indexed on a body-centered tetragonal unit cell with $a \approx 3.8$Å, $c \approx 12.4$Å. (b) Experimental, calculated and difference XRPD patterns of $La_{0.5}Sr_{1.5}NiO_4$ after the Rietveld refinement.

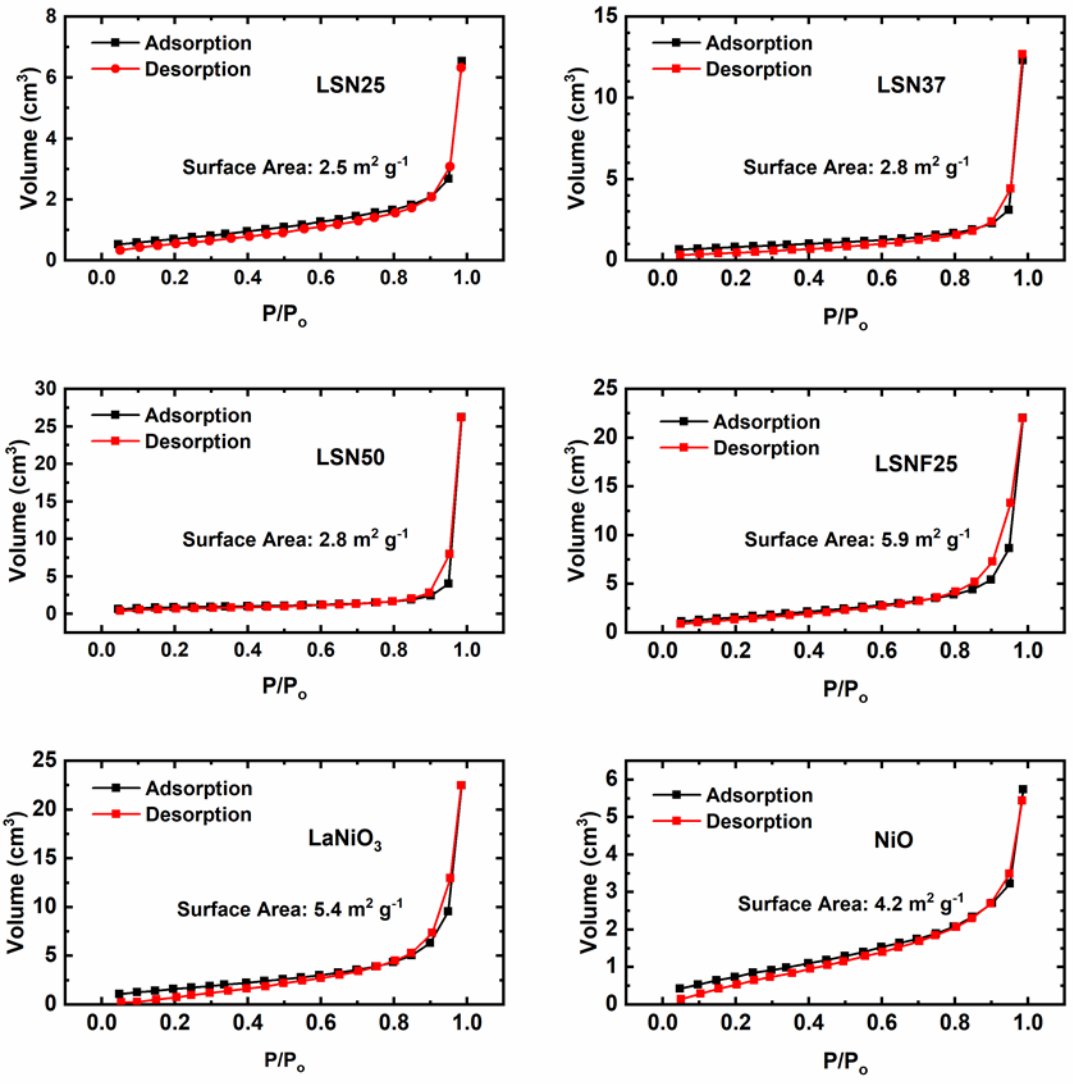

Figure C.2: Nitrogen sorption isotherms (BET).

Samples in the LSN series range in surface area from 2.5 to 2.8 m^2 g^{-1}. All samples underwent the same thermal treatments for mixed metal oxide precursor particle synthesis as well as crystallization and annealing.

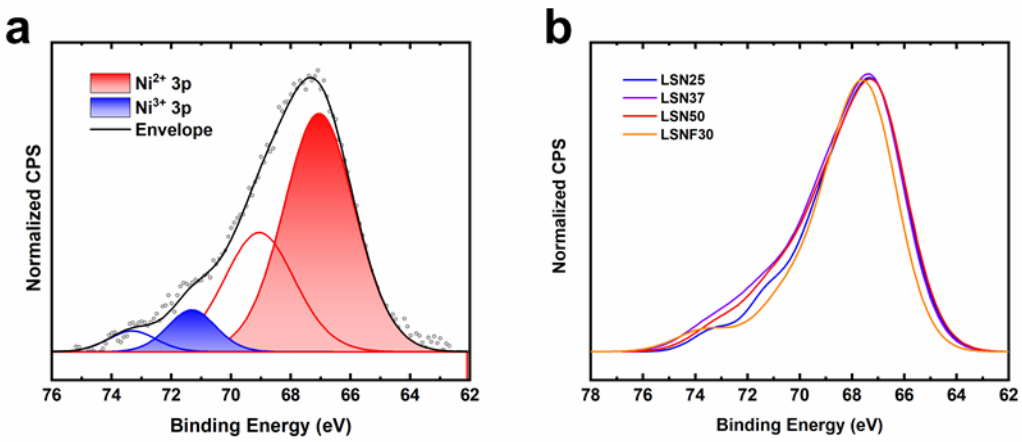

Figure C.3: XPS of the LSN series.

(a) Deconvolution of the Ni 3p spectra for $La_{0.5}Sr_{1.5}NiO_4$, performed by adaptation of the methods developed by Qiao et. al for $LaNiO_{3-\delta}$.[1] The Ni 3*p* spectrum was decomposed into 4 distinct components; Ni^{2+} and $Ni^{3+/4+}$ in both the $3p_{3/2}$ and $3p_{1/2}$ components of the Ni doublet. Deconvolution was achieved by fitting error minimization on the 30% Gaussian/Lorentzian components using the Marquardt methods within CasaXPS. To ensure self-consistency, both components for the same oxidation state were fixed to have the same FWHM and the components assigned to Ni $3p_{1/2}$ were constricted to have exactly half the area of their counterparts in the Ni $3p_{3/2}$. (b) Comparison of the LSN series with LSNF25 showing a shift to higher binding energies for LSNF25.

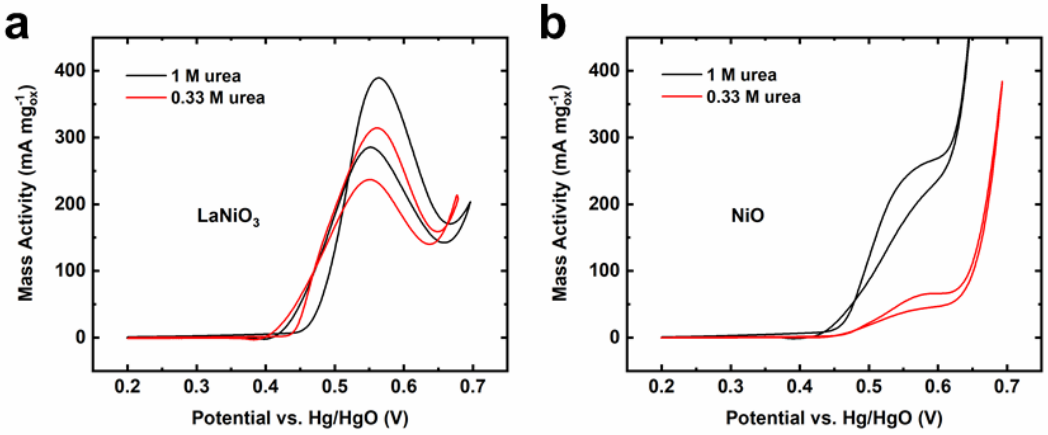

Figure C.4: UOR activities for $LaNiO_3$ and NiO.

Materials were supported at 30 wt% on Vulcan carbon. Representative CVs performed on (a) $LaNiO_3$ and (b) NiO in Ar-saturated 1 M KOH containing either 1 M or 0.33 M urea. All activities were measured at 0.6 V vs. Hg/HgO (1 M KOH) on the anodic scan and all measurements were performed in triplicate on fresh electrodes.

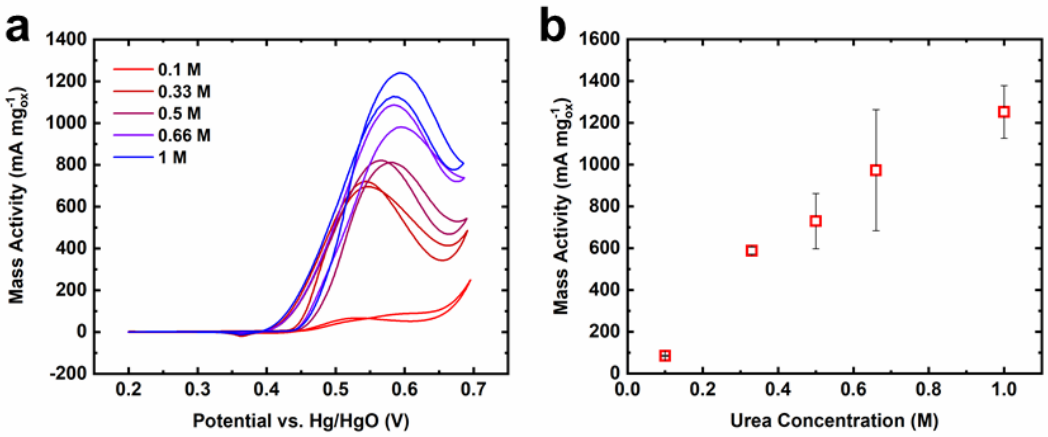

Figure C.5: Dependence of UOR activities on urea concentration for the LSN series.

(a) CVs performed on LSN25 in Ar-saturated 1 M KOH at various concentrations of urea. (b) Activities of LSN25 towards the electrooxidation of urea in 1 M KOH at various concentrations of urea. All activities were measured at 0.6 V vs. Hg/HgO on the anodic scan and all measurements were performed in triplicate on fresh electrodes.

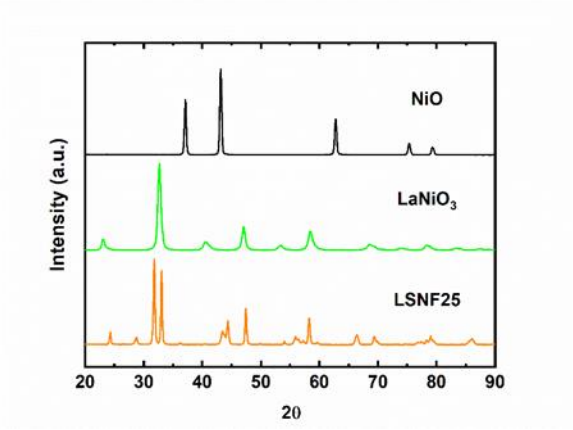

Figure C.6: PXRD patterns for NiO, $LaNiO_3$, and LSNF25.

Diffraction patterns indicate phase-purity for all three samples.

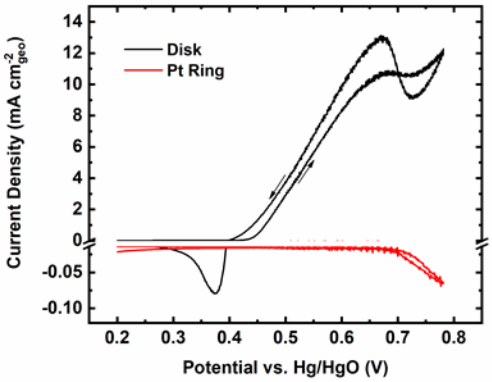

Figure C.7: Rotating ring disk electrode experiments for the UOR.

The urea electrooxidation activity of LSN25 supported at 30 wt% on Vulcan carbon. Measurements were performed in Ar-saturated 1 M KOH containing 1 M urea with a total mass loading of 25.6 μg_{total} cm^{-2}_{geo}, half that for all other activity measurements to reduce bubble formation that may interfere with the current measurement at the ring.

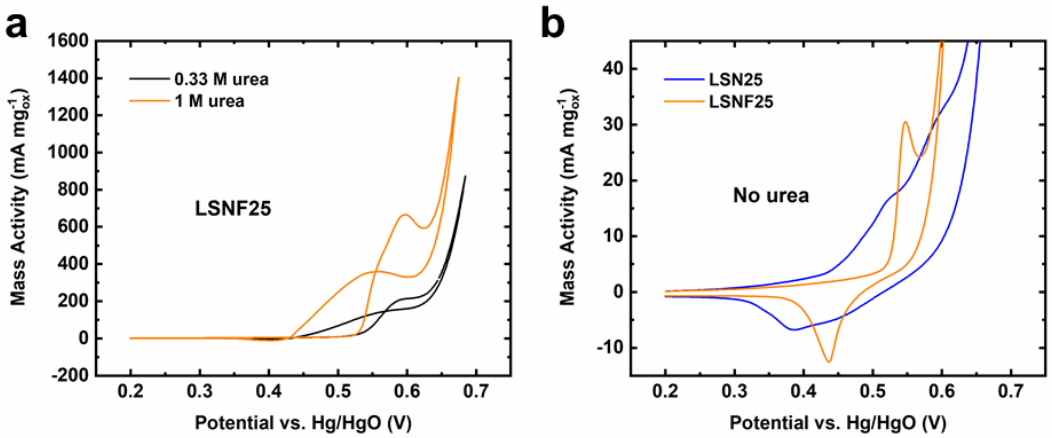

Figure C.8: Urea oxidation activities and Ni redox of LSNF30.

(a) Catalytic activities of LSNF30 for the electrooxidation of urea in 1 M KOH containing either 0.33 M or 1 M urea. (b) Oxidation and reduction surface redox reactions of LSNF30 compared to LSN25 where CVs were performed in 1 M KOH. All CVs were performed at 10 mV s^{-1} on stationary RDEs.

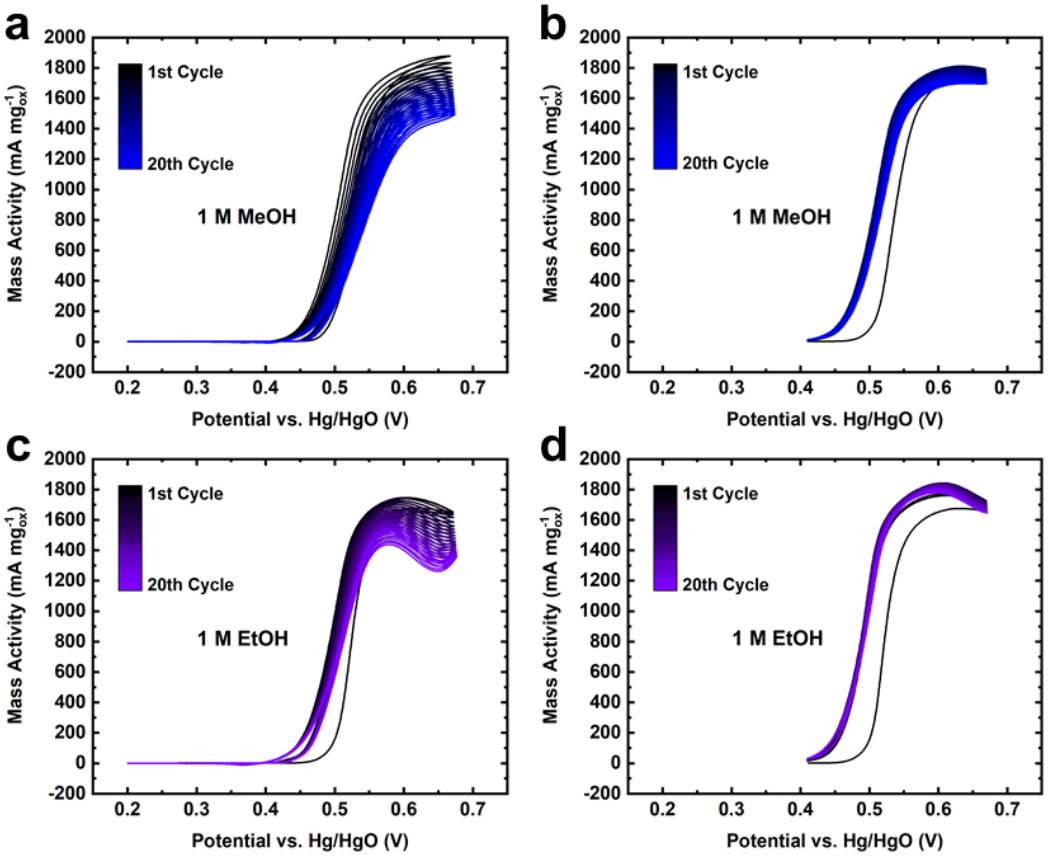

Figure C.9: Cycling stability tests for LSN25 towards methanol and ethanol electrooxidation

CVs were performed in Ar-saturated 1 M KOH with either 1 M methanol or ethanol. 20 cycles were performed over a potential range of 0.2 V to 0.7 V a) or 0.41 V to 0.7 V b) in 1 M methanol at a scan rate of 10 mV s^{-1}. The same experiments were performed in 1 M ethanol over the same potential windows of 0.2 V to 0.7 V c) or 0.41 V to 0.7 V d). CVs shown are from single, representative experiments and all measurements were performed in triplicate.

C.2: Supplementary Tables

Sample	Composition	BET Surface Area ($m^2\ g^{-1}$)	Ni Oxidation State from XPS	Ni Oxidation State from Iodometry	Oxygen Excess (δ)
LSN50	$LaSrNiO_{4+\delta}$	2.8	2.1	3.21 ± 0.05	0.103 ± 0.023
LSN37	$La_{0.75}Sr_{1.25}NiO_{4+\delta}$	2.8	2.1	3.39 ± 0.01	0.069 ± 0.006
LSN25	$La_{0.5}Sr_{1.5}NiO_{4+\delta}$	2.5	2.1	3.54 ± 0.03	0.018 ± 0.013
LSNF25	$La_{0.5}Sr_{1.5}Ni_{0.7}Fe_{0.3}O_{4+\delta}$	5.9[2]	2.2[2]	3.58 ± 0.02[2]	0.042 ± 0.010[2]

Table C.1: Summary of physical characterization for the LSN series as well as LSNF.

Sample	Urea Mass Activity @ 0.6 V (mA/mg_{ox}) (1 M / 0.33 M)	MeOH Mass Activity @ 0.6 V (mA/mg_{ox})	EtOH Mass Activity @ 0.6 V (mA/mg_{ox})	Urea Specific Activity @ 0.6 V (mA/cm_{ox}^2) (1 M / 0.33 M)	MeOH Specific Activity @ 0.6 V (mA/cm_{ox}^2)	EtOH Specific Activity @ 0.6 V (mA/cm_{ox}^2)
LSN50	184 ± 26 / 78 ± 15	661 ± 40	509 ± 41	6.6 ± 0.9 / 2.8 ± 0.5	23.6 ± 1.4	18.2 ± 1.5
LSN37	394 ± 18 / 190 ± 19	1363 ± 33	1012 ± 197	14.1 ± 0.6 / 6.8 ± 0.7	45.7 ± 1.2	36.1 ± 7.0
LSN25	1252 ± 126 / 588 ± 16	1554 ± 102	1547 ± 143	50.1 ± 5.0 / 23.5 ± 0.7	62.2 ± 4.1	61.9 ± 5.7
LSNF25	650 ± 13 / 131 ± 14	-	-	11.0 ± 0.2 / 2.2 ± 0.2	-	-
$LaNiO_3$	314 ± 20 / 323 ± 115	-	-	5.8 ± 0.4 / 6.0 ± 2.1	-	-
NiO	267 ± 16 / 73 ± 22	-	-	6.4 ± 0.4 / 1.7 ± 0.5	-	-

Table C.2: Summary of electrochemical characterization for the LSN series as well as LSNF, $LaNiO_3$, and NiO.

C.3: References

1. Qiao, L.; Bi, X. Direct Observation of Ni^{3+} and Ni^{2+} in Correlated $LaNiO_{3-\delta}$ Films. *EPL* **2011**, *93* (5), 57002.

2. Forslund, R. P.; Hardin, W. G.; Rong, X.; Abakumov, A. M.; Filimonov, D.; Alexander, C. T.; Mefford, J. T.; Iyer, H.; Kolpak, A. M.; Johnston, K. P.; et al. Exceptional Electrocatalytic Oxygen Evolution via Tunable Charge Transfer Interactions in $La_{0.5}Sr_{1.5}Ni_{1-x}Fe_xO_{4\pm\delta}$ Ruddlesden-Popper Oxides. *Nature Communications* **2018**, *9* (1), 3150.

APPENDIX D: COMPARISON OF PEROVSKITE AND PEROVSKITE DERIVATIVES FOR USE IN ANION-BASED PSEUDOCAPACITOR APPLICATIONS

D.1: Supplementary Figures

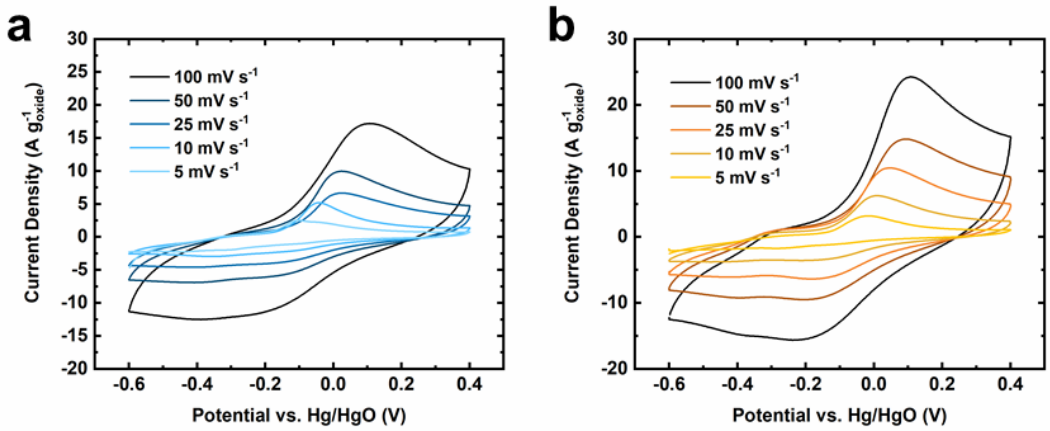

Figure D.1: Electrochemical pseudocapacitance of $CaMnO_{3.11}$ and $Ca_2MnO_{3.85}$

(a) CVs of CMO performed at multiple scan rates over a 1 V window. (b) CVs of CMO RP performed at multiple scan rates over a 1 V window. All CVs were performed in Ar-saturated 1 M KOH and in triplicate.

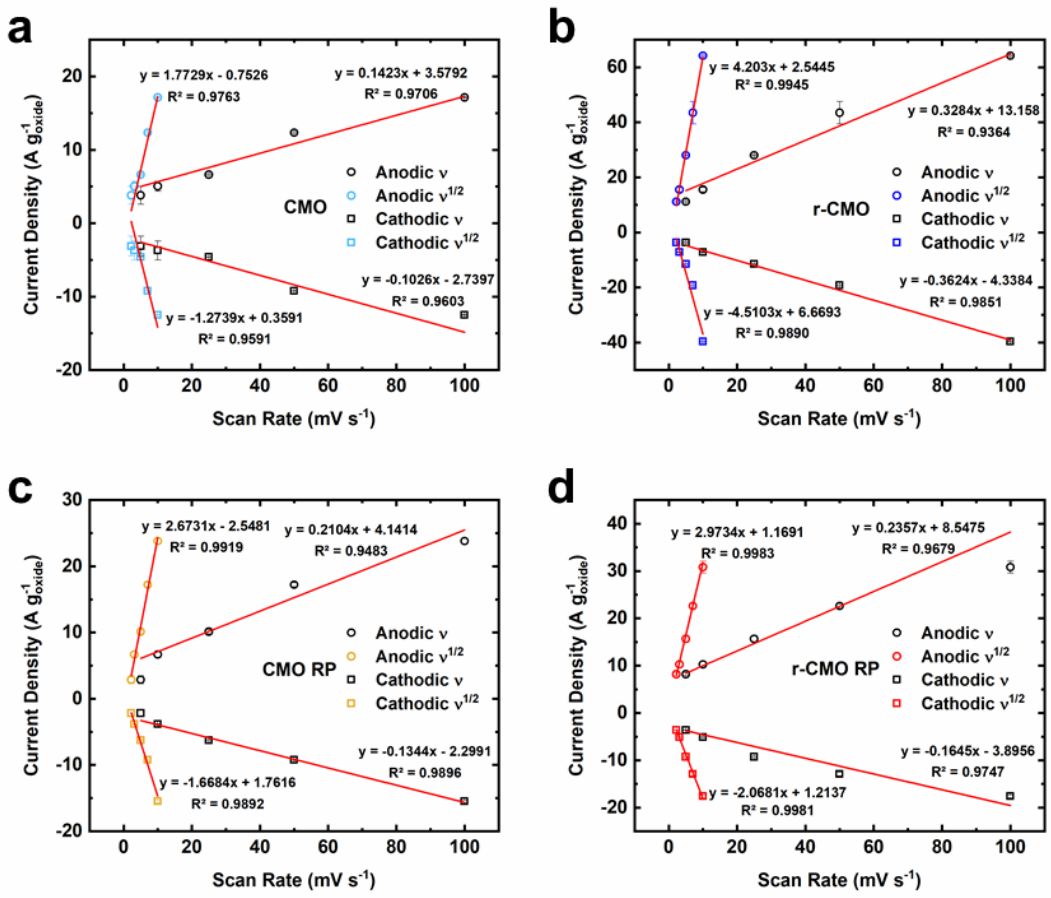

Figure D.2: Comparison of diffusion limited processes versus charge transfer limitations in $Ca_{n+1}Mn_nO_{3n+1-\delta}$ materials.

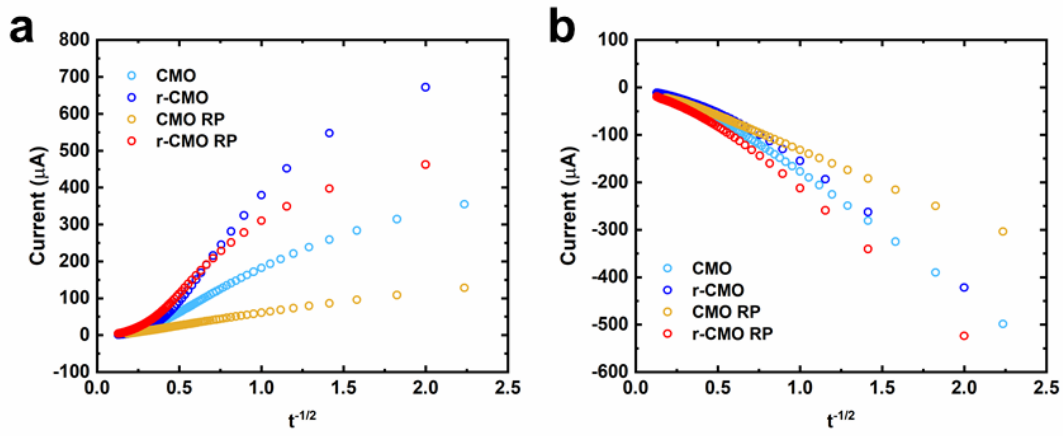

Figure D.3: Electrochemical measurement of oxygen diffusion rates in $Ca_{n+1}Mn_nO_{3n+1-\delta}$ materials.

(a) Chronoamperometry to measure oxygen intercalation into the bulk of pseudocapacitive materials performed at potentials 50 mV more positive of the largest anodic peak at 10 mV s^{-1} for each material from Figures 5.2 and A4.2. (b) Chronoamperometry to measure oxygen deintercalation from the bulk of pseudocapacitive materials performed at potentials 50 mV more negative of the largest cathodic peak at 10 mV s^{-1} for each material from Figures 5.2 and A4.2. All measurements were performed in Ar-saturated 1 M KOH and in triplicate

D.2: Supplementary Tables

Sample	Composition	Intercalation Oxygen Diffusion Rate (cm^2 s^{-1})	Deintercalation Oxygen Diffusion Rate (cm^2 s^{-1})
CMO	$CaMnO_{3.11}$	1.88E-11 ± 5.7E-12	2.44E-11 ± 3.6E-12
r-CMO	$CaMnO_{2.53}$	2.64E-11 ± 2.8E-12	3.71E-11 ± 1.2E-12
CMO RP	$Ca_2MnO_{3.92}$	3.54E-12 ± 1.4E-12	1.68E-12 ± 3.6E-13
r-CMO RP	$Ca_2MnO_{3.61}$	1.60E-11 ± 8.6E-14	1.44E-11 ± 4.9E-14

Table D.1: Electrochemical oxygen diffusion rates in $Ca_{n+1}Mn_nO_{3n+1-\delta}$ materials.

Bibliography

1. Cheng, F. & Chen, J. Metal-air batteries: from oxygen reduction electrochemistry to cathode catalysts. *Chem Soc Rev* **41**, 2172–2192 (2012).

2. Zhu, H., Zhang, P. & Dai, S. Recent Advances of Lanthanum-Based Perovskite Oxides for Catalysis. *ACS Catal.* **5**, 6370–6385 (2015).

3. Rollinson, A. N., Jones, J., Dupont, V. & Twigg, M. V. Urea as a hydrogen carrier: a perspective on its potential for safe, sustainable and long-term energy supply. *Energy Environ. Sci.* **4**, 1216–1224 (2011).

4. Evans, U. R. Cathodic Reduction of Oxygen in Fuel Cells and Corrosion Cells. *Nature* **218**, 602–603 (1968).

5. Ge, X. *et al.* Oxygen Reduction in Alkaline Media: From Mechanisms to Recent Advances of Catalysts. *ACS Catal.* **5**, 4643–4667 (2015).

6. Gorlin, Y. & Jaramillo, T. F. A Bifunctional Nonprecious Metal Catalyst for Oxygen Reduction and Water Oxidation. *J. Am. Chem. Soc.* **132**, 13612–13614 (2010).

7. Tejuca, L. G. Properties of perovskite-type oxides I: Bulk and surface studies. *Journal of the Less Common Metals* **146**, 251–259 (1989).

8. Tejuca, L. G., Fierro, J. L. G. & Tascón, J. M. D. Structure and Reactivity of Perovskite-Type Oxides. in *Advances in Catalysis* (eds. Eley, D. D., Pines, H. & Weisz, P. B.) **36**, 237–328 (Academic Press, 1989).

9. Meadowcroft, D. B. Low-cost Oxygen Electrode Material. *Nature* **226**, 847–848 (1970).

10. Suntivich, J., May, K. J., Gasteiger, H. A., Goodenough, J. B. & Shao-Horn, Y. A Perovskite Oxide Optimized for Oxygen Evolution Catalysis from Molecular Orbital Principles. *Science* **334**, 1383–1385 (2011).

11. Sharma, I. B. & Singh, D. Solid state chemistry of Ruddlesden-Popper type complex oxides. *Bull. Mater. Sci.* **21**, 363–374 (1998).

12. Gilev, A. R., Kiselev, E. A. & Cherepanov, V. A. Homogeneity range, oxygen nonstoichiometry, thermal expansion and transport properties of $La_{2-x}Sr_xNi_{1-y}Fe_yO_{4+\delta}$. *RSC Adv.* **6**, 72905–72917 (2016).

13. Goodenough, J. B. & Cushing, B. L. Oxide-based ORR catalysts. in *Handbook of Fuel Cells* (American Cancer Society, 2010).

14. Matsumoto, Y. & Sato, E. Electrocatalytic properties of transition metal oxides for oxygen evolution reaction. *Materials Chemistry and Physics* **14**, 397–426 (1986).

15. Matsumoto, Y., Yoneyama, H. & Tamura, H. Influence of the nature of the conduction band of transition metal oxides on catalytic activity for oxygen reduction. *Journal of Electroanalytical Chemistry and Interfacial Electrochemistry* **83**, 237–243 (1977).

16. Matsumoto, Y., Manabe, H. & Sato, E. Oxygen Evolution on $La_{1-x}Sr_xCoO_3$ Electrodes in Alkaline Solutions. *J. Electrochem. Soc.* **127**, 811–814 (1980).

17. Matsumoto, Y., Yamada, S., Nishida, T. & Sato, E. Oxygen Evolution on $La_{1-x}Sr_xFe_{1-y}Co_yO_3$ Series Oxides. *J. Electrochem. Soc.* **127**, 2360–2364 (1980).

18. Bockris, J. O. & Otagawa, T. Mechanism of oxygen evolution on perovskites. *J. Phys. Chem.* **87**, 2960–2971 (1983).

19. Bockris, J. O. & Otagawa, T. The Electrocatalysis of Oxygen Evolution on Perovskites. *J. Electrochem. Soc.* **131**, 290–302 (1984).

20. Shao, Z. & Haile, S. M. A high-performance cathode for the next generation of solid-oxide fuel cells. *Nature* **431**, 170–173 (2004).

21. Suntivich, J. *et al.* Design principles for oxygen-reduction activity on perovskite oxide catalysts for fuel cells and metal–air batteries. *Nature Chemistry* **3**, 546–550 (2011).

22. Mefford, J. T. *et al.* Water electrolysis on $La_{1-x}Sr_xCoO_{3-\delta}$ perovskite electrocatalysts. *Nat. Commun.* **7**, 11053 (2016).

23. Grimaud, A. *et al.* Activating lattice oxygen redox reactions in metal oxides to catalyse oxygen evolution. *Nat. Chem.* **9**, 457–465 (2017).

24. Lan, R., Tao, S. & Irvine, J. T. S. A direct urea fuel cell – power from fertiliser and waste. *Energy Environ. Sci.* **3**, 438–441 (2010).

25. Daramola, D. A., Singh, D. & Botte, G. G. Dissociation Rates of Urea in the Presence of NiOOH Catalyst: A DFT Analysis. *J. Phys. Chem. A* **114**, 11513–11521 (2010).

26. Vedharathinam, V. & Botte, G. G. Direct evidence of the mechanism for the electro-oxidation of urea on $Ni(OH)_2$ catalyst in alkaline medium. *Electrochim. Acta* **108**, 660–665 (2013).

27. Vedharathinam, V. & Botte, G. G. Understanding the electro-catalytic oxidation mechanism of urea on nickel electrodes in alkaline medium. *Electrochim. Acta* **81**, 292–300 (2012).

28. Zhang, Z., Liu, J., Gu, J., Su, L. & Cheng, L. An overview of metal oxide materials as electrocatalysts and supports for polymer electrolyte fuel cells. *Energy Environ. Sci.* **7**, 2535–2558 (2014).

29. Antolini, E. Catalysts for direct ethanol fuel cells. *Journal of Power Sources* **170**, 1–12 (2007).

30. Mizushima, K., Jones, P. C., Wiseman, P. J. & Goodenough, J. B. Li_xCoO_2 (0<x<-1): A new cathode material for batteries of high energy density. *Materials Research Bulletin* **15**, 783–789 (1980).

31. Bard, A. J. & Faulkner, L. R. *Electrochemical Methods: Fundamentals and Applications*. (Wiley, 2000).

32. Conway, B. E. *Electrochemical Supercapacitors*. (Springer, 1999).

33. Zhang, L. L., Zhou, R. & Zhao, X. S. Graphene-based materials as supercapacitor electrodes. *J. Mater. Chem.* **20**, 5983–5992 (2010).

34. Wang, H., Casalongue, H. S., Liang, Y. & Dai, H. $Ni(OH)_2$ Nanoplates Grown on Graphene as Advanced Electrochemical Pseudocapacitor Materials. *J. Am. Chem. Soc.* **132**, 7472–7477 (2010).

35. Zolfaghari, A., Chayer, M. & Jerkiewicz, G. Energetics of the Underpotential Deposition of Hydrogen on Platinum Electrodes I. Absence of Coadsorbed Species. *J. Electrochem. Soc.* **144**, 3034–3041 (1997).

36. Marković, N. M., Lucas, C. A., Gasteiger, H. A. & Ross, P. N. Bromide adsorption on Pt(100): rotating ring-Pt(100) disk electrode and surface X-ray scattering measurements. *Surface Science* **365**, 229–240 (1996).

37. Brezesinski, T., Wang, J., Tolbert, S. H. & Dunn, B. Ordered mesoporous α-MoO_3 with iso-oriented nanocrystalline walls for thin-film pseudocapacitors. *Nature Materials* **9**, 146–151 (2010).

38. Mefford, J. T., Hardin, W. G., Dai, S., Johnston, K. P. & Stevenson, K. J. Anion charge storage through oxygen intercalation in $LaMnO_3$ perovskite pseudocapacitor electrodes. *Nat. Mater.* **13**, 726–732 (2014).

39. Conesa, J. C. Electronic Structure of the (Undoped and Fe-Doped) NiOOH O<sub>2 Evolution Electrocatalyst. *J. Phys. Chem. C* **120**, 18999–19010 (2016).

40. Corrigan, D. A. The Catalysis of the Oxygen Evolution Reaction by Iron Impurities in Thin Film Nickel Oxide Electrodes. *J. Electrochem. Soc.* **134**, 377–384 (1987).

41. Trotochaud, L., Young, S. L., Ranney, J. K. & Boettcher, S. W. Nickel–Iron Oxyhydroxide Oxygen-Evolution Electrocatalysts: The Role of Intentional and Incidental Iron Incorporation. *J. Am. Chem. Soc.* **136**, 6744–6753 (2014).

42. Dionigi, F. & Strasser, P. NiFe-Based (Oxy)hydroxide Catalysts for Oxygen Evolution Reaction in Non-Acidic Electrolytes. *Adv. Energy Mater.* **6**, (2016).

43. Chen, J. Y. C. *et al.* Operando Analysis of NiFe and Fe Oxyhydroxide Electrocatalysts for Water Oxidation: Detection of Fe^{4+} by Mössbauer Spectroscopy. *J. Am. Chem. Soc.* **137**, 15090–15093 (2015).

44. Görlin, M. *et al.* Tracking Catalyst Redox States and Reaction Dynamics in Ni–Fe Oxyhydroxide Oxygen Evolution Reaction Electrocatalysts: The Role of Catalyst Support and Electrolyte pH. *J. Am. Chem. Soc.* **139**, 2070–2082 (2017).

45. Hunter, B. M., Gray, H. B. & Müller, A. M. Earth-Abundant Heterogeneous Water Oxidation Catalysts. *Chem. Rev.* **116**, 14120–14136 (2016).

46. Hardin, W. G. *et al.* Tuning the Electrocatalytic Activity of Perovskites through Active Site Variation and Support Interactions. *Chem. Mater.* **26**, 3368–3376 (2014).

47. Structure, Properties and Preparation of Perovskite-Type Compounds. in (ed. Galasso, F. S.) iv (Pergamon, 1969).

48. Yagi, S. *et al.* Covalency-reinforced oxygen evolution reaction catalyst. *Nat. Commun.* **6**, 9249 (2015).

49. Zhou, W., Zhao, M., Liang, F., Smith, S. C. & Zhu, Z. High activity and durability of novel perovskite electrocatalysts for water oxidation. *Mater. Horiz.* **2**, 495–501 (2015).

50. Man, I. C. *et al.* Universality in Oxygen Evolution Electrocatalysis on Oxide Surfaces. *ChemCatChem* **3**, 1159–1165 (2011).

51. Rong, X., Parolin, J. & Kolpak, A. M. A Fundamental Relationship between Reaction Mechanism and Stability in Metal Oxide Catalysts for Oxygen Evolution. *ACS Catal.* **6**, 1153–1158 (2016).

52. Takeda, Y. *et al.* Synthesis of $SrNiO_3$ and related compound, $Sr_2Ni_2O_5$. *J. Inorg. Nucl. Chem.* **34**, 1599–1601 (1972).

53. Oliveira, F. S., Pimentel, P. M., Oliveira, R. M. P. B., Melo, D. M. A. & Melo, M. A. F. Effect of lanthanum replacement by strontium in lanthanum nickelate crystals synthetized using gelatin as organic precursor. *Mater. Lett.* **64**, 2700–2703 (2010).

54. Seki, H., Saito, T. & Shimakawa, Y. High Pressure Synthesis of $SrFe_{1-x}Ni_xO_3$. *J. Jpn. Soc. Powder Powder Metall.* **63**, 609–612 (2016).

55. Amow, G., Davidson, I. J. & Skinner, S. J. A comparative study of the Ruddlesden-Popper series, $La_{n+1}Ni_nO_{3n+1}$ (n=1, 2 and 3), for solid-oxide fuel-cell cathode applications. *Solid State Ion.* **177**, 1205–1210 (2006).

56. Zhang, Z. & Greenblatt, M. Synthesis, Structure, and Properties of $Ln_4Ni_3O_{10-\delta}$ (Ln = La, Pr, and Nd). *J. Solid State Chem.* **117**, 236–246 (1995).

57. Takeda, Y. *et al.* Crystal chemistry and physical properties of $La_{2-x}Sr_xNiO_4$ ($0 \leq x \leq 1.6$). *Mater. Res. Bull.* **25**, 293–306 (1990).

58. Benloucif, R., Nguyen, N., Greneche, J. M. & Raveau, B. $La_{2-2x}Sr_{2x}Ni_{1-x}Fe_xO_{4-(x2)+\delta}$: Magnetic and electron transport properties. *J. Phys. Chem. Solids* **50**, 435–440 (1989).

59. Rao, C. N. R., Ganguly, P., Singh, K. K. & Ram, R. A. M. A comparative study of the magnetic and electrical properties of perovskite oxides and the corresponding two-dimensional oxides of K_2NiF_4 structure. *J. Solid State Chem.* **72**, 14–23 (1988).

60. F. Howlett, J. *et al.* Electronic structure, reactivity and solid-state chemistry of $La_{2-x}Sr_xNi_{1-y}Fe_yO_{4+\delta}$. *Faraday Discuss.* **105**, 337–354 (1996).

61. Cohen, R. E. Origin of ferroelectricity in perovskite oxides. *Nature* **358**, 136–138 (1992).

62. Kakihana, M. & Yoshimura, M. Synthesis and Characteristics of Complex Multicomponent Oxides Prepared by Polymer Complex Method. *Bull. Chem. Soc. Jpn.* **72**, 1427–1443 (1999).

63. Akhade, S. A. & Kitchin, J. R. Effects of strain, *d* -band filling, and oxidation state on the surface electronic structure and reactivity of 3 *d* perovskite surfaces. *J. Chem. Phys.* **137**, 084703 (2012).

64. Corrigan, D. A., Conell, R. S., Fierro, C. A. & Scherson, D. A. In-situ Moessbauer study of redox processes in a composite hydroxide of iron and nickel. *J. Phys. Chem.* **91**, 5009–5011 (1987).

65. Lee, Y.-L. *et al.* Kinetics of Oxygen Surface Exchange on Epitaxial Ruddlesden–Popper Phases and Correlations to First-Principles Descriptors. *J. Phys. Chem. Lett.* **7**, 244–249 (2016).

66. Merkle, R., Mastrikov, Y. A., Kotomin, E. A., Kuklja, M. M. & Maier, J. First Principles Calculations of Oxygen Vacancy Formation and Migration in $Ba_{1-x}Sr_xCo_{1-y}Fe_yO_{3-\delta}$ Perovskites. *J. Electrochem. Soc.* **159**, B219–B226 (2011).

67. Erat, S. *et al.* Entanglement of charge transfer, hole doping, exchange interaction, and octahedron tilting angle and their influence on the conductivity of $La_{1-x}Sr_xFe_{0.75}Ni_{0.25}O_{3-\delta}$: A combination of x-ray spectroscopy and diffraction. *J. Appl. Phys.* **108**, 124906 (2010).

68. Mefford, J. T., Hardin, W. G., Dai, S., Johnston, K. P. & Stevenson, K. J. Anion charge storage through oxygen intercalation in $LaMnO_3$ perovskite pseudocapacitor electrodes. *Nat Mater* **13**, 726–732 (2014).

69. Fabbri, E. *et al.* Dynamic surface self-reconstruction is the key of highly active perovskite nano-electrocatalysts for water splitting. *Nature Materials* **16**, 925–931 (2017).

70. Louie, M. W. & Bell, A. T. An Investigation of Thin-Film Ni–Fe Oxide Catalysts for the Electrochemical Evolution of Oxygen. *J. Am. Chem. Soc.* **135**, 12329–12337 (2013).

71. Forslund, R. P. *et al.* Nanostructured $LaNiO_3$ Perovskite Electrocatalyst for Enhanced Urea Oxidation. *ACS Catal.* **6**, 5044–5051 (2016).

72. Bhavaraju, S., DiCarlo, J. F., Scarfe, D. P., Jacobson, A. J. & Buttrey, D. J. Electrochemical oxygen intercalation in $La_2NiO_{4+\delta}$ crystals. *Solid State Ion.* **86**, 825–831 (1996).

73. Sreedhar, K. & Honig, J. M. Low-Temperature Electron Transport Properties of $La_{2-x}Sr_xNiO_4$ with $0.5 \leq x \leq 1.3$. *J. Solid State Chem.* **111**, 147–150 (1994).

74. Torrance, J. B., Lacorre, P., Nazzal, A. I., Ansaldo, E. J. & Niedermayer, C. Systematic study of insulator-metal transitions in perovskites $RNiO_3$ (R=Pr,Nd,Sm,Eu) due to closing of charge-transfer gap. *Phys. Rev. B* **45**, 8209–8212 (1992).

75. Falcón, H., Carbonio, R. E. & Fierro, J. L. G. Correlation of Oxidation States in $LaFe_xNi_{1-x}O_{3+\delta}$ Oxides with Catalytic Activity for H_2O_2 Decomposition. *J. Catal.* **203**, 264–272 (2001).

76. Ritzmann, A. M., Muñoz-García, A. B., Pavone, M., Keith, J. A. & Carter, E. A. Ab Initio DFT+U Analysis of Oxygen Vacancy Formation and Migration in $La_{1-x}Sr_xFeO_{3-\delta}$ (x = 0, 0.25, 0.50). *Chem. Mater.* **25**, 3011–3019 (2013).

77. Mogni, L. *et al.* Synthesis, crystal chemistry and physical properties of the Ruddlesden–Popper phases $Sr_3Fe_{2-x}Ni_xO_{7-\delta}$ ($0 \leqslant x \leqslant 1.0$). *J. Solid State Chem.* **178**, 1559–1568 (2005).

78. Duan, Y. *et al.* Tailoring the Co 3d-O 2p Covalency in $LaCoO_3$ by Fe Substitution To Promote Oxygen Evolution Reaction. *Chem. Mater.* **29**, 10534–10541 (2017).

79. Zhu, Y. *et al.* $SrNb_{0.1}Co_{0.7}Fe_{0.2}O_{3-\delta}$ Perovskite as a Next-Generation Electrocatalyst for Oxygen Evolution in Alkaline Solution. *Angew. Chem. Int. Ed. Engl.* **127**, 3969–3973 (2015).

80. Boggs, B. K., King, R. L. & Botte, G. G. Urea electrolysis: direct hydrogen production from urine. *Chem. Commun.* 4859–4861 (2009).

81. King, R. L. & Botte, G. G. Investigation of multi-metal catalysts for stable hydrogen production via urea electrolysis. *J. Power Sources* **196**, 9579–9584 (2011).

82. Wang, D., Yan, W., Vijapur, S. H. & Botte, G. G. Enhanced electrocatalytic oxidation of urea based on nickel hydroxide nanoribbons. *J. Power Sources* **217**, 498–502 (2012).

83. Wang, D., Yan, W. & Botte, G. G. Exfoliated nickel hydroxide nanosheets for urea electrolysis. *Electrochemistry Communications* **13**, 1135–1138 (2011).

84. Yan, W., Wang, D. & Botte, G. G. Nickel and cobalt bimetallic hydroxide catalysts for urea electro-oxidation. *Electrochim. Acta* **61**, 25–30 (2012).

85. Yan, W., Wang, D., Diaz, L. A. & Botte, G. G. Nickel nanowires as effective catalysts for urea electro-oxidation. *Electrochim. Acta* **134**, 266–271 (2014).

86. Liang, Y., Liu, Q., Asiri, A. M. & Sun, X. Enhanced electrooxidation of urea using $NiMoO_4 \cdot xH2O$ nanosheet arrays on Ni foam as anode. *Electrochim. Acta* **153**, 456–460 (2015).

87. Hardin, W. G. *et al.* Highly Active, Nonprecious Metal Perovskite Electrocatalysts for Bifunctional Metal–Air Battery Electrodes. *J. Phys. Chem. Lett.* **4**, 1254–1259 (2013).

88. Bezerra, Â. C. S., de Sá, E. L. & Nart, F. C. In Situ Vibrational Study of the Initial Steps during Urea Electrochemical Oxidation. *J. Phys. Chem. B* **101**, 6443–6449 (1997).

89. Wang, G. *et al.* Energy-efficient electrolytic hydrogen production assisted by coupling urea oxidation with a pH-gradient concentration cell. *Chem. Commun.* **54**, 2603–2606 (2018).

90. Tong, Y. *et al.* Oxygen Vacancies Confined in Nickel Molybdenum Oxide Porous Nanosheets for Promoted Electrocatalytic Urea Oxidation. *ACS Catal.* **8**, 1–7 (2018).

91. Kakati, N., Maiti, J., Lee, K. S., Viswanathan, B. & Yoon, Y. S. Hollow Sodium Nickel Fluoride Nanocubes Deposited MWCNT as An Efficient Electrocatalyst for Urea Oxidation. *Electrochimica Acta* **240**, 175–185 (2017).

92. Tran, T. Q. N., Yoon, S. W., Park, B. J. & Yoon, H. H. CeO_2-modified $LaNi_{0.6}Fe_{0.4}O_3$ perovskite and MWCNT nanocomposite for electrocatalytic oxidation and detection of urea. *Journal of Electroanalytical Chemistry* **818**, 76–83 (2018).

93. Wang, L. *et al.* Ni–WC/C nanocluster catalysts for urea electrooxidation. *Journal of Power Sources* **264**, 282–289 (2014).

94. Wang, L. *et al.* Enhanced activity of urea electrooxidation on nickel catalysts supported on tungsten carbides/carbon nanotubes. *Journal of Power Sources* **280**, 550–554 (2015).

95. Song, X. *et al.* Nickel phosphate-based materials with excellent durability for urea electro-oxidation. *Electrochimica Acta* **251**, 284–292 (2017).

96. Das, G., Tesfaye, R. M., Won, Y. & Yoon, H. H. NiO-Fe2O3 based graphene aerogel as urea electrooxidation catalyst. *Electrochimica Acta* **237**, 171–176 (2017).

97. Alexander, C. T., Abakumov, A. M., Forslund, R. P., Johnston, K. P. & Stevenson, K. J. Role of the Carbon Support on the Oxygen Reduction and Evolution Activities in $LaNiO_3$ Composite Electrodes in Alkaline Solution. *ACS Appl. Energy Mater.* **1**, 1549–1558 (2018).

98. Forslund, R. P. *et al.* Exceptional electrocatalytic oxygen evolution via tunable charge transfer interactions in $La_{0.5}Sr_{1.5}Ni_{1-x}Fe_xO_{4\pm\delta}$ Ruddlesden-Popper oxides. *Nature Communications* **9**, 3150 (2018).

99. Levasseur, B. & Kaliaguine, S. Methanol oxidation on $LaBO_3$ (B=Co, Mn, Fe) perovskite-type catalysts prepared by reactive grinding. *Applied Catalysis A: General* **343**, 29–38 (2008).

100. Singh, R. N. *et al.* Perovskite-type $La_{2-x}Sr_xNiO_4$ ($0 \leq x \leq 1$) as active anode materials for methanol oxidation in alkaline solutions. *Electrochimica Acta* **53**, 2322–2330 (2008).

101. Medarde, M. & Rodríguez-Carvajal, J. Oxygen vacancy ordering in $La_{2-x}Sr_xNiO_{4-\delta}$ ($0 \leq \leq 0.5$): the crystal structure and defects investigated by neutron diffraction. *Z. Phys. B* **102**, 307–315 (1997).

102. Millburn, J. E., Green, M. A., Neumann, D. A. & Rosseinsky, M. J. Evolution of the Structure of the K_2NiF_4 Phases $La_{2-x}Sr_xNiO_{4+\delta}$ with Oxidation State: Octahedral Distortion and Phase Separation ($0.2 \leq x \leq 1.0$). *Journal of Solid State Chemistry* **145**, 401–420 (1999).

103. Aguadero, A. *et al.* Effect of Sr content on the crystal structure and electrical properties of the system $La_{2-x}Sr_xNiO_{4+\delta}$ ($0 \leq x \leq 1$). *Dalton Trans.* 4377–4383 (2006). doi:10.1039/B606316K

104. Lan, A. & Mukasyan, A. S. Perovskite-Based Catalysts for Direct Methanol Fuel Cells. *J. Phys. Chem. C* **111**, 9573–9582 (2007).

105. Zhou, J.-S., Marshall, L. G. & Goodenough, J. B. Mass enhancement versus Stoner enhancement in strongly correlated metallic perovskites: $LaNiO_3$ and $LaCuO_3$. *Phys. Rev. B* **89**, 245138 (2014).

106. Miller, J. R. & Simon, P. Electrochemical Capacitors for Energy Management. *Science* **321**, 651–652 (2008).

107. Chernova, N. A., Roppolo, M., Dillon, A. C. & Whittingham, M. S. Layered vanadium and molybdenum oxides: batteries and electrochromics. *J. Mater. Chem.* **19**, 2526–2552 (2009).

108. Brezesinski, K. *et al.* Pseudocapacitive Contributions to Charge Storage in Highly Ordered Mesoporous Group V Transition Metal Oxides with Iso-Oriented Layered Nanocrystalline Domains. *J. Am. Chem. Soc.* **132**, 6982–6990 (2010).

109. Xiong, H. *et al.* Self-Improving Anode for Lithium-Ion Batteries Based on Amorphous to Cubic Phase Transition in TiO_2 Nanotubes. *J. Phys. Chem. C* **116**, 3181–3187 (2012).

110. Frackowiak, E. & Béguin, F. Carbon materials for the electrochemical storage of energy in capacitors. *Carbon* **39**, 937–950 (2001).

111. Simon, P. & Gogotsi, Y. Materials for electrochemical capacitors. *Nature Materials* **7**, 845–854 (2008).

112. Wang, G., Zhang, L. & Zhang, J. A review of electrode materials for electrochemical supercapacitors. *Chem. Soc. Rev.* **41**, 797–828 (2012).

113. Wang, F. *et al.* Electrode materials for aqueous asymmetric supercapacitors. *RSC Adv.* **3**, 13059–13084 (2013).

114. Gu, J. *et al.* Asymmetric capacitors based on TiO_2 and mesoporous MnO_2 electrodes using neutral aqueous electrolyte. *J Nanopart Res* **19**, 322 (2017).

115. Liu, Y., Dinh, J., Tade, M. O. & Shao, Z. Design of Perovskite Oxides as Anion-Intercalation-Type Electrodes for Supercapacitors: Cation Leaching Effect. *ACS Appl. Mater. Interfaces* **8**, 23774–23783 (2016).

116. Che, W. *et al.* Perovskite $LaNiO_{3-\delta}$ oxide as an anion-intercalated pseudocapacitor electrode. *Journal of Alloys and Compounds* **731**, 381–388 (2018).

117. Lang, X., Mo, H., Hu, X. & Tian, H. Supercapacitor performance of perovskite $La_{1-x}Sr_xMnO_3$. *Dalton Trans.* **46**, 13720–13730 (2017).

118. Ali, G. A. M., Wahba, O. A. G., Hassan, A. M., Fouad, O. A. & Feng Chong, K. Calcium-based nanosized mixed metal oxides for supercapacitor application. *Ceramics International* **41**, 8230–8234 (2015).

119. Poeppelmeier, K. R., Leonowicz, M. E. & Longo, J. M. $CaMnO_{2.5}$ and $Ca_2MnO_{3.5}$: New oxygen-defect perovskite-type oxides. *Journal of Solid State Chemistry* **44**, 89–98 (1982).

120. Poeppelmeier, K. R., Leonowicz, M. E., Scanlon, J. C., Longo, J. M. & Yelon, W. B. Structure determination of $CaMnO_3$ and $CaMnO_{2.5}$ by X-ray and neutron methods. *Journal of Solid State Chemistry* **45**, 71–79 (1982).

121. Kim, J., Chen, X., Pan, Y.-T., Shih, P.-C. & Yang, H. W-Doped $CaMnO_{2.5}$ and $CaMnO_3$ Electrocatalysts for Enhanced Performance in Oxygen Evolution and Reduction Reactions. *J. Electrochem. Soc.* **164**, F1074–F1080 (2017).

122. Van Buren, F. R., Broers, G. H. J., Bouman, A. J. & Boesveld, C. An electrochemical method for the determination of oxygen ion diffusion coefficients in $La_{1-x}Sr_xCoO_{3-y}$ compounds. *Journal of Electroanalytical Chemistry and Interfacial Electrochemistry* **87**, 389–394 (1978).

123. Van Buren, F. R., Broers, G. H. J., Bouman, A. J. & Boesveld, C. The electrochemical determination of oxygen ion diffusion coefficients in $La_{0.50}Sr_{0.50}CoO_{3-y}$: Experimental results and related properties. *Journal of Electroanalytical Chemistry and Interfacial Electrochemistry* **88**, 353–361 (1978).

124. Kobussen, A. G. C., van Buren, F. R. & Broers, G. H. J. The influence of the particle size distribution on the measurement of oxygen ion diffusion coefficients in $La_{0.50}Sr_{0.50}CoO_{3-y}$. *Journal of Electroanalytical Chemistry and Interfacial Electrochemistry* **91**, 211–217 (1978).

125. Yu, P., Popov, B. N., Ritter, J. A. & White, R. E. Determination of the Lithium Ion Diffusion Coefficient in Graphite. *J. Electrochem. Soc.* **146**, 8–14 (1999).

126. Wu, M.-S., Lin, G.-W. & Yang, R.-S. Hydrothermal growth of vertically-aligned ordered mesoporous nickel oxide nanosheets on three-dimensional nickel framework for

electrocatalytic oxidation of urea in alkaline medium. *J. Power Sources* **272**, 711–718 (2014).

127. Ding, R., Qi, L., Jia, M. & Wang, H. Facile synthesis of mesoporous spinel $NiCo_2O_4$ nanostructures as highly efficient electrocatalysts for urea electro-oxidation. *Nanoscale* **6**, 1369–1376 (2014).

128. Ferrari, A. C. & Basko, D. M. Raman spectroscopy as a versatile tool for studying the properties of graphene. *Nat. Nanotechnol.* **8**, 235–246 (2013).

129. Frost, R. L., Dickfos, M. J. & Jagannadha Reddy, B. Raman spectroscopy of hydroxy nickel carbonate minerals nullaginite and zaratite. *J. Raman Spectrosc.* **39**, 1250–1256 (2008).

130. Gou, G., Grinberg, I., Rappe, A. M. & Rondinelli, J. M. Lattice normal modes and electronic properties of the correlated metal $LaNiO_3$. *Phys. Rev. B* **84**, 144101 (2011).

131. Hermet, P. & Ghosez, P. First-principles study of the dynamical and nonlinear optical properties of urea single crystals. *Phys. Chem. Chem. Phys.* **12**, 835–843 (2010).

132. Qiao, L. & Bi, X. Direct observation of Ni^{3+} and Ni^{2+} in correlated $LaNiO_{3-\delta}$ films. *EPL* **93**, 57002 (2011).